Interplay of Inversion Symmetry Breaking and Spin-Orbit Coupling
–
From the Rashba Effect to Weyl Semimetals

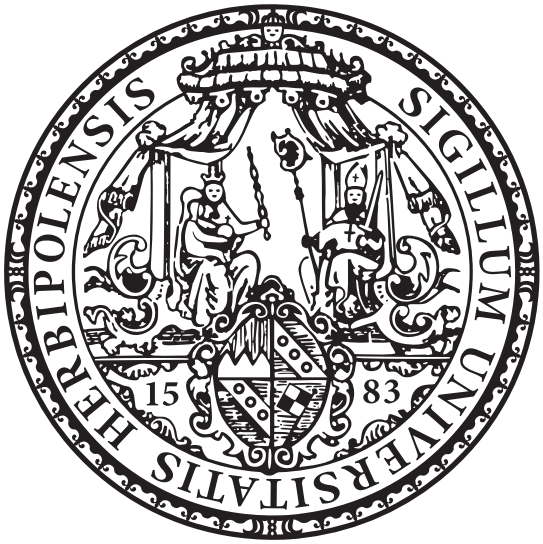

Dissertation zur Erlangung des naturwissenschaftlichen
Doktorgrades der Julius-Maximilians-Universität Würzburg

vorgelegt von

Maximilian Ünzelmann
aus Alsfeld

Würzburg 2021

Eingereicht am: 2.12.2021
bei der Fakultät für Physik und Astronomie

1. Gutachter: Prof. Dr. Friedrich Reinert
2. Gutachter: Prof. Dr. Matthias Bode
3. Gutachter: Prof. Dr. Felix Baumberger
der Dissertation

Vorsitzende(r): Prof. Dr. Vladimir Hinkov
1. Prüfer: Prof. Dr. Friedrich Reinert
2. Prüfer: Prof. Dr. Matthias Bode
3. Prüfer: Prof. Dr. Giorgio Sangiovanni
4. Prüfer: Prof. Dr. Felix Baumberger
im Promotionskolloquium

Tag des Promotionskolloquiums: 4. August 2022

Doktorurkunde ausgehändigt am:

Abstract

Breaking inversion symmetry in crystalline solids enables the formation of spin-polarized electronic states by spin-orbit coupling without the need for magnetism. A variety of interesting physical phenomena related to this effect have been intensively investigated in recent years, including the Rashba effect, topological insulators and Weyl semimetals. In this work, the interplay of inversion symmetry breaking and spin-orbit coupling and, in particular their general influence on the character of electronic states, i.e., on the spin and orbital degrees of freedom, is investigated experimentally. Two different types of suitable model systems are studied: two-dimensional surface states for which the Rashba effect arises from the inherently broken inversion symmetry at the surface, and a Weyl semimetal, for which inversion symmetry is broken in the three-dimensional crystal structure. Angle-resolved photoelectron spectroscopy provides momentum-resolved access to the spin polarization and the orbital composition of electronic states by means of photoelectron spin detection and dichroism with polarized light. The experimental results shown in this work are also complemented and supported by *ab-initio* density functional theory calculations and simple model considerations.

The Rashba effect is fundamental to the physics of two-dimensional electron systems, and deepening the understanding of its microscopic origin is at the heart of this work. In focus is a honeycomb monolayer AgTe epitaxially grown on a Ag(111) substrate. The momentum-resolved orbital texture of the AgTe-induced surface states provides strong experimental and theoretical evidence that the Rashba effect in this system relies on the ISB-induced and SOC-independent formation of a chiral orbital angular momentum structure. Since this mechanism depends on the in-plane orbital symmetry of the bands, the magnitude of the Rashba effect in them is quite different. In particular, the occurrence of Rashba-type spin splittings is directly related to a radial orbital alignment in the respective states, while in bands built from tangentially aligned orbitals, the orbital angular momentum and consequently the Rashba effect vanishes. Based on the respective photoemission intensity distribution, radially- and tangentially-aligned states can be distinguished experimentally, providing direct evidence for the mechanism. Altogether, the present experimental results reveal the validity of the theoretically predicted *orbital-driven* Rashba paradigm. The insights gained are not limited to AgTe, but give a new perspective on the Rashba effect at surfaces in general.

In non-magnetic Weyl semimetals, breaking of inversion symmetry leads to the formation Berry-flux monopoles, which can be considered as momentum space analogues to magnetic monopoles in real space. Such monopoles are called Weyl nodes and occur as crossing points between the spin-polarized valence and conduction bands in the three-dimensional bulk band structure.

In this work, bulk-sensitive soft X-ray angle-resolved photoelectron spectroscopy is used to find experimental signatures of the Berry monopoles in a paradigmatic Weyl semimetal TaAs. Further supported by density functional theory calculations, circular dichroism and spin-resolved measurements reveal a finite orbital angular momentum as well as a spin-polarization in the bulk electronic states, respectively. The occurrence of the former is – as in the case of the Rashba effect – caused by the broken inversion symmetry, suggesting a comparable mechanism for the formation of spin-polarized states also in three-dimensional bulk systems. Furthermore, the momentum-dependent modulation of the orbital angular momentum around the Weyl nodes is studied in detail. Its momentum space field configuration is found to exhibit a topologically non-trivial winding (like the Berry curvature), and the observed circular dichroism pattern shows direct signatures for such a monopole texture. In particular, it turns out that the Weyl nodes in TaAs are crossing points of bands with opposite orbital angular momentum, which can thus be selectively excited by circularly polarized light. The approach thus offers spectroscopic access to the topology of the bulk band structure of a Weyl semimetal.

Altogether, it is shown that the breaking of inversion symmetry has a decisive influence on the Bloch wave function, namely, the formation of an orbital angular momentum. This mechanism is, in turn, of fundamental importance both for the physics of the surface Rashba effect and the topology of the Weyl semimetal TaAs.

Zusammenfassung

Wird die Inversionssymmetrie kristalliner Festkörper gebrochen, ermöglicht dies die Ausbildung von spinpolarisierten elektronischen Zuständen durch Spin-Bahn-Kopplung ohne die Notwendigkeit von Magnetismus. In den vergangenen Jahren wurde eine Vielzahl interessanter physikalischer Phänomene diskutiert, die mit diesem Effekt zusammenhängen, darunter der Rashba-Effekt, topologische Isolatoren sowie Weyl-Halbmetalle. In dieser Arbeit wird das Zusammenspiel von Inversionssymetriebruch und Spin-Bahn-Kopplung sowie insbesondere deren Einfluss auf die Eigenschaften der elektronischen Zustände, also auf die Spin- und Orbital-Freiheitsgrade, experimentell untersucht. Zwei verschiedene Arten geeigneter Modellsysteme werden dazu betrachtet: zweidimensionale Oberflächenzustände, in denen der Rashba-Effekt aufgrund der an der Oberfläche inhärent gebrochenen Inverisonssymetrie auftritt, und ein Weyl-Halbmetall, dessen dreidimensionale Kristallstruktur kein Inversionszentrum besitzt. Winkelaufgelöste Photoelektronenspektroskopie bietet einen impulsaufgelösten Zugang zur Spinpolarisation sowie zur orbitalen Zusammensetzung der elektronischen Zustände mittels Photoelektronenspindetektion und Dichroismus mit polarisiertem Licht. Die in dieser Arbeit gezeigten experimentellen Ergebnisse werden außerdem durch *ab-initio* Dichtefunktionaltheorierechnungen sowie einfachen Modellbetrachtungen ergänzt und untermauert.

Der Rashba-Effekt ist von grundlegender Bedeutung für die Physik zweidimensionaler Elektronensysteme und ein zentraler Aspekt dieser Arbeit ist es, das Verständnis über seinen mikroskopischen Ursprung zu vertiefen. Das Hauptaugenmerk liegt dabei auf einer honigwabenförmigen Monolage AgTe, die epitaktisch auf einem Ag(111)-Substrat hergestellt werden konnte. Die impulsaufgelöste Orbitaltextur der AgTe-induzierten Oberflächenzustände liefert starke experimentelle und theoretische Hinweise darauf, dass der Rashba-Effekt in diesem System auf der ISB-induzierten und SOC-unabhängigen Ausbildung einer chiralen Bahndrehimpulsstruktur beruht. Da dieser Mechanismus von der orbitalen Symmetrie der Bänder abhängt, ist auch das Ausmaß des Rashba-Effekts in diesen Bändern unterschiedlich. Insbesondere wird nämlich das Auftreten von Rashba-Aufspaltungen durch eine radiale Orbitalausrichtung in den jeweiligen Zuständen bedingt, während in Bändern, die aus tangential ausgerichteten Orbitalen aufgebaut sind, der Bahndrehimpuls und folglich auch der Rashba-Effekt verschwinden. Anhand der jeweiligen Verteilung der Photoemissionsintensität lassen sich radial bzw. tangential ausgerichtete Zustände experimentell unterscheiden, was einen direkten Nachweis für den Mechanismus liefert. Insgesamt belegen die vorliegenden experimentellen Ergebnisse die Gültigkeit des theoretisch vorhergesagten *Orbital-bedingten* Rashba-Paradigmas. Die gewon-

nenen Erkenntnisse sind nicht auf AgTe beschränkt, sondern bieten im Allgemeinen einen neuen Blickwinkel auf den Rashba-Effekt an Oberflächen.

In nichtmagnetischen Weyl-Halbmetallen führt das Brechen der Inversionssymmetrie zur Ausbildung von Berry-Fluss-Monopolen, die als Impulsraum-Analoga zu magnetischen Monopolen im Realraum betrachtet werden können. Solche Monopole werden Weyl-Knoten genannt und treten als Kreuzungspunkte zwischen den spinpolarisierten Valenz- und Leitungsbändern in der dreidimensionalen Volumenbandstruktur auf. In dieser Arbeit wird winkelaufgelöste Photoelektronenspektroskopie im weichen Röntgenbereich durchgeführt, um experimentelle Signaturen der Berry-Monopole in dem paradigmatischen Weyl-Halbmetall TaAs zu finden. Untermauert durch Dichtefunktionaltheorierechnungen kann mittels spinaufgelöster Messungen und Zirkulardichroismus sowohl eine Spinpolarisation als auch ein endlicher Bahndrehimpuls in den elektronischen Volumenzuständen nachgewiesen werden. Das Auftreten von letzterem wird – wie auch beim Rashba-Effekt – durch die gebrochene Inversionssymmetrie verursacht, was auf einen vergleichbaren Mechanismus zur Ausbildung von spinpolarisierten Zuständen auch in dreidimensionalen Volumensystemen schließen lässt. Näher wurde außerdem die impulsabhängige Modulation des orbitalen Bahndrehimpulses um die Weyl-Knoten untersucht. Es zeigt sich, dass dessen Feldkonfiguration im Impulsraum (wie die Berry Krümmung) eine topologisch nicht-triviale Windung aufweist. Der beobachtete Zirkulardichroismus zeigt wiederum direkte Signaturen dieser Monopoltextur. Insbesondere stellt sich heraus, dass die Weyl-Knoten in TaAs Kreuzungspunkte von Bändern mit unterschiedlichem Bahndrehimpuls sind, die somit selektiv durch zirkular polarisiertes Licht angeregt werden können. Dieser Ansatz bietet damit einen spektroskopischen Zugang zur Topologie der Volumenbandstruktur eines Weyl Halbmetalls.

Insgesamt zeigt sich, dass das Brechen von Inversionssymmetrie einen entscheidenden Einfluss auf die Bloch-Wellenfunktion hat, nämlich die Ausbildung eines orbitalen Bahndrehimpulses. Dieser Mechanismus ist wiederum von grundlegender Bedeutung sowohl für die Physik des Oberflächen-Rashba-Effekts als auch für die Topologie des Weyl-Halbmetalls TaAs.

Contents

Chapter 1

Introduction

The combination of spin-orbit coupling (SOC) and inversion symmetry breaking (ISB) enables the formation of spin-polarized electronic states in crystalline solids without the need for magnetism. This effect underlies the physics of many modern condensed matter systems, often referred to as quantum materials [1]. SOC describes the relativistic interaction of an electron's spin with its (orbital) motion inside an electrostatic potential [2]. By means of Lorentz transformation, this electric field acts as an effective magnetic field in the rest frame of the electron. Similar to the strong magnetic field responsible for the famous quantized edge conductance in the quantum Hall effect [3–5] – discovered by Klaus von Klitzing in Würzburg in 1980 [3] – SOC can generate non-trivial band topology [6–8], leading to the broad field of topological insulators (TI) [7–19]. Remarkably, the experimental discovery of the first TI was also made in Würzburg in 2007 in the group of Laurens W. Molenkamp [11]. Since then, topological quantum matter, including not just TI but also, e.g., Weyl and Dirac semimetals [20], topological superconductors [21, 22], and topological Kondo insulators [23], has become one of the most active fields in solid-state physics. A hallmark of SOC-driven TI is the formation of spin-polarized, linearly dispersing topological surface states (TSS) [14–19] that occur generically at the edge of a TI as a consequence of the non-trivial topology of the bulk band structure [21, 22]. One of the most striking properties of TSS is the characteristic helical spin texture [18], enabled by the broken inversion symmetry at the surface.

More generally, for two-dimensional (2D) electronic states localized at surfaces or interfaces, where inversion symmetry is inherently broken, ISB causes Rashba-type [24, 25] spin-orbit splittings associated with a characteristic locking of the electrons' spin perpendicular to its momentum. The Rashba effect has been observed in various 2D systems [26–37] and underlies several phenomena [38–40] that have been proposed in the context of spin-based electronic (*spintronic*) applications [25]. Understanding the microscopic origin of Rashba-type spin-orbit splittings is thus of fundamental interest in solid-state physics. Numerous experimental and theoretical approaches, mostly based on angle-resolved photoemission (ARPES) and density functional theory (DFT), are dedicated to this topic [29, 30, 41–46] but provide rather phenomenological insights into the underlying physical mechanisms. Recent studies have presented a more fundamental theory predicting that the formation of orbital angular momentum (OAM) perpendicular to $k_{||}$ – caused by ISB solely and without the need for SOC – generally

underlies the actual Rashba effect [47–50]. Therefore, breaking of inversion symmetry is considered to play a fundamentally important role since it affects the spatial part of the wave function in a very particular way, i.e., leads to the formation of OAM. This novel paradigm has already found application in a number of research studies [37, 48, 49, 51–56], and recent approaches go even further, predicting orbital analogs to spin phenomena, such as the orbital Hall effect [57–59] or orbital torques [60], which take advantage of these orbital degrees of freedom, i.e., in particular, the OAM [61]. Although the *Orbital Rashba Effect* [48, 62, 63] is rather well studied at the theoretical level, several fundamental research questions remain open: Is there actual experimental evidence for the OAM-based Rashba paradigm? What are the relevant hybridization processes leading to the formation of OAM, and under which symmetry conditions do they occur? How does ISB influence the momentum-dependent orbital texture in OAM-carrying surface states or those with vanishing OAM?
Chapter 4 is dedicated to addressing these issues aiming to deepen the understanding of the microscopic origin of the Rashba effect. The main focus is on an epitaxially-grown binary honeycomb monolayer AgTe on a Ag(111) substrate [64]. Noble metal surfaces modified by adsorption of heavy elements, such as Pb, Bi, or Te – for which the atomic SOC-strength is sufficiently large – constitute ideal model systems for studying the Rashba effect occurring in the adsorbate-induced surface states [28–34, 64–66]. Angle-resolved photoelectron spectroscopy provides a perfect experimental tool to study the 2D electronic band structure of such Rashba systems: The method not only allows for a mapping of the band dispersion, but the systematic variation of the light polarization leads to an orbital-symmetry-selective photoexcitation due to strict dipole selection rules derived from the photoemission matrix element. This offers a k-resolved access to the character of the electronic states, i.e., the wave function. The electronic structure of AgTe/Ag(111) is therefore investigated using ARPES combined with light-polarization-dependent measurements, whereby the experimental results are supported by simple model considerations and *ab initio* DFT calculations. The discussion is further extended to related material systems, i.e., various kinds of 2D surface states, to set the results on AgTe in a broader context.
Another crucial manifestation of ISB occurs in the phase transition between trivial band insulators and topological insulators (in three dimensions), which is characterized by an orbital symmetry inversion of the usual band order in the bulk valance and conduction bands [10, 11, 15, 67, 68]. Considering only inversion symmetric systems [13] in which all bulk states are doubly degenerate, there is a single critical point between the two insulating phases [69–72]. Interestingly, ISB opens up an additional dimension in the phase diagram; generically, a novel – gapless – topological phase emerges [69–72], the Weyl semimetal (WSM) [20]. In WSM, the valence and conduction bands touch and form crossing points of spin-polarized bands called Weyl points (WP). The Berry curvature $\mathcal{B}(\boldsymbol{k})$ [73], which can be interpreted as the reciprocal-space analogue of the real-space magnetic field $\mathbf{B}(\boldsymbol{r})$ [74], shows a point-charge-like field configuration around the WP, making them

momentum-space 'magnetic' or more precisely Berry-flux monopoles [75]. Since magnetic monopoles are forbidden as point charges at the level of electromagnetism, WSM constitute important model systems for the k-space realization of quantized magnetic charges. The search for experimental signatures of such Berry-flux monopoles and the understanding of the underlying physical mechanisms in potential WSM is thus of fundamental interest in the field of topological quantum matter.
The present work focuses on the established WSM TaAs, which belongs to the family of transition-metal monopnictides (TMMP) (TaAs, TaP, NbAs, and NbP), one of the most studied classes of WSM candidates. Shortly after the theoretical prediction of the WSM phase [76], ARPES measurements provided evidence for actual experimental confirmation of the WSM-state in these materials [77–83]. Previous experimental approaches were based, on the one hand, on the comparison of the measured band dispersion with bulk band structure calculations [77–81] and, on the other hand, on the detection of topological Fermi-arc surface states [77–83]. Further indications of the non-trivial topology was also found by scanning tunnelling microscopy [84], magnetotransport experiments [85] and via light-induced photocurrents [86]. The systematic solid evidence of a WSM phase in the TMMP makes TaAs an ideal model system for studying the electronic structure of a WSM. However, although these mentioned findings strongly support the assumption of a possible realization of a WSM, the momentum-resolved texture of the bulk electronic wave functions, which directly reflects the topological monopole behavior, has not yet been studied experimentally. Immediately, fundamental scientific questions arise: Which physical observables express the non-trivial topology in TaAs? How does the interplay of SOC and ISB – that stabilizes the WSM phase – affect the momentum-dependent behavior of the spin and orbital degrees of freedoms of the wave functions?
The main focus in Chapter 5 is to find signatures for the Berry-flux monopoles in the wave function properties of the electronic states in TaAs [87]. ARPES performed at bulk-sensitive soft X-ray (SX) photon energies (400...700 eV) combined with circular dichroism (CD) and spin resolution (SR) is employed to find monopole signatures directly in the bulk band structure of TaAs. CD- [37, 48, 51, 88, 89] and SR-ARPES [18, 27] are commonly used at surface-sensitive photon energies (10...200 eV) to address the initial state orbital- and spin angular momentum (SAM), respectively. Yet, energy- and $\boldsymbol{k}_{||}$-resolution in SX-ARPES are comparably limited, making such experiments more challenging, and the combination with CD and SR is not widely used [90]. Chapter 5 is directly dedicated to this issue and aims to establish CD- and SR-ARPES at such excitation energies as a tool for studying the spin and orbital textures of electronic bulk states, particularly in WSM. Primarily, the CD pattern around the WP is studied in detail and discussed in the context of the topological Weyl physics in TaAs.

Taken together, two-dimensional surface states and three-dimensional WSM represent two types of systems in which the interplay of ISB and SOC plays a central role. However, its influence – and in particular that of ISB – on the

electronic wave function has not yet been investigated in detail. This work aims to deepen the understanding of the influence of particularly ISB on the momentum-space spin-orbital texture. Furthermore, the impact of, e.g., the potential formation of OAM on the physical properties in the respective system will be discussed. The main focus is on the fundamental physical aspects in each case, i.e., the Rashba effect in surface states and the Berry monopoles in WSM. ARPES with variable light polarization provides an ideal experimental method for this purpose.

Organization of this Thesis

Chapter 2 provides an overview of the theoretical background and the current state of research concerning the main subjects addressed in this thesis, namely the Rashba effect as well as WSM. Basics about the experimental methods, i.e., photoelectron spectroscopy, are explained in Chapter 3. The main results are presented in Chapters 4 and 5 as outlined in more detail above. Both topics are summarized in Chapter 6 and discussed together in conclusion. For readers interested only in specific parts, all chapters are organized so that they can be read independently.

Chapter 2

Interplay of Spin-Orbit Coupling and Inversion Symmetry Breaking

Spin-orbit interaction is a relativistic effect describing the coupling of an electron's spin to its orbital motion. An electron, which moves in an electric field $\boldsymbol{E}$ with velocity $\boldsymbol{v}$, experiences an effective magnetic field $\boldsymbol{B}_{eff}$. In the rest frame of the electron, Zeeman-coupling of this field to the electron's spin $\boldsymbol{S}$ leads to the energy term $E = -\boldsymbol{\mu}\boldsymbol{B}_{eff} \propto (\boldsymbol{v} \times \boldsymbol{E}) \cdot \boldsymbol{S}$ [91]. To describe spin-orbit coupling (SOC) within the framework of Schrödinger's theory, the relativistic Dirac equation [2] has to be approximated in the non-relativistic limit, i.e., expanded in lowest order in v^2/c^2 [91, 92]. This leads to an additional energy term in the Schrödinger equation resulting in a Hamiltonian H_{SOC}, that reflects the spin-orbit coupling:

$$H_{\mathrm{SOC}} = \frac{1}{2m_e^2c^2}(\boldsymbol{p} \times \boldsymbol{\nabla} V) \cdot \boldsymbol{S}, \tag{2.1}$$

with the reduced Planck constant $\hbar$, the electron mass m_e, the speed of light c, and the gradient of the potential V in which the electron moves with momentum $\boldsymbol{p}$.
Considering the valence band structure of a non-magnetic, inversion symmetric crystal for an electronic state characterized by the wave vector $\boldsymbol{k}$ and spin $\uparrow$ ($\downarrow$), time-reversal symmetry (TRS) and inversion symmetry (IS) require

$$E(\boldsymbol{k},\uparrow) \overset{\mathrm{TRS}}{=} E(-\boldsymbol{k},\downarrow) \qquad \text{and} \qquad E(\boldsymbol{k},\uparrow) \overset{\mathrm{IS}}{=} E(-\boldsymbol{k},\uparrow)\,, \tag{2.2}$$

respectively. The first equation is the so-called Kramer's degeneracy, which states that if there is a Bloch state Ψ_k with wave vector $\boldsymbol{k}$ and spin $\uparrow$ at energy E, there is another state with wave vector $-\boldsymbol{k}$ and opposite spin $\downarrow$ at the same energy. Inversion symmetry, on the other hand, guarantees that the state at $-\boldsymbol{k}$ has the same spin. Thus, the combination of these two conditions ensures that each electronic state is at least two-fold degenerate

$$E(\boldsymbol{k},\uparrow) = E(-\boldsymbol{k},\downarrow) = E(-\boldsymbol{k},\uparrow).$$

However, if inversion symmetry is broken, the spin degeneracy can be lifted by SOC and the Bloch wave function Ψ_k can exhibit a finite spin-polarization. The breaking of inversion symmetry does not only affect the spin part but

mainly the spatial part of a wave function, i.e. the latter does not necessarily have to have even or odd parity under inversion $\boldsymbol{r} \rightarrow -\boldsymbol{r}$. That is, the spatial deformation of the wave function by ISB allows for the lifting of spin degeneracy in the presence of SOC. The potential gradient that causes this deformation – i.e., ISB – can arise, for instance, via external electric fields [93]. Moreover, it is inherently present at surfaces and interfaces [24, 25] as well as in noncentrosymmetric crystal structures [94].

Two types of systems in which the interplay between ISB and SOC plays a significant role are studied in this work; first, 2D surface states with Rashba-type [24, 25] spin-orbit splittings, and second, Weyl semimetals driven by broken inversion symmetry in their three-dimensional crystal structure [20]. Sections 2.1 and 2.2 are dedicated to introducing the basic physics of the Rashba effect and WSM, respectively, and provide an overview of the current state of research in the respective areas relevant to this thesis.

2.1 The Rashba Effect

2.1.1 Original Model by Rashba and Bychkov

Within the Rashba-Bychkov model [24] (short Rashba model) electronic states are described as a two-dimensional electron gas (2DEG) that is confined by a one-dimensional asymmetric potential $V(z)$ perpendicular to it. In this case, the potential gradient becomes $\nabla V = \frac{\partial V}{\partial z}\boldsymbol{z}$ and the SOC-Hamiltonian (Eq. 2.1) reduces to

$$H_{\mathrm{R}} = \alpha_{\mathrm{R}}\boldsymbol{\sigma} \cdot (\boldsymbol{z} \times \boldsymbol{k}). \tag{2.3}$$

The constant α_{R} is the so-called Rashba-parameter and $\boldsymbol{\sigma}$ is a vector of Pauli matrices. The former quantifies the SOC strength and is – in the case of an ideal 2DEG – proportional to the potential gradient [91]. The Hamiltonian H_R results in a splitting of the parabolic band into two branches $E_{\pm}$ (compare Fig.2.1(a)) with the dispersion

$$E_{\pm}(\boldsymbol{k}_{\parallel}) = \frac{\hbar^2 \boldsymbol{k}_{\parallel}^2}{2m^*} \pm \alpha_{\mathrm{R}} k_{\parallel}\,, \tag{2.4}$$

whereby $k_{\parallel} = |\boldsymbol{k}_{\parallel}|$ and m^* denotes the effective mass.
The energetic spin-splitting $\delta E = E_+ - E_- = 2\alpha_{\mathrm{R}} k_{\parallel}$ is proportional to $k_{\parallel}$. Using the eigenstates $|\Psi_{\pm}\rangle$ of H_{R}, the expectation values $\langle\boldsymbol{\sigma}\rangle$ can be calculated:

$$\langle\Psi_{\pm}|\,\boldsymbol{\sigma}\,|\Psi_{\pm}\rangle = \pm\frac{\alpha_{\mathrm{R}}}{|\alpha_{\mathrm{R}}|}\frac{1}{k_{\parallel}}(-k_y, k_x, 0). \tag{2.5}$$

The resulting spin texture is schematically shown in Fig.2.1(b). The spins are in-plane aligned and perpendicular to the wave vector $\boldsymbol{k}_{\parallel}$, with the overall chirality of the two branches being opposite.

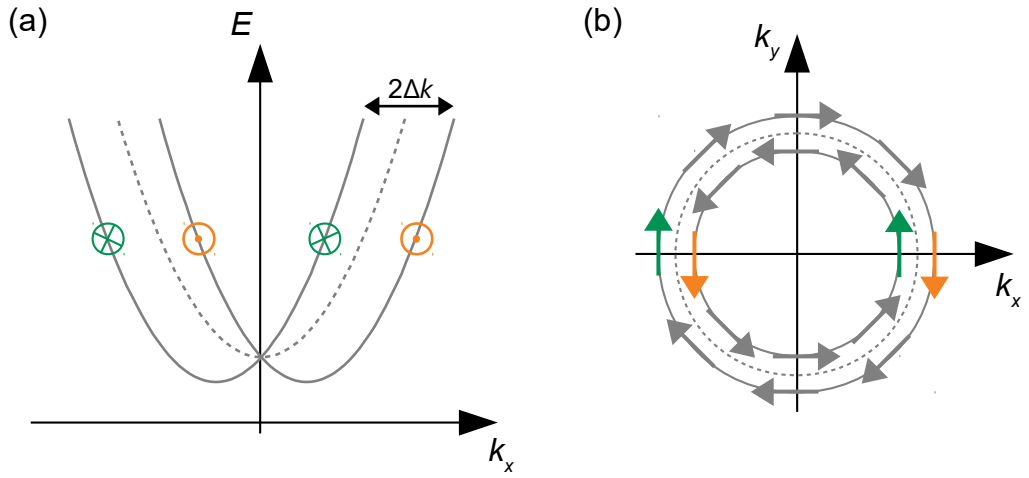

FIGURE 2.1: Schematic band structure (a) and constant energy cut (b) in the Rashba model. A parabolic spin-degenerate band (dashed line) gets split into spin-polarized bands (solid lines) by spin-orbit coupling and inversion symmetry breaking. The spin-polarization is sketched by the arrows, with green and yellow indicating a polarization along $+k_y$ and $-k_y$, respectively.

2.1.2 The Rashba Effect at Surfaces

The Rashba effect can occur, for instance, at solid surfaces or interfaces, where the inversion symmetry is directly broken by the interface in a polar fashion (IS: $z \rightarrow -z$). Indeed, the first experimental observation of a Rashba-type spin splitting was achieved in 1996 by LaShell et al. at the Shockley surface state on Au(111) by means of ARPES [26]. Figure 2.2 (a) shows the result of a typical ARPES measurement on Au(111). It is directly evident that there is not just a single parabola but two branches Ψ_+ and Ψ_-, which are shifted against each other by $2\Delta k$. In agreement with the Rashba model, the energy splitting δE is directly proportional to the wave vector k as can be seen in the upper right panel. Spin-resolved ARPES measurements (see Chapter 3.2) confirm the characteristic in-plane spin polarization perpendicular to $\boldsymbol{k}_{||}$. Hence, both the band dispersion and the spin polarization are consistent with those expected from the Rashba model. The Au(111) surface has therefore been used as a paradigmatic model system for the Rashba effect. In this context, the system has been investigated in several further studies by means of high resolution [41, 95] and spin-resolved [27] ARPES experiments as well as DFT [41, 45, 46, 96, 97] and tight-binding [51, 91, 98] calculations.
A key aspect of this research was to elucidate the physical mechanisms underlying the Rashba effect at the microscopic level. It seems most obvious at first to assume that the surface electrons, behaving like a 2DEG, perceive the surface electric field as a Rashba-like magnetic field $\propto (\boldsymbol{z} \times \boldsymbol{k})$. Yet, already LaShell [26] mentioned that the free electron model itself, underlying the original Rashba model, would lead to an artificially small energy splitting and thus the atomic SOC has to be taken into account [42, 91]. Petersen and Hedegård estimated the splitting to be in the order of $\delta E = \alpha_R k \approx 10^{-6}\,\mathrm{eV}$ by assuming a surface electric field strength in the order of $\sim \mathrm{eV/\AA}$ [91]. Yet,

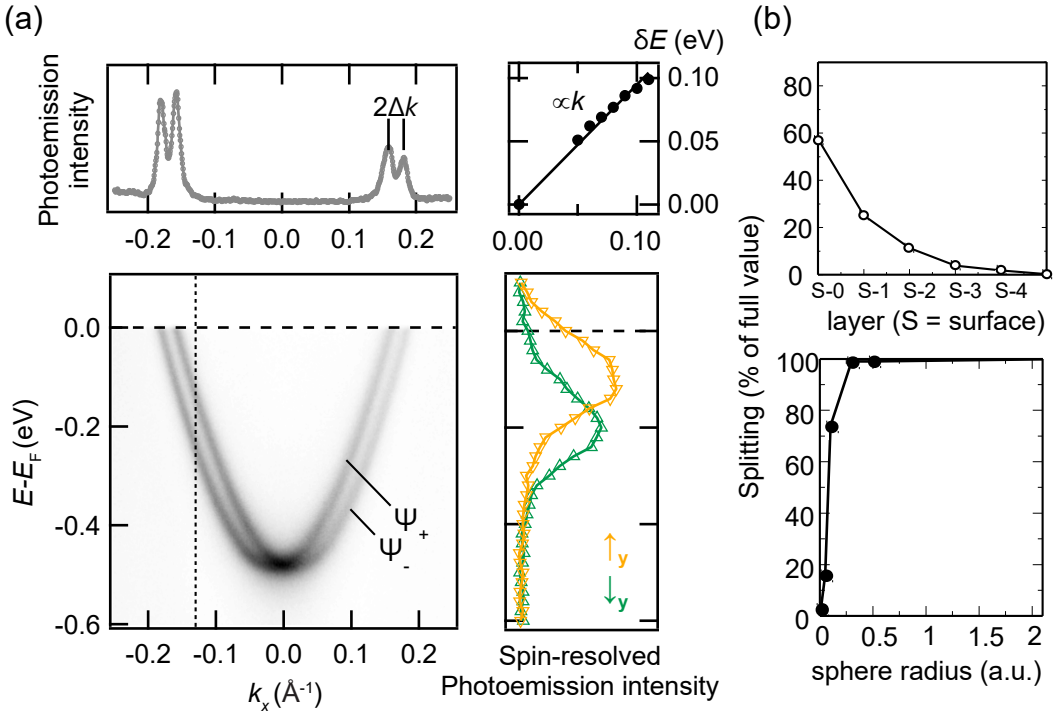

FIGURE 2.2: Rashba effect in the Au(111) Shockley surface state. (a) Result of an angle-resolved photoelectron spectroscopy (ARPES) experiment taken at $h\nu = 21.21\,\text{eV}$. Two parabolic branches Ψ_+ and Ψ_- are resolved which are separated by a constant momentum offset $2\Delta k$, as indicated in the momentum distribution curve in the upper left panel. The energetic splitting δE is proportional to k (upper right panel) and both branches have an opposite spin-polarization ($\uparrow_y\downarrow_y$) along k_y ($\uparrow_y\downarrow_y$) as shown by a spin-resolved energy distribution curve (lower right panel) taken with $h\nu = 24\,\text{eV}$ at a k_x as indicated by the dashed line in the main panel. (b) Spatial-resolved energy splitting obtained by DFT. The upper panel shows a layer decomposition and in the lower panel, the sphere radius around the atoms has been varied. *Graphs in (b) are adapted with permission from [42]. Copyright © (2006) Elsevier B.V. All rights reserved.*

the Rashba-parameter was found to be $\alpha_R = 0.35\,\text{eVÅ}$ [99], which is several orders of magnitude larger. Moreover, even larger Rashba-splittings have meanwhile been found in various types of surface states, reaching values up to $\alpha_R = 3.05\,\text{eVÅ}$, as found in a substitutional surface alloy $Ag_2Bi/Ag(111)$ [28].

In order to verify this discrepancy at a more systematic level, Bihlmayer et al. analyzed the spatial dependence of SOC on Au(111) [42]. By means of DFT, it is possible to artificially switch on SOC only in certain regions. The results are shown in Fig. 2.2 (b). The upper panel shows a layer decomposition of the Rashba-splitting, proving that more than 40% of the full splitting originates from the sub-surface layers. However, the surface electric field should already be sufficiently shielded in this region, suggesting that the potential gradient at the surface contributes weakly to the splitting, consistent with the previous estimates. In another analysis, SOC was taken into account in all layers, but the SOC-active radius of the sphere around the atoms has been

varied, as shown in the lower panel of Fig. 2.2 (b). More than 90 % of the contribution to the full splitting results from a region very close (~ 0.25 a.u.) to the atomic nucleus. This means that SOC is only significant in a small area around the atoms [42], and given its thus atomic origin, it is more reasonable to consider a spherically symmetric Coulomb potential

$$\boldsymbol{\nabla} V = \frac{\partial V}{\partial r}\frac{\boldsymbol{r}}{r}. \tag{2.6}$$

Inserting this into Eq. 2.1 gives the well known atomic SOC Hamiltonian

$$H_{\mathrm{SOC}} = \frac{1}{2m_e^2c^2}\frac{1}{r}\frac{\partial V}{\partial r}(\boldsymbol{L}\cdot\boldsymbol{S}) = \lambda_{\mathrm{SOC}}\boldsymbol{L}\cdot\boldsymbol{S}, \tag{2.7}$$

where $\boldsymbol{L} = \boldsymbol{r}\times\boldsymbol{p}$ is the orbital angular momentum operator and λ_{SOC} is the atomic SOC constant. This Hamiltonian differs from Eq. 2.3 in that it does not explicitly contain the electric field perpendicular to the surface. Nevertheless, band structure calculations based on this approach, such as DFT or tight-binding calculations, reproduce Rashba-like spin splittings in Au(111) and likewise other systems quite well [42]. Thus, the Rashba effect is not only based on the original considerations of the Rashba model, i.e., a 2DEG.
Using $\boldsymbol{k}\cdot\boldsymbol{p}$ perturbation theory [45, 46] it has been demonstrated that the total Rashba-parameter α_R^{tot}, as it can be observed in experiments or band structure calculations, has two contributions:

$$\alpha_R^{\mathrm{tot}} = \alpha_R^{LS} + \alpha_R^{\mathrm{RM}}. \tag{2.8}$$

The first term relies on H_{SOC} (Eq. 2.7) and the second term is the typical Rashba-parameter arising from original model Eq. 2.3 [46]. For real free electron gas α_R^{LS} becomes zero [45, 46] and the splitting is solely described by the Rashba model. However, numerical calculations on Au(111), $Ag_2Bi/Ag(111)$, and $Bi_2Te_3(0001)$ showed that the contribution of α_R^{RM} is an order of magnitude smaller than α_R^{tot} [45]. This demonstrates on a quantitative level that the Rashba effect on real surfaces is mainly determined by Eq. 2.7 resulting in $\alpha_R^{\mathrm{tot}} \approx \alpha_R^{LS}$.
The difference in the two terms in Eq. 2.8 relies on the fact that the orbital angular momentum operator, which is $\boldsymbol{L} = \boldsymbol{r}\times\boldsymbol{p}$ in the case of α_R^{LS}, is replaced by $(\boldsymbol{z}\times\boldsymbol{k})$ in the Rashba model [46]. This gives a direct hint that the operator $\boldsymbol{L}$ contains matrix elements that strongly contribute to the Rashba-splitting. In other words, there are specific orbital hybridization terms that are neglected in the model considerations in Eq. 2.3 because the spatial wave function in it has no local orbital components. In the following section, an alternative model will be presented, in which exactly these microscopic mechanisms are explicitly treated.

2.1.3 Tight Binding Approach to Rashba-Type Spin-Splittings

Motivated by the aforementioned local characteristics, Petersen and Hedegård developed a tight-binding model for the Rashba effect [91], which has formed the basis for several related TB-approaches ever since [48, 62, 98, 100, 101]. The model considers a hexagonal monolayer of atoms with three p-orbitals – expressed in a cubic basis $\{p_x, p_y, p_z\}$ – on each lattice site. The basis orbitals are illustrated in Fig. 2.3 (a).
First, the model will be considered without SOC. In a free-standing scenario, which is inversion symmetric, the three bands can be classified into an in-plane p_{xy} and an out-of-plane p_z manifold. In this case, inversion symmetry prohibits hybridization between in-plane and out-of-plane orbitals. This can be understood in terms of the different symmetries. The p_z state is odd under reflection IS: $z \to -z$, while the p_{xy} orbitals are even (Fig. 2.3 (a)). In other words, there would be an equally large overlap between the latter with the positive and the negative lobe of the p_z orbital, giving a vanishing total overlap [91]. The situation changes when inversion symmetry is broken, for instance by an electric field or a substrate. Considering a broken symmetry IS: $z \to -z$, hopping between p_{xy} and p_z orbitals is now allowed. That means, in the model, there is a parameter given by the matrix element

$$\lambda_{\mathrm{ISB}} \propto \langle p_{xy}| H |p_z\rangle , \tag{2.9}$$

which is a direct measure of ISB.
The resulting band structure without SOC, taken from [91], is shown in Fig. 2.3 (b). There are three bands, referred to as α, β and γ. The hole-like bands have mainly p_{xy} character while the electron-like band γ is mainly composed p_z orbitals [48, 91]. Yet, it is directly evident that an avoided crossing occurs between β and γ (marked by the dashed red line), proving that these states have mixed p_{xy} and p_z orbital characters. In fact, ISB manifests itself directly through this gap, whose size is given by $2\lambda_{\mathrm{ISB}}$. Notably, the protected band crossing, marked by the green dashed line, indicates that α is not affected by ISB.
SOC enters the model via the atomic SOC-Hamiltonian (Eq. 2.7). The components L_i ($i = x, y, z$) of the OAM operator, given in the p orbital basis $\{p_x, p_y, p_z\}$, are

$$L_x = \hbar \begin{pmatrix} 0 & 0 & 0 \\ 0 & 0 & -i \\ 0 & i & 0 \end{pmatrix} \quad L_y = \hbar \begin{pmatrix} 0 & 0 & i \\ 0 & 0 & 0 \\ -i & 0 & 0 \end{pmatrix} \quad L_z = \hbar \begin{pmatrix} 0 & -i & 0 \\ i & 0 & 0 \\ 0 & 0 & 0 \end{pmatrix} \tag{2.10}$$

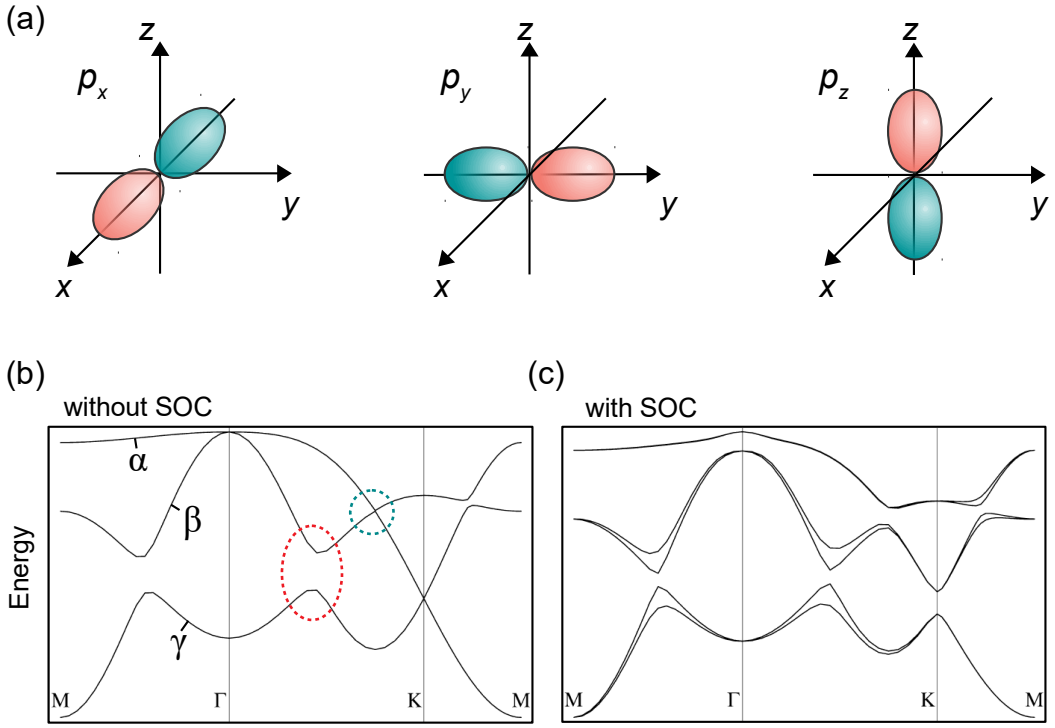

FIGURE 2.3: Tight-binding model by Petersen and Hedegård. (a) Schematic sketch of the basis orbitals $\{p_x, p_y, p_z\}$. The calculated band structures, taken from [91], are shown in (b) and (c). The bands are referred to as α, β and γ. The latter two have mixed $p_{xy} - p_z$ orbital character, as can be seen from the hybridization gap marked by the red dashed line in (b), while α is compost of in-plane p_{xy} orbitals only, as indicated by the protected crossing (green dashed line). Without (b) spin-orbit coupling (SOC) each state is doubly degenerate while a spin-splitting occurs after the inclusion of SOC (c). *Figures (b,c) are adapted with permission from [91]. Copyright © (2000) Elsevier Science B.V. All rights reserved.*

and the SAM-operators are given by $S_i = \frac{\hbar}{2}\sigma_i$ $(i = x, y, z)$. The matrix representation of the SOC Hamiltonian is given by the tensor product of $\boldsymbol{L}$ and $\boldsymbol{S}$

$$\begin{aligned} H_{\mathrm{SOC}} &= \lambda_{\mathrm{SOC}} \boldsymbol{L} \cdot \boldsymbol{S} = \lambda_{\mathrm{SOC}} \left(\boldsymbol{L_x S_x} + \boldsymbol{L_y S_y} + \boldsymbol{L_z S_z} \right) \\ &= \lambda_{\mathrm{SOC}} \frac{\hbar^2}{2} \begin{pmatrix} 0 & -i & 0 & 0 & 0 & 1 \\ i & 0 & 0 & 0 & 0 & -i \\ 0 & 0 & 0 & -1 & i & 0 \\ 0 & 0 & -1 & 0 & i & 0 \\ 0 & 0 & -i & -i & 0 & 0 \\ 1 & i & 0 & 0 & 0 & 0 \end{pmatrix}. \end{aligned} \tag{2.11}$$

The TB band structure involving Eq. 2.11 for each wave vector $\boldsymbol{k}$ is shown in Fig. 2.3 (c). One can see a k-dependent splitting of each band into two spin-branches. In a narrow region around the Γ-point, where the band dispersion is nearly parabolic, the splitting is indeed Rashba-like. Based on this, Petersen and Hedegård derived a direct expression for the Rashba-parameter

in the band γ that is proportional to both λ_{ISB} and λ_{SOC}

$$\alpha_R \propto \lambda_{\mathrm{ISB}} \lambda_{\mathrm{SOC}}. \tag{2.12}$$

The approach thus shows directly how a Rashba-type spin-orbit splitting emerges in a TB model, i.e., from orbital hybridizations. The main consequences resulting from the model can be summarized as follows:

1. Within a TB picture, ISB and SOC enter via two different contributions H_{ISB} and H_{SOC}, whose strengths are parameterized by λ_{ISB} and λ_{SOC}, respectively. The whole Hamiltonian can thus be divided into three parts:

$$H = H_0 + H_{\mathrm{ISB}} + H_{\mathrm{SOC}} \tag{2.13}$$

2. There is no SO-splitting in a band, derived from a single p_i-orbital manifold ($i = x, y, z$). Breaking inversion symmetry[1] always promotes a specific mixing of electronic states with different orbital characters, i.e., between in-plane and out-of-plane orbitals in the case of a Rashba-type ISB.

3. Different bands within a surface band structure (may) have different magnitudes in the spin-splitting. An example is given directly in the calculation in Fig. 2.3 (c), showing that the splitting of α is visibly smaller than that of β and γ.

2.1.4 Orbital Angular Momentum Induced by ISB

In all three mentioned points, the spatial (orbital) part of the wave function and the influence of ISB on it plays a crucial role. An important physical observable reflecting the impact of ISB is the so-called orbital angular momentum (OAM). The OAM can be seen as an orbital counterpart of the electron spin. Within the so-called *atomic centered approximation*, it is defined as the expectation value of the OAM operator (Eq. 2.10) [62]

$$\langle \Psi | \, \boldsymbol{L} \, | \Psi \rangle \,, \tag{2.14}$$

with $\boldsymbol{L} = (L_x, L_y, L_z)$. As an atomic quantity, it denotes the magnetic quantum number m_l and determines the angular part of the orbital wave function. Take for example y as a quantization axis. The operator L_y has eigenvalues $\hbar m_l = \{-\hbar, 0, \hbar\}$ and its eigenvectors are spherical harmonics $|L_y\rangle \propto e^{i m_l \phi}$ (ϕ is the angle between x and z-axis). In the basis of cubic orbitals (Eq. 2.10) latter can be written as $|L_y = \pm 1\rangle = \frac{1}{\sqrt{2}}(|p_x\rangle \mp i\,|p_z\rangle)$ and $|L_y = 0\rangle = |p_y\rangle$[2].

[1] Within this model, inversion symmetry has not necessarily to be broken in a Rashba-like fashion. For instance, also in-plane ISB would lead to specific orbital hybridization terms, allowing for non-Rashba-type SO-splittings. This fact makes the model more generic, as it is not restricted to the Rashba effect at surfaces.

[2] Analogously, the eigenstates of L_x and L_z are given by $|L_x = \pm 1\rangle = \frac{1}{\sqrt{2}}(|p_y\rangle \pm i\,|p_z\rangle)$ and $|L_z = \pm 1\rangle = \frac{1}{\sqrt{2}}(|p_x\rangle \pm i\,|p_y\rangle)$, respectively.

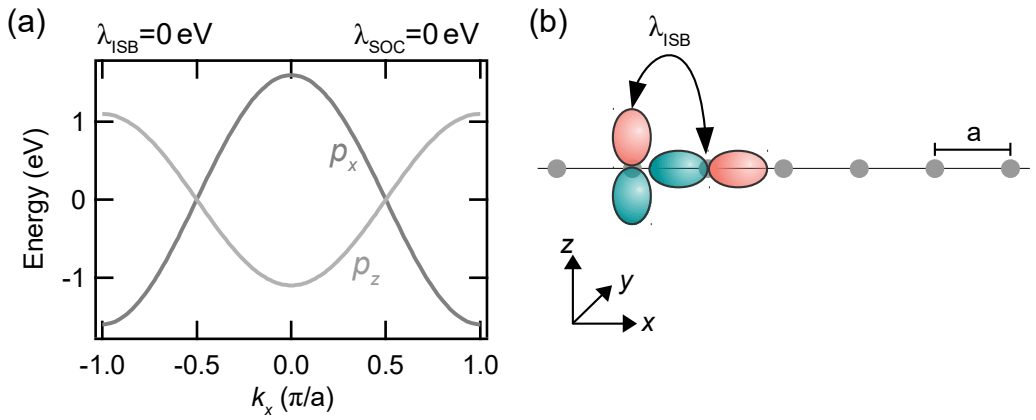

FIGURE 2.4: Tight binding (TB) model for a linear atomic chain with lattice constant a (b) including one p_x one p_z orbital per lattice site. Inversion symmetry breaking can be included by the hopping parameter $\lambda_{\mathrm{ISB}} = \langle p_x | H | p_z \rangle$. (a) calculated TB band structure ($V_\sigma = 1.6\,\mathrm{eV}$, $V_\pi = 1.1\,\mathrm{eV}$) without ISB as well as without SOC. The grayscale indicates the orbital character, which is not mixed due to the vanishing ISB.

The usefulness of OAM in condensed matter and surface physics becomes clear in the TB model explained above. It is immediately apparent that the characteristic mixing of in-plane p_x (p_y) and out-of-plane p_z orbitals is not allowed in an inversion symmetric system. This means that inversion symmetry quenches the OAM $\langle L_y \rangle$ ($\langle L_x \rangle$) in the wave function and thus it is precisely the term H_{ISB}, which leads to the formation of OAM. In general, the OAM in crystalline solids underlies the same symmetry conditions as the spin (compare Eq. 2.2) [61]

$$\langle \boldsymbol{L} \rangle_{\boldsymbol{k}} \overset{\mathrm{TRS}}{=} -\langle \boldsymbol{L} \rangle_{-\boldsymbol{k}} \qquad \text{and} \qquad \langle \boldsymbol{L} \rangle_{\boldsymbol{k}} \overset{\mathrm{IS}}{=} \langle \boldsymbol{L} \rangle_{-\boldsymbol{k}}. \tag{2.15}$$

Thus, inversion symmetry has to be broken to induce a finite OAM in the wave function.
This modification suggests a different classification scheme of the bands. Instead of $\{p_x, p_y, p_z\}$, the bands can be classified by their OAM: $\{p_1, p_0, p_{-1}\}$. As indicated by the presence of hybridization gaps in Fig. 2.3 (a), β and γ belong to the $p_{\pm 1}$ manifold and α has p_0 character. The fact, that only the OAM-carrying band are spin-split suggests that a finite OAM is a prerequisite for a sizable spin-splitting.

While previous conclusions have been rather phenomenological, the relationship between ISB, OAM and SOC has been embedded in a concrete theoretical model of an *OAM-based origin of Rashba-type spin-splittings* [47–50]. The following TB model is intended to illustrate the key findings from this in a simple framework. It describes a linear chain of atoms [53] with one p_x and one p_z orbital per lattice site (Fig. 2.4 (b)). Inversion symmetry is defined as IS: $z \to -z$. The on-site Hamiltonian H_0 is diagonal and has two matrix elements $H_{xx} = V_\sigma \cos(k_x a)$ and $H_{zz} = -V_\pi \cos(k_x a)$. The band structure

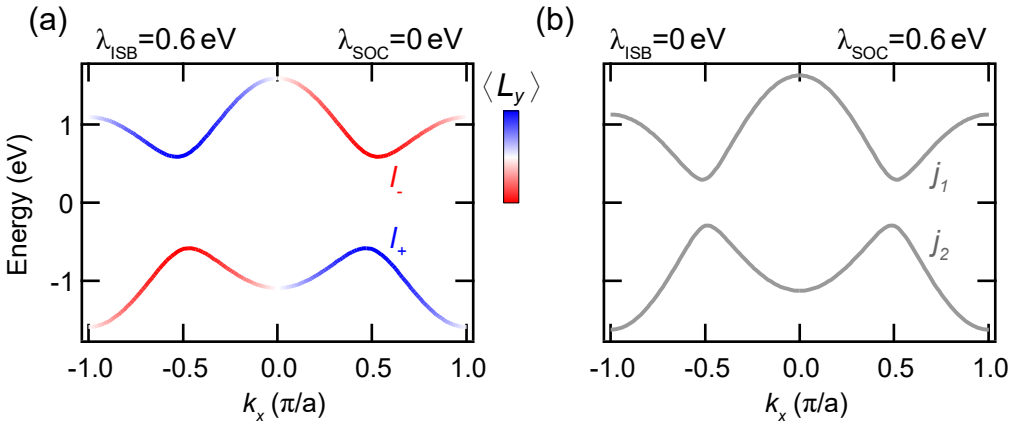

FIGURE 2.5: Band structure calculated in (a) the no-SOC limit ($\lambda_{\mathrm{ISB}} = 0.6\,\mathrm{eV}$, $\lambda_{\mathrm{SOC}} = 0\,\mathrm{eV}$) and in (b) the no-ISB limit ($\lambda_{\mathrm{ISB}} = 0\,\mathrm{eV}$, $\lambda_{\mathrm{SOC}} = 0.6\,\mathrm{eV}$). In both cases a gap opens but only $\lambda_{\mathrm{ISB}} \neq 0$ causes the formation of OAM $\langle L_y \rangle$, which is indicated by the red-blue color code.

without ISB and SOC is shown in Fig. 2.4 (a). The p_x and p_z bands cross at $k_x = \pi/(2a)$ as there is no off-diagonal hybridization term in the Hamiltonian. Consequently, the OAM is quenched by inversion symmetry, as expected from Eq. 2.15.
The Hamiltonian H_{ISB} has two nonzero off-diagonal matrix elements

$$H_{xz} = \lambda_{\mathrm{ISB}} i \sin(k_x a) = -H_{zx}$$

and allows for a p_x-p_z-hybridization via $\lambda_{\mathrm{ISB}} \neq 0$. The energy scale associated with ISB $E_{\mathrm{ISB}} = \langle H_{\mathrm{ISB}} \rangle \propto \lambda_{\mathrm{ISB}} \sin(k_x a)$ is k-dependent with a maximum value of λ_{ISB} and it vanishes at $k_x = 0$. The connection between ISB and the formation of OAM becomes directly evident: There is proportionality between H_{ISB} and L_y and consequently the eigenstates have an OAM $\langle L_y \rangle \propto \pm \sin(k_x a)$. Fig. 2.5 (a) shows how the band structure is modified by ISB. Like in the Petersen-Hedegård model, a gap opens which has the size of $2\lambda_{\mathrm{ISB}}$. The red-blue color code indicates the expectation value of the OAM $\langle L_y \rangle$, which switches its sign from $+k_x$ to $-k_x$. Moreover, there is an overall opposite sign for the two bands showing that they can be characterized by their OAM instead of $p_{x,z}$-character: $\{p_x, p_z\} \rightarrow \{p_{+1}, p_{-1}\}$[3].
The band structure calculation without ISB but with SOC ($\lambda_{\mathrm{SOC}} = 0.6\,\mathrm{eV}$) is shown in Fig. 2.5 (b). Since there is no p_y orbital in the model, H_{SOC} has just the nonzero matrix elements of $L_y S_y$ (Eq. 2.11), coupling p_x and p_z orbitals as well. Thus, a hybridization gap opens but unlike ISB (Fig. 2.5 (a)), SOC alone does not induce an OAM, due to the symmetry condition in Eq. 2.15. The difference in the wave function character for the two scenarios can be seen

[3] Notably, this does only hold for finite k, or more precisely for k, which are no time-reversal invariant momenta (TRIM), where $H_{\mathrm{ISB}}(\boldsymbol{k}_{\mathbf{TRIM}}) = 0$

best at the eigenstates at $k_x = \pi/(2a)$. In the no-SOC-limit one finds

$$\begin{aligned} |l_+, \uparrow (\downarrow)\rangle &= \frac{1}{\sqrt{2}}\Big(|p_x, \uparrow (\downarrow)\rangle + i\,|p_z, \uparrow (\downarrow)\rangle\Big) \\ |l_-, \uparrow (\downarrow)\rangle &= \frac{1}{\sqrt{2}}\Big(|p_x, \uparrow (\downarrow)\rangle - i\,|p_z, \uparrow (\downarrow)\rangle\Big) \end{aligned} \tag{2.16}$$

and in the no-ISB-limit the eigenstates are

$$\begin{aligned} |j_1, \pm\rangle &= \frac{1}{\sqrt{2}}\Big(|p_x, \uparrow (\downarrow)\rangle \pm |p_z, \downarrow (\uparrow)\rangle\Big) \\ |j_2, \pm\rangle &= \frac{1}{\sqrt{2}}\Big(|p_x, \downarrow (\uparrow)\rangle \pm |p_z, \uparrow (\downarrow)\rangle\Big). \end{aligned} \tag{2.17}$$

While ISB mixes states of different orbital characters but same spin, SOC couple states of different orbital characters and opposite spin. Obviously, $|l_\pm\rangle$ are OAM eigenstates but for $|j_{1,2}\rangle$ there is $\langle L_y\rangle = 0$[4].
The model directly demonstrates the different influences of ISB and SOC. Nevertheless, in both cases in Fig. 2.5 spin-degeneracy is preserved. Only the interplay of the two effects enables the lifting of the degeneracy and the formation of spin-polarization. This is shown in Fig. 2.6 with two different parameter combinations chosen in the calculations. Based on the extreme cases (Fig. 2.5), the respective initially missing mechanism was now introduced as a small perturbation. Accordingly, two scenarios arise [37, 49, 51, 100]; a strong ISB limit (left column) in which $E_{\mathrm{ISB}} \gg E_{\mathrm{SOC}}$ and a strong SOC limit (right column) with $E_{\mathrm{ISB}} \ll E_{\mathrm{SOC}}$. In both cases, each band is split into two spin-branches with a Rashba-type spin-polarization $\langle S_y\rangle$ perpendicular to k_x (Fig. 2.6 (c,d)). The occurrence of SO-splittings in the two limits can be understood as follows: In the strong ISB limit, SOC causes the spins to align parallel and antiparallel to the pre-existing OAM (Fig. 2.6 (e)). If SOC is predominant, OAM is initially quenched in $j_{1,2}$ but ISB causes a lifting of OAM-degeneracy within in each j-state, leading to an energy separation of states with different OAM and also different SAM (Fig. 2.6 (f)).
The two cases can be distinguished by their OAM-texture [37, 48, 50, 51] as can be seen in Fig. 2.6 (a,b): The OAM in the two spin-branches have the same sign in the strong ISB case but opposite sign in the strong SOC case. That means it is the interplay of ISB and SOC, i.e., the energy hierarchy between the two quantities, that determines the splitting and the wave function character in the spin-split states.

The model explained above gives a deep insight into the microscopic origin of spin-orbit coupling induced splittings in material systems with broken inversion symmetry. The latter enters via a separate term H_{ISB} in the Hamiltonian and is associated with a characteristic k-dependent energy scale. Moreover, ISB causes the formation of OAM in the wave functions.

[4] For $|j_{1,2}\rangle$ one finds instead a finite value $\langle L_y S_y\rangle$. Importantly, this implies neither the formation of an OAM $\langle L_y\rangle$ nor a SAM polarization $\langle S_y\rangle$, both of which are quenched by the inversion symmetry (see Eq. 2.2 and 2.15).

In the minimal model presented, there are only two orbitals that hybridize, leading to the appearance of OAM. There is no band of vanishing OAM, although it is immediately clear that if the p_y orbital were also included, it would form the $\langle L_y \rangle = 0$ band. This is equivalent to the α band in the Petersen-Hedegård model (Fig. 2.3), for which the Rashba effect vanishes. Taken together, the approach leads to a paradigm in which the occurrence of spin splittings and spin-polarized states in non-magnetic solids rely on the presence of a finite OAM [47–50].

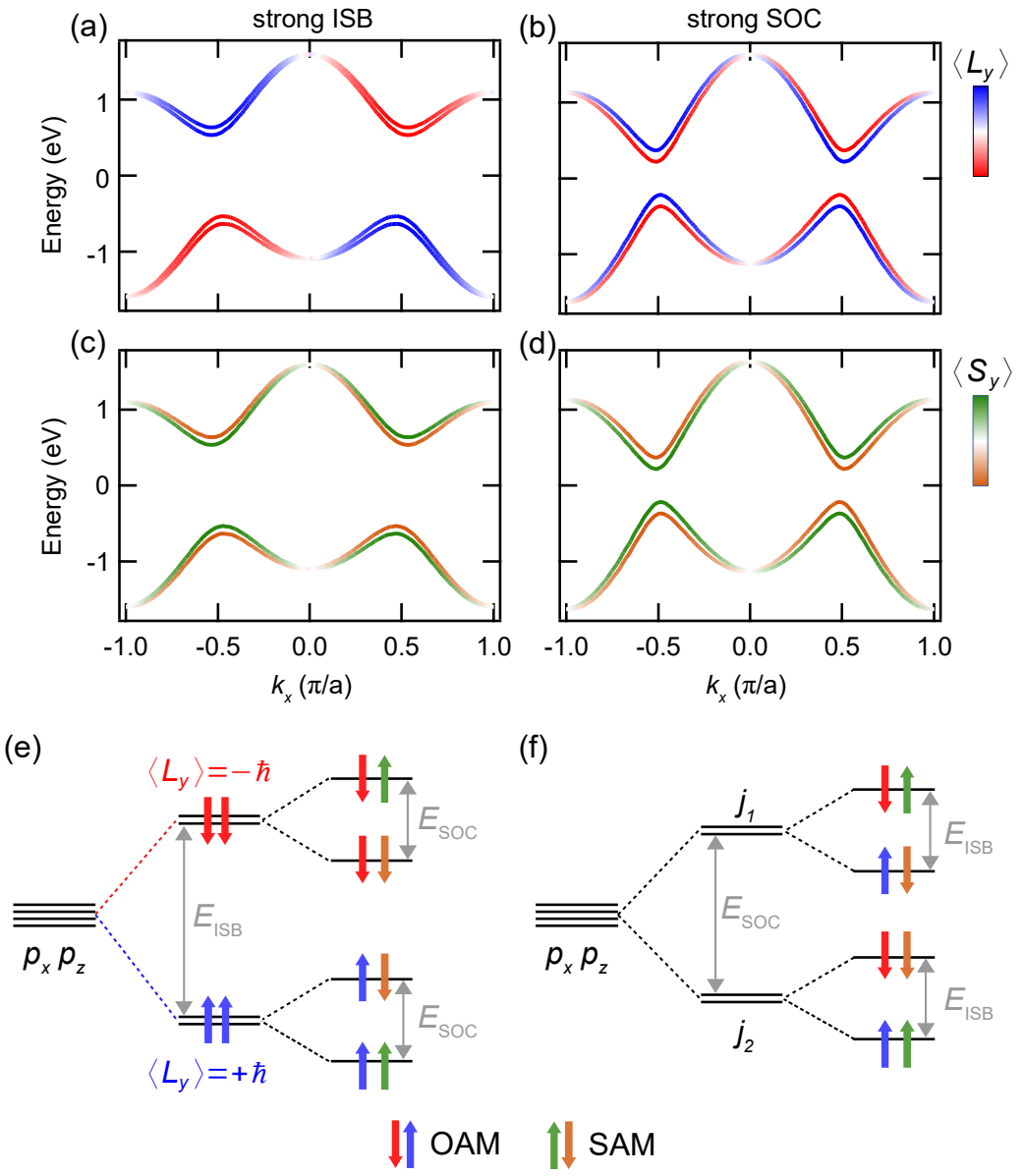

FIGURE 2.6: Interplay of ISB and SOC. Band structure calculations in the (a,c) strong ISB limit ($\lambda_{\mathrm{ISB}} = 0.6\,\mathrm{eV}$, $\lambda_{\mathrm{SOC}} = 0.1\,\mathrm{eV}$) and (b,d) strong SOC limit ($\lambda_{\mathrm{ISB}} = 0.075\,\mathrm{eV}$, $\lambda_{\mathrm{SOC}} = 0.6\,\mathrm{eV}$). Red-blue and orange-green color codes indicate OAM (a,b) and SAM (c,d), respectively. (e,f) Schematic energy diagram of the spin-splitting at a fourfold-degenerate state ($k_x = \pi/(2a)$) in the strong ISB (e) and strong SOC limit (f).

2.2 Weyl Semimetals

With the topological interpretation of band theory in crystalline solids [74], the study of topological quantum matter has become one of the most active areas of modern condensed matter physics in recent years [21, 22]. Initially restricted to band insulators, topological properties of semimetallic systems were also investigated [69–72]. Weyl semimetals (WSM) represent such a class of gapless, three-dimensional topological quantum materials [20]. The linearly dispersing low-energy quasiparticle excitations in the bulk states of WSM can be considered as analogs to elementary particles in high-energy physics. The chiral Weyl fermions [102] exist as band intersections of the spin-polarized valence and conduction bands in non-centrosymmetric or ferromagnetic semimetals. The crossing points, named Weyl points (WP) are topologically protected. This important property is directly linked to a mono pole-like behavior of the WP and – similar as in TI – it causes the formation of topologically protected surface states. The latter have a characteristic non-closed contour in the Fermi surface [75].
While WSM were initially discussed theoretically mainly in magnetic systems since 2011 [75, 103, 104], the first experimental evidence was obtained in non-centrosymmetric transition metal monopnictides (TMMP) in 2015 [76–83], in which the broken inversion symmetry acts as a driving force for the WSM state. Hence, the interplay between ISB and SOC plays a decisive role in the physics underlying topology in non-magnetic WSMs at the microscopic level. The present work, therefore, focuses on this class of materials.

An overview of the physical properties of WSM will be given in this Section. The basic theoretical concepts, including a brief introduction to topological band theory and topological insulators as well as the theoretical description of WSM, are explained in Section 2.2.1. Section 2.2.2 gives an overview of the atomic and electronic properties of TMMP.

2.2.1 Theoretical Concepts

Topological Band Theory

Electrons moving in crystalline solids are described within the framework of band theory [105]. Spatial overlap between the atomic wave functions leads to the formation of energy bands and the eigenstates within these bands are the Bloch wave functions $|\Psi_{n,k}\rangle = e^{ikr}|u_n(\boldsymbol{k})\rangle$, with n being the band index and $|u_n(\boldsymbol{k})\rangle$ is a lattice-periodic function. By filling the bands within the framework of Fermi-Dirac statistics, materials can be classified into metals and insulators. In the 1980th, this basic theory has been extended in a fundamental way; it has been found that there is a topological interpretation that allows for a fundamentally different classification scheme of electronic band structures [4, 5, 73, 106].
In the first place, topology is a mathematical concept in which geometrical shapes can be classified in terms of different equivalence classes characterized by topological invariants. Examples are the number of holes in

three-dimensional geometrical objects or the number of times a closed curve wraps about the origin. When sharing the same invariant, geometrical objects are equivalent in terms of topology, regardless of their detailed shape. The question arises of how lattice periodic Bloch Hamiltonians $H(\boldsymbol{k})$ can be interpreted as 'geometrical objects' and how band structures can be topologically classified. In order to consider equivalence classes of $H(\boldsymbol{k})$, topological invariants are needed which take into account the k-dependent behavior of the eigenstates. One is the so-called Chern number defined as

$$\gamma_n = \frac{1}{2\pi} \int_S \mathcal{B}_n \, d^2\boldsymbol{k}. \tag{2.18}$$

Here, $\mathcal{B}_n(\boldsymbol{k}) = \nabla \times i \langle u_n | \nabla_k | u_n \rangle$ is the Berry curvature (BC) [73] of the nth band and S is a surface in momentum space. While at the first glance this appears to be a rather cumbersome formula, there is a clear physical interpretation of BC; it can be considered as a momentum space analog of the real space magnetic field and $\mathcal{A}_n(\boldsymbol{k}) = i \langle u_n | \nabla_k | u_n \rangle$ is the associated vector potential [74]. The Chern number then represents the total Berry flux of a 'magnetic' monopole through S and, in analogy to the Dirac magnetic monopole in real space [107], γ_n is integer quantized.

To illustrate these issues more concisely, complicated systems are often reduced to an effective two-band model whose Hamiltonian can be generically written as:

$$H(\boldsymbol{k}) = \boldsymbol{d}(\boldsymbol{k}) \cdot \boldsymbol{\sigma} \tag{2.19}$$

The vector $\boldsymbol{d}(\boldsymbol{k})$ contains band-structure-specific parameters and $\boldsymbol{\sigma}$ is a pseudospin vector. A schematic example of such a two-band model is shown in Fig. 2.7. The band structure is gapped by a Dirac mass m and the two cases (Fig. 2.7 (c) and (d)) only differ by the sign of the mass term, which is usually referred to as the so-called *band inversion* [10, 11, 15, 67, 68]. The reason for that is that the eigenstates of valence and conduction band change their energetic order (in this case at the zone boundary). This is illustrated by the red-blue color code, reflecting the pseudospin character of the eigenstates. It can now be shown that such a band inversion is accompanied by a change of the topological invariant. This is given by the winding number γ of the curve $k \mapsto \boldsymbol{d}(k)$, i.e., the number of times $\boldsymbol{d}$ wraps around the origin when k goes through the Brillouin zone. As can be seen in Fig. 2.7 (a,b) one finds $\gamma = 0$ in the non-inverted scenario and $\gamma = 1$ in the inverted case. The mapping $k \mapsto \boldsymbol{d}(k)$ directly reflects the geometric interpretation of the momentum space Hamiltonian and the topological character can be easily illustrated: The invariant, i.e., the winding number, is independent of the concrete shape of the curve. That means the curve can be smoothly deformed by changing band structure parameters, expressed through $\boldsymbol{d}(\boldsymbol{k})$ in the Hamiltonian. This is illustrated by the green dashed curve in Fig. 2.7 (a,b). As long as the winding number is fixed, the corresponding band structures are topologically equivalent, i.e., they are either topologically trivial ($\gamma = 0$) or non-trivial ($\gamma = 1$).

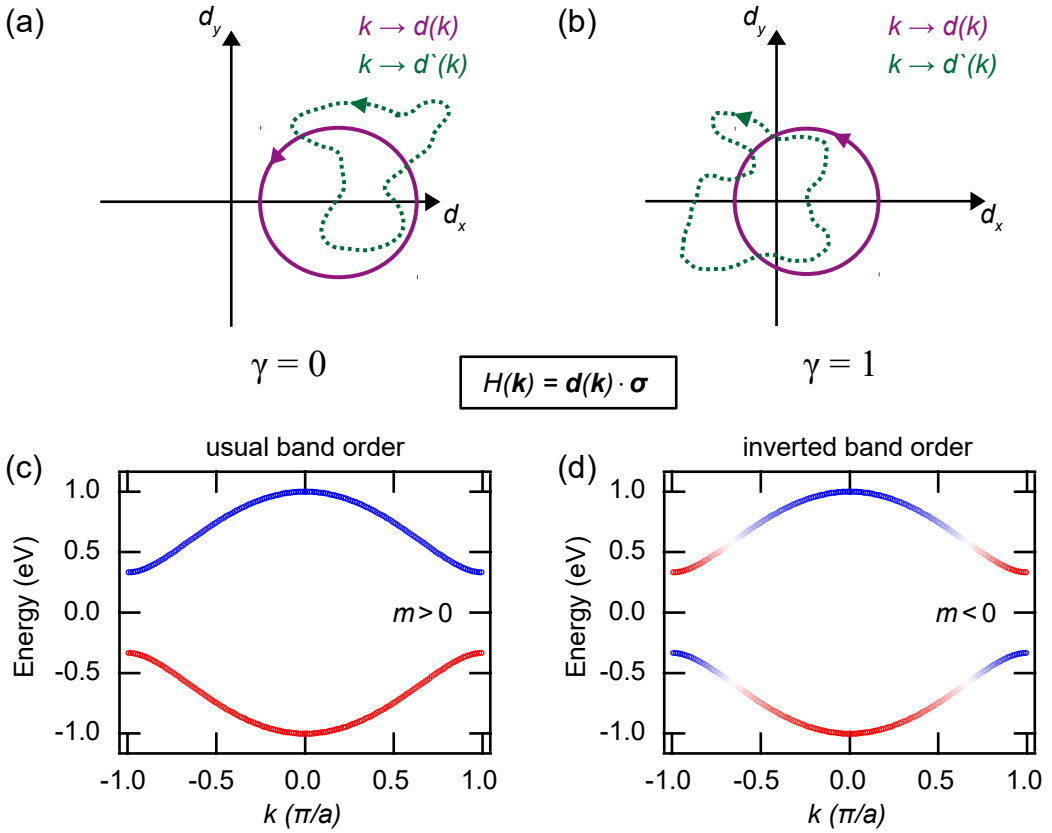

FIGURE 2.7: Relationship between topological classification and band inversion in a schematic two-band Hamiltonian. (a,b) the topological invariant γ is given by the winding number the curve $k \mapsto \boldsymbol{d}(k)$. In the band structure latter results from an inversion of the energetic order of the eigenstates, which is determined by the sign of the Dirac mass m in the Hamiltonian (c,d). The character of the eigenstates – here given by the pseudospin expectation value $\langle\sigma\rangle$ – is indicated by the red-blue color code. The topological classification depends only on the sign of m but is independent of any other deformation of the Hamiltonian. This is schematically shown by the different curves in (a,b).

Already the simple model consideration shows, that topology manifests in the momentum-dependence of the bulk eigenstates in the band structure (see Fig. 2.7 (c,d)). Yet, one of the most important consequences of non-trivial band topology is the existence of boundary modes that occur at the interfaces between materials with different topological invariants [21, 22]. Across the interface, the gap has to be closed in order to change the invariant. Accordingly, there will be in-gap states localized at the boundary, reconnecting inverted states of the same symmetry at both sites of the interface.
To model the interface between two materials with an inverted and a non-inverted band structure, respectively, the mass parameter at the interface has to change its sign smoothly so that $m(z) > 0$ for $\gamma = 0$ and $m(z) < 0$ for $\gamma = 1$. It can be shown that a simple solution exists for such a model in which in-gap states occur that are localized at the interface [108, 109]. In the late 1980th, Volkov and Pankratov developed a similar model using a variable mass parameter $m(z)$ to describe the interface between $Hg_{1-x}Cd_xTe$

layers with different cadmium concentration [67, 68]. Bands of (s-like) Γ_6 and (p-like) Γ_8 character invert as a function of x and the inverted band order causes a sign change of $m(z)$ at the interface. This leads to the formation of linearly-dispersing spin-polarized interface states in the bulk band gap, called topological surface or interface states (TSS) [10, 11, 67, 68, 110].

In 2007, the first 2D topological insulator (TI) has been theoretically predicted [10] and realized experimentally [11] in $Hg_{1-x}Cd_xTe$ quantum well states. Subsequently, the discovery of 3D TI followed [12–19].
Since this breakthrough was made, topological quantum matter has become an important workhorse in solid-state, as well as surface physics. The second main part of this thesis focuses on topological semimetals, more precisely Weyl semimetals. Since their existence requires spin-polarized three-dimensional bulk states, two possibilities arise to realize a WSM phase; the breaking of either time-reversal or inversion symmetry [20]. The latter mechanism is at the heart of this work and will be explained in more detail below.

The Weyl Semimetal Phase

The occurrence of the WSM phase can be particularly well understood by considering the phase transition between three-dimensional normal (topologically trivial) and topologically non-trivial insulators with preserved time-reversal symmetry [69–72]. First, only inversion-symmetric systems are considered (see Fig. 2.8 (b)) in which all bulk states are spin-degenerate. The phase transition manifests itself in the band inversion driven by a mass parameter m. In this phase diagram, there is a single critical point m_c where the valence and conduction band touch. If m is increased beyond the critical point, one directly enters the TI-phase. The situation changes when the inversion symmetry is broken ($\lambda_{\mathrm{ISB}} \neq 0$). A second dimension occurs in the phase diagram, as shown in Fig. 2.8 (a). Murakami showed that generically a novel topological phase occurs, which is not insulating but gapless [69–72]. This is the so-called Weyl semimetal (WSM) phase [75]. The three-dimensional bulk conduction and valence bands in WSM form crossing points of spin-polarized states. Importantly, these band crossings – called Weyl nodes or Weyl points – are topologically protected objects. Each Weyl node is associated with a topological invariant which is determined by the monopole charge of the BC. In other words, the BC integrated over a small sphere around a single Weyl node gives a quantized Chern number of $\gamma = \pm 1$. Weyl points can therefore be considered as a momentum space realization of Dirac magnetic monopoles.
Close to the band touching point $\boldsymbol{k}_W$, the two-band Hamiltonian (cf. Eq. 2.19) can be written as

$$H(\boldsymbol{k}_W + \boldsymbol{q}) = H_W(\boldsymbol{q}) = \sum_{i,j} v_{i,j} q_i \sigma_j \,, \tag{2.20}$$

where $\boldsymbol{q} = \boldsymbol{k} - \boldsymbol{k}_W$ and $i, j = x, y, z$. Moreover $v_{i,j}$ are real coefficients and Chern number is given by $\gamma = \mathrm{sgn}(\det(v_{i,j}))$ [74]. This Hamiltonian is of

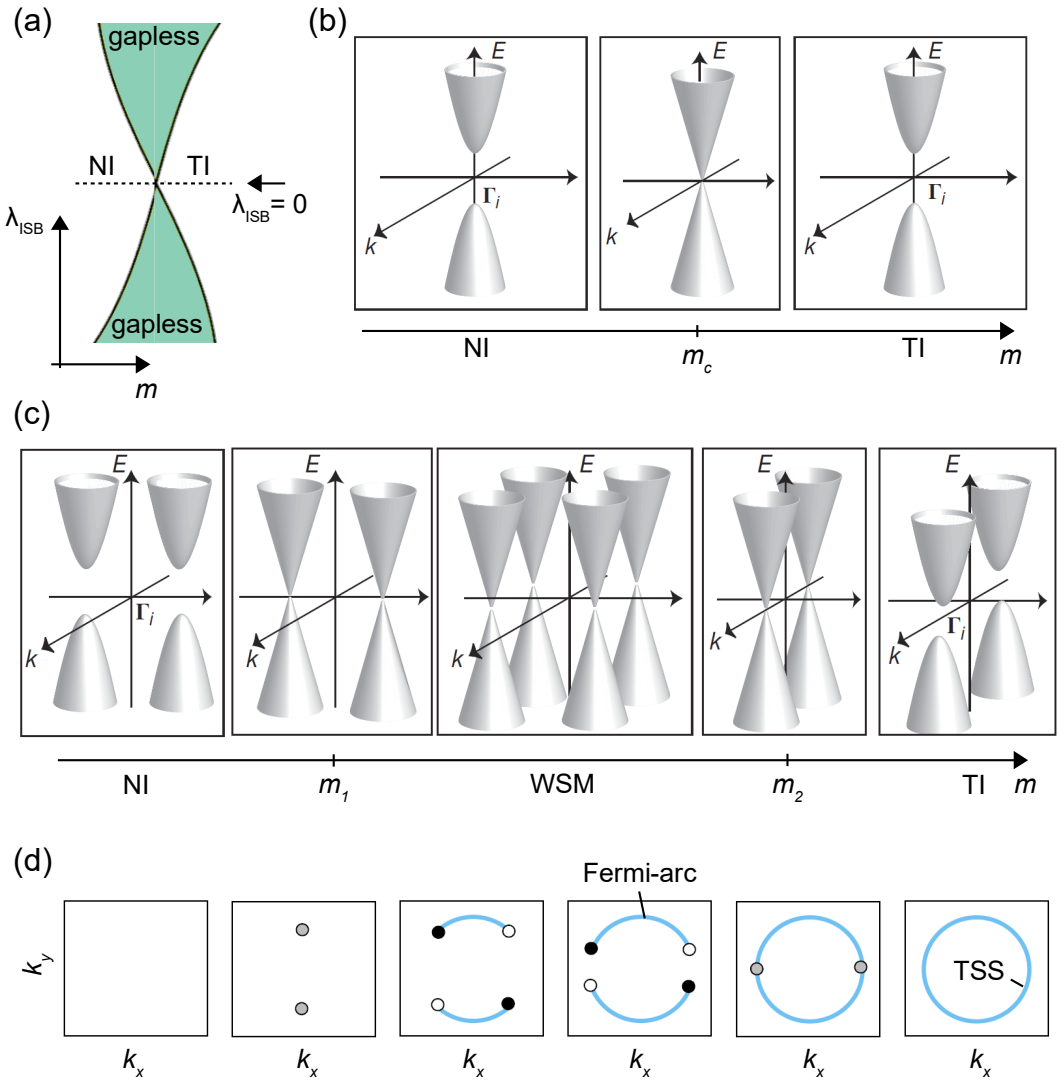

FIGURE 2.8: Generic Weyl semimetal phase in the band inversion transition between three-dimensional normal insulators (NI) and topological insulators (TI) as a function of the Dirac mass m. (b) If inversion symmetry is not broken ($\lambda_{\text{ISB}} = 0$) the phase diagram has a single critical point m_c, where valence and conduction band touch. For $\lambda_{\text{ISB}} \neq 0$ a second dimension enters in the phase diagram in (a). Generically a gapless topological phase corresponding to the Weyl semimetal phase occurs (c) between two critical points m_1 and m_2. (d) Non-trivial topology causes the formation of Fermi-arc surface states (blue lines) connecting Weyl points of different monopole charges (white and black circles). Latter can be considered as open versions of topological surface states (TSS) at TI surfaces. *Figures (a-c) are adapted from [71] under the Creative Commons CC BY-NC-SA 3.0 license and (d) from [111] under the Creative Commons CC BY 4.0 license.*

the same form as the one proposed by Hermann Weyl in 1929 to describe massless, chiral fermions [102]. Consequently, the low-energy quasiparticles in WSM can be regarded as Weyl fermions. Because these states can only appear in pairs of monopoles and anti-monopoles (that means in pairs

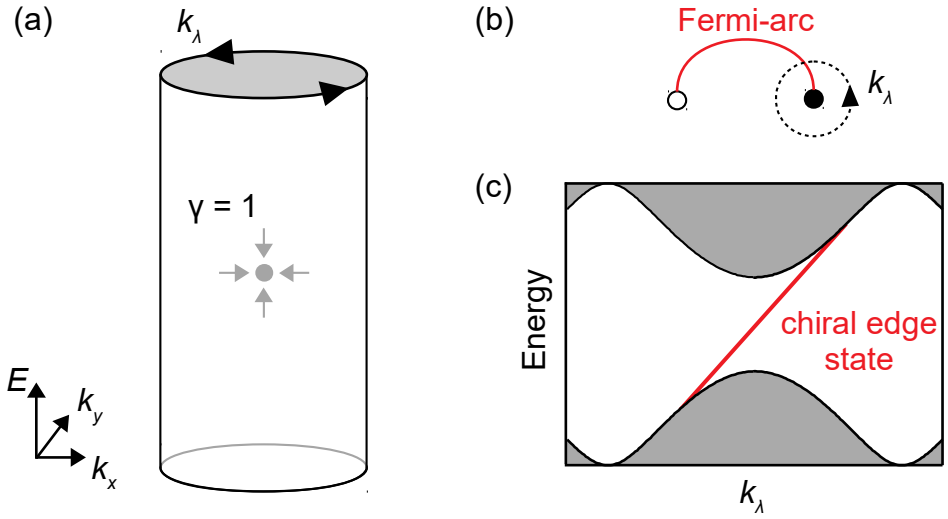

FIGURE 2.9: Illustration of Fermi-arc surface states arising from bulk Weyl points. (a) Consider a cylinder around a Weyl point with a monopole charge of $\gamma = 1$: The k_z-projected bulk band structure $E(k_\lambda)$ (c) along the curve $\lambda \mapsto \boldsymbol{k}_\lambda$ is gapped and a chiral surface state arises due to the non-trivial Chern number of the subspace spanned by k_z and k_λ. This holds for any curve (cylinder) enclosing a single Weyl point, which leads to the formation of a series of such edge modes. On the Fermi surface (b), these form an arc that connects two Weyl points with opposite chirality.

of Weyl fermions with opposite chirality), the band crossings are topologically protected. This can be understood by considering the generic two-band Hamiltonian (Eq. 2.19). At the Weyl point one finds $\boldsymbol{d}(\boldsymbol{k}_W) = 0$. In three-dimensional momentum-space, there are three linear equations ($d_j = 0$) and three variables k_j. That means there will be always a solution in k-space and the existence of the band crossing does not require any symmetry but they are rather robust [74]. Such accidental crossings are also named *diabolic points* and have been discussed in the context of Berry phase already in 1985 [112]. In this sense, it is also plausible that these are associated with a topological invariant, i.e., a Chern number, as outlined above [20]. Moreover, it is directly evident that dimensionality plays a crucial role in WSM. Considering, for instance, a 2D Dirac crossing as it can be found in the π-band structure of graphene [113], the Hamiltonian around the Dirac point can be written as $H(\boldsymbol{q}) = \sigma_x q_x + \sigma_y q_y$. In this case, adding an additional mass term $m\sigma_z$ would directly open a band gap. Thus, the crossing is not protected. In fact, it has been shown that the generic gapless phase (cf. Fig.2.8 (a)) does not appear in the phase diagram in 2D [70, 71]. In the three-dimensional scenario, in contrast, such a mass term, yielding $(q_z \pm m)\sigma_z$ in total, moves the Weyl nodes in momentum-space. The only way to get rid of them is to merge a monopole and an anti-monopole at the same $\boldsymbol{k}$-point [75]. Consequently, in 3D systems with broken inversion symmetry there will be not just a single critical point in the phase transition, but rather two critical points m_1 and m_2, corresponding to pair creation and annihilation, respectively (see Fig. 2.8 (a,c)). In between, there is a finite range in which the system remains gapless; the WSM phase.

Like in TI, non-trivial band topology in WSM causes the formation of topological surface states, called *Fermi-arcs* [75]. Fig. 2.8 (d) shows the same phase transition as in Fig. 2.8 (c) but as constant energy Fermi surfaces (FS). Blue lines correspond to the surface states and the grey, black, and white dots correspond to the bulk crossing points with a monopole charge of 0, 1, and -1, respectively. In the TI phase (right), there is a Dirac-cone-like TSS with a circular shaped FS, whereas no TSS occurs in the trivial case (left). The formation of Fermi-arcs can be imagined as follows; when the mass parameter is decreased beyond the critical point m_2, the TSS opens into two arc-like contours, connecting WP of opposite chirality.
The number of Fermi-arc features connecting two WP is directly related to the bulk band topology around them. This is the so-called *bulk-boundary correspondence*, which states that the difference of left and right moving chiral edge modes corresponds to the topological invariant[5] [21]. As shown in Fig. 2.9 (a,b) one can consider a curve $\lambda \mapsto \boldsymbol{k}_\lambda = (k_x(\lambda), k_y(\lambda))$, which encloses the projection of a single WP with chirality γ when the parameter λ is varied from $-\pi$ to π [75]. The projected bulk band structure $E(k_\lambda)$ along the curve (Fig. 2.9 (c)) defined by the cylinder sketched in Fig. 2.9 (a) is fully gapped as the crossing point of the bulk bands lies inside the cylinder. The 2D subspace spanned by k_λ and k_z is a non-trivial Chern insulator and the topological invariant is determined by the monopole charge of the WP (here, for example, one has $\gamma = 1$). Therefore, as shown in (Fig. 2.9 (c)), there must be a chiral surface state which closes the projected bulk band gap. Following this argument, such a gapless surface state has to occur for every curve enclosing a WP. Consequently, there is an arc-like contour in the constant energy surface (at the energy of the WP) that connects the two WP (see Fig. 2.9 (b)). In particular, the number of these Fermi-arcs has to reflect the net Chern number of the projected band structure. That is, if there are other WP (of different WP pairs) at different k_z within the cylinder, the sum of all projected chiralities must be considered. For example, if there are two WP with opposite chirality, the total Chern number will be zero and there will be no Fermi arcs on the surface. Vice versa, if there is another WP with the same chirality, two Fermi arcs will appear.

2.2.2 Realization in Transition Metal Monopnictides

The theoretical prediction of a WSM phase in the transition metal monopnictide class [76] was subsequently followed by first experimental evidence [77–83]. The latter was based on the comparison of DFT bulk band structure calculations with bulk-sensitive soft X-ray ARPES measurements [77–81] and the detection of Fermi arc surface states [77–83]. Since then, TMMP have become one of the most studied family of WSM candidates. Further hints on the non-trivial topology in these systems have been found by scanning tunneling

[5] More precisely, the difference of left and right moving chiral edge modes corresponds to the difference in the Chern number across the interface [21]. Nevertheless, mostly surface states are considered and the vacuum – to which the surface defines an interface – can be considered as topologically trivial, i.e., $\gamma = 0$.

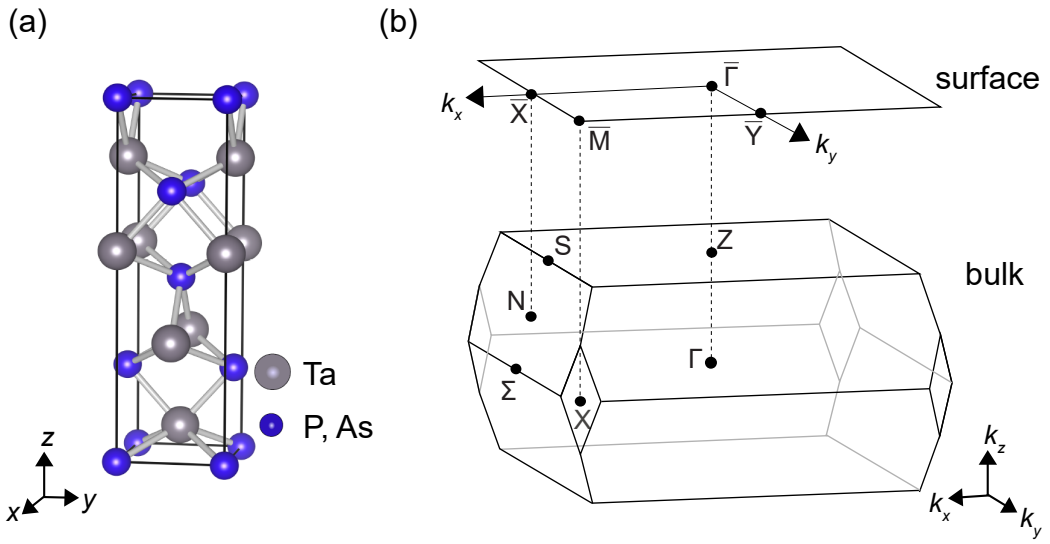

FIGURE 2.10: Real space and reciprocal space structure of Ta(As,P). (a) The crystal structure has no inversion center but two mirror planes corresponding to the ΓZSΣ - planes in the bulk Brillouin zone (b). The surface Brillouin zone of the squared (001) surface is also shown in (b) with the corresponding bulk projections. *Figure (a) has already been published in [87]. Figure (b) is adapted from [76] under the Creative Commons CC BY 3.0 license.*

microscopy [84], magnetotransport experiments [85], and via light-induced photocurrents [86]. The TMMP family represents a perfect model system for studying non-centrosymmetric WSM. In this section, an overview of the atomic and electronic properties relevant to this work is given, which show only minor differences in all four associated compounds NbP, NbAs, TaP and TaAs.

TMMP crystallize in a body-centered-tetragonal structure with the space group $I4_1md$ (no. 109). The crystal structure shown in Fig. 2.10 (a) does not exhibit inversion symmetry, but contains two mirror planes corresponding to the ΓZSΣ planes in the bulk Brillouin zone (Fig. 2.10 (b)). Fig. 2.11 (a) shows a DFT band structure calculation of TaAs without SOC. Qualitatively, a band inversion of the valence and conduction bands is seen, and several crossing points appear, all of which lie in the ΓZSΣ plane. As discussed in the context of topology in Ta(As,P) in [76], valence and conduction bands have different mirror symmetry with respect to the mirror planes. Accordingly, without SOC, all band crossings between them are protected. This leads to the formation of so-called *nodal rings* in the ΓZSΣ mirror planes (12 in each BZ), which are shown as green lines in Fig. 2.11 (c,d). Except for these rings, the band structure around the Fermi level is completely gapped throughout the BZ.
The same band structure calculation but now with SOC being included is shown in Fig. 2.11 (b). Due to ISB in the crystal structure, spin-degeneracy is lifted by SOC and each band splits into two spin-branches. Moreover, SOC allows for a mixing of states with different mirror symmetry and the band crossings are not protected anymore. Although these interband SOC matrix elements appear to be rather small compared to the relatively large intraband

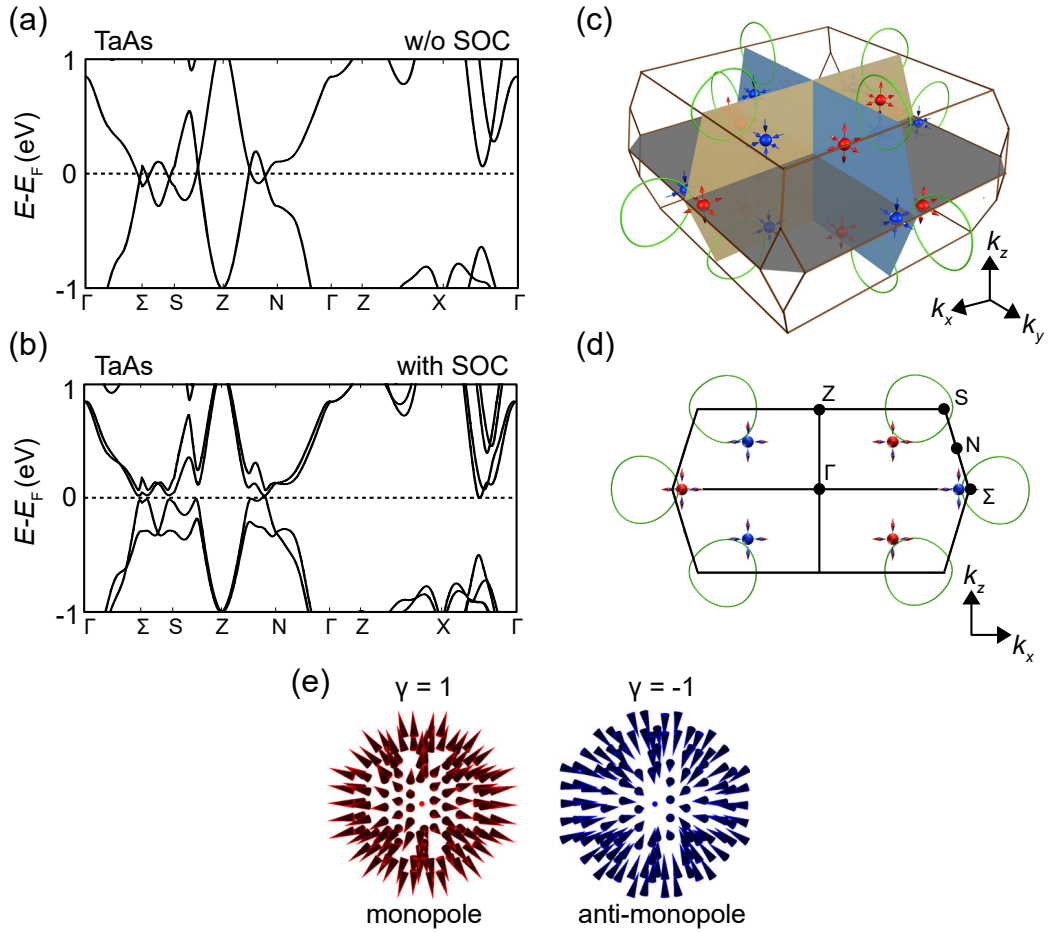

FIGURE 2.11: Bulk electronic structure of TaAs. (a) and (b) Band structure calculations without and with spin-orbit coupling (SOC), respectively. In the absence of SOC, the different mirror symmetry of the valence and conduction band eigenstates leads to the formation of 12 projected nodal rings in the ΓZSΣ - planes in the bulk Brillouin zone, shown as green lines (c,d). When SOC is included, each ring is divided into three pairs of Weyl points (WP) (red and blue points) slightly adjacent to the mirror planes. Each WP denotes a monopole ($\gamma = 1$) or anti-monopole of Berry curvature (e). *All figures are adapted from [76] under the Creative Commons CC BY 3.0 license.*

splittings found in the calculation, the band structure becomes gapped along all high symmetry directions [76]. Consequently, the nodal rings disappear, but isolated band crossings remain, slightly adjacent to the mirror planes. These correspond to the Weyl nodes in Ta(As,P) shown as red and blue points in Fig. 2.11 (c,d), where the color indicates the respective monopole charge. In total one finds 24 WP in the BZ; four equivalent pairs are lying in the $k_z = 0$ - plane and are named W_1, another eight pairs, called W_2, are lying at $k_z = \pm 0.592 \frac{2\pi}{c} = 0.32\,\text{Å}^{-1}$ in TaAs.
The topology can be analyzed in detail on a theoretical level by calculating the BC. The calculated momentum space field configuration of the BC of two different WP is shown in Fig. 2.11 (e). It can be seen that the two WP act as source and sink of Berry flux and therefore can be identified as monopole

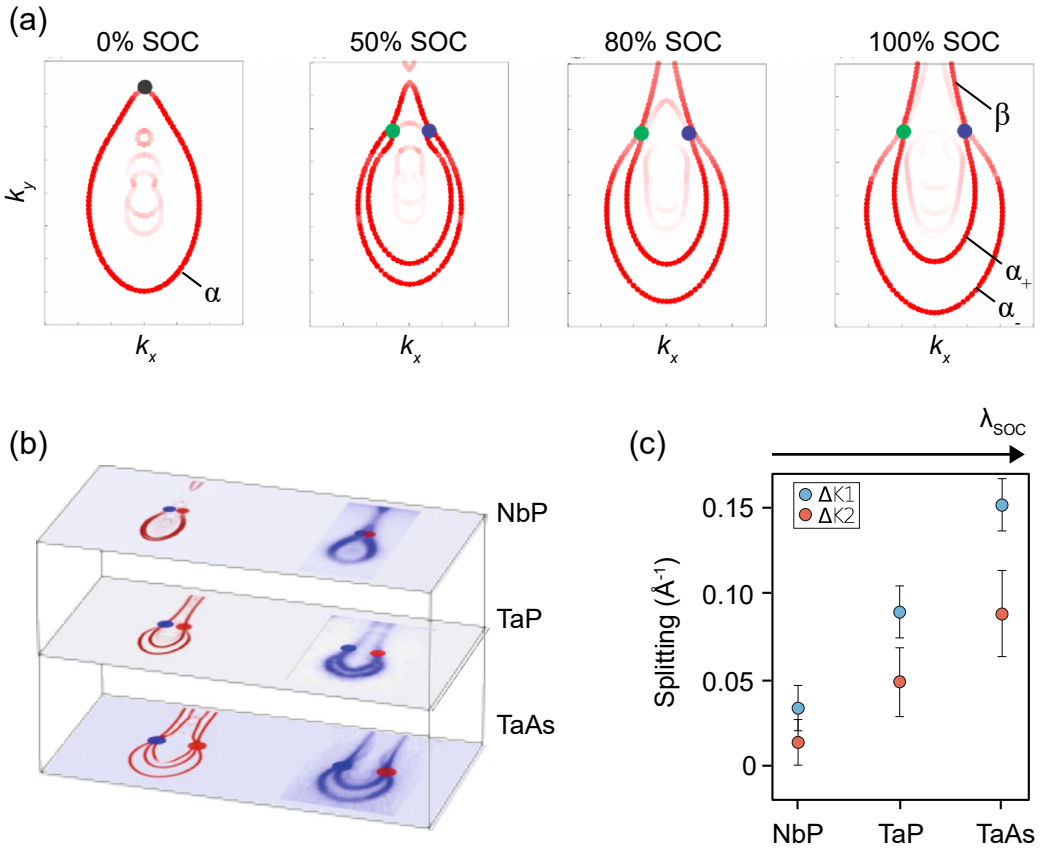

FIGURE 2.12: Fermi-arcs connecting the W_2 Weyl points at the (001) surface of transition metal monopnictides. (a) DFT surface band structure calculation around the W_2-points as a function of SOC strength. The color saturation of the red lines indicates the spatial localization of the states at the surface. The SOC-induced splitting of the bulk Weyl points as well as of the surface state α increases with increasing SOC strength. This can be seen by comparing TMMP compounds with different atomic SOC strengths as shown in (b,c). (b) Fermi surfaces of different TMMP compounds obtained from DFT calculation and ARPES experiments. (c) k-splitting of the W_2 points (ΔK1) and of the surface state spin-branches $\alpha_\pm$ (ΔK2) extracted from the ARPES data in (b). *Figure (a) is adapted with permission from [114]. Copyright © (2015) by the American Physical Society. All rights reserved. Figures (b,c) are adapted with permission from [82]. Copyright © (2015) Nature Publishing Group.*

and anti-monopole respectively. A deep theoretical analysis of the topology in TMMP can be found in Ref. [76].

As elaborated in Section 2.2.1, another important aspect in WSM is the occurrence of Fermi-arc surface states. DFT surface band structure calculations of the TMMP compounds [114] typically agree extremely well with surface-sensitive ARPES measurements (see Fig. 2.12 (b)) [77–83]. To explore the formation of Fermi-arcs, Fig. 2.12 (a) shows a DFT calculation of the TaP(001) surface in a small $k_{||}$ area around a pair of W_2 Weyl points, where the SOC strength has been varied artificially. The red lines correspond to surface states whereas the solid points denote the crossing points of the bulk bands. Without SOC, the system is not in the Weyl phase, but the single crossing point

corresponds to the nodal loop band crossing of the spin-degenerate bands. A surface state terminating at the nodal loop appears, but the Fermi surface is a closed contour rather than an open arc in agreement with a bulk monopole charge of zero. However, when SOC is switched on, the two WP are separated in momentum space. Notably, along the [001]-direction there are two pairs of WP projected on the same point in the surface Brillouin zone (compare Fig. 2.11 (c,d)). Therefore, the net Chern number of a projected WP has to be ± 2 instead of ± 1. Spin-degeneracy gets also lifted by SOC in the surface states, and now two branches appear. Both end at the projected WP and form an open Fermi-arc. Importantly, there is a third surface feature that terminates at the WP. This is in contrast to the expectation from the bulk perspective, from which two Fermi-arcs (reflecting a net chirality of ± 2) would be expected. Thus, one of the three features has to be a trivial surface state [76], and the question arises, which one it is. A priori, there is no simple answer to this question and for TaAs contradictory assignments even arise in literature [77, 83]. While in [77] the two spin branches α_+ and α_- have been assigned to the non-trivial surface states, in [83] is has been argued that the outer branch α_+, as well as, β are the two Fermi-arcs connecting the W_2 Weyl points. Even a detailed and systematic DFT-based analysis – performed on a small k-grid and including an analysis of the spin texture – does not allow for a conclusive statement on this issue [76]. This makes topology analysis in TMMP based only on surface states quite difficult and a deeper knowledge of the surface-bulk connectivity is required. A recent combined ARPES and DFT study [115] has addressed this very issue, revealing that β most likely corresponds to a surface resonance that arises when α_+ connects to the bulk WP. Accordingly, $\alpha_\pm$ are probably rather the Fermi arcs and β a trivial surface state or resonance.

Finally, the dependence of the electronic structure on the SOC strength will be briefly discussed. As can be seen in Fig. 2.12 (a), both the separation of the WP as well as the k-splitting in α increases with increased SOC strength. This can be also observed – in theory and experiment – by comparing the different compounds (NbP, TaP, and TaAs) as shown in Fig. 2.12 (b,c). The splittings increase directly with the average atomic SOC strength in the compounds, i.e., $\lambda_{\mathrm{SOC}}^{\mathrm{Nb}} < \lambda_{\mathrm{SOC}}^{\mathrm{Ta}}$ and $\lambda_{\mathrm{SOC}}^{\mathrm{P}} < \lambda_{\mathrm{SOC}}^{\mathrm{As}}$. The compounds Ta(As,P) studied in this work are thus those with the largest possible splitting in the material class.

Chapter 3

Photoelectron Spectroscopy

3.1 Basic Principles

Photoelectron spectroscopy (PES) is a valuable experimental technique for studying the electronic properties of crystalline solids and surfaces. The method is based on the photoelectric effect, which was discovered by Heinrich Hertz in 1887 [116] and explained by Albert Einstein in 1905 [117].
If a sample surface is exposed to light with energy $h\nu$, electrons can be emitted from the sample, provided that the light energy is larger than the work function Φ_S of the sample. In this case, electrons get excited from an occupied initial state of energy E_i to an unoccupied final state of energy E_f above the vacuum level. Emitted electrons leave the sample with a kinetic energy E^S_{kin}, and energy conservation ($h\nu = E_f - E_i$) yields

$$E_B = h\nu - \Phi_S - E^S_{\text{kin}} \tag{3.1}$$

using the reference energies as sketched in Fig. 3.1 (a). When passing the electron energy analyzer, which is electrically connected to the sample and thus both are at the same chemical potential, the photoelectrons feel another potential that refers to the work function of the analyzer Φ_A. Therefore, the kinetic energy measured in the experiment E^A_{kin} changes compared to E^S_{kin} giving

$$E_B = h\nu - \Phi_A - E^A_{\text{kin}}. \tag{3.2}$$

In the photoemission process, crystalline bulk translation symmetry is broken by the potential step perpendicular to the surface. Thus, when the electron escapes the sample, the crystal momentum perpendicular to the surface changes (see Fig. 3.1 (b)), and only $\boldsymbol{k}_\parallel$ is conserved except for reciprocal lattice vectors $\boldsymbol{G}_\parallel$:

$$\boldsymbol{k}^f_\parallel = \boldsymbol{k}^i_\parallel + \boldsymbol{q}_\parallel + \boldsymbol{G}_\parallel \quad , \tag{3.3}$$

where the wave vector of the light $\boldsymbol{q}$ can be neglected for low photon energies, where its magnitude is small compared to the size of the Brillouin zone. The parallel final state momentum is given by the kinetic energy of the free electron and the emission angle θ, as shown in Fig. 3.1 (b):

$$k^i_\parallel - G_\parallel \approx k^f_\parallel = \frac{\sqrt{2m_e}}{\hbar}\sqrt{E_{\text{kin}}}\sin(\theta). \tag{3.4}$$

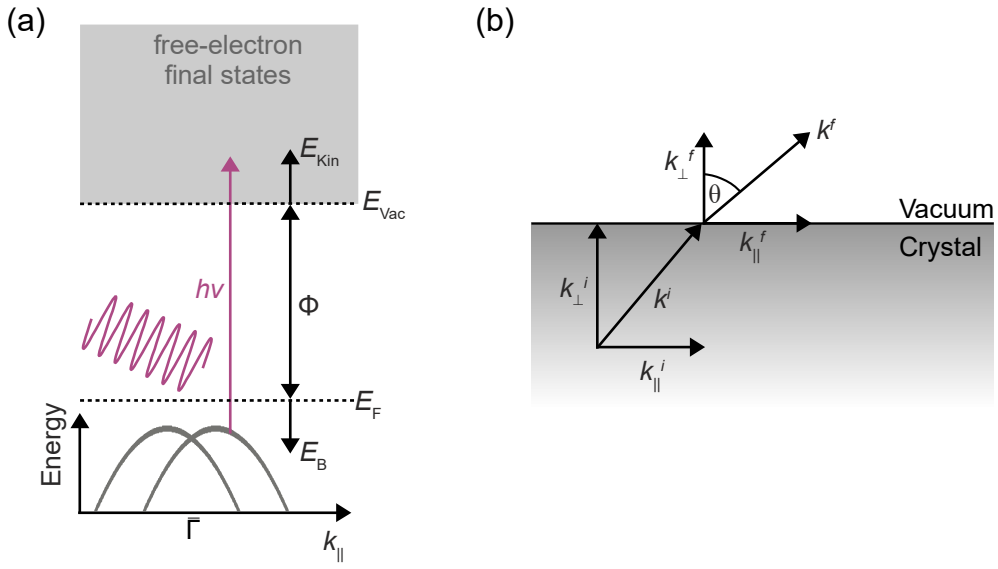

FIGURE 3.1: Energy diagram (a) and momentum conservation (b) in the photoemission process.

Thus, angle-resolved photoelectron spectroscopy (ARPES) can be used to map the single-particle band structure $E_B(\boldsymbol{k}_{\parallel})$ of crystalline solids along the parallel momentum.
In contrast, the determination of $k^i_\perp$ is not straightforward since this quantity is not conserved. However, there is another way to map the out-of-plane band structure $E(k^i_\perp)$ as well, namely by changing the photon energy. This is shown schematically in Fig. 3.2. First, consider photoemission from a surface initial state (Fig. 3.2 (a)), for which the out-of-plane spectrum is constant. In this case, changing the photon energy simply results in excitation into different final states. Hence, the observed binding energy is the same for all $h\nu$. On the other hand, if photoemission from a $k_\perp$-dispersing bulk initial state is considered, the change in the photon energy depends on the dispersion of both the initial and the final state as shown in Fig. 3.2 (b). Consequently, the observed binding energy will change. The final state dispersion is a priori not known but can be approximated by assuming a free-electron-like dispersion (Fig. 3.2 (c)) [118]:

$$E(k^f_\perp) = \frac{\hbar^2 {k^f_\perp}^2}{2m_e} - V_0, \tag{3.5}$$

resulting in

$$k^i_\perp - G_\perp \approx k^f_\perp \approx \frac{\sqrt{2m_e}}{\hbar}\sqrt{E_{\text{kin}}\cos^2(\theta) - V_0}. \tag{3.6}$$

The inner potential V_0 denotes the bottom of the free-electron parabola relative to E_{Vac}. It can be considered as the depth of the surface potential and is typically retrieved by matching bulk band structure calculations to the experimentally observed periodicity as a function of $h\nu$.

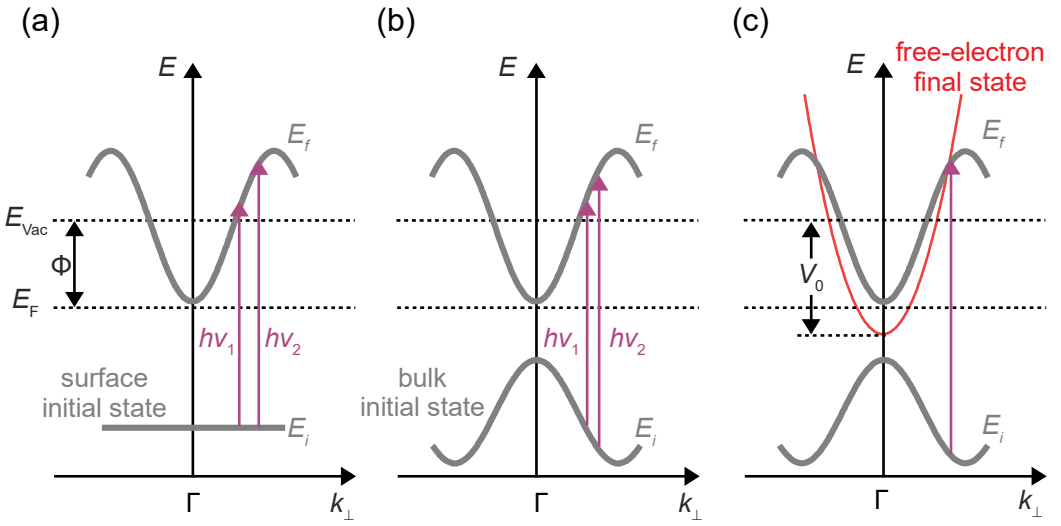

FIGURE 3.2: Photoemission in dependence of photon energy. (a) A surface initial state E_i has no dispersion along $k_\perp$ and changing the photon energy leads to excitation into different final states E_f. The observed binding energy is thus independent of $h\nu$. For bulk initials states (b,c) the change of the photon energy depends on both the initial state and final state dispersion as illustrated in (b). The observed binding energy changes in this case. The final state dispersion is in general unknown but can be approximated by a free-electron final state parabola whose vertex is at $E_{\text{Vac}} - V_0$. V_0 is the inner potential.

3.2 Photoemission Matrix Elements and Dichroism

The photoemission process is typically described in a semiclassical approach in which the system is optically excited by a classical electromagnetic wave

$$\boldsymbol{A} = \boldsymbol{A_0} \exp(i(\boldsymbol{qr} - \omega t)),$$

where $\boldsymbol{q}$ is lying within in xz- plane of the experimental setup as shown in Fig. 3.3. In first order perturbation theory, the photocurrent is then given by the transition rate $w_{i\to f}$ from an initial state $|i\rangle$ to a final state $|f\rangle$, which are eigenstates of the unperturbed Hamiltonian H_0. Fermi's golden rule yields

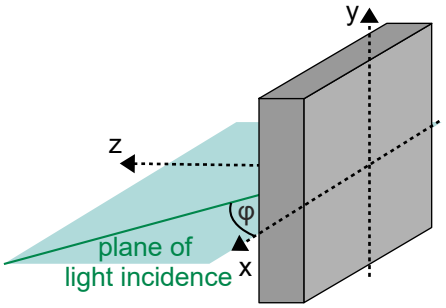

FIGURE 3.3: Experimental geometry.

$$w_{i\to f} = \frac{2\pi}{\hbar} |\langle f| H_{\text{int}} |i\rangle|^2 \delta(E_f - E_i - h\nu) \tag{3.7}$$

and the perturbation H_{int} is found by substituting $\boldsymbol{p} \to \boldsymbol{p} - e\boldsymbol{A}$ in H_0:

$$H_{\text{int}} = -\frac{e}{2m}(\boldsymbol{pA} + \boldsymbol{Ap} - e\boldsymbol{A}^2) = -\frac{e}{2m}(2\boldsymbol{Ap} + i\hbar(\nabla \boldsymbol{A}) - e\boldsymbol{A}^2) \approx -\frac{e}{m}\boldsymbol{Ap} \tag{3.8}$$

The quadratic term in $\boldsymbol{A}$ has been neglected, since it makes a significant contribution only for very strong light fields [119]. Furthermore, if specific surface photoemission effects [120] are neglected, $\nabla \boldsymbol{A} = 0$ is obtained.
At photon energies in both the VUV and the soft X-ray regime, the corresponding wavelengths are large compared to the atomic distances yielding $qr \ll 1$, and consequently, dipole approximation ($\exp(i\boldsymbol{qr}) \approx 1 + i\boldsymbol{qr} + ... \approx 1$) can be applied. The direction of $\boldsymbol{A}_0$ gives the light polarization $\boldsymbol{E} = (\mathcal{E}_x, \mathcal{E}_y, \mathcal{E}_z)$ and one gets

$$H_{\text{int}} \propto \boldsymbol{Ep} \propto \boldsymbol{Er}. \tag{3.9}$$

Although the term $\boldsymbol{Ep}$ is in principle sufficient to establish photoemission selection rules, in the last step, the permutation $[H, \boldsymbol{r}] \propto \boldsymbol{p}$ was applied in order not to confuse the components of the momentum operator with the p-orbital initial states, which are often needed in this thesis.

Dipole Selection Rules for Linear Light Polarization

The resulting matrix element can be written component-wise

$$T = \langle f | \boldsymbol{Er} | i \rangle = \langle f | \mathcal{E}_x x | i \rangle + \langle f | \mathcal{E}_y y | i \rangle + \langle f | \mathcal{E}_z z | i \rangle . \tag{3.10}$$

By a suitable choice of light polarization, certain components of the total matrix elements can be picked up selectively [121]. Within the experimental geometry used (see Fig. 3.3), the light polarization vectors for s and p polarization are $\boldsymbol{E}_s = (0, \mathcal{E}_y, 0)$ and $\boldsymbol{E}_p = (\mathcal{E}_x, 0, \mathcal{E}_z)$, respectively. The angle of light incidence is given by $\tan\varphi = \mathcal{E}_z / \mathcal{E}_x$. The resulting matrix elements are:

$$\begin{aligned} T_s &= \langle f | \mathcal{E}_y y | i \rangle \\ T_p &= \langle f | \mathcal{E}_x x | i \rangle + \langle f | \mathcal{E}_z z | i \rangle . \end{aligned} \tag{3.11}$$

The xz-plane ($y = 0$) is considered to match a mirror plane of the sample, and the electrons are emitted within this plane. A plane wave final state $\propto \exp(i\boldsymbol{kr})$, which leaves the surface in the mirror plane $k_y = 0$, is generically even with respect to mirror symmetry $M_y \colon y \to -y$ [121]. The position operators x, z and y are obviously even and odd, respectively. Since the total integrand has to be even to yield finite results, $T_s \neq 0$ ($T_p \neq 0$) is found for odd (even) initial states.
Using similar arguments, one finds for electrons emitted within the yz-plane, that $T_s \neq 0$ for states which are even under mirror symmetry $M_x \colon x \to -x$. For p polarization, the different matrix element components are instead non-vanishing for initial states with different mirror symmetry, i.e., $T_x \neq 0$ for odd states and $T_z \neq 0$ for even states.
Taken together, an appropriate choice of the light polarization gives rise to strict dipole selection rules providing deep information about the spatial symmetry of the initial state wave functions.

Circular and Linear Dichroism

Circular dichroism (CD) in the photoelectron intensity distribution describes the photoemission intensity difference for ARPES measurements taken with left and right circularly polarized light.

$$\mathrm{CD}(k_x, k_y) = I_R(k_x, k_y) - I_L(k_x, k_y) \tag{3.12}$$

Within the experimental lab frame (Fig. 3.3), the corresponding light polarization vectors are $\boldsymbol{E}_{\mathrm{R,L}} = (\mathcal{E}_x, \pm i\mathcal{E}_y, \mathcal{E}_z)$. This results in a photoemission intensity

$$\begin{aligned} I_{\mathrm{R,L}} &\propto |T_x \pm iT_y + T_z|^2 \\ &\propto |T_x|^2 + |T_y|^2 + |T_z|^2 + 2\Re(T_x^* T_z) \pm 2\Im(T_x^* T_y) \pm 2\Im(T_y^* T_z), \end{aligned} \tag{3.13}$$

with the matrix elements $T_{x,y,z} = \langle f | \, \mathcal{E}_{x,y,z} \, | i \rangle$. The resulting CD reads

$$\mathrm{CD}(k_x, k_y) \propto 4\Im(T_x^* T_y) + 4\Im(T_y^* T_z). \tag{3.14}$$

In general, asymmetries can occur in the photoelectron angular distribution, and the CD is by definition anti-symmetric with respect to $k_y \rightarrow -k_y$ and vanishes within the plane of light incidence ($k_y = 0$). Moreover, it can be seen that a finite CD can occur only if $|T_y| \neq 0$ and in addition it has to be either $|T_x| \neq 0$ or $|T_z| \neq 0$ [1]. The CD-asymmetry can be considered as an interference effect. Each matrix element denotes a specific photoemission channel, and the matrix element products in Eq. 3.14 describe the interference terms between these channels.

CD-ARPES has been performed on various condensed matter systems, such as organic molecules [122], graphene [123], transition metal dichalcogenides [89] or surface states of topological insulators [88, 124–127] or Rashba systems [37, 48, 51, 126, 128–130]. Rather contradicting statements are found regarding the overall information content of CD-ARPES. While some research studies *assign the dichroism to a final-state effect* [sic] [127] it is stated to be rather a result of the experimental geometry in Ref. [125]. Other than that, it is claimed that CD-ARPES is sensitive to the spin [124] or orbital angular momentum [37, 48, 51, 88, 89, 126] in the initial state. More generally, it can be said that CD-ARPES is a photoemission matrix element effect and thus depends on the experimental geometry as well as on the initial and the final state. In this regard – similar to each matrix element effect – initial state information, which are usually in the focus of interest, can be gained. However, experimental geometry as well as final state effects have to be carefully considered.
Especially in spin-split electronic states, the CD is of great interest, and there is broad experimental evidence [37, 48, 51, 88, 89] that the main source of the CD in the initial state is most likely the local OAM-component $\langle L_p \rangle$ parallel to the light propagation direction $\boldsymbol{q}_p$ [48, 88]. The interplay of SOC and

[1] With that, the CD depends also on the angle of light incidence as discussed below.

ISB plays a decisive role in this context. As elaborated in Chapter 2.1.4, the OAM in spin-split branches with opposite spin polarization can either have the same sign as in the case of ISB-dominated systems, but also the opposite sign when SOC is dominant (cf. Fig. 2.6) [37, 48, 50, 51]. This theoretically expected behavior is directly reflected in CD-ARPES experiments, for instance, on the Rashba-type spin-split surface states on Au(111) [51, 129] and $Ag_2Bi/Ag(111)$ [128, 130], respectively.
The importance of the experimental geometry, in particular the angle of light incidence φ, also becomes clear [88, 129]. In an idealized Rashba-scenario, a purely in-plane helical OAM texture is expected. Only the second term in Eq. 3.14 contributes to the in-plane OAM $\langle L_x \rangle$, while the first term is sensitive to $\langle L_z \rangle$. This means that in the two highly symmetric cases (grazing or normal incidence), full sensitivity to the in-plane or out-of-plane OAM is expected [129]. For any other φ, CD contributions from both components can occur.

In contrast to CD, linear dichroism (LD) in the photoelectron angular distribution is not widely used. It has been reported in graphene [131] and recently discussed in the context of spin-split electronic states such as the Rashba-system $Ag_2Bi/Ag(111)$ [132] and for Fermi-arc surface states on the Weyl semimetal TaP(001) [115]. The former system is discussed moreover in more detail in [133].
The LD is defined as the intensity asymmetry that can occur between $+k_x$ and $-k_x$ for ARPES measurements conducted with p polarized light

$$\mathrm{LD}(k_x, k_y) = I(+k_x, k_y) - I(-k_x, k_y). \tag{3.15}$$

The photoemission intensity can be written as:

$$I(\pm k_x, k_y) \propto |T_z \pm T_x|^2 = |T_x|^2 + |T_z|^2 \pm 2\Re(T_x^* T_z) \tag{3.16}$$

and the LD results in:

$$\mathrm{LD}(k_x, k_y) \propto 4\Re(T_x^* T_z) \tag{3.17}$$

Similar to the CD, LD is an interference effect that emerges from different photoemission channels T_x and T_z, which both have to be finite in order to observe LD. Therefore, it also depends on the angle of light incidence.
It becomes clear that there might be a relation between CD and LD, both of which include a product of an in-plane and an out-of-plane matrix element. One can expect a similar information content for the CD in grazing light incidence and the LD under $\varphi = 45°$, whereby the asymmetry is of course along k_y and k_x, respectively. This aspect has not yet been discussed thoroughly in literature. Nevertheless, an opposite LD sign has been reported for the Rashba branches in $Ag_2Bi/Ag(111)$ [132, 133] in agreement with the observed CD [128, 130].

Spin-Resolved Photoemission

The spin polarization of the emitted photoelectrons can be determined by spin-resolved photoemission experiments [27, 134]. After excitation, the photoelectrons hit a target and scatter in dependency of their spin-polarization along a certain direction. In recent years, various targets have been developed that rely on different spin-selective scattering mechanisms. The most prominent examples are Mott-targets [135] or (V,SP)LEED detectors in which the spin-selective reflectivity can rely either on a macroscopic magnetization [136] of the target or strong spin-orbit coupling in the target material [137].
The spin polarization P is determined from the observed scattering asymmetry:

$$P = \frac{1}{S_{eff}} \frac{I_\uparrow - I_\downarrow}{I_\uparrow + I_\downarrow} \quad , \tag{3.18}$$

where the Sherman function S_{eff} represents the efficiency of the scattering target and can be determined experimentally by scattering experiments with electrons of defined spin polarization.
To what degree the measured photoelectron spin polarization reflects the spin polarization in the initial state is a rather complex issue. Notably, the interplay of ISB and SOC might also play an important role in this question. Nevertheless, this is beyond the framework of this thesis and will be discussed only partially in the respective sections. Readers wishing to explore this topic in more detail are referred to the following thesis [133], which also discusses in detail the dependence of the measured spin polarization on the light polarization, final state effects, and linear dichroism in spin-resolved ARPES experiments.

3.3 Experimental Setups

Photoemission experiments presented in this work were conducted at different experimental setups, including the laboratory setup in Würzburg and different synchrotron facilities. In all cases, ARPES experiments have been performed in ultrahigh-vacuum (UHV) chambers with a base pressure below $3 \cdot 10^{-10}$ mbar and at a sample temperature of ≈ 30 K. While the light sources differ at each setup, the hemispherical electron analyzer is a Scienta R4000 in each case. In this type of analyzer, electrons are forced into a circular path by an electric field between the two hemispheres. The energy needed for the electrons to pass through depends only on the geometry and the voltage applied between the hemispheres. This so-called pass energy is kept constant in the experiment, and an additional accelerating voltage is applied to vary the kinetic energy beforehand. In addition, the emission angle θ of the electrons (see Fig. 3.1 (b)) within the plane of the entrance slit (perpendicular to the analyzer radius) can be mapped onto the multichannel plate placed behind the hemispheres. Two different lens modes, *Angular 14* and *Angular 30* can be selected, in which an acceptance angle of $\pm 7^\circ$ and $\pm 15^\circ$ is achieved, respectively.

Laboratory in Würzburg

The high-resolution ARPES setup in Würzburg consists of three UHV chambers, namely a loadlock, a preparation chamber, and the main chamber, all of which are connected by gate valves. The preparation chamber is equipped with a sputter gun for Ar-ion bombardment, an electron beam heater, a low-energy electron diffraction (LEED) apparatus, and several effusion cells. The sample temperature during annealing can be controlled by a pyrometer. ARPES measurements are conducted in the main chamber, which is equipped with a hemispherical analyzer as well as an X-ray source and a He discharge lamp (MB Scientific AB), both of which are monochromatized. The plane of light incidence has an angle of 45° relative to the analyzer slit. In order to measure the entire k-space (along k_x and k_y), the sample has to be rotated. Measurements shown in this thesis were conducted using a pass energy of 10 eV, which yields a reasonable compromise of adequate count rates and sufficiently good total energy resolution of $\Delta E \approx 8$ meV [138]. The angular resolution amounts to $\Delta\theta \approx 0.3°$, as determined in previous works [99].

μARPES Setup at Beamline 7 of the Advanced Light Source, Berkeley

The μARPES setup is situated at the MAESTRO beamline (BL7) of the Advanced Light Source (ALS) in Berkeley. The synchrotron beamline provides photon energies of 20...1000 eV and variable light polarization that can be adjusted to s (≥ 65 eV), p as well as left and right circularly polarized light. The analyzer can be rotated azimuthally and has been aligned so that the entrance slit is parallel to the plane of light incidence. ARPES data can be acquired as a function of both in-plane momentum directions without rotating the sample by using custom-made deflectors. The angle of light incidence (compare Fig. 3.3) is fixed at $\varphi = 35.25°$. In measurements presented in this work, the pass energy was set to 40 eV yielding an energy resolution of $\Delta E \approx 20$ meV.

ASPHERE Setup at PETRA 3, Hamburg

The ASPHERE setup is situated at the soft X-ray beamline P04 of the PETRA 3 synchrotron at DESY in Hamburg. Photon energies of 200...3000 eV are provided, and the light polarization can be set to left and right circularly polarized light. Similar to the μARPES facility, ARPES data can be acquired in both in-plane k-directions without the need for sample rotation by either rotating the analyzer or using a commercial deflector mode (Scienta, DA30-L). The latter option was used in this work. The angle of light incidence is $\varphi \approx 17°$, and the plane of light incidence is parallel to the analyzer entrance slit. For the SX-ARPES experiments, a pass energy of 50 meV was chosen, which results in an energy resolution of $\Delta E \approx 90$ meV.
The analyzer is equipped with a Mott-type spin detector (Scienta Omicron), which allows for the detection of all three spin components. The Au scattering target has a Sherman function of $S_{eff} = 0.1$. In spin-resolved measurements, energy and angular resolution are reduced to $\Delta E \approx 600$ meV and $\Delta\theta \approx 6°$, respectively.

Chapter 4

Orbital-Driven Origin of Rashba-Type Spin-Orbit-Splittings

The growth of atomically thin monolayer materials on single crystal substrates allows the investigation of their versatile two-dimensional electronic properties using ARPES [28, 101, 139–143]. Moreover, inversion symmetry is inherently broken at the surface, which enables the occurrence of Rashba-type [24, 25] spin-orbit splittings in the surface band structure [26–28, 32, 35–37]. The electronic structure of submonolayer Tellurium grown on an Ag(111) substrate will be the subject of this chapter. Tellurium (Te) is the heaviest ($Z = 52$) non-radioactive element in the chalcogen group in the periodic table. Spin-orbit coupling effects – that scale with the atomic number – become relevant in *high-Z* materials hosting heavy elements such as Te in their crystal structure [144–147]. For instance, thin films of Sb, Pb, or Bi grown on Cu(111) and Ag(111) substrates form substitutional surface alloys for which giant Rashba-type spin-splittings have been found in their two-dimensional electronic band structure [28–31, 33, 34, 65, 66]. In these systems, the latter can be easily modified with the choice of the appropriate adatom; the Rashba parameter increases with increasing atomic numbers (Sb $\rightarrow$ Pb $\rightarrow$ Bi) [148, 149], and the Fermi level can be shifted by electron doping (Pb $\rightarrow$ Sb/Bi) [148, 149]. The tunability makes this class of thin-film materials a model system for the Rashba effect and provides a playground to study its microscopic origin [29, 30, 43, 44, 54, 62].
Systematic substitution of the established atomic species with Te would allow further modification of the band structure. Te has one more valence electron than Sb and Bi, which means that higher-lying states would also be occupied and thus accessible with ARPES. Furthermore, even new topological phases are predicted, such as a QSHI phase in monolayers of Ag_2Te and Cu_2Te [150], which are isostructural to the mentioned alloys, or two-dimensional Dirac nodal lines in binary honeycomb compounds [151].
Together this motivates the investigation of submonolayer Te grown on Ag(111), which will be the main subject of this chapter. After characterizing the surface atomic and electronic structure in Sect. 4.1 the main focus will be on the Rashba effect, which has been demonstrated to occur in the band structure of the grown AgTe film (Sect. 4.2). The experimental findings are underpinned by DFT calculations, and explained by a minimal tight-binding model. The results show that AgTe is a potential model system for an OAM-based origin of the Rashba effect [47–50]. Signatures in the

momentum-dependent orbital texture, which is accessible with ARPES, give strong evidence that the model assumptions indeed correctly describe the Rashba physics in AgTe as shown in Sect. 4.3.

Details of ARPES Experiments

ARPES data shown in this chapter have been taken at two different experimental setups with a base-pressure below 2×10^{-10} mbar and a sample temperature of 30 K.
High-resolution data as shown in Fig. 4.2 and 4.3 were recorded at the Würzburg setup, which was explained in Chapter 3. Samples were prepared *in situ* and directly transferred to the ARPES chamber. Preparation and surface quality have been controlled by LEED and photoemission (see Sect. 4.1.1).
Polarization and photon-energy-dependent measurements were conducted at the MAESTRO endstation at the Advanced Light Source (Berkeley, USA). At the μ-ARPES setup at MAESTRO, ARPES data was acquired as a function of both in-plane momentum components by employing custom-made deflectors [64]. Thus, the sample did not have to be rotated, and the experimental geometry was not changed during data acquisition. For these measurements, the sample was prepared at the Würzburg setup and transferred to MAESTRO in air. Annealing the surface in UHV at 800 K resulted in ARPES data of similar quality as for an in situ preparation.

Further Experimental and Theoretical Methods

LEED-IV and scanning tunneling microscopy (STM) measurements, STM simulations, structural DFT calculations, and a quantitative structure analysis have been performed in the group of Prof. Dr. M. Alexander Schneider (Erlangen). Angle-resolved two-photon photoemission (2PPE) experiments were executed by Begmuhammet Geldiyev in the group of Prof. Dr. Thomas Fauster (Erlangen). Further details of the 2PPE measurements can be found in [152]. Samples were prepared directly in Erlangen in two different experimental setups explained in more detail in [64] and [153], respectively.

DFT band structure calculations were performed by Philipp Eck in the group of Prof. Dr. Giorgio Sangiovanni (Würzburg). For this purpose, a 7-layer-thick Ag slab in (111) direction was considered with the experimentally determined atomic structure (see Sect. 4.1.1). Further details on the DFT parameters used are given in [64].

4.1 Characterization of Submonolayer Te Grown on Ag(111)

4.1.1 Preparation and Surface Characterization

Tellurium films were grown epitaxially on freshly prepared Ag(111) substrates. The substrate surfaces were cleaned by a standard procedure consisting of repeating cycles of bombardment with argon ions ($E_{\mathrm{kin}}^{\mathrm{ion}} \approx 1\,\mathrm{kV}$) and subsequent annealing to 900 K. This procedure was repeated until sharp and well-defined diffraction spots from the hexagonal surface unit cell were visible in the LEED pattern.
For the film growth, elemental Tellurium was evaporated from a thermal effusion cell on the Ag(111) surface, which was kept at room temperature. Deposition of 1/3 ML Te led to the formation of a well-ordered $(\sqrt{3} \times \sqrt{3})R30^\circ$ superstructure as shown in the LEED pattern in Fig. 4.1 (a). The correct coverage can be achieved in two ways: One can approach it from below until the intensity of the third-order diffraction spots (marked in blue in Fig. 4.1 (a)) becomes most intense. Or, if the initial deposition was more than 1/3 ML, excess Te can be desorbed by post-annealing the sample at 800 K for some minutes. The observed thermal stability of the film allows such high annealing temperatures, resulting in flat and well-ordered films, as can be seen from the large area STM image in Fig. 4.1 (b).
Similar to the present case, $(\sqrt{3} \times \sqrt{3})R30^\circ$ superstructures have been found for 1/3 ML Ge [154, 155], Sn [156], Sb[31, 66], Pb [31, 34, 65] or Bi [28, 31, 33] on Ag(111) and for similar adsorbates also on Cu(111) [29, 30, 157]. According to literature, these systems tend to form substitutional surface alloys (SSA) from the type M_2X / M(111), where M denotes the transition metal substrate and X the adsorbate. In this structure, every third atom of the metal surface gets replaced by an X-atom, resulting in M(111)-$(\sqrt{3} \times \sqrt{3})R30^\circ$-X superstructures. Concerning, that Te is next to Sb in the periodic table, a first assumption would be, that the present system corresponds to such a Ag_2Te SSA as well. A quantitative LEED-IV analysis instead gives a rather bad Pendry R factor of $R > 0.4$ for this structure model, so that a Ag_2Te structure can be safely excluded. The STM image with atomic resolution in Fig. 4.1 (d) indicates instead a honeycomb-like arrangement of the Tellurium-covered surface. A quantitative LEED-IV structure analysis indeed yields a Pendry R factor of 0.15 for a honeycomb-arranged AgTe structure of the uppermost atomic layer in hcp-hollow sites. The remarkably good agreement between the structure model and the experimental LEED-IV curves is illustrated by two exemplary spectra in Fig. 4.1 (c). A best-fit structure model is shown in Figs. 4.1 (e,f) from a side and top view, respectively. Experimentally determined atomic positions agree within 1.5 pm with the values calculated by DFT. The AgTe honeycomb layer is slightly buckled with a small outward-relaxation of the Te-atoms of less than 0.1Å. Moreover, STM measurements and DFT calculations [151] published immediately after completion of this analysis, agree with the present finding of a AgTe honeycomb structure.

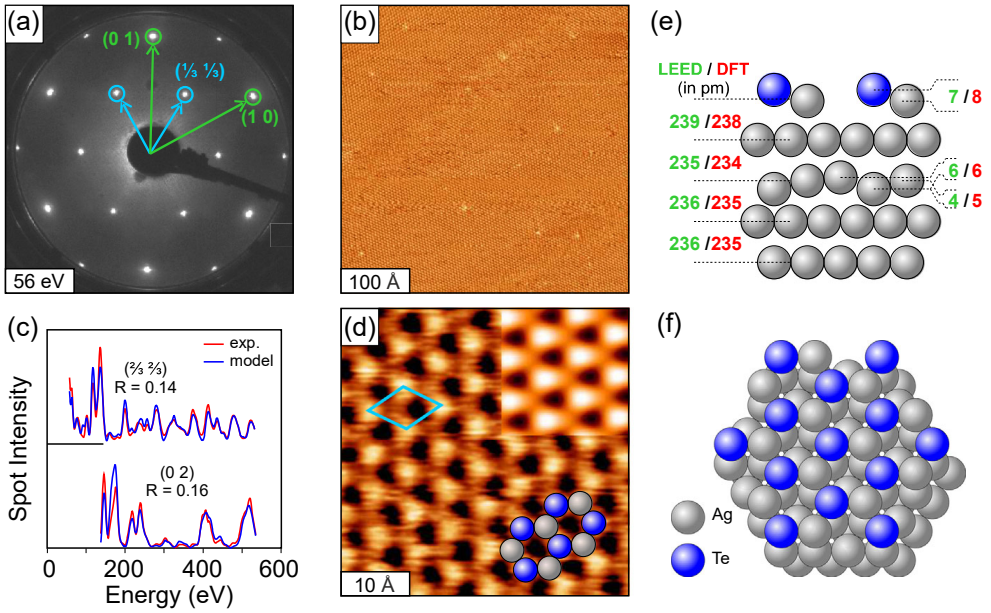

FIGURE 4.1: Atomic structure of Te / Ag(111). (a) LEED image of the $(\sqrt{3} \times \sqrt{3})R30°$-Te superstructure. (b) Large scale STM image (tunneling parameter $U = 80\,\text{meV}$ and $I_t = 1\,\text{nA}$) show a flat, well ordered AgTe film. (c) Representative LEED-IV curves (red) and best-fit curves (blue) reveal a AgTe honeycomb structure that can also be seen in the STM image with atomic resolution in (d) (tunneling parameters $U = 100\,\text{meV}$ and $I_t = 1\,\text{nA}$). The inset corresponds to a simulated STM image obtained by a DFT calculation. (e) Top view and (f) side view of the structure model obtained by the LEED-IV analysis. *This figure has already been published in [64].*

The good surface quality is also reflected in the photoemission spectra. A normal emission (NE) energy distribution curve (EDC) from AgTe / Ag(111) is shown in Fig. 4.2(a). Two occupied surface states at $-0.74\,\text{eV}$ and $-1.1\,\text{eV}$, which in the following will be labeled as α and β, respectively, can be seen. These bands are not apparent on the clean Ag(111) surface and can therefore be described as Te-induced surface states. Instead, the intrinsic Shockley-type [158] surface state (SS) of the Ag-substrate (Fig. 4.2 (b)) no longer appears in the ARPES spectra (see Fig. 4.3 (a)). The spectrum in Fig. 4.2 (a) has been fitted by the sum of two Lorentzian-profiles (black line). The extracted full width at half maximum (FWHM) of α gives a value of 29 meV, which is in the range of the minimum values found for the SS on noble metal (111) surfaces (Fig. 4.2 (b) [95]). Photoemission linewidths of the SS are known to be extremely narrow and the associated long quasiparticle lifetimes of the photohole can be seen as a benchmark for a remarkable good surface quality. Notably, the AgTe states do not even lie within the projected bulk band gap of Ag(111), which in principle allows for larger decay rates due to scattering process with the bulk states. Despite this fact, a narrow linewidth occurs in the AgTe / Ag(111) system, suggesting a surface quality comparable to clean noble metal surfaces. Noticeable is also the vastly different linewidth of α and β. With a value of 114 meV, the FWHM is almost four times larger for β, while both peaks have the same integral intensity. A possible cause might

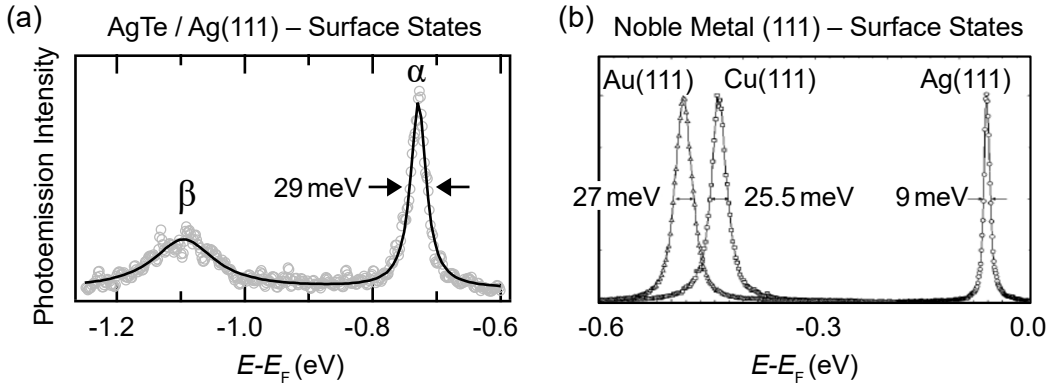

FIGURE 4.2: Normal emission spectra of surface states in (a) AgTe / Ag(111) and (b) Au, Cu, and Ag noble metal (111) surfaces, as labeled. Grey circles correspond to experimental data points and black lines to the corresponding fit functions. The numbers indicate the respective extracted full width at half maximum. *Panel (b) is adapted with permission from [95]. Copyright © (2001) by the American Physical Society. All rights reserved.*

be an additional energy broadening as a result of the finite k-resolution. The group velocity of β at $k_{\parallel} = 0$ is nonzero ($v_G = \alpha_R = 0.88\,\text{eVÅ}$), due to a Rashba-type spin-splitting (see Chapter 4.2.1). Nevertheless, with the resolution in the experimental setup of $\approx 0.01\,\text{Å}^{-1}$ (see Chapter 3.3), this broadening would be $< 10\,\text{meV}$, and therefore much less than what is observed. The strong difference in the linewidth can thus be attributed to a vastly different lifetime of the respective photoholes. What exactly causes the different lifetime has yet not been conclusively clarified. One possible explanation could be a different symmetry of the wave functions and therefore a different coupling to the sp-bulk state continuum of the Ag substrate. Such a behavior has been reported for adsorbate-induced surface states on Cu(110)-(2×1)-O [159]. However, the evaluation of the wave function symmetries in AgTe (see Appendix A.1.1) suggests a rather similar character of the spatial wave function at $k_{\parallel} = 0$, which contradicts this explanation. Besides the mere wave function symmetries of the states at the $\bar{\Gamma}$-point, band structure effects also play an important role in the photohole-decay mechanism [160]. The band dispersion as well as the momentum-dependent character of the electronic states are discussed in the previous sections of this chapter.

4.1.2 Key Features of the Band Dispersion

In order to investigate the band structure of AgTe, APRES as well as angle-resolved two-photon photoemission (AR-2PPE) measurements were performed. The results close to the Fermi-level are shown in Fig. 4.3 (a). The occupied bands α and β show a holelike band dispersion. Thus, there are no bands crossing E_F, suggesting an overall semiconducting two-dimensional band structure of the AgTe layer, with the first two valence bands α and β. Above all, it is striking that there are three distinct peaks for wave vectors $|k_{\parallel}| > 0$ instead of two, like in the case for $k_{\parallel} = 0$. This is also visualized

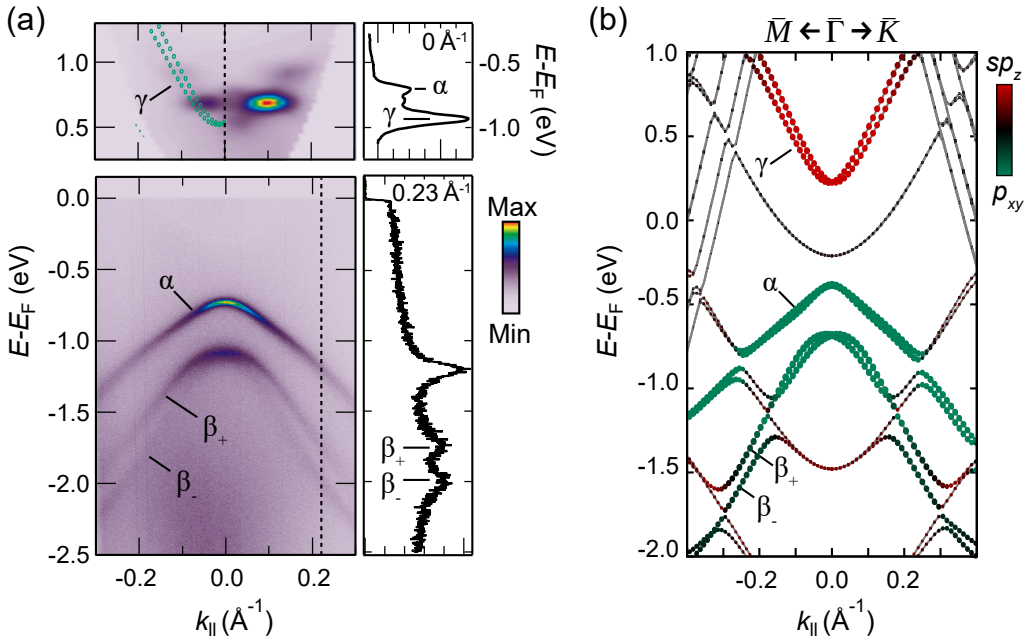

FIGURE 4.3: Band structure of AgTe / Ag(111). (a) ARPES ($h\nu = 21.21\,\text{eV}$, He-I$_\alpha$) and AR-2PPE ($h\nu = 1.55\,\text{eV} + 4.65\,\text{eV}$) measurements taken along $\bar{\Gamma}\bar{K}$ and $\bar{\Gamma}\bar{M}$ respectively. Two occupied bands α and β and an unoccupied band γ correspond to the AgTe valence and conduction bands. For β a splitting into two branches β_+ and β_- occur, as also visualized in the EDC at $k_{||} = 0.23\,\text{Å}^{-1}$. (b) DFT band structure calculations done for monolayer AgTe on a seven layer Ag slab. The dotsize indicate the localization of the electronic states within the AgTe layer, reproducing three AgTe bands α, $\beta_\pm$, and γ as well as a Rashba-type spin-splitting of $\beta_\pm$. *This figure has already been published in [64].*

in the EDC at $0.23\,\text{Å}^{-1}$ (Fig. 4.3)(a), which clearly shows a three-peak structure. That means while α is a single band over the entire $k_{||}$-range shown, β splits up into two subbands labeled as β_+ and β_-. A third band γ can be found at 0.53 eV above E_F in the AR-2PPE measurement. As can be seen in the NE spectrum, α occurs as an initial state and γ as an unoccupied intermediate state in the 2PPE spectra, which can both be probed with a single 2PPE measurement. A spectrum can thus be plotted with different energy scales – the initial state- and the intermediate state energy – that differ by the energy of the pump pulse ($h\nu_1 = 1.55\,\text{eV}$). For a better understanding, the initial state energy scale for 2PPE was additionally added at the upper right site in Fig. 4.3 (a). Photon-energy-dependent and time-resolved measurements (see Ref. [152]) allow a clear assignment of the features in the 2PPE spectrum of α as an initial state and γ as an intermediate state. AR-2PPE reveals an electron-like dispersion of γ. The intense spots at $|k_{||}| \approx 0.1\,\text{Å}^{-1}$ correspond to resonant transitions between α and γ.

The band structure was calculated by means of DFT along the high symmetry directions $\bar{\Gamma}\bar{M}$ and $\bar{\Gamma}\bar{K}$ as shown in Fig. 4.3 (b). The dotsize reflects the localization of the states within the AgTe layer and the color indicates their orbital character. There are three bands that can be assigned to the AgTe monolayer, labeled α, $\beta_\pm$ and γ. Additional appearing states correspond to

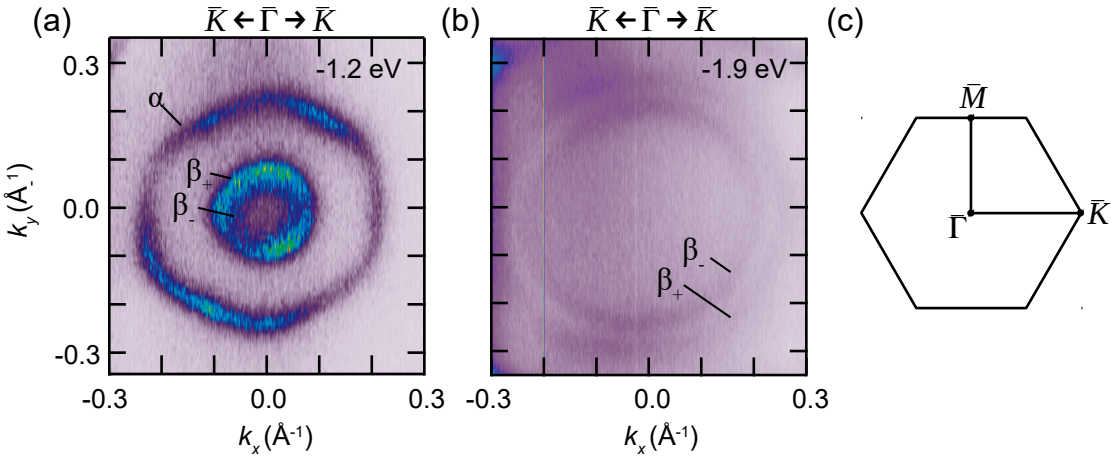

FIGURE 4.4: Constant energy cuts obtained by ARPES ($h\nu = 21.21\,\text{eV}$, He-I$_\alpha$) for energies of $-1.2\,\text{eV}$ (a) and $-1.9\,\text{eV}$ (b) relative to E_F. The outermost contour in (a) correspond to α while the inner features correspond to $\beta_\pm$. In (b) solely the Rashba-branches $\beta_\pm$ can be seen at wave vectors comparable to α in (a). The overall orientation of the surface Brillouin zone is sketched in (c).

quantum well states (QWS) and the Shockley surface state (at $-0.22\,\text{eV}$). Importantly, the latter does not correspond to the SS of the actual AgTe surface but is rather located at the backside of the 7-layer Ag-slab. The QWS result from the finite size of the employed slab and can be regarded as discrete representatives of the projected bulk bands of the substrate.

By comparing the experimental results to the band structure calculations (Fig. 4.3 (a,b)), one finds an overall good agreement. The valence bands α and β correspond mainly to Te-p_{xy} states, while γ has mixed Ag-s and Te-p_z character. The calculations reveal also a splitting of β into two branches β_+ and β_-, as it has been found in the ARPES data. This splitting appears only if SOC is taken into account in the calculation and refers to a Rashba-type spin-orbit splitting, as further discussed in section 4.2.1. It should be noted already, that even though there is a non-vanishing splitting of α in the calculation as well, it is much smaller than in the case of β and thus, the vastly different behavior of the two valence bands is reflected in both, experiment and calculation. It is worth noting that a Rashba splitting is also found for γ in the calculations, but this cannot be resolved in the 2PPE measurement due to the poorer energy resolution.

By comparing the band structure calculations along the high symmetry directions, one finds a nearly isotropic behavior for $\beta_\pm$ as well as for γ, while α has a an more anisotropic dispersion. The bandwidth of the latter is noticeably larger along $\bar{\Gamma}\bar{K}$ compared to $\bar{\Gamma}\bar{M}$ (plotted along positive and negative $k_{||}$ in Fig. 4.3 (b), respectively). In order to compare this to the experimental findings, constant energy cuts (CEC) for two different energies are shown in Fig. 4.4 (a,b). The corresponding orientation of the surface Brillouin zone (BZ) is sketched in Fig. 4.4(c). The outer contour in Fig. 4.4 (a) can be assigned

to α and is clearly hexagonal, with a larger wave vector $\boldsymbol{k}_{\parallel}$ along $\bar{\Gamma}\bar{\mathrm{M}}$ (corresponding to the *corners* of the hexagon). This directly confirms the smaller bandwidth of α along $\bar{\Gamma}\bar{\mathrm{M}}$ compared to $\bar{\Gamma}\bar{\mathrm{K}}$, exactly like expected from the calculation (Fig. 4.3 (b)). To compare this to the anisotropy of $\beta_{\pm}$, it is useful to consider a CEC at an energy where $\beta_{\pm}$ appear at comparable $\boldsymbol{k}_{\parallel}$ (Fig. 4.4 (b)). In contrast to α, $\beta_{\pm}$ have an almost perfect circular shape, which again agrees well with the DFT calculation.

4.1.3 Orbital Composition and Hybridization with Substrate States

To get a better understanding of the character of the electronic states found in APRES measurements and DFT calculations, it is useful to take a further look onto their orbital composition. As can be seen in Fig. 4.5 (a-d), the occupied bands α and β are mainly built from in-plane Te-p_{xy}-orbitals and the unoccupied state γ has predominantly Ag-s character ($\sim$ 80%) with an admixture of out-of-plane Te-p_z orbitals ($\sim$ 20%). This observation is further supported by photoemission experiments performed with different linear light polarization. Normal emission ($k_{\parallel} = 0$) one- and two-photon photoemission spectra are shown in Fig. 4.5 (e). For s-polarized light, the light electric field vector $\boldsymbol{E_s} = (0, \mathcal{E}_y, 0)$ is parallel to the sample surface, and the photoemission cross section will be large for in-plane orbitals [161]. Instead for p-polarized light, there is also a strong z-component ($\mathcal{E}_z \gg 0$) and the cross section becomes large for out-of-plane orbitals. In the normal emission ARPES spectrum one finds an enhanced photoemission intensity for the occupied states with s-polarized light compared to the spectrum taken with p-polarization. This behavior is completely reversed in the 2PPE spectra, indicating that γ is predominantly built from out-of-plane orbitals, while α and β have in-plane p_{xy}-orbital character. The experimental observations are therefore in good agreement with the calculated orbital character. In particular, the polarization-dependent data reveal a certain Te-p_z character in γ, since a purely s-like and thus isotropic state would likely not result in such a strong difference in the s-pol and p-pol spectra.

An important issue that follows is what causes the Ag-s Te-p_z hybridization in $|\gamma\rangle = |s\rangle + \tilde{V}_{sp_z}|p_z\rangle$. Regarding for instance a free-standing layer of AgTe, which shows a similar band dispersion in the calculations (see Appendix A.1.4), one finds a pure Ag-s character in γ ($\tilde{V}_{sp_z} = 0$, Fig. 4.5 (f)). Moreover, an additional Te-p_z band occurs below α and β (see Fig. 4.13 (a-c)), which has not been found in present ARPES measurements and DFT calculations as shown in Fig. 4.3. Thus, the behavior of a free-standing ML AgTe is contradicting to the findings in the AgTe/Ag(111) hybrid system, suggesting a significant influence of the monolayer-substrate interaction. Due to its high relevance, especially for the Rashba effect in AgTe/Ag(111) (see Chapter 4.2.2), the hybridization process will now be examined in more detail in a simple model consideration.

The first question is which states should be included in the model. In-plane

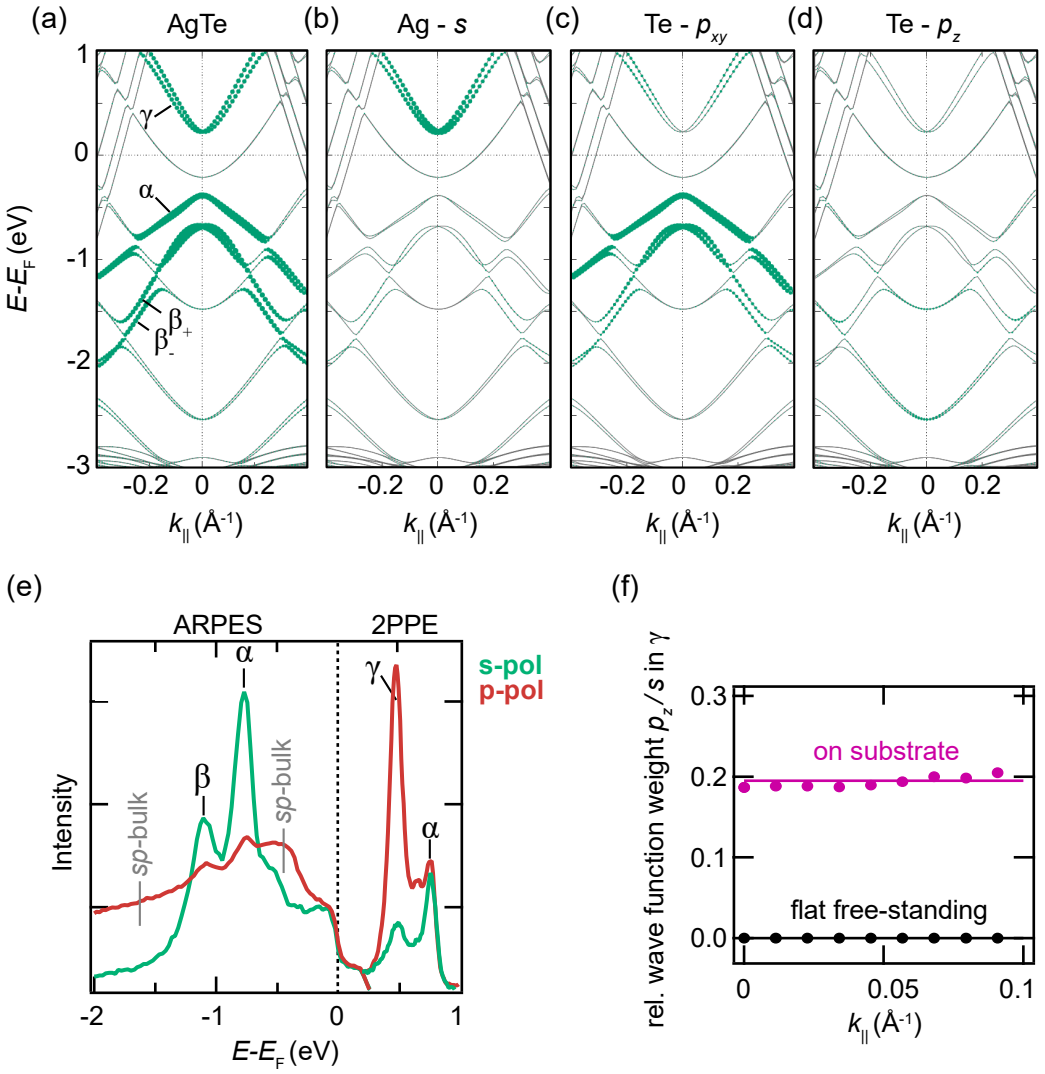

FIGURE 4.5: Orbital projected DFT band structure calculations of AgTe / Ag(111). The dotsize represents the projection of the states within the AgTe layer onto (a) all orbitals, (b) the Ag-*s* orbital, (c) Te-p_{xy} orbitals, and (d) the Te-p_z orbital. Negative and positive wave vectors correspond to a path along $\bar{\Gamma}\bar{M}$ and $\bar{\Gamma}\bar{K}$ respectively (compare Fig. 4.3 (b)). (e) Normal emission ($\boldsymbol{k}_{||} = 0\,\text{Å}^{-1}$) ARPES ($h\nu = 65\,\text{eV}$) and 2PPE ($h\nu = 1.55 + 4.65\,\text{eV}$) spectra probed with *s*- and *p*-polarized light (dashed and solid line respectively). (f) Relative orbital wave function weight p_z/s in γ as a function of $\boldsymbol{k}_{||}$ obtained by DFT for a flat and free-standing AgTe layer (black) and the AgTe/Ag(111) hybrid system (purple). *Figures a-e have already been published in [64].*

p_{xy} states are not affected as much during adsorption because of their comparatively small overlap of their wave function with the substrate orbitals. On the other hand, quenching of the out-of-plane Te p_z-band as well as the Ag(111) surface state indicates strong chemisorption to which both contribute. To capture this chemical bonding, a tight-binding model will be considered. The hybridization is nearly independent of $\boldsymbol{k}_{||}$ as shown in Fig. 4.5 (f) and the band dispersion is almost the same for both the free-standing and hybridized

scenario. In-plane and out-of-plane potential are thus sufficiently decoupled and the model can be restricted to be a one-dimensional model perpendicular to the surface plane. The Ag-crystal is modeled by a chain of Ag-atoms with one Gaussian-shaped (s-like[1]) orbital per lattice site. A more detailed formal description of the model can be found in Appendix A.1.2. One end of the chain represents the surface and the AgTe layer, or more precisely the Te-atom, is represented by another orbital in front of this surface. To capture the SS, which might probably act as a possible binding partner to the Te-orbital, a surface potential can be included by changing the on-site energy of the last Ag-atom. This leads to the formation of a surface state in the energy gap of the projected bulk band structure, which is localized at the edge of the chain but penetrates into the bulk with a certain exponential damping.
Fig. 4.6 (a) shows the square modulus of the surface state wave function (black) in an energy diagram as a function of the position z along the chain. The Ag-surface is at $z = z_0$ and the AgTe plane is marked by the red dashed line. The grey shaded area indicates the projected bulk band. Hopping between the AgTe plane and the surface atom, and therefore the chemisorption process is described by the parameter V. The on-site energy of the Te-state was set slightly below the energy of the SS also within the bulk band gap[2]. For $V = 0$, there is no hybridization; the Ag-surface state as well as the Te-state (red line) simply coexist and there would be no covalent bonding. Raising the hopping parameter sightly to $V = 0.2\,\mathrm{eV}$ (Fig. 4.6 (b)), the SS and Te orbital hybridize and form a bonding and an anti-bonding hybrid states, which are slightly shifted in energy compared to the unperturbed system. The SS wave function (or more precisely the wave function of the anti-bonding state) consequently has a non-zero probability density at the Te atom and the Te state becomes a bound surface state decaying exponentially into the bulk. This situation is likely comparable to the bonding of organic molecules on noble metal (111) surfaces [139, 162]. There, the hybridization between molecular orbitals and the SS leads to a modification of the SS wave function, having an enhanced probability density at the metal-organic interface.
Further increasing the hybridization strength (Fig. 4.6 (c,d)) leads to a larger energy shift and an even stronger modification of the wave functions. The bulk penetration of the original SS reduces and the probability density at the last Ag atom and the Te atom equalizes. This means, as a result of the hybridization with the Te orbitals, SS develops into a strongly localized Ag-AgTe hybrid state. On the other hand, the bulk penetration of the original Te state increases by approaching the projected bulk band. Like a textbook example, it develops from a genuine surface state ($0\,\mathrm{eV} < V \leq 0.5\,\mathrm{eV}$) to a surface resonance (Fig. 4.6 (d)); meaning that electrons can propagate through the bulk, but have a slightly enlarged probability density at the surface. As

[1] Notably, the correct shape of the wave functions included might be important in the process. Nevertheless, to keep the model as simple as possible, all orbitals are just considered as s-like.

[2] The parameters in this model are chosen for illustrative reasons solely and have no direct physical meaning for the real AgTe system.

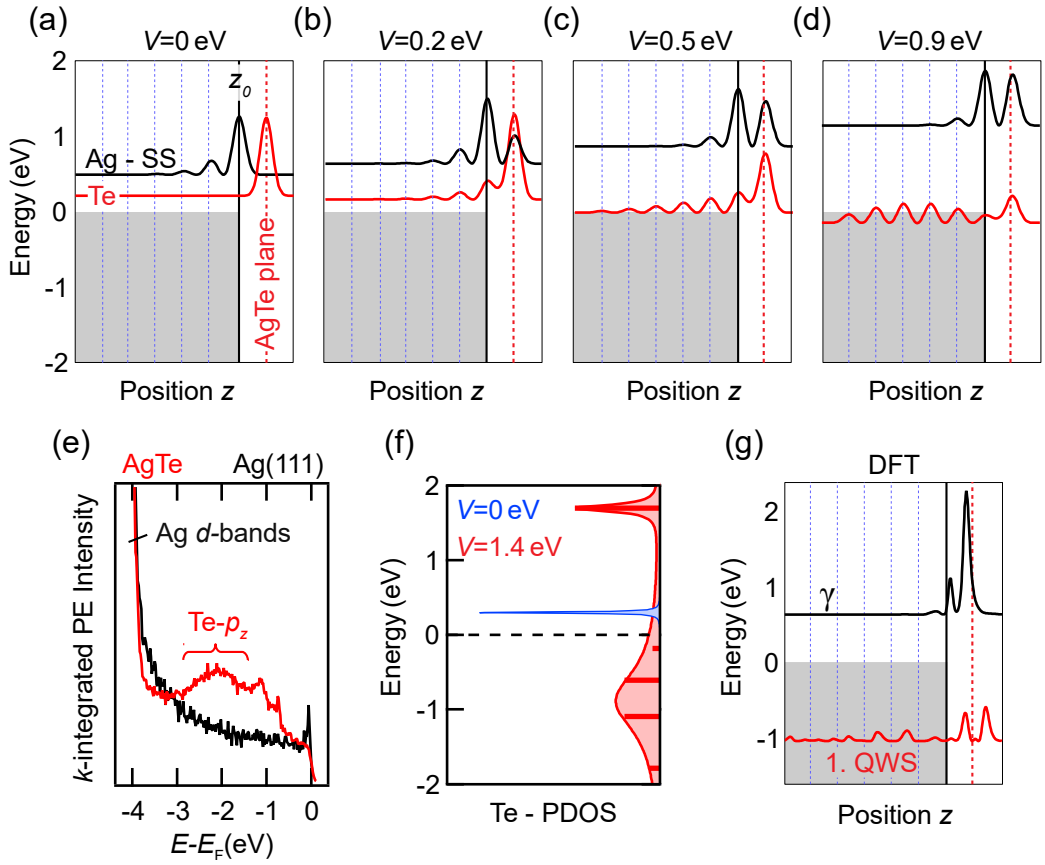

FIGURE 4.6: One-dimensional hybridization model of Te atoms with the Ag-substrate via the intrinsic SS and the bulk bands. (a-d) Energy diagram and probability density along the one-dimensional chain of atoms. The energy is given with respect to the upper edge of the projected bulk band, visualized by the grey shaded area. The probability density of the SS and the Te adatom is plotted in black and red, respectively. While increasing the hopping-integral V between the Te atom and the last Ag atom, SS and the Te-state form bonding and antibonding states. The former develops from a surface state (b,c) to a surface resonance when entering the projected bulk band (d). This leads to an energy broadening in the Te-projected DOS (f). An energetically broad spectral feature can also be seen in the k-integrated photoemission spectrum (e), which cannot be found on the clean Ag(111) substrate. The model wave functions are comparable with the charge densities of γ and the first QWS calculated by DFT (g).

a result of the interaction with the broad substrate band, electrons can easily hop between the substrate and the AgTe layer. This delocalization of the electrons in the Te orbital is linked to a reduced lifetime of the Te-state and therefore typically results in an energy broadening, explained by the so-called Newns-Anderson model [163, 164], which is conventionally used to describe the hybridization between an adsorbate orbital and the electronic band structure of the substrate [165]. In other words, there will be not just one state, with Te-character, but rather all the bulk states will get some Te contribution.

To verify whether this holds in the present model, one can plot the density

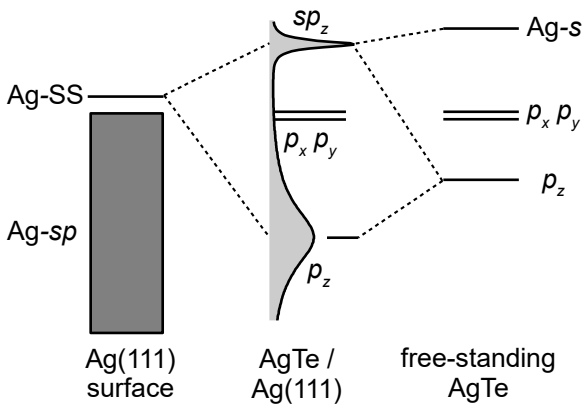

FIGURE 4.7: Schematic energy level diagram for the hybridization process of the AgTe states with the Ag(111) substrate. The energies of the unperturbed Ag(111) substrate states are shown on the left and the energy levels for the free-standing AgTe film are shown on the right. Hybridization (middle panel) keeps the p_{xy}-states untouched but modifies the s and p_z state. Latter becomes a broad surface resonance, which is hidden in the projected bulk bands. The unoccupied state γ has to be considered as a hybrid sp_z-state with contributions from the Ag(111) surface state, the Ag-s orbital, and the Te-p_z state.

of states (PDOS) projected on the Te-atom (Fig. 4.6 (f)). Without hybridization (blue) the Te-PDOS is a delta-function at the energy of the Te state. If the hybridization is instead strong (here $V = 1.4\,\text{eV}$) two main peaks occur; the upper one corresponds to the anti-bonding state and is an energetically sharp signature. The bonding state is on the other hand not a single feature but all the bulk states get a specific energy-dependent Te admixture, plotted as bars in Fig. 4.6 (f). Assuming a real continuum of bulk bands, the bonding state will be broadened in energy, visualized by the Lorentzian peak, exactly like expected from previous assumptions.
Despite its highly simplified character, the one-dimensional tight-binding model helps to explain the experimental data as well as the DFT calculations, both of which do not show an energetically sharp Te-p_z band (Fig. 4.3 and 4.5), in contrast to the free-standing scenario (Fig. 4.13 (a,b)). To check whether there is an experimental signature for a Te-p_z-resonance at all, the $k_{||}$-integrated photoemission intensity is plotted in Fig. 4.6 (e) and compared to the spectrum of the bare Ag(111) substrate (black line). Besides the two Te-p_{xy} states α and β another peak at $-2\,\text{eV}$ can be seen which is energetically much broader. As this feature was not found on the clean Ag(111) surface, it can be attributed to the AgTe/Ag(111) system. The large FWHM of $\sim 1.5\,\text{eV}$ leads to the interpretation that this spectral signature indeed corresponds to a Te-p_z-resonance, as expected from the model. A similar observation has been made for a ML Pb on Ag(111) [166]. Using ARPES, authors found a Pb-p_z state, that was strongly energy-broadened as a result of hybridization with the substrate. They came to a similar conclusion, namely a SS-mediated interaction of the p_z-state with the substrate bulk bands.
The DFT calculations cannot reveal a continuum of bulk bands, but discreet quantum well states (QWS), due to the finite size of the employed slab [64].

Even though, the QWS represent the Ag-sp bulk bands (comparable to the situation in the finite chain in the model). In fact, the first two QWS have a notable Te-p_z character (Fig. 4.5 (d)), indicating the adsorbate-substrate-interaction. The calculated charge density of γ and the first QWS at $k_{\parallel} = 0$ are plotted in Fig. 4.6 (g). Similar to the model wave function in Fig. 4.6 (d) the QWS has an enhanced charge density at the AgTe-plane and thus possesses the characteristics of a Te-p_z surface resonance. The second QWS is not shown here but shows a similar behavior, indicating the expected energy broadening. To analyze this in more detail, DFT-calculations of a thicker slab – resulting in a higher density of QWS in this energy range – or a calculation in a semi-infinite surface geometry [46] would be needed. For γ one finds a similar behavior as for the modeled anti-bonding state: The charge density of γ (Fig. 4.6 (d)) is localized at the Ag-AgTe interface and the band has a mixed Ag-s and Te-p_z character.

The elaborated model is of course oversimplified. Nevertheless, one finds similarities in the real AgTe/Ag(111) system and it helps to get an idea about the complex hybridization process. This is schematically sketched in Fig. 4.7 and can be summarized as follows: The character of the unoccupied band γ is different in the AgTe/Ag(111) hybrid system than in the free-standing AgTe scenario. In the former case, it has to be considered as a strongly modified version of the Ag(111) surface state with strong contributions of Te-p_z character. The s-p_z hybridization results from a complex adsorption process of the Te atoms at the Ag(111) surface. The original Te-p_z band becomes an energetically broad resonance within the projected bulk bands. The low energy electronic structure is thus best described by three bands; two p_{xy}-states and one sp_z-like hybrid state $|\gamma\rangle = |s\rangle + \tilde{V}_{sp_z}|p_z\rangle$. The $\boldsymbol{k}_{\parallel}$-independent parameter $\tilde{V}_{sp_z}(\boldsymbol{k}_{\parallel}) = \tilde{V}_{sp_z}$ gives the hybridization strength and is $\tilde{V}_{sp_z} = 0$ in the free-standing case and $\tilde{V}_{sp_z} \approx 0.2$ in AgTe/Ag(111) as determined by DFT (Fig. 4.5 (f)).

4.2 Rashba Effect in a Honeycomb Monolayer AgTe

4.2.1 Rashba-Type Spin-Orbit Splittings in AgTe

After establishing the main orbital character of the low energy electronic states, the focus will now be on the splitting, which was observed in the β-band. A close-up of the high-resolution ARPES measurement is shown in Fig. 4.8 (a). As already mentioned, there is no experimentally resolvable splitting for α while β clearly has two different branches β_+ and β_-. For a quantitative analysis of this splitting, the dispersion has been extracted as shown in Fig. 4.8 (b). In order to do that, momentum-distribution curves (MDC) (Fig. 4.8 (a)) and EDC (compare Fig. 4.3 (a)), in which the two branches $\beta_{\pm}$ directly appear as two well-separated spectral features, were fitted by a sum of two Lorentzian profiles subtracted by a linear background. The peak positions are plotted in Fig. 4.8 (b), where the filled (open) triangles correspond to

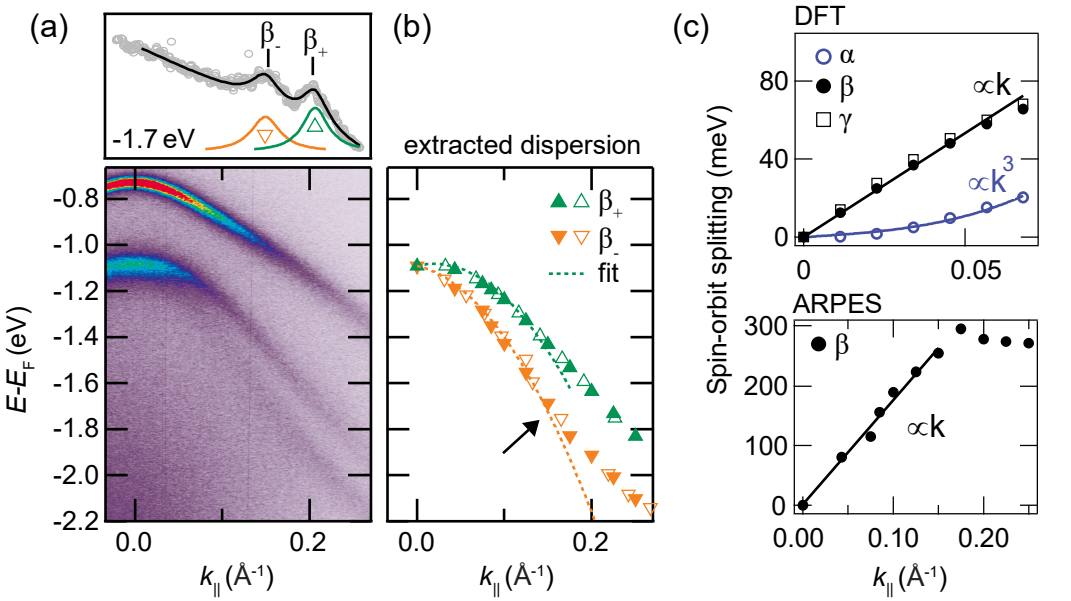

FIGURE 4.8: Spin-orbit splitting in AgTe / Ag(111). (a) close up ARPES measurement ($h\nu = 21.21\,\text{eV}$, He-I$_\alpha$) showing the bands α and $\beta_\pm$. Latter are clearly split, visualized also in the MDC in the upper panel, while no resolvable splitting can be observed in α. (b) extracted band dispersion of $\beta_\pm$. Dashed lines correspond to a fit of Rashba-type split bands using a fixed Rashba-parameter of $\alpha_R = 0.88\,\text{eVÅ}^{-1}$, as obtained from the lower panel of (c). The experimentally determined dispersion deviates from the extrapolated parabolic dispersion for $k_\parallel > 0.15\,\text{Å}^{-1}$, indicated by the arrow. (c) Spin-orbit splitting of the AgTe bands extracted from the DFT calculation (upper panel) and the ARPES data (lower panel). Lines correspond to the respective fits to the data points. *Figures in (c) have already been published in [64].*

the results of the EDC (MDC) fits. The energy splitting can be directly calculated ($\delta E = E_{\beta_+} - E_{\beta_-}$), as shown in the lower panel of Fig. 4.8 (c) plotted as a function of $k_\parallel$. Near the $\bar{\Gamma}$ point the splitting increases linearly with increasing $k_\parallel$, in accordance to the Rashba model, resulting in a Rashba-parameter $\alpha_R = 0.88 \pm 0.02\,\text{eVÅ}$ (see Chapter 2.1). In contrast, for larger wave vectors ($k_\parallel > 0.15\,\text{Å}^{-1}$) δE reaches a nearly constant value of $280 \pm 10\,\text{meV}$. This deviation from the Rashba model can also be seen in the band dispersion. Data points in Fig. 4.8 (b) were fitted, using a Rashba-type band dispersion (Eq. 2.4), where the parameters $E_{k=0} = -1.1\,\text{eV}$ and $\alpha_R = \pm 0.88\,\text{eVÅ}$ were fixed and the data range was restricted to $k_\parallel < 0.15\,\text{Å}^{-1}$. Independent fitting of both branches $\beta_\pm$ results in an effective mass $m^* = -0.173\,m_e$. The extrapolated parabolic dispersion (shown for a better overview only for β_-) deviates strongly from the experimentally determined, which kinks for $k_\parallel > 0.15\,\text{Å}^{-1}$ and thus prevents a larger splitting.

In order to investigate the spin-splittings in AgTe that occur in the DFT calculations, δE_{DFT} has been extracted and plotted in the upper panel of Fig. 4.8 (c). The analysis is restricted to a narrow region around the $\bar{\Gamma}$ point since for larger wave vectors, the energy splitting gets distorted by hybridization with the QWS (see Fig. 4.3 (b)). The calculations confirm the experimentally observed different behavior of α and β. On the one hand, the splitting of β as

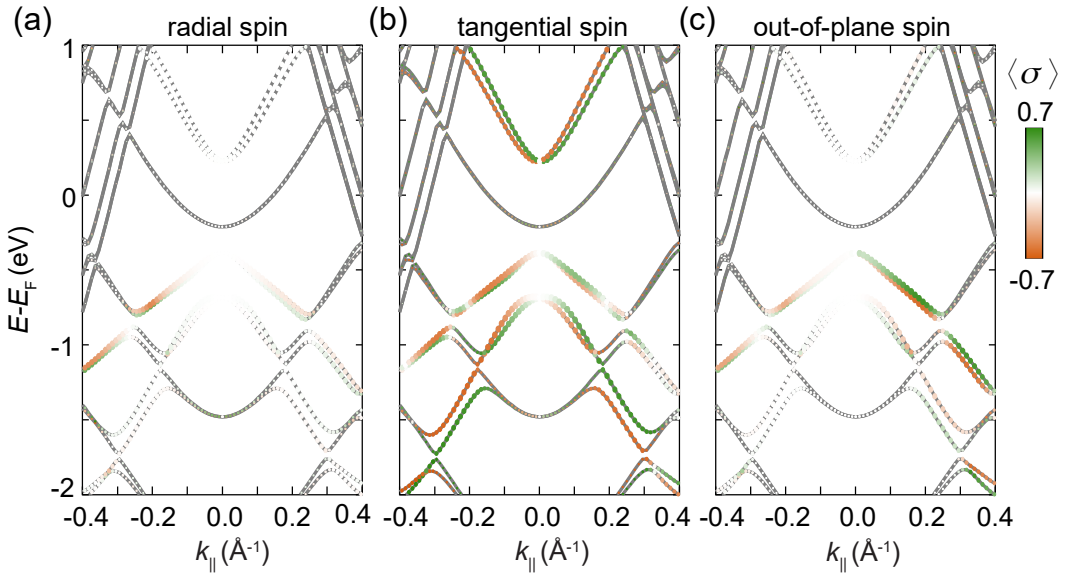

FIGURE 4.9: Spin polarization in the AgTe / Ag(111) bandstructure calculated by DFT for the radial (a), tangential (b), and out-of-plane (c) spin component. The dotsize represents localization of the states within the AgTe layer and the colorcode indicate the value of the spin polarization. Negative and positive wave vectors correspond to a path along $\bar{\Gamma}\bar{M}$ and $\bar{\Gamma}\bar{K}$ respectively (compare Fig. 4.3 (b)). *This figure has already been published in [64].*

well as of γ is much larger than that of α, as already discussed on a qualitative level before. Moreover, δE_α shows a $k_\parallel^3$ dependence with a negligible contribution of the linear term, while $\delta E_{\beta,\gamma}$ are indeed linear in $k_\parallel$, in accordance with the Rashba model.

These findings are further supported by the calculated spin texture shown in Fig. 4.9. The spin-polarization of $\beta_\pm$ and $\gamma_\pm$ is almost entirely in-plane and points perpendicular to $\boldsymbol{k}_\parallel$. This is consistent with the Rashba model, which suggests tangentially aligned counter-rotating spins for the two branches. For α, one finds a rather more complex and different behavior. Here, the main contribution to the overall spin-polarization comes from the out-of-plane spin component (Fig. 4.9 (c)). Moreover, a strong anisotropy is found for this out-of-plane spin polarization, which is much more pronounced along $\bar{\Gamma}\bar{K}$ compared to $\bar{\Gamma}\bar{M}$, where it vanishes almost completely. A similar behavior has been found for instance in the topological surface state of Bi_2Te_3 [167–170], substitutional surface alloys [28, 171, 172] and further systems [173, 174]. Similar to the AgTe honeycomb structure, all these systems have a three-fold symmetry C_{3h}, which allows for a finite out-of-plane spin-polarization as a result of the additional breaking of the in-plane symmetry. According to preliminary spin-resolved ARPES measurements and DFT calculations on different types of surface states [28, 167–171, 173], the out-of-plane spin-polarization has a three-fold modulation, which is suppressed in the mirror-plane, i.e., $\bar{\Gamma}\bar{M}$ in AgTe. Thus, there is a significant influence of the in-plane potential gradient in AgTe on the spin-splitting in α. The fact that α feels this in-plane potential more strongly than β and γ is consistent with the rather

anisotropic band dispersion of α found in the present APRES experiments (Fig. 4.4) and DFT calculations (see for example Fig. 4.9). Such a hexagonal deformation[3] (often called *warping*) of a constant energy surface goes beyond the isotropic picture in the conventional Rashba effect. With the help of $\boldsymbol{k} \cdot \boldsymbol{p}$ theory, the model can be extended by an additional warping-term [167]

$$H_w = \frac{\lambda}{2}(k_+^3 + k_-^3)\sigma_z, \tag{4.1}$$

with $k_\pm = k_x \pm ik_y$ and where λ is a SOC-constant that scales the warping. The cubic k-dependence of this effect is furthermore consistent with the behavior of the spin-splitting in α (Fig. 4.8 (c)).
Finally, it should be mentioned that the cubic splitting in α occurs in the calculations regardless of whether they were performed for a flat free-standing, a buckled free-standing, or an AgTe monolayer on the substrate (see Fig. A.3). This further indicates that the effect is caused only by the honeycomb structure of the AgTe layer. Overall, it appears that the two effects – i.e., the Rashba effect at the surface as it appears in β and γ, and the cubic effect in α – are based on two independent decoupled mechanisms. In the following, the focus is only on the k-linear splitting, that is, the Rashba effect.

Interim Conclusion

A two-dimensional honeycomb material AgTe has been synthesized on a Ag(111) substrate. The excellent film quality leads to sharp features in the ARPES measurements and allows for a detailed analysis of Rashba-type spin-splittings found in the experimental data and the DFT calculations. Interestingly, even though the occupied bands both exhibit a comparably strong localization in the AgTe layer and mainly derive from the same atomic orbitals (Te 5 p_{xy}), they show a vastly different behavior: For the upper valence band α the Rashba-splitting vanishes completely, whereas in the second valence band β a remarkably large splitting occurs. The experimentally determined Rashba-parameter of latter ($\alpha_R = 0.88$ eVÅ) is more than twice as large as in the prototypical SS on Au(111) [175]. It is moreover of similar magnitude as found in structurally related Pb- and Bi-based SSA, Ag_2Pb [31, 34, 65] and Cu_2Bi [29], despite their much larger atomic SOC-constants. The Rashba-parameter in Ag_2Sb, which on the other hand has a similar atomic SOC, is more than two times smaller than for AgTe [31, 66].
Together, there is a contradictory behavior for the spin-spitting in the AgTe bands that cannot be explained within the framework of the conventional Rashba model. Instead, strong similarities emerge with the results of the

[3] Notably, the Hamiltonian H_w is a SOC Hamiltonian. Of course, there can be hexagonal warping even in the absence of SOC, and the hexagonal deformation of the CEC in AgTe is not a strict proof for this effect. It only demonstrates an influence of the in-plane potential gradient on α, which is at the same time responsible for H_w.

Petersen-Hedegård model (Chapter. 2.1.3). There also, two states with Rashba-type splitting and one without have been found (Fig. 2.3). Park et al. explained this behavior with an occurrence or non-occurrence of OAM in the wave function [48].

4.2.2 Model Hamiltonian for AgTe

The question arises whether the system AgTe/Ag(111) is a candidate for an OAM-based Rashba paradigm. This motivates the design of a minimal tight-binding model, providing deeper insights into the physics behind the spin-split AgTe band structure. The model does not aim to reproduce the band dispersion as detailed as possible but to extract the relevant mechanisms. Therefore, the models developed in [48] and [62] are used as a basis and only slightly adapted according to the specific requirements in AgTe.
As discussed in Sect. 4.1.3 a good set of basis wave functions for AgTe are the in-plane Te-p_{xy} orbitals and the sp_z-hybrid state, $\{p_x, p_y, sp_z\}$. The latter can be written as $|sp_z\rangle \approx |s\rangle + \tilde{V}_{sp_z} |p_z\rangle$, where $\tilde{V}_{sp_z}$ is an external dimensionless parameter expressing the effective s-p_z mixing explained within the framework of the one-dimensional adsorption model in Chapter 4.1.3 and determined, e.g., using DFT. To explore the potential formation of OAM within the model, one has to discuss the possible hoppings between the respective basis orbitals. Due to the relatively large distance of 5 Å between the Te atoms, which is larger than typical covalent bond lengths of ~ 2 Å, one can assume that there will be a vanishing direct pp-hybridization between the Te orbitals. An effective Te-Te hopping will instead occur mainly via an Ag-atom on the other honeycomb sublattice, and the model can therefore be restricted to the nearest neighbor hoppings. In the three-band picture the resulting matrix elements include just one parameter t_{sp}, which determines the bandwidth of the system and can thus be regarded as a *kinetic* hopping term. Importantly, the integral t_{sp} changes with the s-p_z hybridization strength $\tilde{V}_{sp_z}$: For $\tilde{V}_{sp_z} = 0$ – such as in the case of a of a flat and freestanding AgTe monolayer – it describes an in-plane s-p_{xy} hopping and the Hamiltonian is inversion symmetric. For $\tilde{V}_{sp_z} \neq 0$, it becomes a sp_z-p_{xy} hopping-term breaking inversion symmetry. In other words, the effective Te-Ag-Te hopping (parameterized by t_{sp}) becomes asymmetric due to the additional s-p_z hybridization mediated by the substrate surface. Such a kinetic-energy-coupled ISB is likely comparable to a mechanism recently found for delafossite oxid surface states [37], which was a breakthrough for maximizing large spin-orbit splittings by ISB [176].

Formation of OAM in AgTe

Before discussing the Rashba effect in AgTe, the band structure will be calculated without spin-orbit coupling. The small-k Hamiltonian linearized

around $k = 0$ can be written as [48, 62]:

$$H_{\mathrm{AgTe}} = \begin{pmatrix} E_{p_{xy}} & 0 & -ik_x a t_{sp} \\ 0 & E_{p_{xy}} & -ik_y a t_{sp} \\ ik_x a t_{sp} & ik_y a t_{sp} & E_{sp_z} \end{pmatrix}, \tag{4.2}$$

with the hopping distance $a = 2.89\,\text{Å}$ (corresponding to the Ag-Te distance). Diagonalization gives three energy eigenvalues. The calculated band structure along k_x is plotted in Fig. 4.10 (a). The parameters ($E_{p_{xy}} = -1.1\,\text{eV}$, $E_{sp_z} = 0.5\,\text{eV}$, $t_{\mathrm{sp}} = 2.3\,\text{eV}$) were approximately fitted to the experimental data. Two nearly parabolic as well as a non-dispersive band can be seen, labeled β, γ and α, respectively. The circular-shaped constant energy cut through β (Fig. 4.10 (b), $E = -2.7\,\text{eV}$) reflects the isotropy of the system. The eigenstates of the three bands are given by:

$$\begin{aligned} |\alpha\rangle &= |p_t\rangle \\ |\beta\rangle &= |p_r\rangle + \frac{ikat_{sp}}{\Delta E} |sp_z\rangle \\ |\gamma\rangle &= |sp_z\rangle + \frac{ikat_{sp}}{\Delta E} |p_r\rangle , \end{aligned} \tag{4.3}$$

where $\Delta E = E_{sp_z} - E_{p_{xy}}$ and $|p_t\rangle$ and $|p_r\rangle$ are the in-plane wave functions written as tangential and radial aligned p-orbitals:

$$\begin{aligned} |p_t\rangle &= \frac{k_y}{k} |p_x\rangle - \frac{k_x}{k} |p_y\rangle \\ |p_r\rangle &= \frac{k_x}{k} |p_x\rangle + \frac{k_y}{k} |p_y\rangle . \end{aligned} \tag{4.4}$$

It's important to discuss the general shape of the eigenstates (Eq. 4.3). First of all, $|p_t\rangle$ remains decoupled from $|p_r\rangle$ and $|sp_z\rangle$ due to its odd in-plane mirror symmetry, which prevents hybridization with the even wave functions. In contrast $|\beta\rangle$ and $|\gamma\rangle$ are mixed states with radial-aligned in-plane- and out-of-plane orbital components, which are both even under mirror reflection[4]. The mixing scales linearly with $k\frac{t_{sp}}{\Delta E}$ and the phase between the different orbital parts is complex. These characteristics indicate that the AgTe bands can be written in terms of spherical harmonics or, in other words, that they carry an in-plane OAM. To show this explicitly, one can use the OAM-operators defined in Eq. 2.10 and calculate the in-plane OAM expectation values. One directly finds $\langle\alpha| L_x |\alpha\rangle = \langle\alpha| L_y |\alpha\rangle = 0$, due to the pure in-plane and non-complex shape of $|\alpha\rangle$. In contrast, for $|\beta\rangle$ and $|\gamma\rangle$ there is

[4] Since full rotational symmetry is assumed close to $k = 0$, each $\boldsymbol{k}_{\parallel}$-path denotes a mirror plane.

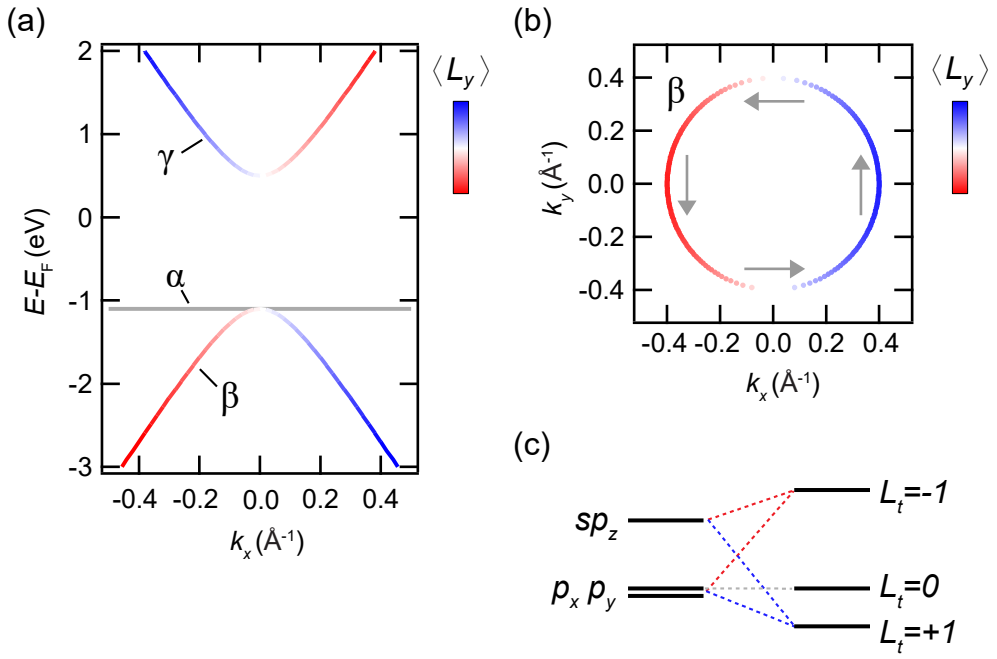

FIGURE 4.10: Band structure (a) and constant energy cut at $-2.7\,\mathrm{eV}$ (b) calculated from the sp-model Hamiltonian 4.10 without SOC ($E_{p_{xy}} = -1.1\,\mathrm{eV}$, $E_{sp_z} = 0.5\,\mathrm{eV}$, $t_{\mathrm{sp}} = 2.3\,\mathrm{eV}$). Each band contains to a different OAM-manifold $L_t = \{-1, 0, 1\}$ as a result of the k-dependent hybridization of sp_z and p_{xy} orbitals, as sketched in (c). The OAM-texture of β and γ is chiral, meaning that $\boldsymbol{L}$ is perpendicular to $\boldsymbol{k}_{\parallel}$, as shown explicitly for β in (b).

$$\begin{aligned} \langle\beta|\, L_x\, |\beta\rangle &= +k_y a \tilde{V}_{sp_z} \frac{t_{sp}}{\Delta E} = -\langle\gamma|\, L_x\, |\gamma\rangle \\ \langle\beta|\, L_y\, |\beta\rangle &= -k_x a \tilde{V}_{sp_z} \frac{t_{sp}}{\Delta E} = -\langle\gamma|\, L_y\, |\gamma\rangle\,. \end{aligned} \tag{4.5}$$

The combination of s-p_z hybridization and the in-plane sublattice hopping induces a nonzero OAM in β and γ, which increases linearly with k. The OAM vector $\boldsymbol{L}$ is perpendicular to $\boldsymbol{k}_{\parallel}$ giving a helical OAM structure, as shown in Fig. 4.10 (b). Importantly, there is an overall opposite helicity for β and γ (see also Fig. 4.10 (a)). So, if inversion symmetry is broken, the three bands (Fig. 4.10 (a)) can be considered as OAM-characterized bands $\langle L_t\rangle = L_t = \{-1, 0, 1\}$, instead of eigenstates of the pure cubic orbitals p_{xy} and sp_z, as schematically sketched in Fig. 4.10 (c). The index t describes the tangential-pointing quantization axis of L. In full analogy to the magnetic quantum number in an isolated atomic orbital, the orbital, which aligns with the quantization axis ($|\alpha\rangle = |p_t\rangle$) carry zero OAM, while a complex superposition $|p_r\rangle \pm i\,|p_z\rangle$ leads to an OAM $L_t = \pm 1$.
The analysis shows that the model Hamiltonian for AgTe is associated with a formation of chiral and, thus, Rashba-type OAM. This can also be understood by writing the ISB part of the Hamiltonian H_{ISB} as a linear combination

of the OAM operators L_{xy} (Eq. 2.10), giving:

$$H_{\mathrm{ISB}} = \tilde{V}_{sp_z} t_{sp} a \cdot \boldsymbol{L}(\boldsymbol{z} \times \boldsymbol{k}) \tag{4.6}$$

This term has the same form as the Rashba-Hamiltonian (Eq. 2.3) but with OAM instead of spin. The effect of ISB in a Rashba-like out-of-plane fashion was therefore also named *Orbital Rashba Effect* [48, 62] as an orbital analog of the conventional *Spin Rashba Effect*.
The factor $\alpha_{\mathrm{ISB}} = \tilde{V}_{sp_z} t_{sp} a$ (in analogy also named *Orbital Rashba parameter* [62]) parameterizes the ISB strength. Using the parameters for AgTe/Ag(111) results in $\alpha_{\mathrm{ISB}} \approx 1.4\,\mathrm{eV\AA}$. Even though, this is a rather estimated value, it is considerably larger than the experimentally determined (spin) Rashba parameter suggesting an ISB-dominated scenario, i.e., $E_{\mathrm{ISB}} > E_{\mathrm{SOC}}$, in AgTe.

Inclusion of Spin-Orbit Coupling

Now, one can show that the *Orbital Rashba Effect* acts as a precursor for conventional Rashba-type spin-splittings, including a k-linear energy splitting and chiral spin texture. Remarkably, this is despite the fact that the original Rashba-Hamiltonian H_R (Eq. 2.3) will be neglected. Instead of this, the atomic SOC Hamiltonian (Eq. 2.7) is used:

$$H_{\mathrm{SOC}} = \frac{\lambda_{\mathrm{SOC}}}{2} \boldsymbol{L} \cdot \boldsymbol{S} = \frac{\lambda_{\mathrm{SOC}}}{2} (L_x \sigma_x + L_y \sigma_y + L_z \sigma_z) \tag{4.7}$$

It has already been shown in Chapter 2.1.3 that this Hamiltonian in combination with H_{ISB} leads to a spin-split electronic structure and a finite spin polarization in the wave functions. To make the relation to the Rashba effect more pithy, one can use an OAM basis instead of $\{p_x, p_y, sp_z\}$. The bands within their OAM manifold are considered to be sufficiently decoupled[5] and SOC acts as a perturbation. That means the interband matrix elements in 4.7 will be ignored and the focus is instead on the intraband SOC submatrices $H_{\mathrm{SOC}}^{\Psi_i}$ of each band $\Psi_i = \{\alpha, \beta, \gamma\}$ (Fig. 4.10) with its respective OAM expectation values $\langle L \rangle$ [48]:

$$H_{\mathrm{SOC}}^{\Psi_i} = \frac{\lambda_{\mathrm{SOC}}}{2} (\langle L_x \rangle \sigma_x + \langle L_y \rangle \sigma_y + \langle L_z \rangle \sigma_z) \tag{4.8}$$

$H_{\mathrm{SOC}}^{\Psi_i}$ are written in the spinfull OAM-basis $\{\Psi_{i,\uparrow}, \Psi_{i,\downarrow}\}$ and couple states of same OAM but different spin (the spin quantization axis is along z). It is immediately clear that only the OAM-carrying bands ($\langle L \rangle \neq 0$) can show a spin-orbit splitting. Thus, one gets a sizable splitting for β and γ while for α one finds $H_{\mathrm{SOC}}^{\alpha} = 0$. Using the expectation values (Eq. 4.5), H_{SOC}^{β} and $H_{\mathrm{SOC}}^{\gamma}$

[5] Note that this argument does not hold, for instance, directly at the $\bar{\Gamma}$-point, where $|\alpha\rangle$ and $|\beta\rangle$ are degenerate. The behavior at $k = 0$ is not so important at this point and is discussed in more detail in Appendix A.1.1.

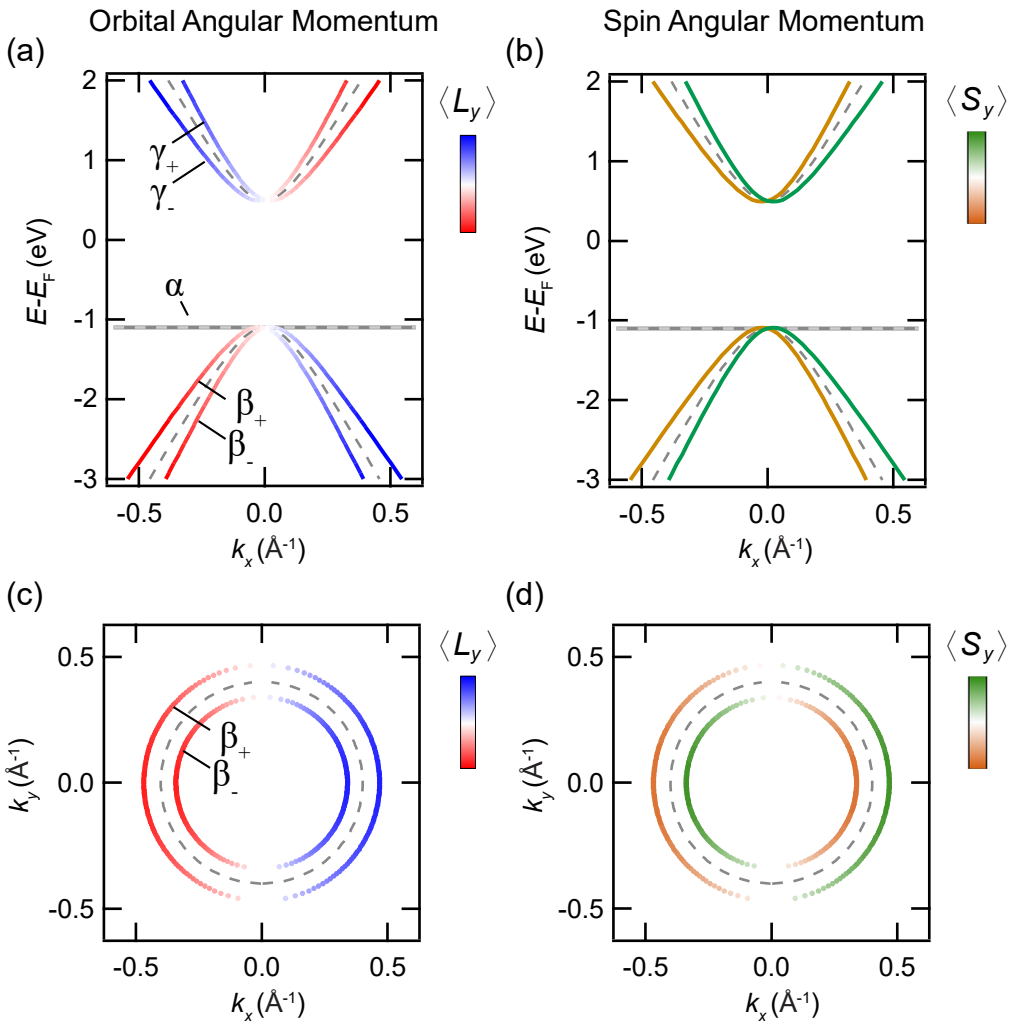

FIGURE 4.11: Band structure (a,b) and constant energy cut at -2.7 eV (c,d) calculated with SOC ($E_{p_{xy}} = -1.1$ eV, $E_{sp_z} = 0.5$ eV, $t_{\mathrm{sp}} = 2.3$ eV, $\alpha_{\mathrm{R}} = 0.88$ eVÅ). The OAM $\langle L_y \rangle$ (a,c) is parallel aligned within a pair of spin-split branches, while the SAM $\langle S_y \rangle$ (b,d) is anti parallel. Spin- and Orbital textures are linked as SOC leads to a (anti) parallel alignment of SAM to the preexisting OAM.

become:

$$H^{\beta}_{\mathrm{SOC}} = \frac{\lambda_{\mathrm{SOC}}}{2} \tilde{V}_{sp_z} \frac{a t_{sp}}{\Delta E} \begin{pmatrix} 0 & k_y + ik_x \\ k_y - ik_x & 0 \end{pmatrix} = -H^{\gamma}_{\mathrm{SOC}} \tag{4.9}$$

These Hamiltonians are of the same form as the original Rashba-Hamiltonian H_R (Eq. 2.3), suggesting a similar effect on the band dispersion and the resulting spin texture. Yet, there is an important difference to the Rashba model; the spatial part of the basis wave functions are OAM eigenstates instead of plane waves $e^{ik_{\parallel} r_{\parallel}}$ as in a 2DEG. This makes a decisive difference, as already discussed in Chapter 2.1.2: The Rashba effect in the present model relies on the local atomic SOC Hamiltonian and has thus a microscopically different physical origin. According to DFT calculations [45], the Rashba parameter that is related to this effect α_R^{LS} is the relevant quantity. From Eq. 4.9 one

finds $\alpha_R^{LS} = \frac{\lambda_{SOC}}{2}\tilde{V}_{sp_z}\frac{at_{sp}}{\Delta E}$. Notably, the model considerations might be too simplified for a quantitative analysis of α_R^{LS}. Yet, using the parameters as described above and estimating $\lambda_{SOC} = 0.36\,\text{eV}$ (see Appendix A.1.1) results in $\alpha_R^{LS} \approx 0.15\,\text{eVÅ}$. Even though this is much smaller compared to the experimentally observed value, it has at least the correct order of magnitude, while α_R^{RM} was estimated to be generally several orders of magnitude smaller (see Sect. 2.1.2).
The band dispersion calculated with SOC is shown in Fig. 4.11 (a,b), where $\alpha_R = 0.88\,\text{eVÅ}$ (corresponding to the observed experimental value) is used in the calculation. One can directly recognize a spin-splitting for β and γ instead of one single degenerate band as in the absence of SOC (dashed line), while α remains unperturbed, due to its vanishing OAM. As there are no OAM-mixing terms in Eq. 4.9 the two spin branches carry the same tangential OAM $\langle L_t \rangle$ (Fig. 4.11 (a,c)) but opposite SAM $\langle S_t \rangle$ (Fig. 4.11 (b,d)), i.e., the model is completely described within the strong-ISB-limit.
The model qualitatively reflects the experimental and theoretical results in AgTe, particularly the different manifestations of the Rashba effect in α and β as well as the associated spin texture. The main difference occurs at the fourfold degenerate point at $k_\parallel = 0$. This degeneracy is lifted by SOC in the real AgTe system. This is because the SOC matrix elements which are responsible for this are not included in the simplified SOC-Hamiltonian in Eq. 4.8, meaning it is an intraband SOC effect. At $k_\parallel = 0$, the radial and tangential states are equivalent and thus degenerate without SOC. The part of H_{SOC} that acts on the p_{xy}-orbitals is $L_z S_z$ (see Eq. 2.11). These hybridization terms are not included in the model, and the degeneracy is thus preserved. Nevertheless, this effect becomes only relevant very close to the $\bar{\Gamma}$-point, where $E_{ISB}(k_\parallel \approx 0) < E_{SOC}$. Thus, it does not matter crucially for the main message of this model and can therefore be neglected for simplicity.

4.2.3 Conclusions from the Minimal Model

The tight-binding approach shows that the Rashba effect cannot be described exclusively by the original free-electron model. In the above model assumptions, it results from the k-dependent behavior of the OAM, namely a chiral OAM-texture (Fig. 4.10 (b)) – caused by ISB – and an overall linear k-dependency (Eq. 4.5). This gives counter-rotating spin states with a splitting $\delta E \propto \langle L \rangle \propto k$. The commonality in the two approaches is the symmetry, i.e., the combination of in-plane isotropy and the polar ISB (IS: $z \to -z$). It is precisely this symmetry that enforces the characteristic spin-momentum locking, which then occurs independently of its underlying physical mechanism. The symmetry constraints are directly reflected in the orbital symmetries of the eigenstates (Eq. 4.3) in the tight-binding model, which in turn are expressed by the momentum-dependent OAM texture. Thus, the approach shows that the existence of Rashba splittings is directly related to the presence or absence of OAM.
The OAM-based origin of spin-splittings, can be summarized in two steps, schematically sketched in Fig. 4.12:

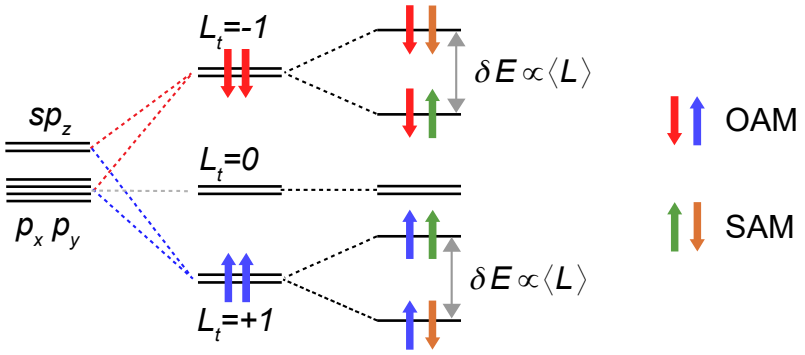

FIGURE 4.12: Energy level diagram for illustration of the formation of OAM and SAM in AgTe. First ($t_{sp}k = 0$), ISB leads to an effective sp_z hybridization that gives in total one two fold degenerate sp_z band and one four fold degenerate $p_x p_y$ state. Kinetic hopping ($t_{sp}k \neq 0$) couples sp_z and in-plane p_r-orbitals, leading to the formation of three two fold degenerate levels, separated by their OAM $L_t = \{-1, 0, +1\}$. Lastly, SOC introduces a splitting of states, whose spins are parallel and anti-parallel to the preexisting OAM. The magnitude of the splitting is proportional to the OAM, which for a small-k *Orbital Rashba-like* band in turn is proportional to k. In the end, there are two spin-split bands and one band, that remains degenerate.

1. First, breaking of inversion symmetry causes a modification of the electronic states, namely the formation of OAM. Consequently, each band contains to a specific OAM manifold labeled by its magnetic quantum number $L_t = \{-1, 0, +1\}$.

2. Due to SOC, the electron spins align parallel or anti-parallel to the preexisting OAM (Eq. 4.9), leading to an energy separation between the two spin-states. The magnitude of the splitting as well as the k-dependent spin texture are thus not a result of SOC but already predetermined in the first step.

4.3 Evidence for the OAM-Based Rashba Model

The minimal model shows that Rashba-type spin-splittings occur selectively on their orbital character. More precisely, their existence depends on the presence or absence of OAM in the wave functions. In the AgTe case, there are three bands with vastly different Rashba-splittings, in good agreement with the findings of the simple model. Nevertheless, it needs to be carefully evaluated whether there is evidence for such an OAM-based origin of the Rashba-splitting directly in the realistic band structure of AgTe.

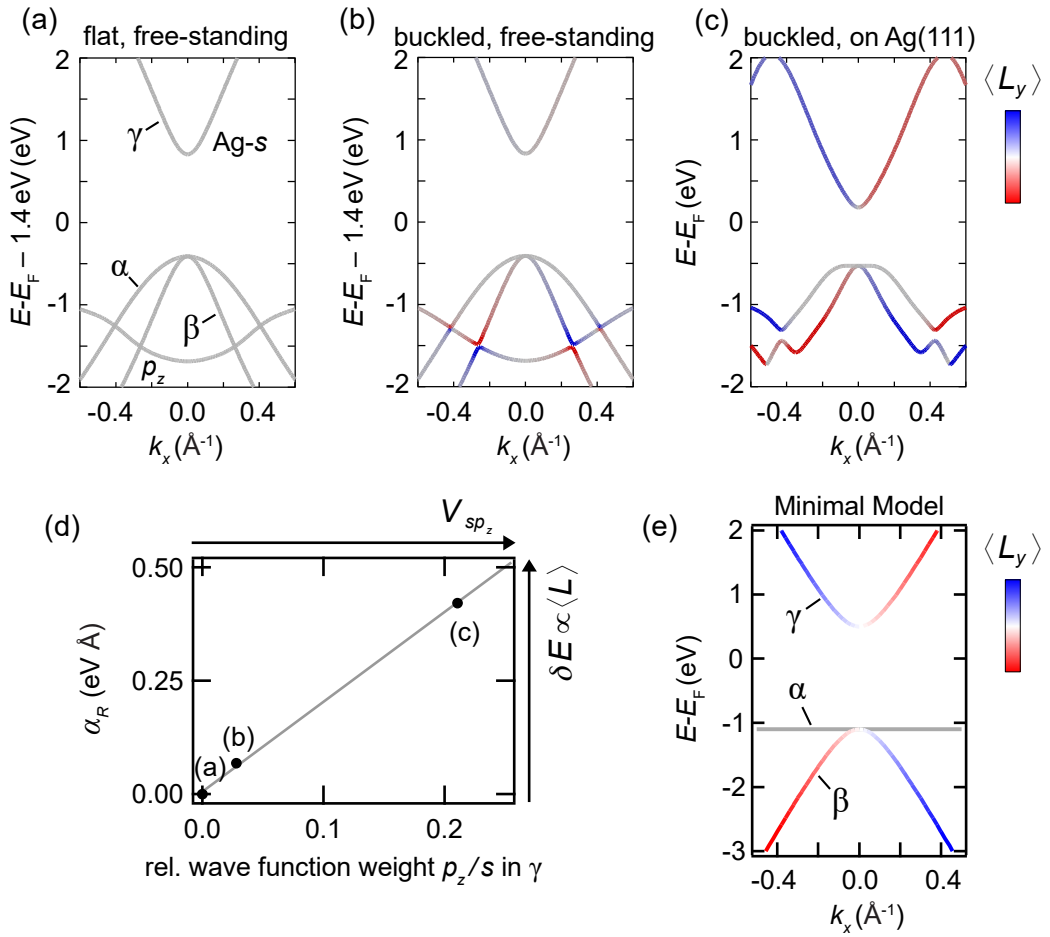

FIGURE 4.13: Inversion symmetry breaking for different AgTe modifications: (a-c) band structure calculated by using a Wannier-Hamiltonian without SOC. The calculations were done for (a) a flat and free-standing AgTe layer, (b) a buckled (7 pm) free-standing AgTe layer and (c) a buckled monolayer on Ag(111). The OAM $\langle L_y \rangle$, indicated by the color code, increases from (a) to (b) to (c) as a result of the larger sp_z hybridization, which is reflected by the relative wave function weight p_z / s in γ. The Rashba-parameter of β is proportional to the OAM and thus to p_z / s in γ as shown in (d). (e) Band structure calculation using the minimal model for comparison to DFT (c).

4.3.1 OAM Calculated by DFT

To determine the OAM in the band structure calculated by DFT, the Kohm-Sham wave functions were projected onto Te-p and Ag-s type Wannier functions. The eigenstates of the resulting Wannier-Hamiltonian were then projected onto spherical harmonics, giving the OAM expectation values [64]. The band structure of AgTe/Ag(111), obtained from the Wannier-model, is shown in Fig. 4.13 (c). As expected from the model assumptions, β and γ carry an in-plane OAM with an overall opposite sign. For α, in contrast, one finds $\langle L_y \rangle = 0$. Moreover, OAM appears already in the absence of SOC, and only slight changes in the OAM texture are seen after inclusion (compare Fig. 4.14 (a,b)). Overall, the OAM calculated by DFT closely reflects the simple model assumptions, as can be seen by directly comparing the respective

band structure calculations (Fig. 4.13 (c,e)).
It is also important to prove that OAM is really induced by ISB, i.e., by a sp_z-hybridization that occurs upon hybridization with the substrate atomic orbitals. Regarding the atomic structure of AgTe/Ag(111) (Fig. 4.1 (e,f)) there a two possible contributions to ISB. First, there is a slight outward relaxation of the Te-atoms, and second, there is the coupling of the AgTe monolayer to the Ag(111) substrate. In order to check which one is most relevant, DFT calculations were done for three different modifications; (a) flat and free-standing (inversion-symmetric), (b) free-standing with a 7 pm buckling (which corresponds to the experimentally determined outward relaxation) and (c) the buckled layer on a seven-layer Ag(111)-slab. The corresponding band structure calculations are shown in Fig. 4.13 (a-c), respectively. The dispersion of all three bands α, β, and γ is nearly the same in all modifications indicating negligible changes in the in-plane potential. However, the wave function of the different electronic states is modified. As expected, there is a completely vanishing OAM in the inversion symmetric flat, free-standing AgTe layer (Fig. 4.13 (a)). Breaking inversion symmetry by a buckling (Fig. 4.13 (b)) directly leads to the formation of OAM in a narrow region around the small hybridization gaps between β and the p_z-band. A stronger effect occurs, when AgTe is put on a Ag(111) slab (Fig. 4.13 (c)): The p_z-band vanishes completely – as explained in the adsorption model (Chapter 4.1.3) – and OAM is formed over the entire bandwidth. The comparison of the three different AgTe modifications directly proves that ISB induces OAM, and the latter is mainly driven upon interaction with the Ag(111) substrate. To show that this interaction is indeed manifested by a s-p_z hybridization, the relative contribution of s and p_z orbitals can be compared (bottom axis of Fig. 4.13 (d), see also Appendix A.1.4 for the respective orbital-projected DFT calculations). In the flat and free-standing scenario, γ contains to a pure Ag-s-band without any Te-p_z character ($\rightarrow \tilde{V}_{sp_z} = 0$). In the buckled AgTe monolayer (b), one finds just a small admixture of $\sim 3\,\%$, indicating a minor (but non-vanishing) contribution of the slight outward relaxation to the absolute magnitude of $\tilde{V}_{sp_z}$. After adsorption the relative p_z contribution becomes about 7 times larger ($\sim 21\,\%$) in agreement with an even more pronounced OAM in β and γ. This analysis proves that the formation of OAM in AgTe indeed goes hand in hand with a substrate-mediated s-p_z hybridization.
Since the mechanisms relevant for the OAM-physics in AgTe/Ag(111) are almost independent of the presence of SOC, the theoretical analysis was performed for calculations without SOC. In order to explore the impact of OAM in the wave function on the (spin) Rashba effect in a quantitative way, the calculated Rashba-parameter for the different AgTe modifications can be compared. The extracted values for α_R are plotted on the left axis in Fig. 4.13 (d), the respective DFT band structure calculations can be found in Appendix A.1.4. There is a direct proportionality between the Rashba parameter in β and relative wave function weight p_z / s in γ. Latter reflects $\tilde{V}_{sp_z}$, proving that $\alpha_R \propto \langle L \rangle \propto \tilde{V}_{sp_z}$, as predicted in the minimal model.

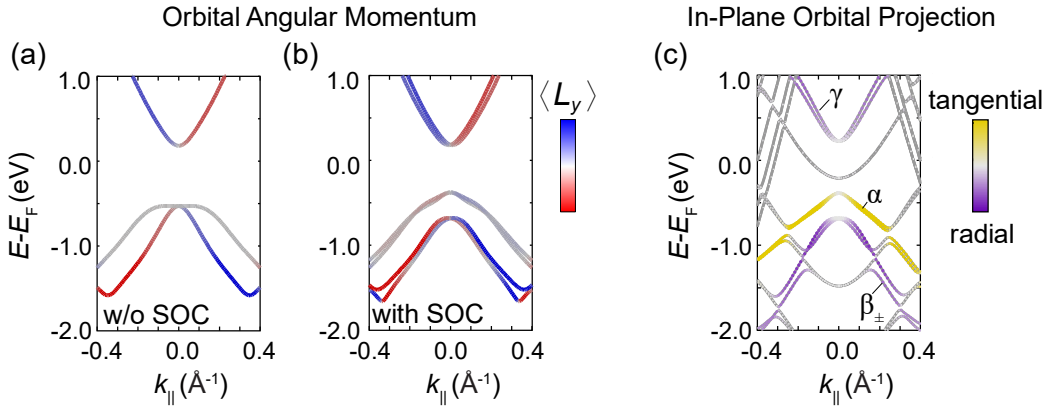

FIGURE 4.14: Relation between OAM and in-plane orbital texture in AgTe obtained by DFT. (a,b) OAM $\langle L_y \rangle$ calculated by DFT using a downfolded Wannier-model, without (a) and after switching on SOC (b). The band α contains to a $L_t = 0$ manifold while β and γ carry a (opposite) chiral OAM. The existence of OAM is linked to the in-plane orbital texture (c) in a way that just the radial aligned states carry non zero OAM. The calculation in (c) was not done by using the Wannier-Hamiltonian but directly refers to the slab calculations. Negative and positive wave vectors in (c) correspond to a path along $\bar{\Gamma}\bar{M}$ and $\bar{\Gamma}\bar{K}$ respectively (compare Fig. 4.3 (b)). *This figures have already been published in [64].*

4.3.2 Relation Between OAM and In-Plane Orbital Texture

Another important signature of the model eigenstates (Eq. 4.3) is that the bands with $L_t = \pm 1$ can be distinguished from the one with $L_t = 0$ by their respective in-plane p-orbital symmetry. One finds an tangential orbital alignment (p_t) for α and a radial alignment (p_r) for the bands showing an chiral OAM and a Rashba-type spin-splitting, namely β and γ. Fig. 4.14 (c) shows the DFT band structure calculation projected onto the in-plane orbital symmetry. Indeed, the calculated orbital contribution closely reflects the model considerations (Eq. 4.3). It is found that α is of p_t character while β and γ carry p_r character.

It is important to note that there is no difference in the in-plane orbital projection between the two Rashba-branches β_+ and β_-. Such a difference can occur due to strong SOC and a resulting non-negligible magnitude of the interband SOC matrix elements in Eq. 4.7. In-plane orbital texture switches above and below the crossing point of two spin-branches has been observed for topological surface states in $Bi_2(Se,Te)_3$ [161] and in the giant Rashba-systems $Ag_2Bi/Ag(111)$ [133, 177] and BiTeI [174] by ARPES measurements and DFT calculations (see Chapter 4.4 for further discussion on this issue). The fact that such changes do not appear in the AgTe band structure calculation (Fig. 4.14 (c)) proves that the assumption of neglecting the spin-mixing terms in Eq. 4.8 is reasonable in AgTe. Thus, AgTe is well described in a weak-SOC ($\leftrightarrow$ strong-ISB) limit, and the wave functions are mainly shaped by the non-relativistic part of the Hamiltonian, i.e., H_{ISB}.

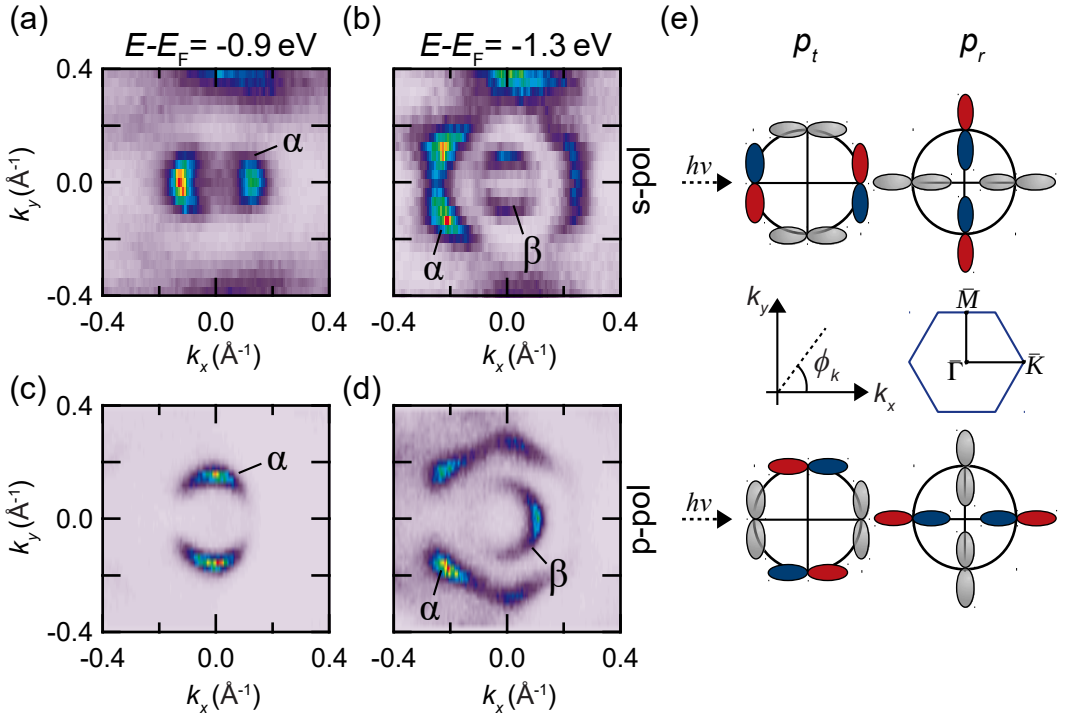

FIGURE 4.15: Orbital texture of the AgTe bands obtained in CECs measured with varied light polarization. (a-d) show CECs at $E - E_F = -0.9\,\text{eV}$ (a,c) and $E - E_F = -1.3\,\text{eV}$ (b,d) taken with *s*-polarized light at $h\nu = 65\,\text{eV}$ (a,b) and *p*-polarized light at $h\nu = 25\,\text{eV}$ (c,d). The intensity distribution, that is expected for radial p_r or tangential p_t orbital configurations with the respective light polarization is schematically shown in (e). Colored (grey shaded) orbitals representing a high (low) photoemission intensity. *This figure has already been published in [64].*

To confirm experimentally the calculated orbital textures, ARPES measurement were performed using linearly polarized light. Due to strict dipol selection rules in the photoemission process (see Chapter 3.2), orbital symmetries can be distinguished by the angular-dependent intensity distribution of the emitted photoelectrons. This is schematically sketched in Fig. 4.15 (e) for different initial state orbital textures p_t and p_r and different light polarizations. The plane of light incidence matches with the $\phi_k = 0$ plane, where ϕ_k denotes the azimuthal angle along a constant energy contour. Colored (grey-shaded) *p*-orbitals reveal an expected high (low) photoemission intensity for the respective combination of light polarization and initial state wave function. The ARPES data in Fig. 4.15 (a,b) and 4.15 (c,d) were taken with *s*- and *p*-polarized light, respectively. The contour in Fig. 4.15 (a,c) corresponds to α and has a vastly different intensity distribution for the varied light polarization. The photoemission intensity using *s*-polarized light (4.15 (a)) is high for $\phi_k = 0$ and strongly suppressed for $\phi_k = \pi/2$. Vice versa, one finds an opposite behavior for *p*-polarized light, namely suppression for $\phi_k = 0$ and an enhanced intensity along $\phi_k = \pi/2$ (4.15 (c)). Consistently, both measurements reveal a tangential orbital alignment for α (Fig. 4.15 (e)) in good agreement to the DFT calculations (Fig. 4.14 (c)).
At a lower energy (Fig. 4.15 (b,d)), there are two features in the CEC which

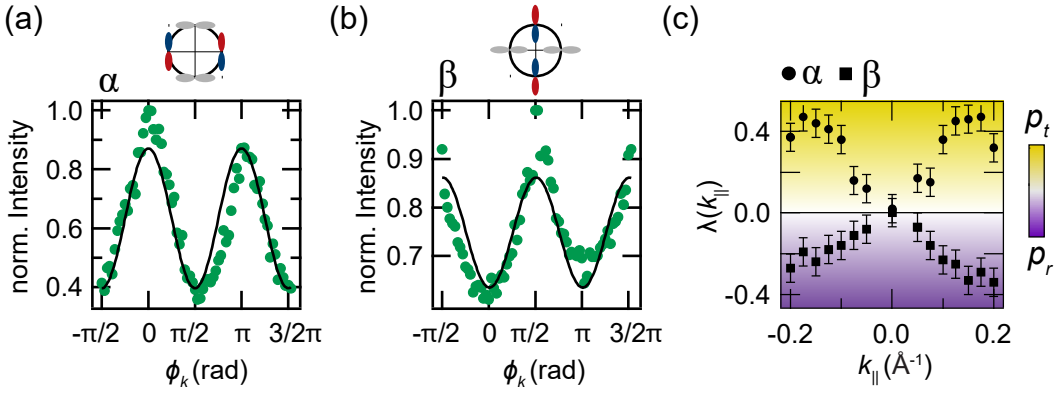

FIGURE 4.16: Evaluation of the momentum-dependent in-plane orbital texture in AgTe. Dependency of the photoemission intensity on the azimuthal angle ϕ_k for α (a) and β (b), extracted from the CECs, taken with s-polarized light (Fig. 4.15 (a) and (b), respectively). Green dots correspond to the data points and the solid lines are fits to the data, proofing a p_t character for α and p_r character for β. The ADF $\lambda(k_\parallel)$ (c) shows, that the orbital polarization holds over the entire $k_\parallel$ range and drops towards zero at $\bar{\Gamma}$. *Figure (c) has already been published in [64].*

can be assigned to α (outer contour) and β (inner contour). The intensity distribution of α is overall the same as in Fig. 4.15 (a,c). In contrast, for β the behavior is just the opposite, with a maximum intensity at $\phi_k = \pi/2$ for s-polarized light (Fig. 4.15 (c)) and along $\phi_k = 0$ with p-polarized light (Fig. 4.15 (d)). Thus, both measurements consistently confirm the expected p_r-character of β (Fig. 4.14 (c)).
For a more quantitative analysis of the $k_\parallel$-dependent in-plane orbital polarization, the photoemission intensity along a CEC can be extracted and plotted as a function of ϕ_k. In order to understand what would be expected from p_r or p_t states it is useful to write the eigenstates (Eq. 4.3) in polar cooradinates $(k_x, k_y) \rightarrow (k, \phi_k)$. The in-plane wave functions can be written as:

$$\begin{aligned} |p_t\rangle &= \sin(\phi_k)\,|p_x\rangle - \cos(\phi_k)\,|p_y\rangle \\ |p_r\rangle &= \cos(\phi_k)\,|p_x\rangle + \sin(\phi_k)\,|p_y\rangle\,. \end{aligned} \tag{4.10}$$

The focus is now on the measurements using s-polarized light. In this case, the light electric field $\boldsymbol{E}_s = (0, \mathcal{E}_y, 0)$ couples mainly to the p_y orbital contribution of the total wave function [170]. Thus, one expects $I_s(\phi_k) \propto \cos^2(\phi_k)$ for p_t and a $\sin^2(\phi_k)$-dependence for p_r.
The normalized photoemission intensity of α and β extracted from the data sets in Fig. 4.15 (a,b), respectively, and plotted as a function of ϕ_k is shown in Fig. 4.16 (a,b). The data systematically reflects the expected ϕ_k-dependence on the entire CEC. One finds $I_s(\phi_k) = I_{\text{min}} + I_{\text{max}} \cos^2(\phi_k)$ for α (Fig. 4.16 (a)) and $I_s(\phi_k) = I_{\text{min}} + I_{\text{max}} \sin^2(\phi_k)$ for β (Fig. 4.16 (b)). The lines are the respective fits to the data points, with I_{min} and I_{max} being the only free parameters. This analysis not just verifies the orbital texture over the entire CEC in a systematic way. It moreover allows for a quantitative view on the orbital polarization by comparing the minimum and maximum intensities. A reasonable

parameter for that is the so-called angular distribution factor (ADF) [174] $\lambda(k_\parallel)$. The ADF is defined as the normalized intensity difference:

$$\lambda(k_\parallel) = \frac{I_0(k_\parallel) - I_{\pi/2}(k_\parallel)}{I_0(k_\parallel) + I_{\pi/2}(k_\parallel)} \tag{4.11}$$

For s-polarized light λ parameterizes the relative p_y-orbital character along k_x ($\phi_k = 0$) and k_y ($\phi_k = \pi/2$) and therefore quantitatively reflects the in-plane orbital texture: One expects $\lambda > 0$ for a p_t-dominated band and $\lambda < 0$ for a p_r-dominated band. To get an overview about the orbital polarization within the band structure of AgTe, λ can be calculated for different energies and consequently different wave vectors. In Fig. 4.16 (c), $\lambda(k_\parallel)$ is plotted as a function of $k_\parallel$. The orbital polarization of α and β holds over the entire $k_\parallel$-range. Moreover it can be seen, that $\lambda(k_\parallel)$ drops smoothly towards zero for $k_\parallel \to 0$, similar to the calculated in-plane projection (Fig. 4.14 (c)). At the $\bar{\Gamma}$-point p_r and p_t become equivalent and both states have mixed p_x and p_y character (see also Appendix A.1.1 for further discussion on the eigenstates at $k = 0$).

4.3.3 Linear Dichroism

The analysis of the in-plane orbital texture can be used as rigorous proof for the existence or absence of OAM. This relation relies on fundamental symmetry conditions, namely the isotropy of the system close to $k = 0$ and the mirror symmetry of the orbital wave functions. Nevertheless, the formation of a chiral OAM $L_t = \pm 1$ itself is the result of an orbital mixing between the even orbitals $p_r \pm ip_z$. As a final step, it would therefore be useful to find an experimental probe that is sensitive to this mixing and therefore addresses the OAM texture more directly. Circular dichroism has been found to give information about the OAM [37, 48, 51, 88, 89]. Inspired by this, the so-called linear dichroism [132] will be analyzed in the following.

Considering the ϕ_k-dependent intensity distribution of an ARPES experiment taken with p-polarized light, as shown in Fig. 4.17. The light electric field $\boldsymbol{E}_p = (\mathcal{E}_x, 0, \mathcal{E}_z)$ couples predominantly to p_x as well as to sp_z orbital contributions [170]. Using the same arguments as for s-polarized light, one would expect a $\cos^2(\phi_k)$-dependence for a band having p_r in-plane orbital character, like it is the case for the OAM-carrying band β. No ϕ_k-dependency would be expected for the sp_z-orbital contribution of β due to its full rotational isotropy.

A measurement taken with a photon energy of $h\nu = 25\,\mathrm{eV}$ is shown in Fig. 4.17 (a-c). The extracted normalized photoemission intensity of β is plotted as a function of ϕ_k in Fig. 4.17 (b). Interestingly, one finds a total intensity distribution $I_p(\phi_k) = I_{\mathrm{min}} + I_r \cos^2(\phi_k) + \epsilon \cos(\phi_k)$. Thus, $I_p(\phi_k)$ has two different ϕ_k-dependent terms. On the one hand there is $I_{\mathrm{min}} + I_r \cos^2(\phi_k)$ representing the p_r-character in analogy to the measurement taken with s-polarized light. The dashed line in Fig. 4.17 (b,e) corresponds to the overall contribution of these terms, extracted from the total fit function. Other than

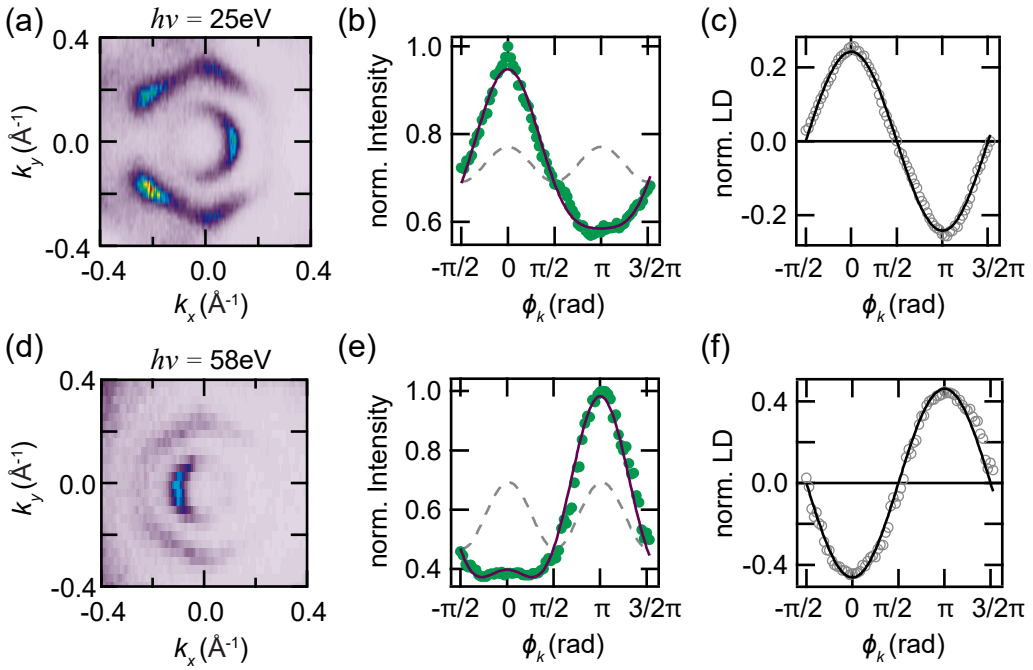

FIGURE 4.17: Momentum-dependent orbital texture in AgTe obtained from CECs taken with p-polarized light at $h\nu = 25\,\text{eV}$ (a-c) and $h\nu = 58\,\text{eV}$ (d-f). Dependency (b,e) of the photoemission intensity on the azimuthal angle ϕ_k. Green dots correspond to data points and solid lines are fits to the data. The pronounced asymmetry between positive and negative k_x, the linear dichroism (LD), changes its sign between (a-c) and (d-f). The dependency of the normalized LD (c,f) on ϕ_k shows a perfect $\cos(\phi_k)$-behavior. *Figures (a,b) have already been published in [64].*

that, there is another term $\epsilon\cos(\phi_k)$, which expresses the intensity asymmetry of β between $+k_x$ and $-k_x$, which is clearly visible in the CEC (Fig. 4.17 (a)). This asymmetry refers to the linear dichroism (LD) and will be further discussed in the following.

LD in the photoemission angular distribution can occur as a result of breaking experimental mirror symmetry with p-polarized light hitting the sample under an angle of light incidence $0 < \tan^{-1}(\frac{\mathcal{E}_z}{\mathcal{E}_x}) < \pi/2$. The broken $x \rightarrow -x$ symmetry allows for asymmetric intensity distributions between electrons with wave vectors $+k_x$ and $-k_x$. As already mentioned in Chapter 3.2, LD appears due to the fact that the light electric field vector has two non-vanishing components $\mathcal{E}_x \neq 0 \neq \mathcal{E}_z$. This leads to different emission channels for photoelectrons, as deduced in detail hereafter. According to that, LD is a real matrix element effect and thus depends on the initial state and on the photoemission final state. Before discussing further the information depth of the former, it shall be noted that the final state can have a notable impact on the experimental result [132]. To show that, measurements were done using different photon energies. A data set taken with $h\nu = 58\,\text{eV}$ is shown in Fig. 4.17 (d-f). It is directly apparent that a complete sign reversal of the LD occurs by changing the photon energy between 25 eV and 58 eV. In contrast, the remaining part of $I_p(\phi_k)$ is of the same shape for both photon energies, besides some small changes in the absolute magnitude of the

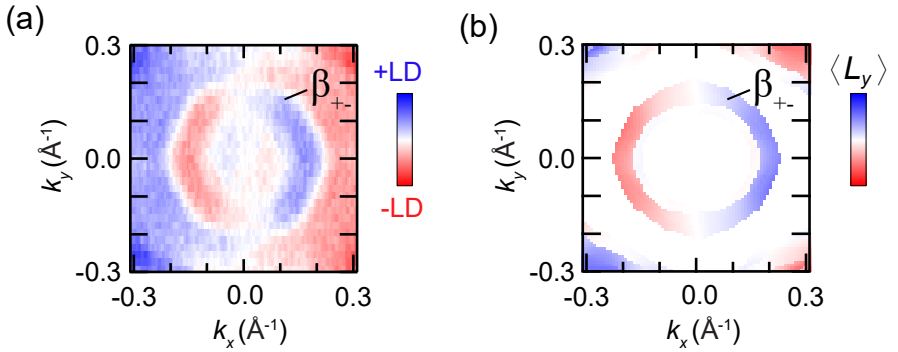

FIGURE 4.18: Comparison between (a) the measured LD ($h\nu = 25\,\mathrm{eV}$) and (b) the calculated OAM $\langle L_y \rangle$ (obtained from the Wannier-model with SOC being included) of $\beta_\pm$ in the band structure of AgTe. The LD pattern qualitatively matches with the OAM $\langle L_y \rangle$, that reflects the chiral OAM texture. *This figures have already been published in [64].*

individual terms, which will generically modulate as a function of photon energy. Even if the final state dependence of the LD initially makes an evaluation of the effect more complicated, it directly verifies that the observed asymmetry is de facto a property of the photoemission matrix element rather than a mere experimental artifact. It is consequently worth evaluating the LD further with particular attention to the initial state dependency.
In order to model the expected intensity distribution a p-orbital initial state $|\Psi\rangle$, which carries a chiral OAM, is constructed. Its wave function can generically be written as $|\Psi\rangle = c_x \cos(\phi_k) |p_x\rangle + c_y \sin(\phi_k) |p_y\rangle + i c_z |p_z\rangle$. The coefficients $c_{x,y,z}$ are real, k-dependent parameters. The expectation value $\langle L_y \rangle$ can be calculated, using the operator L_y defined in the cubic basis (see Eq. 2.10):

$$\langle \Psi | L_y | \Psi \rangle = 2 c_x c_z \cos(\phi_k). \tag{4.12}$$

The photoemission intensity at $\pm k_x$ for p-polarized light can be written as

$$I_p(\pm k_x) \propto | \langle f | \mathcal{E}_z z | \Psi \rangle \pm \langle f | \mathcal{E}_x x | \Psi \rangle |^2. \tag{4.13}$$

As it has been already applied in the beginning of this paragraph, one finds $\langle f | \mathcal{E}_p r | p_y \rangle = 0$ by standard dipol selection rules. Yet, another assumption can be made: A light field component $\mathcal{E}_i$ ($i = \{x, y, z\}$) will most likely couple predominantly to orbitals p_i whose orbital axis points along the direction i. Than, the remaining matrix element components become $\langle f | \mathcal{E}_x x | \Psi \rangle = c_x \cos(\phi_k) \langle f | \mathcal{E}_x x | p_x \rangle =: c_x \cos(\phi_k) T_x$ and $\langle f | \mathcal{E}_z z | \Psi \rangle = c_z \langle f | \mathcal{E}_z z | p_z \rangle =: c_z T_z$. The resulting photoemission intensity is

$$I_p(\pm k_x) \propto |T_z|^2 c_z^2 + |T_x|^2 c_x^2 \cos^2(\phi_k) \pm 2 c_x c_z \cos(\phi_k) \Re(i T_x^* T_z). \tag{4.14}$$

This is exactly the behavior of the photoemission intensity distribution found for the β-band in AgTe (Fig. 4.17). The asymmetry term, which is the one that is $\propto \cos(\phi_k)$ can only occur if both c_x and c_z are nonzero, indicating an initial state, which has $\langle L_y \rangle \neq 0$ (cf. Eq 4.12). This means that there

is a connection between an OAM in the initial state wave function and the occurrence of LD. To make this more pithy, one can write the LD using its definition $\mathrm{LD}(k_x, k_y) = I_p(+k_x, k_y) - I_p(-k_x, k_y)$, resulting in the following expression with $I_p(\pm k_x)$ as deduced before:

$$\mathrm{LD}(k_x, k_y) \propto f_{\mathrm{LD}} \cdot 2c_x c_z \cos(\phi_k) = f_{\mathrm{LD}} \cdot \langle L_y \rangle. \tag{4.15}$$

The expression $f_{\mathrm{LD}} = -2\Im(T_x^* T_z)$ can be regarded as a *LD form factor*. It entails the dependency of the LD on the atomic-orbital cross section, the experimental geometry (in particular the angle of light incidence), the photoemission final state, and – as a consequence of the latter – the photon energy. In literature one finds this term also called *interference term* [97]. The existence of LD relies on the fact that there are two excitation channels in the photoemission process given by separate excitation of different parts of the initial state wave function by different components of the light electric field. The interference is given by the matrix element product $T_x^* T_z$, which is expressed by their absolute values and the phase difference, both of which depend generically on the parameters described above [133]. Since it has many variables, the form factor can thus be rather complicated. Nevertheless, for a given experimental condition, in which all these variables are fixed, f_{LD} is just a pre-factor, and the LD is proportional to the OAM $\langle L_y \rangle$. In Fig. 4.17 (c,f), the LD normalized to the absolute photoemission intensity is plotted as function of ϕ_k. It is directly apparent that for both photon energies, it shows a clear $\cos(\phi_k)$-dependent behavior. This is precisely what is expected for a chiral OAM texture of the initial state. The LD pattern can also be presented using a false-color plot, as shown in Fig. 4.18 (a). Blue and red colors represent a positive or negative LD-sign, respectively, and the pattern is by definition perfectly antisymmetric with respect to the k_x-axis. Besides some background LD, resulting from the projected bulk bands of the substrate, the LD of β agrees likely with the calculated $\langle L_y \rangle$ pattern in Fig. 4.18 (b).
Finally, it should be mentioned that quite divergent LD results are obtained for α, as shown and discussed in more detail in Appendix A.1.3. Again, in good agreement with the expectation of a vanishing OAM ($\langle L_y \rangle = 0$ along k_x), a disappearing LD is also obtained.

4.4 Discussion and Impact on Various Material Systems

A binary honeycomb monolayer AgTe grown on Ag(111) represents a perfect model system for a paradigm in which the existence of Rashba-type spin splittings relies on the presence of OAM in the wave function. The vastly different behavior concerning the Rashba-splitting in the valence bands of AgTe is directly related to the fact that the bands correspond to different OAM-manifolds. The existence of OAM relies on ISB, which manifests in a strong hybridization of the out-of-plane AgTe orbitals with the substrate electronic surface and bulk states. By a minimal three-band tight-binding model, it can

be shown that the resulting asymmetric in-plane hopping leads to the formation of OAM. One of the main findings is that this mechanism depends on the in-plane orbital wave function symmetry: A chiral OAM-texture always accompanies a radial alignment of the in-plane p-orbitals. The band that has a tangential orbital character, in turn, forms the $L_t = 0$ manifold. DFT band structure calculations on AgTe/Ag(111) directly confirm these model results. Based on dipole approximation, photoemission matrix element effects allows for a momentum-resolved mapping of the orbital wave function by means of ARPES, using linearly polarized light. Systematically, the experimental results prove a radial (tangential) orbital texture for the bands with a sizable (vanishing) Rashba-type spin-orbit splitting. This gives strong experimental evidence for an OAM-based origin of the Rashba-effect.
Previous experimental approaches rely on ARPES with left and right-handed circularly polarized light, i.e., circular dichroism, that is to a certain extend sensitive to OAM [37, 48, 51, 88, 89]. However, even if signatures of the latter could have been found in the respective CD patterns, none of these results provided systematic evidence that the occurrence of spin-orbit splittings indeed relies on its existence. For example, no ARPES experiment could show the absence of any dichroic signature for a band with vanishing Rashba-splitting and/or vanishing OAM. On the one hand, this may be due to a lack of materials with such a model-like band structure as AgTe with two occupied bands that belong to different OAM-manifolds and thus have a significantly different Rashba-splitting. In addition, however, it might be challenging to refer the dichroic signal exclusively to an Orbital-Rashba-like OAM in the initial state. Even final state effects [127, 129, 178, 179] or the simultaneous probe of in- and additional out-of-plane OAM-components [55, 129, 180] can affect the resulting matrix elements and, with that, the CD results. In this regard, the in-plane orbital symmetry analysis, shown here, is more credible to distinguish between bands with sizable and vanishing OAM.
Nevertheless, the importance of CD should not be underestimated. On the contrary, dichroic ARPES provides more direct access to the OAM in the initial state, or at least to the OAM-characteristic orbital mixture. Based on these ideas, the LD in AgTe has been analyzed in this Chapter. Comparable to CD results on other Rashba-type spin-split surface states [37, 51, 129], the LD-signal in the Rashba-branches $\beta_\pm$ in AgTe (Figs. 4.17 and 4.18) can likely be attributed to a helical OAM texture of the initial states (Eq. 4.12). Further discussion about the LD, including a more detailed comparison to CD and its applicability to other Rashba systems, can be found in the following sections of the Chapter.

The experimental and theoretical findings from the previous sections are based on the model system AgTe/Ag(111). However, the OAM-based Rashba model has already found application in the interpretation of experimental data and DFT calculations on a variety of different material systems [37, 49, 51–56]. The applicability of the specific findings in AgTe to various materials will be briefly touched upon in the following.
Based on the conclusions in AgTe/Ag(111), the relation between spin and

orbital texture in the topological surface states of a Weyl semimetal TaP(001) will be discussed in the first paragraph. APRES measurements were performed at the MAESTRO endstation at the Advanced Light Source (Berkeley, USA), i.e., the same setup used for the polarization-dependent measurements on AgTe. A comprehensive discussion of this data and the respective DFT calculations as well as further experimental and theoretical details can be found in [115].
The second part of this section takes a closer look at the interplay between SOC and ISB. It has been shown that SOC has only a minor effect on the orbital texture in AgTe. This opens the question of whether the AgTe-specific findings are transferable to material systems in which SOC – and thus not ISB – is predominant. In a combined analysis of metadata and further LD results, the findings of this chapter will be placed in a broader context. ARPES data on Au(111) was taken at the APE endstation at the Elettra synchrotron light source (Trieste, Italy) [181, 182]. Ag_2(Bi,Pb)/Ag(111) data sets were kindly provided by Dr. Henriette Maaß and Dr. Hendrik Bentmann for further analysis. Additional information about the experimental setup and a detailed analysis of the results can be found in [132, 133].

Spin-Orbital Texture of Topological Fermi-Arc Surface States on TaP(001)

In order to investigate a material system with an electronic structure that is different from that of a model-like Rashba system as AgTe, ARPES measurements on a paradigmatic Weyl semimetal TaP(001) are shown in Fig. 4.19 (a,b). Data was taken using a photon energy of $h\nu = 105\,\mathrm{eV}$, belonging to a photon energy range in which APRES measurements are sensitive to the surface states of TaP(001) [79, 81, 115]. The measurements are, therefore, in good agreement with the calculated surface state Fermi surface (Figs. 4.19 (d-f)) and previous experimental and theoretical findings [79, 81, 114]. Three main features, labeled as $\alpha_\pm$, β and γ in Fig. 4.19 (a), can be identified. The focus here is on the band α, which is split into branches α_+ and α_- due to ISB and SOC. The topologically non-trivial surface states connect the bulk Weyl points in the bulk band structure of TaP. The resulting arc-like shape of α is thus very different from an isotropic circular-shaped CEC of a classical Rashba-system. Despite this fact, the spin texture (Fig. 4.19 (c)) close to the high symmetry lines $\bar{\Gamma}\bar{X}$ and $\bar{\Gamma}\bar{Y}$ can be regarded as Rashba-like in the sense that the spin polarization there is mainly perpendicular to $\boldsymbol{k}_\parallel$. Therefore, it is worth proving whether the orbital symmetries of $\alpha_\pm$ coincide with the orbital texture found in AgTe. For simplicity and comparability, the analysis will be restricted to the P-p orbitals (Figs. 4.19 (d-f))[6]. Comparing the photoemission intensity close to the k_x-plane for the different linear light polarization, one finds a large photoemission intensity of $\alpha_\pm$ with p-polarized light (Fig. 4.19 (a)) and a nearly full suppression with s-polarization (Fig. 4.19 (b)). The spin branches $\alpha_\pm$ are thus built from orbitals that are even with respect to $y \rightarrow -y$ mirror symmetry in good agreement with the calculated p_x and p_z

[6] Symmetries of further contributing Ta-d orbitals are consistent with the mirror symmetry of the p orbitals depicted in this paragraph [115].

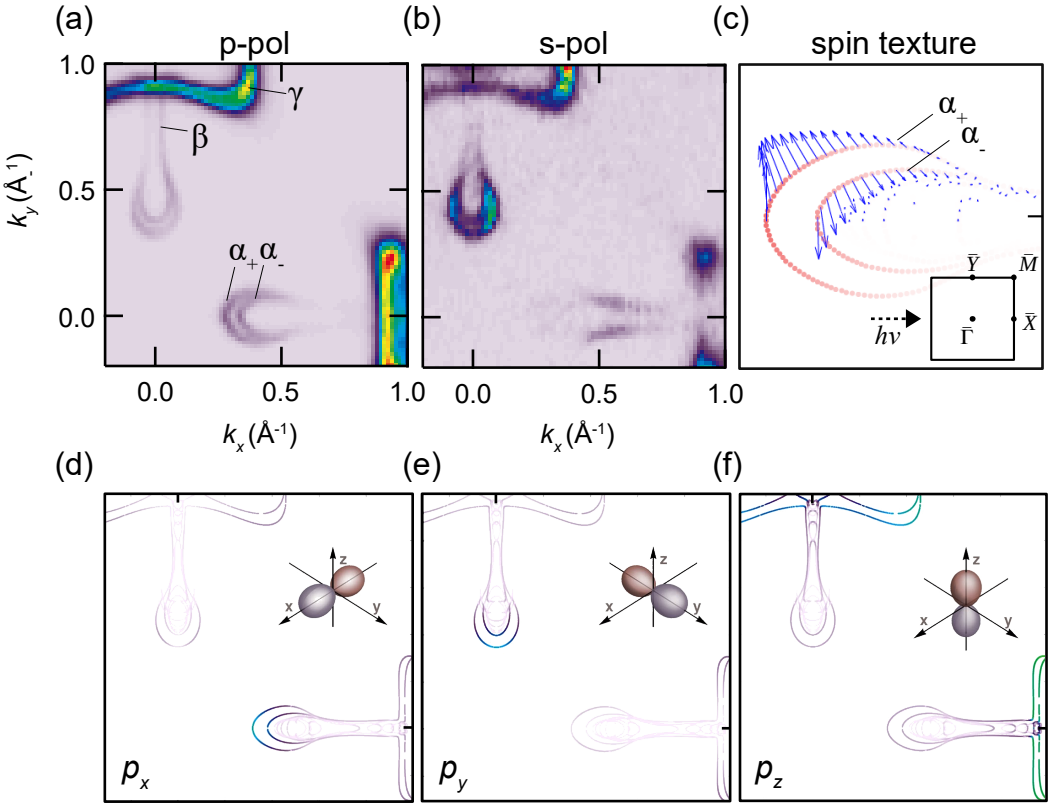

FIGURE 4.19: Spin-orbital texture of the Fermi-arc surface states in TaP(001). (a,b) Fermi surfaces obtained by (a,b) ARPES ($h\nu = 105\,\text{eV}$) using (a) p-polarized light and (b) s-polarized light and (d-f) DFT band structure calculations projected onto As p_x (d), p_y (e) and p_z (f) orbitals. Measurements and calculations both reveal a mixed p_r and p_z orbital texture of $\alpha_\pm$, indicating Rashba-type spin-texture comparable to the calculation in (c). *These figures have already been published in [115].*

orbital character (Fig. 4.19 (d,f)) and a vanishing contribution of p_y-orbitals (Fig. 4.19 (e)). The fact that both spin branches carry the same orbital character and have nearly no contribution of orbitals with odd mirror symmetry indicates a minor modification of the orbital wave function by SOC. This is further supported by a rather large absolute spin-polarization of $\sim 96\%$, calculated by DFT [115]. In other words, the surface band structure of TaP(001) contains most likely to a limit dominated by ISB rather than SOC, like in the case of AgTe/Ag(111).

A closer look on the measurement in Fig. 4.19 (b) shows that – in contrast to the intensity suppression along k_x – there is a large photoemission intensity along k_y, suggesting that $\alpha_\pm$ has predominantly p_y-character close to the k_y-plane. This is again in good agreement with the calculated orbital texture (Fig. 4.19 (e)). Thus, the resulting ADF (Eq. 4.11) for s-polarization is negative ($\lambda_s(k_\text{F}) \approx -0.6$) reflecting a radial in-plane orbital texture for $\alpha_\pm$. Of course, the designation *radial* is actually based on an isotropic picture, which obviously does not apply to the Fermi-arcs in TaP(001). What is meant in this case with p_r, is p_x character along k_x and p_y character along k_y. That means,

despite the decisive difference between TaP(001) and AgTe/Ag(111) concerning the topological origin and the isotropy, the link between a tangential spin texture and a radial orbital character can also be confirmed on the Fermi-arc surface states on TaP(001).
The measurement performed with p-polarized light (Fig. 4.19 (a)) further supports the p_r character of $\alpha_\pm$, since it shows a larger photoemission intensity along k_x compared to the signal along k_y, resulting in a positive ADF $\lambda_p(k_\mathrm{F}) \approx 0.39$. A smaller absolute value of $|\lambda_p|$ compared to $|\lambda_s|$ could be explained by assuming that the z-component of the light electric field $\mathcal{E}_z$ predominantly couples to the out-of-plane orbitals such as P-p_z[7]. Than $|\lambda_p| \ll |\lambda_s|$ would reflect an additional admixture of p_z orbitals to the spin branches $\alpha_\pm$ as predicted by the DFT calculation in Fig. 4.19 (f). Even there are no calculations for the OAM in TaP(001) available so far, a mixed p_r and p_z character of $\alpha_\pm$ portends a tangential aligned OAM in the wave function. This is further underlined by the LD along k_x shown in Fig. 4.20 (a). Both branches show a clear LD signal suggesting an OAM $\langle L_y \rangle$ (Eq. 4.15) with the same sign for α_+ and α_-. Latter agrees well with the interpretation that the electronic states in TaP(001) are dominated by ISB as discussed above.
The bottom line is that the findings in TaP(001) – regarding the spin and orbital character of the Fermi-arcs – underpin the conclusion from the AgTe results, namely a relation between spin and orbital texture via the OAM. However, the comparison made is on a phenomenological level, and OAM-calculations of the surface states in TaP(001) would be needed for a more concluding statement. In addition, for a more comprehensive analysis, the contribution of the Ta d orbitals should also be considered.

Interplay of ISB and SOC in Various Spin-Split Surface States

Both materials discussed so far in this chapter most likely belong to a regime where the characteristic energy scale E_ISB associated with ISB dominates over E_SOC. This manifests, for instance, in an almost pure radial in-plane orbital texture, a sizable absolute spin polarization, and a parallel OAM alignment in the spin branches of spin-orbit split bands (from now on labeled as $\Psi_\pm$). An overview of these properties in various material systems can be found in Table 4.1.
In order to shed more light on the interplay of ISB and SOC, the influence of the latter is examined in more detail below. Considering an electronic structure in which E_SOC is prevalent, the interband matrix elements coupling the submatrices $H_\mathrm{SOC}^{L_t}$ ($L_t = \{-1, 0, 1\}$) (Eq. 4.8) are no longer negligible or even rather predominant. It becomes immediately clear that the resulting eigenstates are characteristically different from the wave functions discussed so far. This applies to both the spatial (orbital) and spin sectors, which are no longer separable for large E_SOC. Instead of a pure p_r character

[7] Dipol selection rules would also allow for transition from p_y-like initial states, which are even under $x \to -x$ reflection with respect to the k_y-plane. However, a predominant coupling from $\mathcal{E}_z$ to p_z is also corroborated by the strong signal of γ (Fig. 4.19 (a)), which has mainly p_z character (Fig. 4.19 (f)).

TABLE 4.1: Comparison of the in-plane orbital texture λ (where $p_r \leftrightarrow p_t$ denotes a texture switch between the two spin-branches), the absolute magnitude of the spin polarization P, dependency of the photoelectron spin polarization on the linear light polarization (Rev.), relative sign of circular dichroism (CD), linear dichroism (LD) and OAM between two spin-branches, where $\uparrow\uparrow$ ($\uparrow\downarrow$) denote a (anti)-parallel alignment.

Material	λ	P	Rev.	CD	LD	OAM	
AgTe/Ag(111)[1]	p_r	>90 %	—	—	$\uparrow\uparrow$	$\uparrow\uparrow$	strong ISB
Au(111)[1,2]	p_r	96 %	no	$\uparrow\uparrow$	$\uparrow\uparrow$	$\uparrow\uparrow$	strong ISB
Cu(111)[3]	—	—	no	$\uparrow\uparrow$	—	$\uparrow\uparrow$	strong ISB
(Pt,Pd)CoO_2(0001)[4]	—	—	—	$\uparrow\uparrow$	—	$\uparrow\uparrow$	strong ISB
Ta(P,As)(001)[1,5]	p_r	96 %	no	—	$\uparrow\uparrow$	—	strong ISB
Ag_2Pb/Ag(111)[1,6]	p_r	—	—	—	$\uparrow\downarrow(\uparrow\uparrow)$	—	$\longleftrightarrow$
Cu_2Bi/Cu(111)[7]	—	—	yes	—	$\uparrow\downarrow$	—	strong SOC
Sb(111), Bi(111)[8]	—	—	yes	—	$\uparrow\downarrow$	—	strong SOC
BiTeI[9]	$p_r \leftrightarrow p_t$	—	yes	$\uparrow\downarrow$	—	—	strong SOC
Ag_2Bi/Ag(111)[1,10]	$p_r \leftrightarrow p_t$	80 %	yes	$\uparrow\downarrow$	$\uparrow\downarrow$	$\uparrow\downarrow$	strong SOC
Bi_2(Te,Se)$_3$(0001)[11]	$p_r \leftrightarrow p_t$	50 %	yes	$\uparrow\downarrow$	$\uparrow\downarrow$	$\uparrow\downarrow$	strong SOC

1 This work
2 References [52, 53], [97], [183, 184], [51, 129] and [51, 52]
3 References [185] and [51, 55]
4 Reference [37]
5 Reference [115] and [186, 187]
6 Reference [34, 133]. Relative LD-sign changes as a function of $h\nu$ (see Appendix A.2).
7 Reference [188]. LD was not discussed in the reference but clearly showed up in the data.
8 Reference [189] for Sb(111) and [190] for Bi(111). In both cases, LD was not discussed in the respective reference but clearly showed up in the data.
9 Referemces: [174], [191] and [192]. Relative CD-sign changes as a function of $h\nu$.
10 References [133, 177], [28], [132, 133, 188], [128, 130], [132, 133] and [54]
11 References [161, 193], [194], [183, 193, 195], [88, 124, 127, 179] and [47]. LD was not discussed in the reference (see for example [193]) but clearly showed up in the data.

and therefore even mirror symmetry in both spin branches $\Psi_\pm$, as observed in AgTe/Ag(111) and TaP(001), a significant admixture of odd p_t orbital parts occur [196]. This is a generic effect induced by strong SOC and is directly associated with a coupling of different spin structures to the different orbital components [197]. By means of ARPES measurements and DFT calculations, complex in-plane orbital texture switches have been observed in several compounds such as topological surface states of Bi_2(Se,Te)$_3$ [161, 193] or in giant Rashba-systems like Ag_2Bi/Ag(111) [133, 177] as well as BiTeI [174]. Moreover, ARPES combined with spin resolution and variable linear light polarization allows for disentangling the spin and orbital parts of the wave function. More precisely, this means that by changing from p to s polarized light, sign changes in the measured spin polarization could be detected in exactly

these materials [133, 183, 188, 191, 193, 195] as well as further Rashba systems [188, 189] (see column *Rev.* in Table 4.1). These findings, which clearly provide evidence for a substantial spin-orbital entanglement, verify the significant impact of SOC on the electronic wave functions in those materials. In contrast, it has been shown that, for example, in TaAs(001), there is no dependency of the measured photoelectron spin polarization on the light polarization [186, 187] confirming a negligible spin mixing in Ta(P,As)(001). This agrees quite well with the interpretation of the orbital texture and the parallel OAM alignment (expected from the LD pattern) as discussed in the previous paragraph.

The focus is now back on the OAM. As discussed in Chapter 2.1.4, the two regimes dominated by either E_{SOC} or E_{ISB} can be distinguished by the relative sign of the OAM in the spin branches Ψ_+ and Ψ_-, as schematically sketched in Fig. 4.20 (e). In contrast to the strong ISB limit, where both branches have the same OAM sign, there is an anti-parallel OAM alignment for $E_{\mathrm{SOC}} \gg E_{\mathrm{ISB}}$.

For AgTe/Ag(111) and TaP(001), OAM has been discussed in the context of the LD pattern that can appear in ARPES measurements taken with p polarized light. The conclusion that LD is, in fact, related to the OAM in the initial state (see Sect. 4.3.3) is indeed merely on a phenomenological level. However, to make this relation more significant, it is worthwhile to analyze the LD on a broader spectrum of materials, including systems in which $E_{\mathrm{SOC}} \ll E_{\mathrm{ISB}}$ but also $E_{\mathrm{SOC}} \gg E_{\mathrm{ISB}}$. A general overview about this is also given in Table 4.1 and can be directly compared to the spin-mixing properties discussed above. The discussion will now be restricted to one well-established representative of each regime; the SSA Ag_2Bi/Ag(111) and the SS on Au(111). Both systems have been studied in the context of OAM and clearly belong to the SOC-dominated and the ISB-dominated limit, respectively [51–54]. The corresponding LD is shown in Fig. 4.20 (b,d). Both measurements reveal a strong LD signal in the respective bands $\Psi_\pm$. For Au(111), the LD-sign is the same in the two Rashba branches Ψ_+ and Ψ_- in good agreement to CD [51, 129], and a consequently estimated parallel alignment of the OAM $\langle L_y \rangle$ [51–53]. The LD pattern observed for Ag_2Bi/Ag(111) is indeed different. In this case, the LD of Ψ_+ is negative and for Ψ_- it is positive, independent of the sign of k_x. This is again exactly what is expected for a material that is placed the weak ISB limit with an anti-parallel alignment of $\langle L_y \rangle$ in the initial state wave functions of $\Psi_\pm$ (compare Fig. 4.20 (e)). The LD results shown here, therefore, complements the findings in CD ARPES [128, 130] and the anti-parallel OAM alignment calculated by DFT [54]. Together with the findings on Au(111) and several other systems (Table 4.1) there is a significant experimental systematic, giving a hint for a relation between LD and OAM.

LD in Ag_2Bi has previously been studied extensively in [132, 133] including systematic photon-energy-dependent measurements and one-step photoemission calculations. Moreover, similar observations have also been made in the isostructural SSA Ag_2Pb [133] as shown in Fig. 4.20 (c). Notably, the observed absolute LD-sign in Ag_2(Pb,Bi)/Ag(111) depends strongly on

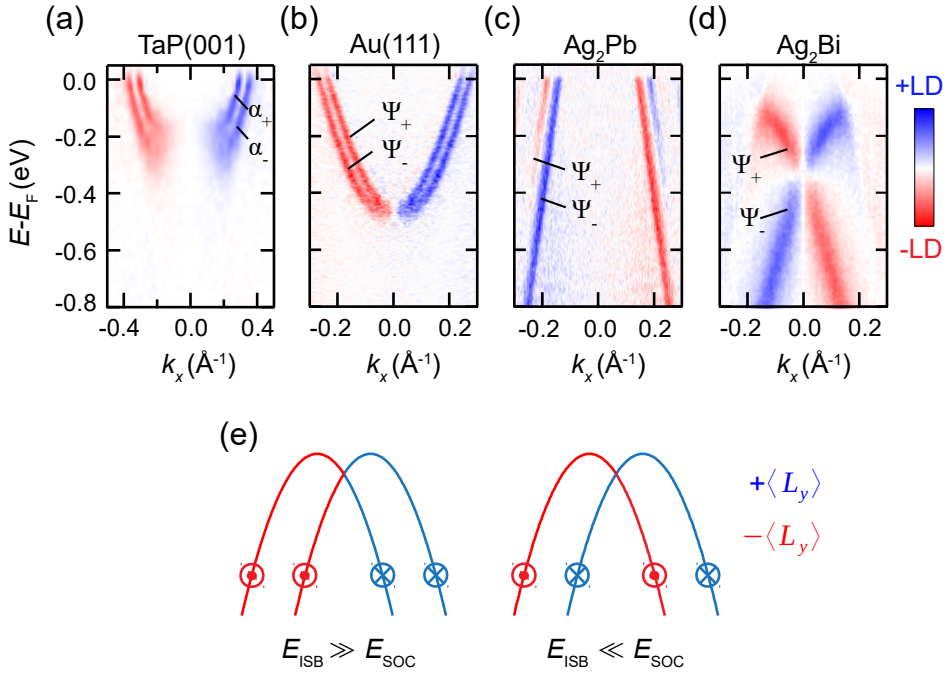

FIGURE 4.20: Linear dichroism in spin-split electronic states $\Psi_{\pm}$ of different material systems. (a) Topological Fermi-arc surface states of the TaP(001) ($h\nu = 105\,\text{eV}$), (b-d) Rashba-type spin-split surfaces states of (b) Au(111) ($h\nu = 18\,\text{eV}$), (c) $Ag_2Pb/Ag(111)$ ($h\nu = 18\,\text{eV}$) and (d) $Ag_2Bi/Ag(111)$ ($h\nu = 18\,\text{eV}$). The relative LD-sign of the two spin branches can be either parallel (a,b) or anti parallel (c,d), corresponding to OAM-textures estimated for the strong ($E_{\text{ISB}} \gg E_{\text{SOC}}$) and weak ($E_{\text{ISB}} \ll E_{\text{SOC}}$) ISB limit, respectively, as sketched in (e).

the photon energy. Similar to AgTe/Ag(111) (and also TaP(001) [115]) complete sign changes occur due to final state effects [132, 133] underpinning the importance of latter on the experimental results. Systematic analysis of the photon-energy-dependent LD in Au(111), confirming a similar behavior as for Ag_2(Pb,Bi) /Ag(111), can be found in Appendix A.2. Despite these strong final state effects, the relative sign between the branches Ψ_+ and Ψ_- is always parallel or rather anti-parallel in Au(111) and $Ag_2Bi/Ag(111)$, respectively. The assignment of both systems to the respective regime is therefore independent of the photon energy.

Taken together, the assumption derived from the AgTe results, namely that there is a link between the LD-ARPES signal and the initial state OAM, is based on a rather simplified picture. However, there is systematic experimental evidence underpinning such a relation. This holds for a wide range of materials featuring Rashba-type spin-orbit splittings, which can be dominated either by ISB or SOC. An overview of several experimental and theoretical signatures such as in-plane orbital texture, LD, CD, or OAM is given in Table 4.1 for a variety of materials systems. Based on all these aspects, a systematic division into the two regimes, i.e., a strong-ISB and a strong-SOC limit, can be clearly discerned.

4.5 Summary and Conclusion

The central subject of this chapter was the interplay between ISB and SOC in Rashba-type spin-split surface states and its impact on the momentum-dependence of the orbital wave functions. The main focus was on an epitaxially grown binary honeycomb surface alloy AgTe/Ag(111). Using Te to modify the Ag(111) surface turned out to be a suitable choice: Two completely filled Te-p_{xy} surface states appeared in the overall semiconducting 2D AgTe band structure and, due to the relatively large atomic SOC strength of Te, a sizable Rashba-type spin-splitting could be observed. The magnitude of the splitting is vastly different for the two occupied surface states. This behavior can be explained within an OAM-based Rashba paradigm [47–50]. Employing polarization-dependent ARPES measurements combined with linear dichroism and supported by DFT calculations, it has been shown that the formation of a chiral OAM texture – caused solely by ISB – is a prerequisite for the Rashba effect in AgTe/Ag(111).
Within this model, the characteristic Rashba-type spin-momentum locking is a direct consequence of the momentum dependence of the OAM, i.e.; SOC leads to parallel and antiparallel alignment of SAM with the preexisting OAM. A key finding is that such a chiral (tangential) OAM pattern is directly related to a radial alignment of the in-plane p-orbitals. If the energy scale associated with SOC is small compared to ISB, this holds strictly for various surface states with sizable Rashba-splittings such as AgTe/Ag(111) or Au(111). The ISB induced hybridization between p_r and p_z orbitals as well as a vanishing p_z-p_t coupling rely on fundamental orbital symmetry arguments. The combination of in-plane isotropy and out-of-plane broken inversion symmetry determines the characteristic helical OAM and thus also SAM alignment. Beyond the original Rashba model, which is based on the same symmetries, the novel paradigm represents a fundamental connection between orbital and spin texture and the underlying symmetries.
Analysis of the in-plane orbital texture in spin-momentum-locked Rashba-type or topological surface states has been the subject of several previous ARPES and DFT studies [133, 161, 174, 193]. In these, the emphasis was on the spin-orbital entanglement of the wave function due to strong SOC. However, the impact of ISB was not discussed at all. Within the OAM-based Rashba model, as discussed here, these results can be viewed from a different angle: SOC can couple states with different OAM – formed by ISB – via interband matrix elements that become relevant with increasing atomic SOC-strength. This effect can result in a mixed radial and tangential in-plane orbital character reported previously [133, 161, 174, 193].
Another aspect related to the interplay of SOC and ISB is the OAM texture itself, i.e., the relative OAM-alignment in the spin-branches. According to literature, experimental access to the momentum-dependent OAM is provided by ARPES combined with circular dichroism [37, 48, 51, 88, 89]. Inspired by this, special attention in this chapter was also paid to the linear dichroism in the photoelectron angular distribution. Analysis of the photoemission

matrix elements yields a similar depth of information from LD and CD, taking into account the respective experimental geometry. In both cases, the dichroic signal is directly related to an interference term originating from different photoemission channels. In a simple picture of selection rules and an idealized-constructed initial state, it was shown that the LD could indeed be expressed as a term proportional to the in-plane OAM component perpendicular to the plane of light incidence. While this derivation is likely oversimplified and therefore requires deeper theoretical approaches, actual evidence for a link between LD and OAM emerges from broad experimental systematics. The LD has been analyzed not only for AgTe but also in the Fermi-arc surface states of TaP(001) as well as other Rashba systems such as Au(111) and Ag_2Bi. It is shown that the LD sign can be the same but also the opposite in the two spin branches, and the results for the respective material system are in agreement with the expected OAM alignment as well as with previous CD results, if available.
In general, experimental access to the OAM is an important subject, in particular, in the physics of topological quantum materials. In recent studies, it has been predicted that ARPES, in combination with CD, can provide access to the momentum-dependent behavior of the Berry curvature in a system in this way [89, 198]. This relation will also be one of the major topics in the next chapter. However, the LD has not yet been discussed in the context of OAM, and the present results demonstrate that this method might represent a complementary approach to the CD.

Chapter 5

Spin and Orbital Angular Momentum in Weyl Semimetals

One of the most exciting features of Weyl semimetals is that the crossing points of the spin-polarized valence and conduction bands – the Weyl points – are momentum space realizations of magnetic monopoles, i.e., Berry curvature monopoles [20, 75]. This behavior is directly related to the topological protection of these band degeneracies. The two-band Hamiltonian around the WP can be written as $H \propto \pm\sigma \cdot \boldsymbol{k}$, leading to a linear band dispersion in three-dimensional momentum space. However, the topological structure, i.e., the integer quantized monopole charge that stabilizes the topological robustness of the WP, is determined by the non-trivial winding of the pseudospin σ. Thus, the topology in WSM is not encoded in the linear dispersion relation but rather manifests itself in the momentum-space texture of the eigenstates, i.e., the bulk electronic wave functions [87].
Previous experimental approaches addressing the three-dimensional bulk band structure of WSM were focused on the comparison of the measured dispersion to bulk band structure calculations [77–81]. For the paradigmatic WSM of the transition metal monopnictide family, ARPES measurements performed at bulk-sensitive light energies in the soft X-ray regime generally agree quite well with DFT calculations [77–81]. Nevertheless, the momentum-dependent spin and orbital character, which is supposed to entail the topological information, has not yet been investigated thoroughly.
This motivates the search for monopole signatures in the accessible physical observables, such as spin and orbital degrees of freedom. In the previous Chapter, it was shown for 2D surface states that ISB determines the k-dependent character of the wave functions significantly. In particular, the formation of a characteristic OAM texture – caused by the broken inversion symmetry at the surface – is fundamental to the Rashba effect. Although intensively studied for 2D systems [37, 48, 49, 51–56], the OAM-based origin for the formation of spin-polarized states has not yet been investigated in 3D bulk systems with broken inversion symmetry. However, particularly in (non-magnetic) WSM, the interplay of ISB and SOC is supposed to play a significant role for the non-trivial topology [20].
This chapter focuses on the bulk band structure of TaAs. The choice of this material system is made as it is one of the most established and studied WSM. Utilising soft X-ray ARPES, combined with circular dichroism and spin-resolved measurements, the aim is to address the properties of the wave

functions, which have hardly been investigated so far. As elaborated in the previous Chapter, both techniques are commonly used at low photon energies (10...200 eV) to study the spin-orbital texture in surface-localized states [18, 27, 37, 48, 51, 88, 89]. Spin-ARPES and CD at SX energies, on the other hand, are more demanding and not widespread [90]. Therefore, the information content of these measurements is still largely unclear. Chapter 5.1.2 is directly dedicated to these issues by comparing the experimental data with spin and orbital projected DFT band structure calculations. Subsequently, the CD pattern near the W_2 Weyl points and the topology around them will be discussed in more detail in Chapter 5.1.3 and 5.1.4, respectively. Further potential experimental signatures for the monopoles are added to the discussion in Chapter 5.1.5 as an outlook.

Experimental and Theoretical Details

SX-ARPES data shown in this chapter were taken at the ASPHERE Setup at PETRA 3 in Hamburg (see Chapter 3.3). TaAs single crystals have been grown via chemical vapor transport [87] in the group of Prof. Dr. Theo Siegrist at the FAMU-FSU College of Engineering in Tallahassee. Crystals were cleaved *in situ* parallel to the (001) surface using a top-post at temperatures below 100 K and pressure below $5 \cdot 10^{-9}$ mbar. Further details on the sample growth, preparation, and alignment can be found in Ref. [87, 199].

DFT band structure calculations were performed by Philipp Eck in the group of Prof. Dr. Giorgio Sangiovanni in Würzburg. Details on the DFT calculations are given in Ref. [87].

5.1 Topological Monopoles in the Bulk Band Structure of TaAs

5.1.1 Bulk Band Structure of TaAs Observed by SX-ARPES

Fig. 5.1 (a) shows an ARPES spectrum on TaAs(001) taken with a photon energy of $h\nu = 433$ eV. The parallel momentum axis k_x lies within the ΓZSΣ plane of the bulk BZ of TaAs (see Fig. 5.2 (b)). In contrast to the VUV regime in which ARPES is sensitive to the surface states of Ta(As,P)(001), SX-ARPES is supposed to probe predominantly the bulk bands [77, 79, 81, 200]. For instance, the Fermi-arcs, also discussed in the last chapter for TaP(001), are completely absent in the measurement in Fig. 5.1 (a). The DFT bulk band structure calculation in Fig. 5.1 (b) is on the other hand in good agreement with the experimental data, further supporting the expected bulk sensitivity in agreement to previous studies [77, 200]. Based on the good comparability, it can be directly concluded that using a photon energy of approximately 433 eV a final state momentum is reached that corresponds to an even integer multiple of $\frac{2\pi}{c}$ (see Fig. 5.1 (d), $k_z \approx 20\,\frac{2\pi}{c}$).

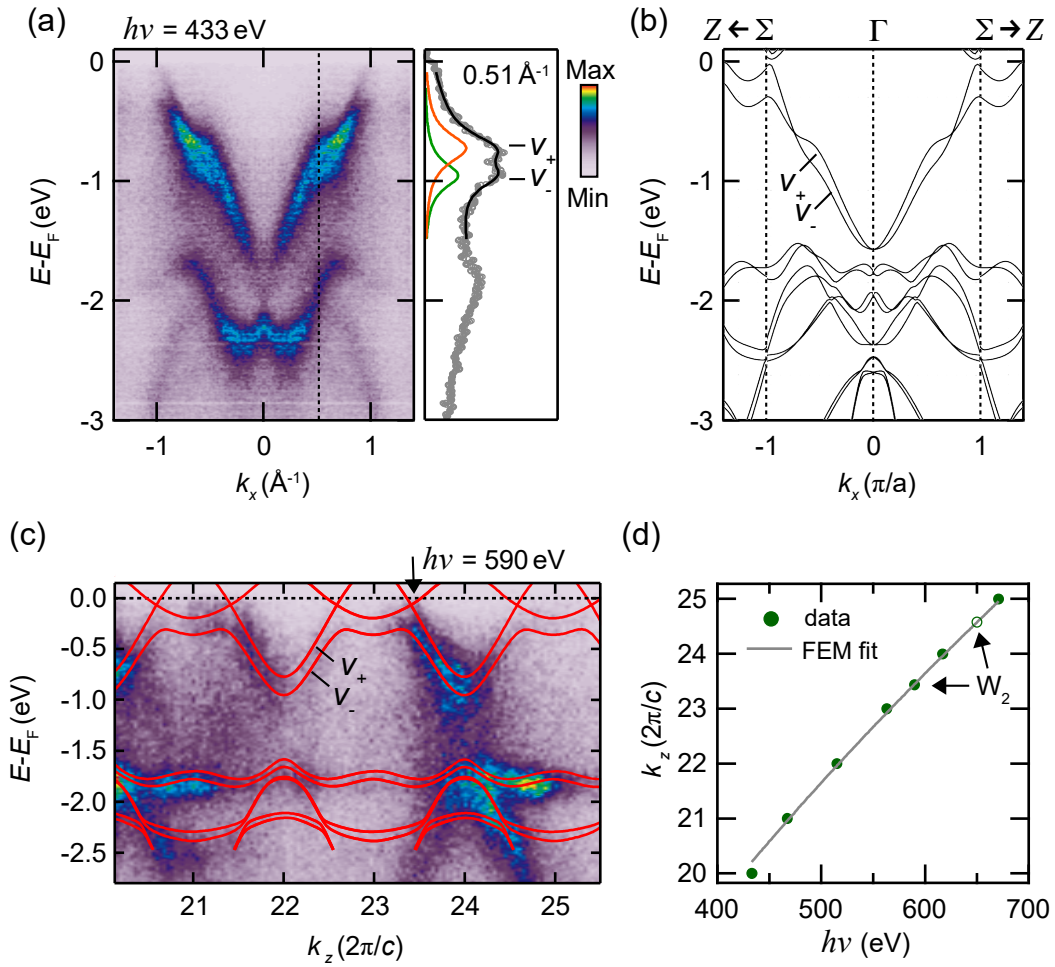

FIGURE 5.1: Bulk band structure of TaAs. (a,b) ARPES measurement taken with $h\nu = 433\,\text{eV}$ (symmetrized) and DFT band structure calculation along the ΓΣ high-symmetry direction of the bulk Brillouin zone, respectively. The valence band shows a spin splitting into branches v_+ and v_- further visualized by the EDC at $k_x = 0.51\,\text{Å}^{-1}$ in (a). (c) ARPES data set ($h\nu$ series) along k_z taken at $k_x = 0.51\,\text{Å}^{-1}$, corresponding to the calculated k_x position of the W_2 Weyl point. Red solid lines represent a DFT band structure calculation through a Weyl node. (d) Extracted high symmetry points (green dots) along k_z as a function of photon energy. The grey line corresponds to a free-electron final state model (FEM) fit to the data giving an inner potential of $V_0 = 25 \pm 2\,\text{eV}$. The green open circle is taken from [77]. *Figures (a-c) have already been published in [87].*

The first $\sim 1.5\,\text{eV}$ below E_F are spanned exclusively by the uppermost valence band $v_\pm$. As a result of SOC and the broken inversion symmetry in the crystal structure, a splitting occurs into the branches v_+ and v_-. This SO-splitting is also seen in the ARPES data, further emphasized by the EDC at $k_x = 0.51\,\text{Å}^{-1}$, clearly showing a double-peak structure in $v_\pm$. As discussed already in Chapter 2.2, a SO-splitting in the valence and conduction bands is essential for the formation of Weyl cones in non-magnetic WSM. The measurement in Fig. 5.1 (a) proves that spin-splittings in the bulk band structure of TaAs can be resolved within the experimental resolution.

The bulk sensitivity and in particular the decreased final-state broadening Δk_z allows moreover to determine the k_z dispersion by taking ARPES spectra as a function of photon energy (see Chapter 3). A $h\nu$ series at $k_x = 0.51\,\text{Å}^{-1}$, corresponding to the calculated parallel momentum of the W_2 points, is shown in Fig. 5.1 (c). Clearly, the energy positions change periodically, reflecting the k_z dispersion of the TaAs bulk bands. The inner potential was determined (Fig. 5.1 (d)) using the free-electron final state model[1], yielding a value of $V_0 = 25 \pm 2\,\text{eV}$. Even though there is no V_0 given in previous SX-ARPES studies on TaAs [77, 200], the W_2 photon energy of 650 eV estimated by Xu et al. [77] is directly on the fit curve in Fig. 5.1(d) (open circle) demonstrating a good agreement to the previous works.
DFT band structure calculations through a Weyl node along k_z matches well with the measured band dispersion. The valence band $v_\pm$ has a notable bandwidth along k_z and the Weyl cones occur as crossing points between valence and conduction bands. From this, it follows that with a photon energy of about $h\nu = 590\,\text{eV}$ a final state momentum $k_z \approx 23.4\,\frac{2\pi}{c}$, which corresponds to the W_2 Weyl points, can be reached. Further SX-ARPES measurements and DFT calculations shown in the following sections are restricted to this photon energy and the corresponding out-of-plane momentum k_z.
To get an overview of the band dispersion along $k_\parallel$, a series of CEC measured at $h\nu = 590\,\text{eV}$ is shown for different energies in Fig. 5.2 (a). The equi-k_z plane[2] doesn't contain any high symmetry point of the bulk BZ of TaAs, as further visualized in Fig. 5.2 (b). At $E = E_\text{F}$, the valence band $v_\pm$ forms four almost stripe-like features crossing the edges of the BZ boundary along the k_x and k_y axis. With lower energy, the bands open up into almost parallel stripes resulting in an overall triangular prism-shaped dispersion $E(k_x, k_y)$. A cut through such a prism along the BZ boundary is shown in Fig. 5.2 (c) in which the *triangular shape* of $v_\pm$ around $k_y = 0$ can be seen. Measurements in the upper and lower panel are taken with left and right-handed circularly polarized light, respectively. The k_y axis is perpendicular to the plane of light incidence as sketched in Fig. 5.2 (a) and in consequence, CD can appear along k_y. It is directly evident that there is a strong CD in the spin branches v_+ and v_-. This behavior will be further discussed in the following sections.

5.1.2 SX-ARPES Combined with Spin Resolution and Circular Dichroism

As shown in the previous section, the combination of SOC and ISB in TaAs splits the bulk valence and conduction bands into branches $v_\pm$ and $c_\pm$, respectively. However, the focus in the following is not on the mere band dispersion, but rather on the wave function character in these bulk bands. In order to address the spin-orbital texture, SX-ARPES experiments have been performed in combination with spin detection and circular dichroism. Both

1 $k_z = \sqrt{2m_e/\hbar^2}(V_0 + E_k - \hbar^2 k_\parallel^2/2m_e)^{1/2}$ (cf. Chapter 3, Eq. 3.6)

2 The curvature of the equi-k_z plane has been neglected here for simplicity.

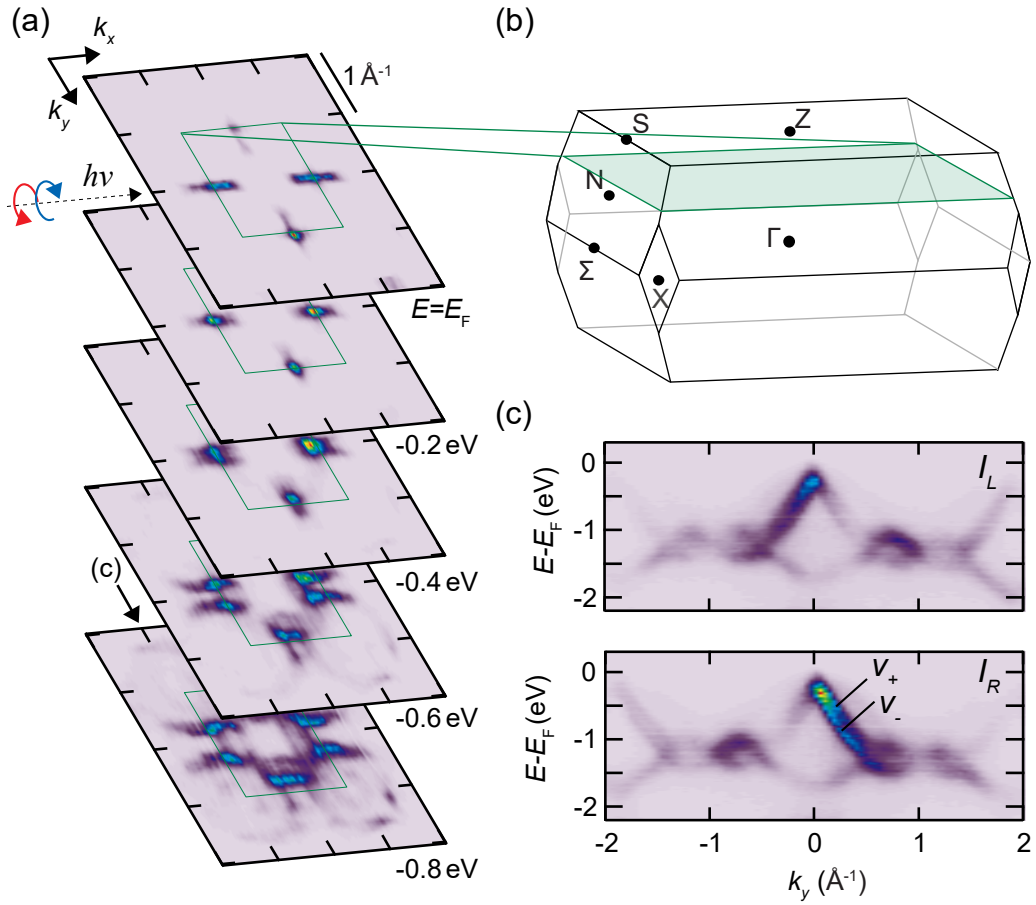

FIGURE 5.2: Overview of the in-plane bulk band dispersion measured at $h\nu = 590\,\text{eV}$. The constant energy cuts at different binding energies (a) correspond to an equi-k_z cut through the bulk Brillouin zone as indicated in (b). (c) $E(k_y)$ band structure cut along the zone boundary as marked in (a) taken with left (I_R) and right (I_L) circularly polarized light. *Figure (c) has already been published in [87].*

of these ARPES-based techniques are routinely used in the VUV photon energy regime and give access to the initial state spin [18, 27] and orbital angular momentum [37, 48, 51, 88, 89], respectively. On the other hand, the combination of SX-ARPES with SR or CD is not widely used [90]. For this reason, there have been no momentum-resolved experimental approaches investigating the spin-orbital texture in the bulk band structure of TaAs or other WSM candidates so far [201].

Spin-Resolved Measurements

First of all, the existence of Weyl nodes requires a finite spin-polarization in the bulk valence and conduction bands. Fig. 5.3 (a,b) show a band structure cut along k_y at $k_x = -1\,\text{Å}^{-1}$ (compare Fig. 5.2). The band dispersion calculated by DFT (Fig. 5.3 (a)) of the valence band branches v_+ and v_- agrees well with the spin-integrated SX-ARPES measurement in Fig. 5.3 (b). Moreover, the DFT calculation reveals a spin-polarization $\langle S_x \rangle$ with opposite signs

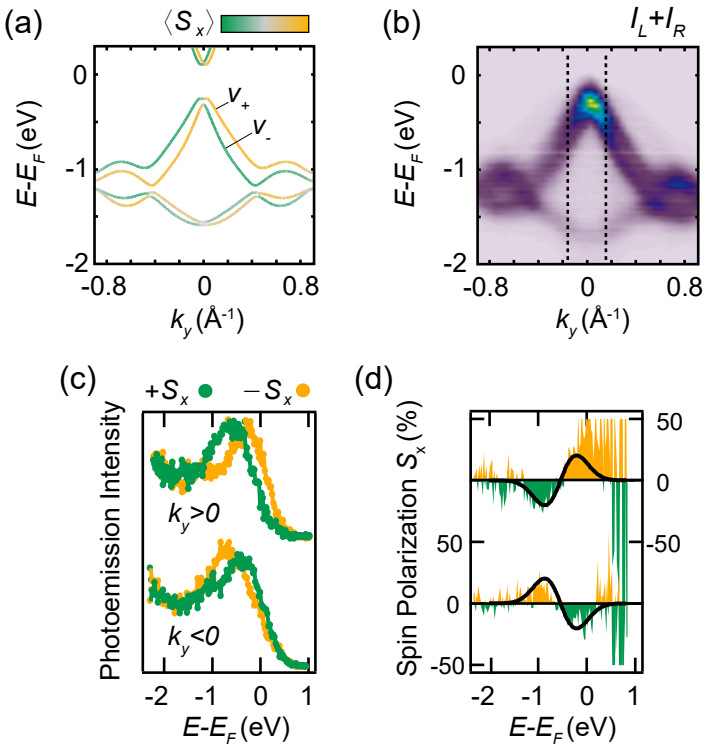

FIGURE 5.3: Spin polarization of the bulk bands in TaAs. (a) DFT-calculated band dispersion along k_y at $k_x = -1\,\text{Å}^{-1}$ and $k_z = 0.59\,(2\pi)/c$ corresponding to the W_2 k_z-plane. The color code indicates the calculated spin polarization $\langle S_x \rangle$, which proves an opposite spin polarization of the valence band branches $v_\pm$. (b) Same cut as in (a) measured by ARPES at $h\nu = 590\,\text{eV}$. (c) Spin-resolved energy distribution curves and (d) corresponding spin polarization taken at k_y marked in (b). *This figure has already been published in [87].*

in both branches v_+ and v_-. To confirm the calculated spin-polarization experimentally, spin-resolved SX-ARPES measurements have been performed. Fig. 5.3 (c) shows spin-resolved spectra taken at positive and negative[3] k_y as marked in Fig. 5.3 (b). The respective photoelectron spin-polarization is shown in Fig. 5.3 (d). It is directly evident from the measurements that the two spin branches v_+ and v_- have an opposite spin-polarization in the in-plane component $\langle S_x \rangle$. Moreover, it can be seen that the spin-polarization changes its sign for positive and negative k_y, as expected for $\langle S_x \rangle$ under mirror operation $M_y\colon y \to -y$. This is in good agreement with the DFT calculation in Fig. 5.3 (a) and can also be seen in the calculated band-resolved momentum texture of $\langle S_x \rangle$ for v_+ and v_- as shown in Figs. 5.4 (b) and (c), respectively. The spin-polarization is opposite in both bands within the whole BZ and $\langle S_x \rangle$ is antisymmetric with respect to the k_y axis, as outlined above. On the other hand, one finds that $\langle S_x \rangle$ is invariant under $M_x\colon x \to -x$ mirror symmetry, which is further supported by spin-resolved measurements at

[3] Spin-resolved measurements at positive and negative k_y were done using right- and left-handed circularly polarized light, respectively. Due to the strong CD (see Fig. 5.2), the photoemission intensity would otherwise be much too low to obtain reasonable count rates in the spin-resolved spectra.

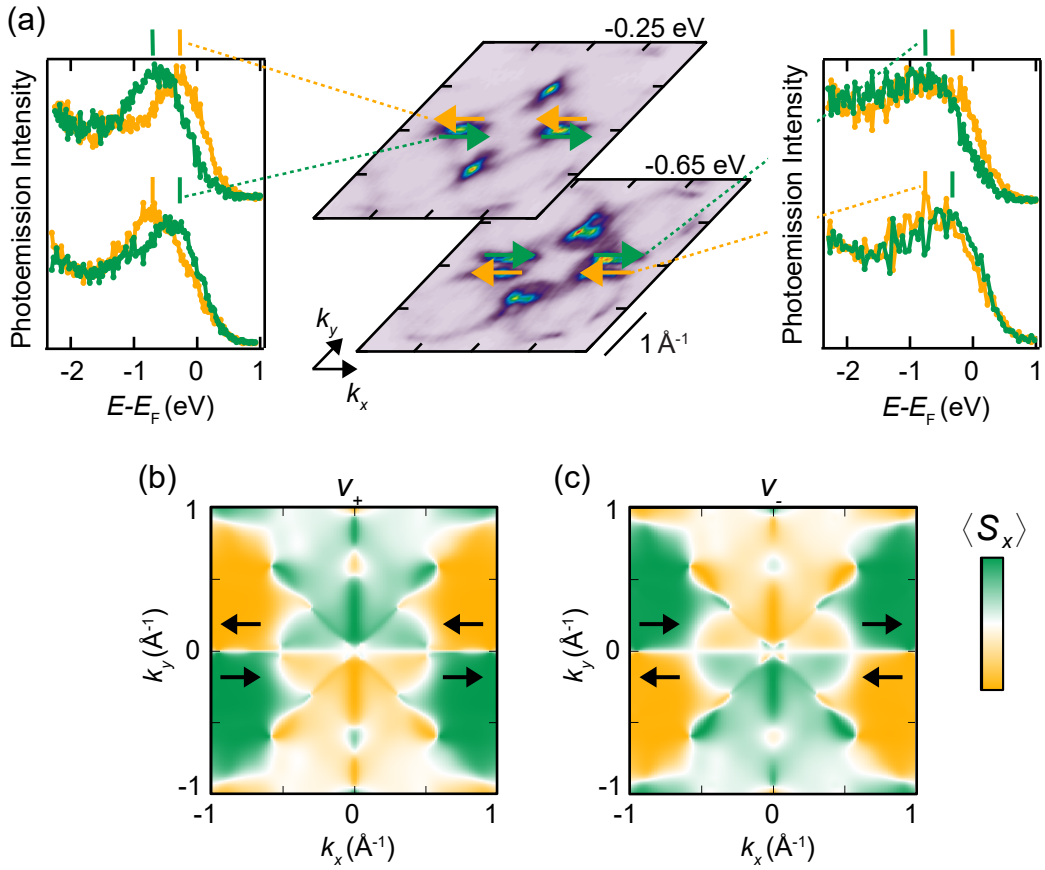

FIGURE 5.4: Systematic analysis of the spin polarization $\langle S_x \rangle$ of the bulk valence bands $v_\pm$. (a) Spin-resolved energy distribution curves taken at four different k-points confirm a sign change of the spin polarization when going from $+k_y$ to $-k_y$ and invariance of $\langle S_x \rangle$ under mirror operation M_x: $x \rightarrow -x$ in agreement to the DFT-calculated band-resolved spin texture of v_+ (b) and v_- (c). *Figures (a-c) have already been published in [87].*

$k_x = +1\,\text{Å}^{-1}$ (Fig. 5.4 (a)).
Taken together, the spin-resolved SX-ARPES experiments give strong systematic experimental evidence for spin-polarization in the bulk valence band states in TaAs.

Circular Dichroism

The formation of spin-polarized states in non-magnetic WSM, and hence the WSM state itself, relies in general on the presence of ISB. Assuming the transferability of the model discussed in the previous chapter to three-dimensional bulk systems, the breaking of inversion symmetry is directly related to the formation of OAM $\langle L \rangle$ in the bulk electronic states. Indeed, according to the DFT calculation in the top panel of Fig. 5.5 (a) and Fig. 5.5 (b), there is a finite OAM $\langle L_x \rangle$ in the wave functions of these bands as a direct consequence of the broken inversion symmetry in the TaAs crystal structure. It is directly apparent that the respective spin branches in v and c carry a parallel $\langle L_x \rangle$. The SAM $\langle S_x \rangle$, on the other hand, is antiparallel, as it has been shown

before (Fig. 5.3 and Fig. 5.4). Thus, the relative alignment between the two quantities, as calculated by DFT, suggests that the bulk electronic structure of TaAs can be assigned to a regime in which ISB dominates over SOC. It is worth mentioning that this would be in harmony with the conclusions on the Fermi-arc surface states on TaP(001) (see Chapter 4.4). However, a direct comparison might be difficult because, for one thing, E_{SOC} is slightly different in the two compounds, and in addition, ISB may also behave differently at the surface, which could result in a different energy E_{ISB} at the surface compared to the bulk. Nevertheless, both findings together give a strong indication of an ISB-dominated surface and bulk band structure in the WSM Ta(As,P)(001).

The finding of significant OAM polarization in the bulk bands naturally motivates an experimental investigation to directly prove the theoretical results. CD-ARPES measurements taken at $h\nu = 590\,\mathrm{eV}$ are shown in Fig. 5.5 (a, lower panel) and (c). It is directly apparent that – within the experimental geometry used – the CD is completely antisymmetric with respect to the plane of light incidence (xz), but rather symmetric with respect to the yz-plane. This behavior is similar to the x-component of the OAM $\langle L_x \rangle$, as can be seen in Fig. 5.6 (b). Overall, the rather complex OAM texture is remarkably well reflected by the measured CD over a wide range in momentum space (see also Fig. 5.6). Various sign changes of $\langle L_x \rangle$ appearing in the DFT calculation are reproduced in the experimental data. The overall good agreement gives a strong hint that the CD signal in SX-ARPES is indeed sensitive to the OAM in the initial state. At a very detailed level, the present results support the previously predicted proportionality between the CD to the OAM component $\langle L_p \rangle$, whose quantization axis is parallel to the light propagation direction $\boldsymbol{k_p}$ [48, 88]. The detailed agreement between experiment and calculation shown here might be attributed to two main factors: First, previous explanations describing the connection between OAM and CD are based on the free-electron final state approximation [48, 88], which should be sufficiently well satisfied in the photon energy range used [202–205]. Furthermore, the experimental geometry, in particular the grazing light incidence, allows a simplified interpretation. The light electric field vector is $\boldsymbol{E}_{R,L} = (\mathcal{E}_x, \pm i\mathcal{E}_y, \mathcal{E}_z)$, whereby the grazing light incidence in the xz plane of the experimental setup (see Fig. 5.2 (a)) implies that $\mathcal{E}_x \ll \mathcal{E}_{y,z}$. The x component of the electric field can thus be neglected in a first approximation ($\mathcal{E}_x \approx 0$). Exactly like in the case of LD, there are two excitation channels in the photoemission process given by the matrix element components T_y and T_z. Therefore, using similar arguments as for the LD in Sect. 4.3.3, the CD expresses as the interference term between them

$$\mathrm{CD}(k_x, k_y) \propto \Re(T_y^* T_z) \cdot \langle L_x \rangle. \tag{5.1}$$

In conclusion, a comprehensive picture has been obtained for the bulk bands in TaAs. They carry both orbital and spin angular momentum in their wave functions, which has been demonstrated using DFT calculations and SX-ARPES measurements in combination with spin resolution and circular di-

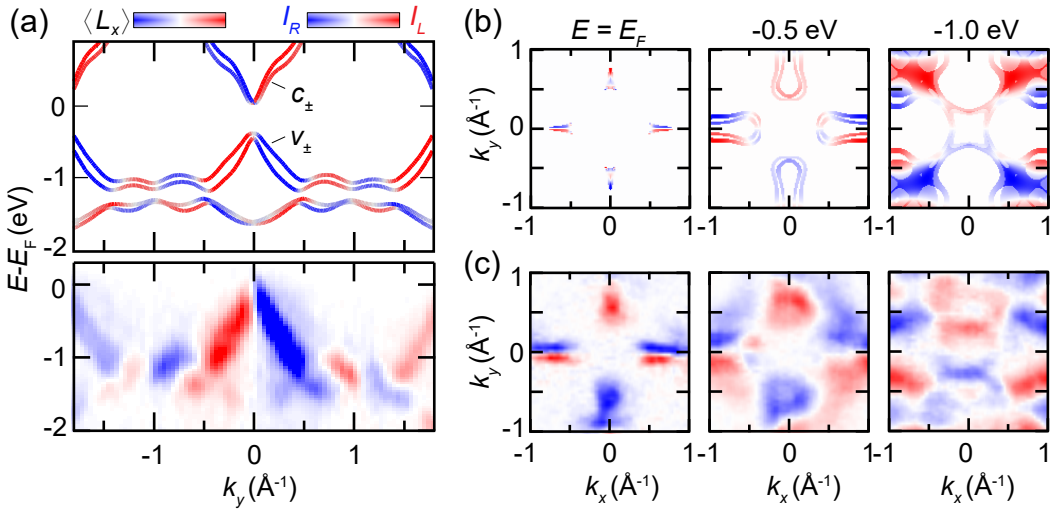

FIGURE 5.5: Comparison between the calculated OAM $\langle L_x \rangle$ the measured CD. (a) Band structure cut along k_y at $k_x = -1\,\text{Å}^{-1}$ and $k_z = 0.59\,(2\pi)/c$ corresponding to the W_2 k_z-plane. Both the calculated OAM (upper panel) and the CD (lower panel) consistently reveal a parallel OAM in the spin branches $v_\pm$. The OAM of the conduction band $c_\pm$ has an overall opposite sign as the valence band, indicating that both contain to different OAM manifolds. Overall, there is a good agreement between theory and experiment, which is also seen in the calculated (b) and measured (c) constant energy cuts. *This figures have already been published in [87].*

chroism. The calculated parallel OAM alignment in the spin branches can also be confirmed experimentally (Fig. 5.5 (a)) and the bulk band structure of TaAs is clearly dominated by ISB rather than SOC. The latter acts as a perturbation, implying that the eigenstates are predominantly shaped by the broken inversion symmetry. Nevertheless, despite its perturbative character, spin-orbit interaction has an important impact on the properties in WSM, namely, it leads to a lifting of spin degeneracy. The resulting spin-polarization of the bulk states could be directly observed in the experimental spectra.

5.1.3 Circular Dichroism Near the W_2 Weyl Points

In order to explore the role of spin and orbital character in the bulk electronic states on the Weyl-physics in TaAs, the momentum distribution of the OAM $\langle L_x \rangle$ will be discussed in more detail below. Fig. 5.6 (a) shows a CD momentum map, which was integrated in energy over the first 1.2 eV below E_F. The band structure in this energy range is solely spanned by the valence band $v_\pm$ and the resulting k_x-k_y map provides a good overview about the momentum-dependent behavior of the OAM in $v_\pm$. Indeed there is again a good agreement to the calculated OAM-texture shown in Fig. 5.6 (b). It is directly evident from both the CD and the calculation that the OAM texture changes characteristically at the pair of Weyl nodes marked in Fig. 5.6 (b). A characteristic checkerboard pattern appears around the W_2 points, which manifests itself in a sign change of the OAM upon passing a Weyl node. This

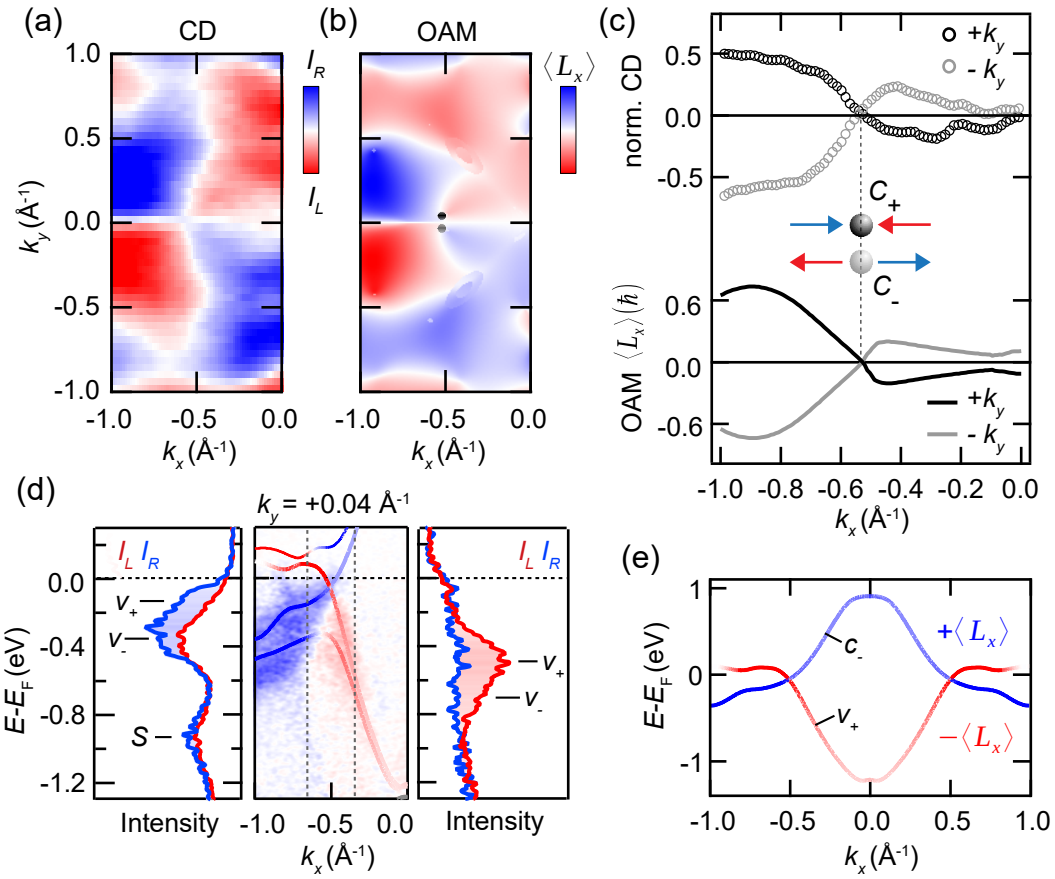

FIGURE 5.6: Momentum distribution of measured CD and calculated OAM $\langle L_x \rangle$ at $k_z = 0.59\,(2\pi)/c$ corresponding to the W_2 nodes. Data sets in (a-c) were integrated over the bandwidth of $v_\pm$, i.e., from 0 eV to −1.2 eV. CD (a) and OAM (b) show a checkerboard pattern around the Weyl point pair marked by the black and grey dots in (b). (c) Normalized CD and OAM $\langle L_x \rangle$ along k_x cuts through the Weyl nodes. Chirality-dependent sign changes at the Weyl node momentum are revealed on a quantitative level. (d) Band structure cut $E(k_x)$ (CD and OAM) through a Weyl point and energy distribution curves left and right of the crossing point. The state S corresponds to a surface state feature that can be neglected due to its vanishing CD signal. (e) The calculated band dispersion of the bands forming the Weyl cone (v_+ and c_-) shows that a Weyl node in TaAs denotes a crossing point of bands from different OAM manifolds. *Figures (a-c) have already been published in [87].*

can also be seen at a more quantitative level, as shown by k_x-cuts through the Weyl cones of different chirality (at positive and negative k_y) in Fig. 5.6 (c). The experiment directly reveals a sign change of the OAM at a parallel momentum $k_x \approx 0.5\,\text{Å}^{-1}$ close to the position of the Weyl node. Moreover, there is an opposite overall sign for the nodes of different chirality in good agreement with the calculated OAM. It is important to say that while the latter is directly enforced by mirror symmetry $M_y\colon y \to -y$, the sign reversal along k_x is not related to any symmetry. It occurs at an arbitrary point in momentum space and therefore directly reveals a distinctive change in the wave function character in the valence band around the Weyl point.

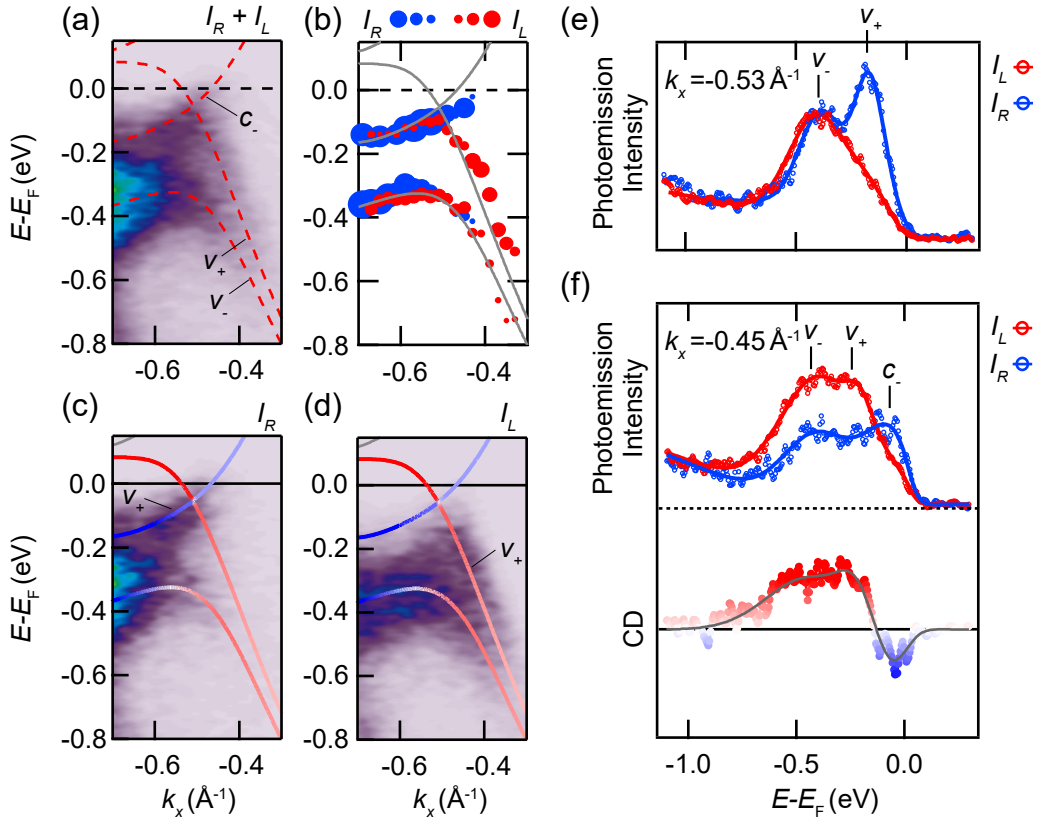

FIGURE 5.7: CD and OAM near the W_2 Weyl point. (a-d) ARPES data sets and calculated $\langle L_x \rangle$-projected band dispersion along k_x through a Weyl node. Measurements were taken with right I_R (c) and left I_L (d) circularly polarized light. The sum is shown in (a). (b) Measured (dots) and calculated (lines) band dispersion. The dot size indicates the extracted intensities for I_R (blue) and I_L (red). (e,f) Energy distribution curves for I_L and I_R and corresponding CD (in (f)). The circles represent the experimental data and the lines are the corresponding fits. To the left of the Weyl node (f), only two peaks are observed, while to the right of the crossing point (f), three peaks are found, assigned to the bands v_-, v_+ and c_-. *This figure has already been published in [87].*

To further elaborate on this aspect, the band structure along k_x across a W_2 Weyl cone at $k_y = +0.04\,\text{Å}^{-1}$ is shown in Figs. 5.6 (d). The lower part of the cone is spanned by v_+ and the upper part by c_-, both showing a sign reversal of $\langle L_x \rangle$ at the Weyl node. In other words, the Weyl cones in TaAs appear as crossings of bands from different OAM manifolds. This can nicely be seen in the calculation in Fig. 5.6 (e), where just the band v_+ and c_- are plotted and both bands show an opposite OAM sign over the entire width of the bulk Brillouin zone. The CD in Fig. 5.6 (d) closely reflects the calculated OAM texture of the valence band branches v_+ and v_-, both of which change their OAM-sign by passing the Weyl-node. This is further visualized by EDC left and right from the band crossing point, which directly reveal this sign change.

To take a closer look at the Weyl-cone dispersion and the OAM of the bands forming the cone, namely v_+ and c_-, Figs. 5.7 (a-d) show the same cut

on a smaller energy and k_x-range. It is directly evident that the individual branches are selectively probed by opposite light helicities: For right circularly polarized light (Fig. 5.7 (c)) there is a high photoemission intensity for the left branch of v_+. The right branch is on the other hand suppressed for I_R but has a high intensity using left circular light polarization (Fig. 5.7 (d)), which in turn suppresses the left branch of v_+. This characteristic behavior is summarized in Fig. 5.7 (b), showing the band dispersion, which has been extracted from the experimental data by fitting several EDC by a sum of gaussian profiles and a linear background multiplied by a Fermi-Dirac distribution. The dot size indicates the intensities and therefore represents the CD, which is in good agreement with the calculated OAM. Energy distribution curves at two exemplary parallel momenta slightly left and right from the Weyl node are shown in Figs. 5.7 (e) and (f), respectively. It is directly evident that for $k_x = -0.45\,\text{Å}^{-1}$ there are three peaks in the spectra, which can be attributed to the branches v_-, v_+, and c_-. Accordingly, also the upper part of the Weyl cone c_- is probed and shows an opposite CD compared to v_+ in agreement with the calculated OAM. Spectra at $k_x = -0.53\,\text{Å}^{-1}$ are in contrast better described by a two-peak structure representing the valence band branches v_+ and v_-. From the calculation, one would expect that also at this parallel momentum c_- can be seen, in this case with an enhanced intensity for I_L. This discrepancy can most likely be explained by the fact that the energy difference of v_+ and c_- on the left side of the Weyl cone ($\Delta E_{-0.53\,\text{Å}^{-1}} \approx 60\,\text{meV}$) is much smaller compared to the right side ($\Delta E_{-0.45\,\text{Å}^{-1}} \approx 125\,\text{meV}$). The experimental energy resolution of $\sim 90\,\text{meV}$ already limits the resolvability of the two states. Besides the mere energy resolution in the experimental setup additional energy broadening appears as a result of a finite $k_\parallel$-resolution $\Delta k_\parallel \approx 0.06\,\text{Å}^{-1}$, k_z-broadening due to damping of the final state wave function as well as intrinsic lifetime broadening. Moreover, a momentum-dependent intensity drop towards the Fermi level can be observed for the downward-dispersing branch of the Weyl-cone (Fig. 5.7 (d)). Altogether, these circumstances prevent a possible observation of the sign change between v_+ and c_- on the left side of the Weyl-cone. Nevertheless, there is an overall excellent agreement between the CD and calculated OAM in the bands forming the Weyl-cone.
Taken together, the experimental and theoretical findings show that the Weyl cones are crossing points of bands with opposite OAM signs (Figs. 5.7). When passing the Weyl node along a momentum path k_x, the OAM component $\langle L_x \rangle$ parallel to the momentum changes its sign. This behavior leads to the formation of a characteristic checkerboard pattern in the momentum distribution of $\langle L_x \rangle$ (Fig. 5.6 (b)), which could be clearly confirmed by the CD measurements (Fig. 5.6 (a)).

5.1.4 Topological Winding of OAM and Berry Curvature

The question comes up, whether these OAM-related properties of the Weyl fermions in TaAs are linked to the non-trivial topology in the system. Based

on the general theory of Weyl semimetals (see Chapter 2.2), the latter manifests itself in a non-trivial winding of the Berry curvature $\mathcal{B}$ around the Weyl node (see Figs. 5.8 (c,d)). Interestingly, recent studies predicted an intrinsic connection between BC and OAM [198]. This relation is based on the so-called *modern theory of polarization* delineating an orbital magnetization [62], which can be considered as the OAM $\mathcal{L}$ of a delocalized Bloch state. By definition, $\mathcal{L}$ and $\mathcal{B}$ are (anti)-parallel and the orbital magnetization thus directly reflects the topology of a system.
First, it is worth comparing the OAM texture around the Weyl points with the momentum-dependent BC in the bands forming the Weyl cones. Therefore, constant energy cuts of the measured CD, the OAM $\langle L_x \rangle$, and the x-component of the BC $\mathcal{B}_x$ are compared in Figs. 5.8 (a-c), respectively. The contour at this energy ($E - E_\mathrm{F} = -0.2\,\mathrm{eV}$) reflects solely the lower part of the Weyl cones v_+ (compare Fig. 5.7) and has no further contribution from trivial bands, i.e., v_-. Indeed one finds that the calculated momentum texture of $\mathcal{B}_x$ resembles the characteristics of the OAM and the CD around the Weyl point pair. This qualitative comparison provides evidence that the local OAM, which in turn can be addressed by CD, indeed reflects the non-trivial topology of the Berry-flux monopoles in TaAs. In order to examine the topological character in more detail, it is necessary to go beyond the previous considerations and analyze the complete three-dimensional momentum-space configuration of BC and OAM. This can be done very precisely at the theoretical level, as discussed further below. Fig. 5.8 (d,e) show the momentum textures of the BC as well as of the OAM, respectively, on a sphere with a radius $0.03\,\mathrm{Å}^{-1}$ around a W_2 point. It is directly evident that the BC (Fig. 5.8 (d)) forms a hedgehog-like structure, with all arrows pointing away from the Weyl point, revealing the latter to be a source of Berry-flux. To prove this mathematically, a stereographic projection onto a plane has been performed, in which the so-called Pontryagin index χ can be calculated

$$\chi = \frac{1}{4\pi} \int \mathbf{n} \left[\frac{\partial \mathbf{n}}{\partial x} \times \frac{\partial \mathbf{n}}{\partial y} \right] dxdy, \tag{5.2}$$

where $\mathbf{n}$ is a unit vector of the field and the integral is taken over the sphere. χ characterizes the topological charge of the respective point in momentum space and is proportional to the Berry phase accumulated by an electron encircling this point [87]. Unlike the orbital magnetization $\mathcal{L}$, OAM and BC are not completely parallel aligned (see discussion below). Nevertheless, both share a non-trivial winding number $\chi = 1$ around the Weyl point shown in Fig. 5.8 (d,e). The OAM momentum space texture can therefore be considered as a distorted hedgehog and this, in turn, implies that its field configurations can be adiabatically transformed into BC-like hedgehog without changing the topological invariant. Moreover, the sign of the Pontryagin index changes when the other Weyl point of the pair is considered and it vanishes at all k-points except at the Weyl nodes themselves [87]. From this analysis, it is clear that in the WSM TaAs, the topology is indeed manifested in the momentum space texture of the local OAM $\langle L \rangle$, which in turn is accessible by CD-ARPES.

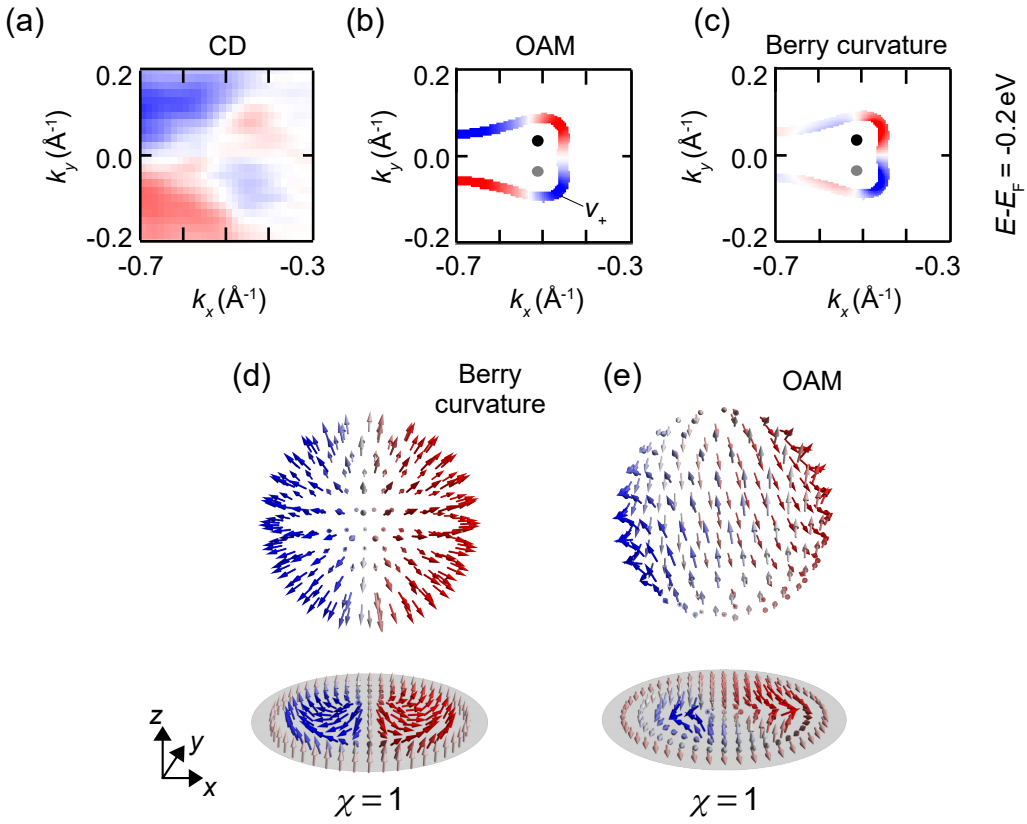

FIGURE 5.8: Topological winding of OAM and Berry curvature. (a-c) Constant energy cuts integrated over an energy range from $-0.16\,\text{eV}$ to $-0.24\,\text{eV}$. The contour corresponds to the band forming the lower part of the Weyl cone v_+. CD (a), $\langle L_x \rangle$ (b), and the x-component of the Berry curvature $\mathcal{L}_x$ (c) show a qualitatively similar modulation around the Weyl point pair. (d,e) Three-dimensional field configuration and the corresponding azimuthal equidistant projections of Berry curvature (d) and OAM (e) calculated on a small sphere around a Weyl point. Both textures are characterized by a non-trivial Pontryagin index of $\chi = 1$. *These figures have already been published in [87].*

Interestingly, the calculations show that the Pontryagin index of the SAM field configuration is zero ($\chi = 0$, see Appendix A.3). That means, the SAM doesn't wind around the Berry-flux monopoles in TaAs and the topological character of the latter derives only from the orbital degrees of freedom, i.e., the OAM.

5.1.5 Discussion and Outlook

The formation of OAM relies on the broken inversion symmetry in the crystal structure of TaAs, while the formation of SAM is secondary due to the additional presence of SOC. This OAM-based microscopic origin of SOC-induced spin splittings has been previously discussed only in the context of surface states or more general two-dimensional systems [37, 48, 49, 51–56, 64], as detailed in the previous chapter. The findings on TaAs directly demonstrate that the paradigm is moreover applicable to three-dimensional

bulk systems with broken inversion symmetry. As such, it also underlies the physics of non-magnetic WSM at the microscopic level [87]. Based on the combined experimental and theoretical results, shown in the previous section, i.e., the parallel OAM alignment in the different spin-branches, it is evident that the energy scale associated with ISB E_{ISB} clearly dominates over E_{SOC}. This means that the weaker SOC does not lead to a significant magnitude of interband matrix elements in the Hamiltonian and the electronic states can be classified in terms of their OAM, i.e., each bulk band in TaAs contains to a specific OAM manifold. As a consequence, the Weyl cone denotes a crossing of bands with different OAM signs indicating an orbital-symmetry band inversion (see Fig. 5.6 (e)), which determines the topology in the system. This underlines the theoretical prediction by Weng *et al.*, that the non-trivial topology in the TaAs family arises from a band inversion between bands of different orbital symmetries [76]. The observed OAM and CD pattern is a combined footprint of the broken inversion symmetry and the band inversion, the two mechanisms spanning the WSM phase diagram (cf. Chapter 2, Fig. 2.8).

Taken together, it appears that the local OAM reflects the topological properties of the BC in TaAs. On the one hand, this directly underlines theoretical predictions for the use of CD-ARPES as a tool to probe the BC [198]. On the other hand, however, the present results go beyond and prove that the orbital magnetization $\mathcal{L}$ is in principle not directly related to the local OAM since the latter in turn has not exactly the same field configuration. Nevertheless, from the point of view of topology, the Hamiltonian governing the OAM texture in TaAs is fully equivalent to a Weyl-like Hamiltonian leading to a hedgehog-like monopole field.
The Hamiltonian linearized around a Weyl point $\boldsymbol{k}_W$ is in first order determined by the matrix elements arising from ISB $H_{\mathrm{ISB}}(\boldsymbol{q} = \boldsymbol{k} \pm \boldsymbol{k}_W)$, which presumably has the largest magnitude of the full TaAs Hamiltonian. This causes an OAM momentum space texture as shown in Fig. 5.8 (b,e). The non-trivial OAM winding allows for an adiabatic transformation into a Weyl-like Hamiltonian with a linear relation between OAM $\boldsymbol{L}$ and momentum $\boldsymbol{q}$:

$$H_{\mathrm{ISB}}(\boldsymbol{q}_\pm) \xleftrightarrow{\text{adiabatic}} H_W(\boldsymbol{q}_\pm) = \chi(\boldsymbol{L} \cdot \boldsymbol{q}_\pm), \tag{5.3}$$

where $\chi = \pm 1$ is the Pontryagin index (Eq. 5.2) and $\boldsymbol{q}_\pm$ denote the momenta of two Weyl points of a pair around a mirror plane. $H_{\mathrm{ISB}}(\boldsymbol{q})$ and $H_W(\boldsymbol{q})$ are thus equivalent in terms of topology and the OAM texture obtained by CD provides a direct signature of a Berry-flux monopole.
Two scientific questions remain open at this point: First, how are the local OAM $\langle L \rangle$ and the orbital magnetization $\mathcal{L}$ related? And second, how universal is the OAM-winding found in TaAs? In order to tackle these questions, other WSM have already been investigated by our theory collaborators. It turns out that the OAM winding is in fact not a universal feature (in contrast to $\mathcal{L}$ that universally winds around the WP). Instead, there are other WSM such as strained HgTe or BiTeI under high pressure, in which the OAM does

not wind. On the other hand, TaAs was also not the only compound for which a non-trivial winding around the WP has been found. For instance, in the WSM LaAlGe the OAM monopole winding could be confirmed [87]. Yet, under which conditions the winding occurs or not remains an open question at this point. Further theoretical as well as experimental investigations on a broad material base are required to resolve these issues.
Returning to the case at hand. The role of SOC in TaAs is of important but rather perturbative character. It is implicit in the present picture (Eq. 5.3) and shifts the Weyl cones at $\boldsymbol{q}_{\pm}$ away from the mirror planes $k_x k_z$ and $k_y k_z$. With that, SOC separates two Weyl fermions of opposite chirality χ in momentum space. In this regard, the extreme scenario ($E_{\mathrm{SOC}} = 0$) can be considered as a case in which two Weyl fermions of opposite chirality coincide at the same point in momentum space within a mirror plane, i.e., the total chirality sums up to zero. Such a treatment implies a non-Weyl-like but yet topological character of TaAs even without SOC, and SOC in turn simply transforms the system into the Weyl state. This interpretation is consistent with previous analysis of the bulk [76] as well as of the surface electronic structure [114] of Ta(As,P). Studying this disparate topological phase with regard to OAM and ISB might be an interesting task for future theoretical investigations, in which SOC can be artificially switched off. On the experimental side, it might be interesting to examine the related TMMP NbP where the SOC strength is sufficiently weak that it can be neglected in the first approximation.

Outlook: Experimental Access to the Other OAM-Components

The results shown in this Chapter have demonstrated that the CD in the experimental setup used is sensitive to the OAM component $\langle L_x \rangle$ in the initial state. However, the DFT calculations revealed a complex three-dimensional winding of the OAM around the WP, which leads directly to the question of whether signatures might also be found experimentally in the other components. Possible indications and further perspectives will be briefly discussed in this section.

Again, when the plane of light incidence corresponds to the xz-plane in the experimental setup, the electric field vector for circularly polarized light is $\boldsymbol{E}_{\pm} = (\mathcal{E}_x, \pm i\mathcal{E}_y, \mathcal{E}_z)$. Without any further assumptions, the photoemission intensity is

$$I_{\pm} \propto |T_x|^2 + |T_y|^2 + |T_z|^2 + 2\Re(T_x^* T_z) \pm 2\Im(T_x^* T_y) \pm 2\Im(T_y^* T_z), \tag{5.4}$$

with the matrix elements $T_{x,y,z} = \langle f | \, \mathcal{E}_{x,y,z} \, | \Psi \rangle$. The resulting CD reads

$$\mathrm{CD}(k_x, k_y) \propto 4\Im(T_x^* T_y) + 4\Im(T_y^* T_z). \tag{5.5}$$

The first term is linked to $\langle L_z \rangle$ and the second term to $\langle L_x \rangle$ and they are weighted by the angle of light incidence $\tan(\vartheta) = \frac{\mathcal{E}_x}{\mathcal{E}_z}$. This is directly related to the statement that CD is sensitive to the OAM component $\langle L_p \rangle$ pointing in the direction of light propagation $\boldsymbol{k}_p$ [48, 88]. In the present experimental

geometry, there is $\vartheta = 17^\circ$, giving $\mathcal{E}_z \approx 3\mathcal{E}_x$ and consequently a major contribution of $\langle L_x \rangle$ to the CD.
It becomes directly evident that the current setup would need to be drastically modified in order to be more sensitive to the out-of-plane OAM $\langle L_z \rangle$. Since changing the angle of light incidence is rather not realistic, one would have to look for other SX-ARPES endstations with $\vartheta > 45^\circ$ to achieve $\mathcal{E}_x > \mathcal{E}_z$.
In contrast, more realistic might be to get access to the other in-plane component $\langle L_y \rangle$. Although there is no term in Eq. 5.5 which is sensitive to this component, one can make use of the 4-fold rotation symmetry of the TaAs sample around the z-axis. Hence, another two WP pairs exist close to the k_y-axis equivalent to the WP pair at k_x considered so far. One can thus consider the OAM $\langle L_x \rangle$ around k_y instead $\langle L_y \rangle$ near k_x. The results are presented in Fig. 5.9. Panel (d) shows the calculated OAM pattern ($\langle L_x \rangle$) around k_y. The WP at $k_y = \pm 0.51\,\text{Å}^{-1}$ are marked by the grey and black dots. Clearly, also here a sign change occurs in a small k area around the W_2 points. As shown in Fig. 5.9 (b), this sign change cannot be observed in the experimental data. However, a small intensity dip near the position of the WP can be found. This is also seen in the band structure cut along k_y shown in Fig. 5.9 (a) and more quantitatively in the MDC in Fig. 5.9 (e), marked by the arrow in both cases. The question is, whether this intensity variation is related to the OAM sign change and why no complete sign change in the CD can be observed. A possible explanation might be the strong k_z-dependency of this OAM-signature. As can be seen in Fig. 5.9 (c,e), already by changing k_z from $0.32\,\text{Å}^{-1}$ to $0.30\,\text{Å}^{-1}$, the sign change vanishes in the calculation. This makes it more difficult to observe this subtle effect experimentally. In particular, the exponential damping of the final state wave function causes an intrinsic broadening of the out-of-plane momentum $\Delta k_z = \lambda^{-1}$, where λ corresponds to the inelastic mean free path. Taking the universal curve as a first approximation, one gets $\lambda(590\,\text{eV}) \approx 13\,\text{Å}$, resulting in a k_z-broadening of $\Delta k_z \approx 0.077\text{Å}^{-1}$. This is considerably larger than the k_z range in which the OAM sign change can be observed. Therefore, as this rough estimate shows, it might simply not be possible to observe such a strongly k_z-dependent effect with SX-ARPES. It is important to note that the broadening effect is not related to experimental energy or momentum resolution, but is an intrinsic physical effect. Nevertheless, despite these differences, there is overall good agreement between CD and calculated OAM, as shown in particular by the quantitative k_y dependence in Fig. 5.9 (e). This provides evidence that the observed intensity variation is indeed related to the change of $\langle L_x \rangle$ around the W_2 points, but less pronounced due to the k_z broadening.
In summary, the 4-fold rotational symmetry of the TaAs crystal structure allows to addressing not only the OAM component parallel to the wave vector but also the component perpendicular to $\boldsymbol{k}_\parallel$. Also in this component characteristic changes appear around the WP. Yet, these sign changes are more subtle and consequently more difficult to confirm experimentally. Future experiments could include, for instance, a systematic photon-energy-dependent study. This would on the one hand deepen the understanding of final-state

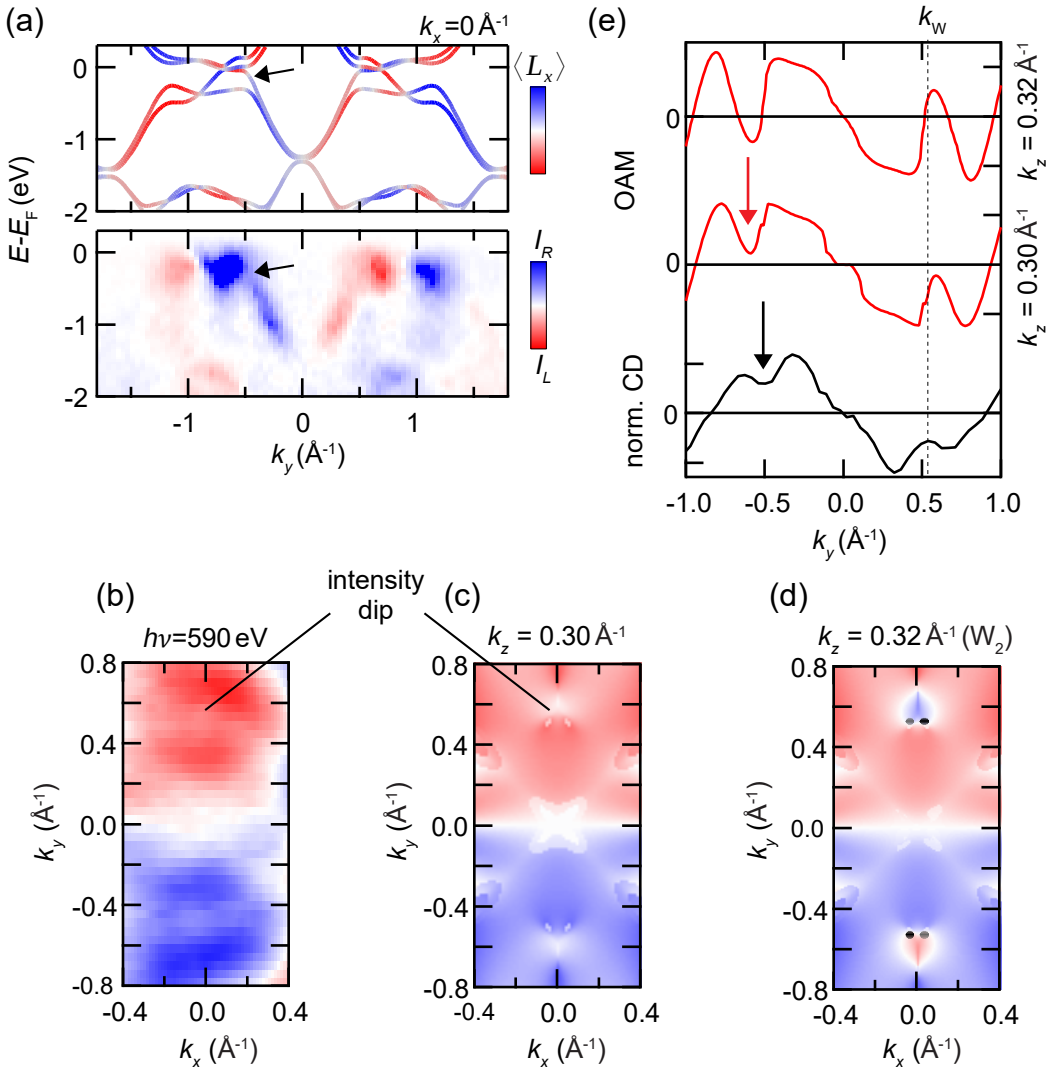

FIGURE 5.9: Characteristics of the in-plane OAM component perpendicular to the wave vector and CD around the W_2 Weyl points. The Weyl point pairs marked in (d) around the k_y-axis ($k_x = 0$) are considered. (a) Measured CD and $\langle L_x \rangle$-projected band structure cut $E(k_y)$ at $k_x = 0\,\text{Å}^{-1}$ and $k_z = 0.59\,(2\pi)/c$ corresponding to the W_2 k_z-plane. Data sets in (b-e) were integrated over the bandwidth of $v_\pm$, i.e., from 0 eV to -1.2 eV. (b-d) Momentum distribution of the CD (b) and $\langle L_x \rangle$ (c,d). The calculated OAM sign change close to the Weyl point pairs (d, $k_z = 0.32\,\text{Å}^{-1}$) appears only in a small k_z range and vanishes at $k_z = 0.30\,\text{Å}^{-1}$ (c). (e) Momentum distribution curves of the calculated OAM $\langle L_x \rangle$ (upper two panels, for different k_z) and normalized CD (lower panel). Arrows in (a,e) indicate the intensity dips of OAM and CD close to the Weyl point momenta k_W. *This figure has already been published in [87].*

effects on the observed CD pattern, but moreover to study the k_z-dependent in-plane OAM texture.

5.2 Summary and Conclusion

The momentum-dependent behavior of the electronic wave function, i.e., the spin and orbital texture, has been studied in a paradigmatic Weyl semimetal TaAs by means of SX-ARPES combined with circular dichroism and spin-resolved measurements. This goes beyond previous approaches, in which only the bulk band dispersion has been investigated [77–81]. In agreement with these studies, it is shown that ARPES performed at photon energies in the range of 400...700 eV is predominantly sensitive to the bulk bands of TaAs. Compared to lower photon energies in the VUV range, the probing depth λ is increased and this in turn directly accompanies with a decreased broadening of the out-of-plane momentum $\Delta k_z = \lambda^{-1}$. Moreover, the final-state wave function becomes more free-electron-like [202–205], which tends to reduce strong final-state-induced modulations of the photoemission matrix elements. Most measurements were conducted at a photon energy of 590 eV, which was shown to correspond to an equi-k_z-plane ($k_z \approx 23.4\,\frac{2\pi}{c}$) in which the W_2 Weyl points lie. Thus, the $\boldsymbol{k}_{\parallel}$-resolved spin and orbital texture around the WP can be studied. Spin-resolved measurements systematically reveal a spin-polarization of the bulk valance bands forming the Weyl cones in agreement to the calculated spin texture. For the first time, the spin-polarization of the bulk bands could be demonstrated experimentally in a paradigmatic WSM of the transition metal monopnictides class.

Photoemission intensities for measurements taken with left- and right-circularly polarized light show a strong selectivity of the exited states in bulk band structure. The observed circular dichroism pattern impressively matches the calculated orbital angular momentum in the initial state, more precisely its x-component $\langle L_x \rangle$. Several OAM sign changes in the entire Brillouin zone are reproduced in the experimental data, which provides strong evidence for a relation between OAM and CD, as proposed in previous studies [48, 88]. The OAM in TaAs relies on the broken inversion symmetry in the crystal structure and its existence is independent of the presence of SOC [87]. This suggests a direct applicability of the model discussed in Chapter 4 for two-dimensional systems to three-dimensional bulk states. An OAM-based origin of spin-orbit splittings is thus not limited to the Rashba effect. The latter is only a special case in which ISB occurs in a polar fashion at the surface, while the model seems to be more universal and likely applies to any system with broken inversion symmetry. The spin-split valance band branches in TaAs carry the same OAM-sign, proving that the energy scale associated with ISB is considerably larger than the SOC-strength. From a perturbation theory point of view this means that SOC – acting as a small perturbation – does not significantly modify the eigenstates in the WSM. The contribution of ISB is instead strong and the eigenstates can be classified in terms of their ISB-induced OAM.

Accompanied by a topological band inversion, the interplay of ISB and SOC forms the central physical mechanism of the topology in non-magnetic WSM. Considering the band inversion transition between topologically trivial and non-trivial insulators, ISB opens a second dimension in the phase diagram,

generally causing the WSM phase to appear. This suggests that ISB also leaves topological footprints in the momentum-dependent orbital texture. It is indeed found – in excellent agreement between DFT and CD – that the wave functions around the WP is strongly modified. The OAM forms a characteristic checkerboard pattern around them, which is manifested by two sign changes. On the one hand $\langle L_x \rangle$ is invariant under mirror symmetry $y \rightarrow -y$ causing a sign change between $+k_y$ and $-k_y$, i.e., when a WP of opposite chirality is considered. Moreover $\langle L_x \rangle$ changes its sign by passing the Weyl node along k_x. In particular this effect is rather important as it is not enforced by any symmetry but rather represents an orbital symmetry inversion of the bands forming the Weyl cones. In TaAs, the latter are crossing points of bands with opposite OAM, which is related to the topology in the system. In a deeper theoretical consideration, it can be shown that the three-dimensional field configuration of the OAM winds around the WP – from a topological point of view just like the BC does – and therefore represents a monopole or anti-monopole texture. Signatures for this monopole texture are experimentally accessible directly through the CD.
More broadly, even beyond WSM the results presented in this chapter demonstrate that CD-ARPES can provide an experimental access to BC. On the one hand, this underpins previous studies that have suggested such a link [198]. On the other hand, it also directly shows that the connection of the BC $\mathcal{B}$ and the local OAM $\langle L \rangle$ is less stringent in contrast to the orbital magnetisation $\mathcal{L}$. This must therefore be taken into account in each material system studied. Further broad theoretical as well as experimental investigations are necessary to understand this interconnection more deeply.

Chapter 6

Conclusion

In this thesis, the interplay of spin-orbit coupling (SOC) and inversion symmetry breaking (ISB) in crystalline solids is studied using angle-resolved photoelectron spectroscopy (ARPES). Two solid-state systems whose electronic structure is fundamentally affected by this interplay are investigated: two-dimensional Rashba-type spin-split surface states and the three-dimensional bulk band structure of the paradigmatic Weyl semimetal TaAs. The focus is particularly on the impact of ISB on the momentum dependence of the Bloch wave functions, i.e., on the orbital texture of the spin-split electronic states. This aspect has – in contrast to the role of SOC – not yet been investigated in detail experimentally.
Before discussing the main results of this work, it is useful to recall the key underlying physical aspects. A spin-split electronic band structure can commonly be expressed by a Hamiltonian in which ISB and SOC enter via two independent terms H_{ISB} and H_{SOC}:

$$H = H_0 + H_{\mathrm{ISB}} + H_{\mathrm{SOC}} \tag{6.1}$$

SOC is usually well described by a local atomic Hamiltonian $H_{\mathrm{SOC}} \propto \lambda_{\mathrm{SOC}} \boldsymbol{L} \cdot \boldsymbol{S}$. The k-independent energy scale of this term is given by the atomic SOC-strength $\langle H_{\mathrm{SOC}} \rangle = E_{\mathrm{SOC}} \propto \lambda_{\mathrm{SOC}}$. Both the orbital angular momentum $\boldsymbol{L}$ and the spin angular momentum $\boldsymbol{S}$ are not independent and thus are no longer good quantum numbers. The eigenstates have mixed spin and orbital character and are rather eigenfunctions of the total angular momentum operator $\boldsymbol{J} = \boldsymbol{L} + \boldsymbol{S}$. The influence of ISB is different from that of SOC. Obviously, ISB alone cannot couple to the spin sector but strongly influences the orbital part of the wave functions, i.e., the OAM. Similar to the spin, time-reversal and inversion symmetry imply $\langle \boldsymbol{L} \rangle_{\boldsymbol{k}} = -\langle \boldsymbol{L} \rangle_{-\boldsymbol{k}}$ and $\langle \boldsymbol{L} \rangle_{\boldsymbol{k}} = \langle \boldsymbol{L} \rangle_{-\boldsymbol{k}}$, respectively [61]. Consequently, in non-magnetic inversion symmetric systems, the OAM is quenched in each state. Nevertheless, for states at finite $\boldsymbol{k}$, or more precisely at $\boldsymbol{k}$ that are no time-reversal invariant momenta, ISB can induce a finite $\langle \boldsymbol{L} \rangle$. The energy scale associated with ISB $E_{\mathrm{ISB}}(\boldsymbol{k}) = \langle H_{\mathrm{ISB}} \rangle$ is generally k-dependent (in contrast to the local SOC Hamiltonian), and ISB causes a momentum-dependent orbital texture.
Finally, the combination of ISB and SOC can induce a spin-splitting as well as a finite spin polarization (spin angular momentum) $\langle \boldsymbol{S} \rangle$. However, the electronic states can still have nonzero OAM expectation values, and if ISB dominates over SOC, they are actually approximated to be eigenstates of the

OAM [37, 48]. The key physics in both Rashba systems and non-magnetic Weyl semimetals is usually an interplay of the two terms. In the present thesis, both systems are discussed in terms of the individual and combined contribution of SOC and particularly ISB.

It becomes apparent that especially the orbital degrees of freedom of the Bloch wave functions are decisively influenced by ISB. Consequently, k-resolved experimental access to the latter is required and ARPES provides the ideal method for this purpose: In particular, light-polarization-dependent measurements allow to address the momentum space orbital texture. Moreover, linear- and circular dichroism (LD and CD) can be used to study the OAM, as discussed in detail in this work. This approach is thus complementary to spin-resolved ARPES, which is commonly used to address the spin angular momentum $\langle S \rangle$.
In conclusion, this work provides direct experimental hints that ISB can lead to the formation of OAM. This mechanism is discussed for two different types of systems, namely two-dimensional surfaces states and a three-dimensional Weyl semimetal. Moreover, it turns out that this mechanism plays a crucial role for the underlying physics in both systems: In the AgTe surface states, it acts as a precursor for the surface Rashba effect, and in the Weyl semimetal TaAs, it determines the topology of the bulk band structure.

A honeycomb monolayer of AgTe on Ag(111) provided a suitable model system for the formation of OAM in Rashba-type spin-split surface states. Well-ordered AgTe films were prepared by epitaxial growth of Te on a clean Ag(111) surface. Sharp LEED diffraction spots and narrow photoemission line widths in the surface states suggested an excellent surface quality. As obtained by ARPES and two-photon photoemission experiments and further supported by DFT band structure calculations, the low-energy electronic structure is determined by two completely filled hole-like bands mainly built from Te-p_{xy} orbitals as well as an electron-like dispersing sp_z-state above E_F. The s-p_z hybridization likely results from the incorporation of the Te atoms in the Ag(111) surface, as explained by a simple one-dimensional adsorption model.
High-resolution ARPES measurements revealed a Rashba-type spin-splitting in the lower valence band β with a Rashba parameter of $\alpha_R = 0.88\,\text{eVÅ}$. This is further supported by an almost entirely helical Rashba-type spin texture obtained from the DFT calculations. In the upper valance band, in contrast, the Rashba effect vanishes completely. Such a contradicting behavior has been predicted in a theoretical model [48], which states that the Rashba effect relies on the formation of a helical OAM texture caused by ISB [47–50]. Within a model consideration, the ISB part of the Hamiltonian in AgTe can be written as

$$H_{\text{ISB}}^{\text{AgTe}} = \tilde{V}_{sp_z} a t_{sp} \cdot \boldsymbol{L}(\boldsymbol{z} \times \boldsymbol{k}) \quad , \tag{6.2}$$

and is exactly in the form of a proposed *Orbital Rashba effect* [48, 62, 63], yielding an OAM analog of the spin Rashba effect. In this scenario, the eigenstates can be classified in terms of their helical (tangential) OAM $\langle L_t \rangle = \{-1, 0, 1\}$. The driving forces for the effect in AgTe are the s-p_z hybridization strength

$\tilde{V}_{sp_z}$ as well as the in-plane nearest-neighbor hopping t_{sp} between the two sublattices in the honeycomb structure. Since the latter scales the bandwidth, the energy scale associated with ISB is likely large in AgTe, i.e., $E_{\mathrm{ISB}} \gg E_{\mathrm{SOC}}$. This argument justifies neglecting interband SOC effects to a first approximation, and the Rashba effect occurs only in the two bands with chiral OAM and vanishes in the band with $\langle L_t \rangle = 0$.
Evidence for these model assumptions is found in the real AgTe band structure. DFT calculations reveal the expected OAM texture, particularly a vanishing in-plane OAM in the band with vanishing Rashba splitting and vice versa a helical OAM structure in β. This is corroborated experimentally through the linear dichroism, which is possibly sensitive to the in-plane OAM. While experiments on other materials support this statement, the relationship between LD and OAM has yet to be confirmed by a deeper theoretical consideration. However, another important hint for the validity of the OAM-based Rashba effect in AgTe emerges when considering the in-plane orbital texture. A key observation is that the OAM-carrying bands have a radial in-plane p-orbital character, whereas the band with vanishing OAM and thus vanishing Rashba spin-splitting is built from tangentially aligned p-orbitals. This connection arises fundamentally from the underlying symmetries, i.e., full rotational symmetry, out-of-plane ISB, and the associated hybridizations that lead to the formation of the OAM. The DFT calculations as well as the ARPES data directly reveal this orbital character in AgTe. ARPES measurements with variable linear light polarization give detailed information about the orbital symmetries and allow a momentum-resolved mapping of the wave function character. More precisely, radial and tangential orbital textures can be distinguished on the basis of the respective photoemission intensity distribution. Overall, this provides strong experimental and theoretical evidence for the correctness of the OAM-based Rashba paradigm, for which AgTe/Ag(111) is a perfect model system.

Based on these findings, one can also extrapolate to material systems, which are rather placed in the strong SOC limit by continuously increasing SOC in a model-like manner. Due to interband SOC matrix elements, bands from different OAM manifolds become no longer separated but rather mix up. Based on the orbital symmetry analysis in AgTe, it becomes evident that this is directly accompanied by the mixing of states with radial and tangential orbital character. This is reported in several previous studies – indeed as an effect of strong SOC – whereby the impact of ISB was not discussed at all [133, 161, 174, 193]. The present findings show that not only SOC but rather the interplay between SOC and ISB has to be considered to understand both orbital and spin structure. The previous results can thus be viewed from a different angle. Moreover, the presented approach demonstrates that although SOC-induced spin-orbit entanglement generally occurs, it can be suppressed when ISB becomes predominant. Thus, increasing ISB could provide a generic mechanism for generating spin-split electronic states with large absolute spin polarization, which is generally limited by strong SOC [132].

In the second part of the thesis, presented in Chapter 5, the three-dimensional bulk electronic structure of a non-magnetic Weyl semimetal TaAs is studied by means of soft X-ray photoelectron spectroscopy, combined with circular dichroism and spin-resolved measurements. The main focus was on the investigation of the momentum-dependent spin and orbital texture of the bands forming the Weyl cones, i.e., giving rise to the Berry curvature monopoles. For the first time, the spin polarization of the bulk bands in TaAs, essential for the Weyl physics, has been experimentally demonstrated in good agreement with DFT calculations.
The observed circular dichroism pattern is compared to the calculated OAM texture, which shows remarkable agreement for the $\langle L_x \rangle$ component in the experimental geometry used. The comparison between theory and experiment by itself shows conclusively that the measured CD directly reflects the OAM in the initial state. The formation of OAM relies on ISB, demonstrating that the OAM-based origin of spin-orbit splittings is not restricted to two-dimensional Rashba systems but is – as shown here – applicable to three-dimensional bulk states. As such, it moreover underlies the Weyl physics at the microscopic level. Parallel alignment of the OAM in the spin-branches of the bands directly suggests that the energy scale associated with ISB is larger than that of SOC. The latter acts as a perturbation to the full Hamiltonian, and the electronic states in TaAs can therefore be classified in terms of their OAM.
Considering the role of OAM in the Weyl physics in TaAs, the momentum-dependence of CD and OAM near the W_2 Weyl points has been analyzed in more detail. It turns out that the OAM is strongly modulated close to the monopoles. In particular, it is shown that the Weyl points in TaAs denote crossing points of bands with opposite OAM signs. This is a combined footprint of the topological band inversion and the broken inversion symmetry, together spanning the phase diagram in which the WSM phase occurs (cf. Chapter 2.2, Fig. 2.8) [69–72]. ISB determines the OAM texture, which has been shown in a detailed theoretical analysis to reflect the topological winding of the wave function. That is, the non-trivial behavior of the Berry curvature (BC) manifests itself in the momentum dependence of the OAM. Although OAM and BC are not entirely parallel aligned, the OAM field configuration around the WP constitutes an (anti)-monopole, as shown in the DFT calculations. The observed CD pattern, in turn, is a direct experimental signature of such a momentum-space 'magnetic' monopole.

Fig. 6.1 summarizes schematically key features of spin-split electronic states, as deduced from the experiments in this thesis. The interplay of ISB and SOC – that causes the formation of spin-polarized states – has been investigated in two-dimensional surface states and a three-dimensional bulk system. In both cases, this interplay underlies the key physics in the system, i.e., the Rashba effect and the Weyl physics, respectively. It is shown that the breaking of inversion symmetry itself has an important impact; it leads to the formation of OAM in the wave function, denoting a prerequisite for the lifting of spin-degeneracy by SOC. The resulting momentum-space OAM texture plays a

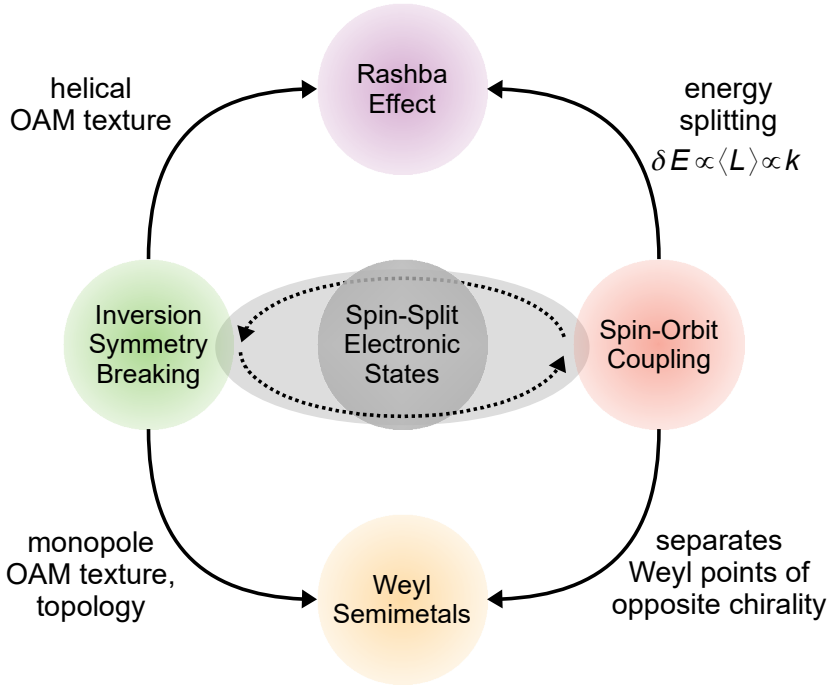

FIGURE 6.1: The interplay of inversion symmetry breaking and spin-orbit coupling leading in general to the formation of spin-polarized electronic states has been investigated in two types of spin-split electronic structures: First, two-dimensional Rashba-type spin-split surface states and second, three-dimensional Weyl semimetals.

decisive role: In surface states, the helical OAM alignment – one could call it *orbital-momentum-locking* – is a direct precursor for the formation of a Rashba-type spin structure, that is, the spin-momentum-locking. In the paradigmatic WSM TaAs, a characteristic OAM texture – reflecting the monopole charge – is formed around the Weyl points, i.e., the Berry curvature monopoles. First of all, this in itself is an important observation in the field of WSM. However, it also shows that CD-ARPES can provide experimental access to the bulk band topology. This approach, in turn, is not necessarily limited to WSM but is likely applicable to a variety of topological quantum materials with broken inversion symmetry, e.g., the two-dimensional quantum spin Hall insulator candidates Bismuthene [142] and Indenene [101] on SiC(0001).
Moreover, the importance of OAM itself as an orbital analog of the electron spin becomes directly apparent. Recent studies predicted orbital analogs of spintronic phenomena leading to the field of so-called *orbittronics* [57–61]. Compared to spin-based devices, materials would not require spin-polarized electronic states and consequently neither magnetism nor SOC but rather a finite OAM. Although the present work does not aim directly in this application-related direction, the insights gained can be beneficial in this field. For example, the analogy between orbital and spin Rashba effect [48, 62, 63] discussed in Chapter 4 is directly related to the analogy between orbital and spin Hall effect [58, 61]. The orbital mechanism represents a precursor in both cases, and SOC translates the orbital effect to a spin effect.

This could be explicitly shown here for the Rashba effect, likely indicating transferability to the orbital and spin Hall effect. In addition, other interesting research issues arise, such as the study of the orbital Hall effect in WSM, i.e., in particular TaAs, in which a large spin Hall conductivity has been theoretically predicted [206]. More broadly, the present work establishes the importance of OAM and ISB in spin-split electronic structures. Furthermore, the findings could be applied to potential quantum materials in which SOC is too small to cause large splittings, but ISB itself could give rise to novel physical phenomena [207–209].

Appendix A

Appendix

A.1 AgTe/Ag(111)

A.1.1 Splitting of α and β at the $\bar{\Gamma}$-point

The bands α and β in AgTe/Ag(111) are split through spin-orbit coupling at $k = 0$. Here, the two states $\alpha_{k=0}$ and $\beta_{k=0}$ are doubly spin-degenerate. In turn, without SOC the resulting state is fourfold-degenerate. The four eigenstates are built only from in-plane p_{xy} orbitals. The p_z orbital is separated by the two-dimensional crystal field (CF) (Fig. A.1 (b)) and moreover hybridizes strongly with the substrate electronic states (see Chapter 4.1.3). The character of the resulting wave functions and the energy of the splitting between $\alpha_{k=0}$ and $\beta_{k=0}$ can be easily understood by considering the atomic SOC-Hamiltonian $H_{\mathrm{SOC}} = (\lambda_{\mathrm{SOC}}/2) \cdot \boldsymbol{LS}$ (see Eq. 2.11). This is reduced at $k = 0$ to the only term that acts on the p_{xy} orbitals, namely $L_z S_z$. Notably, this term has has been neglected in the model consideration in Chapter 4.2.2 since it makes a negligible contribution for higher wave vectors, where E_{ISB} dominates.
Diagonalization results in an energy splitting $\Delta E = \lambda_{\mathrm{SOC}}$ and the eigenstates are

$$\begin{aligned} |\alpha_{k=0}, \pm\rangle &= \frac{1}{\sqrt{2}}\Big(\pm |p_x, \uparrow (\downarrow)\rangle - i\, |p_y, \uparrow (\downarrow)\rangle\Big) \\ |\beta_{k=0}, \pm\rangle &= \frac{1}{\sqrt{2}}\Big(\pm |p_x, \downarrow (\uparrow)\rangle - i\, |p_y, \downarrow (\uparrow)\rangle\Big) \end{aligned} \tag{A.1}$$

For comparison, when all three p-orbitals are considered, i.e., when $\lambda_{\mathrm{CF}} = 0$, all terms in the SOC-Hamiltonian contribute, which gives the conventional $J_{3/2}$-$J_{1/2}$-splitting, as sketched in Fig. A.1 (a). The crystal field instead quenches the contribution of p_z orbitals yielding the wave functions in Eq. A.1.

Since the energy splitting in this case is exactly the atomic SOC constant (of Te in the case of AgTe), the latter can be extracted from the photoemission data. This results in a value of

$$\lambda_{\mathrm{SOC}}^{\mathrm{Te}} \approx 0.36\,\mathrm{eV}.$$

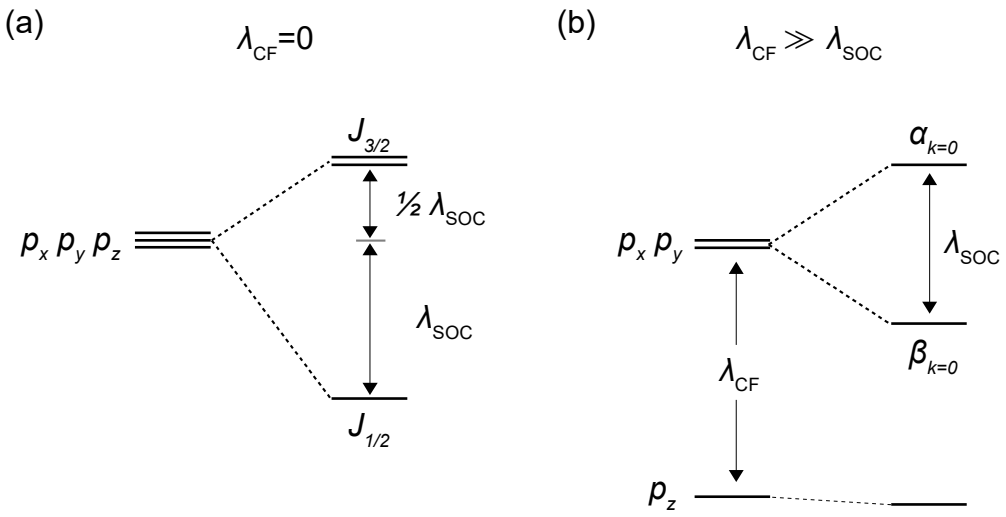

FIGURE A.1: Spin-orbit coupling (SOC) versus crystal field (CF) splitting for a two-dimensional electron system with three p orbitals. Each state (bar) is doubly spin-degenerate. (a) Without crystal field splitting (λCF $= 0$) the three p orbitals are degenerate without SOC and gets split by SOC into a four-fold degenerate $J_{3/2}$ and a two-fold degenerate $J_{1/2}$ state separated by an energy of $3/2 \cdot \lambda_{SOC}$. (b) If CF is large, the p_z orbital gets separated from the p_{xy} orbital manifold and SOC splits the two p_{xy} states in two two-fold degenerate levels, while the p_z state is nearly unperturbed, since $\lambda_{CF} \gg \lambda_{SOC}$.

It is moreover interesting to consider the spatial wave function symmetries of the eigenstates (Eq. A.1). Similarly, $\alpha_{k=0}$ and $\beta_{k=0}$ have mixed p_x and p_y character. On the one hand, this explains the drop of radial-tangential orbital polarization for $k_{||} \rightarrow 0$, as found in both the ARPES data as well as the DFT calculations. On the other hand, this does not explain the different photoemission linewidths of the two features. Given the spatial symmetries, it is rather unexpected that $\beta_{k=0}$ hybridizes more strongly with the Ag-sp bulk bands compared to $\alpha_{k=0}$. The origin of the different quasiparticle hole lifetimes are thus unlikely caused by the different wave function symmetries.

A.1.2 One-dimensional Adsorption Model

The adsorption model presented in Chapter 4.1.3 is based on a one-dimensional chain of atoms with one s-orbital per lattice site. The atoms in the chain represent the layers of the Ag-substrate perpendicular to the sample surface. The projected bulk band is calculated using a tight-binding model of an infinite chain of atoms. The bulk band dispersion along k_z is given by

$$E(k_z) = \epsilon_0 - 2t\cos(k_z d), \tag{A.2}$$

where $d \equiv 1$ is the distance of the atoms and $t = 1\,\text{eV}$ is the nearest neighbor hopping integral between them. The energy offset is (arbitrarily) referred to the band maximum $\epsilon_0 = 2t$.
In order to model the adsorption of a Te atom on the Ag surface, a finite chain

of $N = 8$ atoms has been considered. The Hamiltonian is defined as:

$$\begin{aligned} H =& \epsilon_{\mathrm{Te}} |0\rangle \langle 0| + \epsilon_{\mathrm{SS}} |1\rangle \langle 1| + V(|1\rangle \langle 0| + |0\rangle \langle 1|) \\ &+ \epsilon_0 \sum_{j=2}^{8} |j\rangle \langle j| + t \sum_{j=1}^{8} (|j+1\rangle \langle j| + |j\rangle \langle j+1|) \end{aligned} \tag{A.3}$$

The first three terms describe the surface and the last two terms the Ag bulk. A surface potential is introduced at $j = 1$ by changing the on-site energy of the last Ag atom to $\epsilon_{\mathrm{SS}} - \epsilon_0 = 2\,\mathrm{eV}$. Because $\epsilon_{\mathrm{SS}} - \epsilon_0 > t$, this leads to the formation of a surface state SS, which lies energetically above the projected bulk band states ($E_{\mathrm{SS}} - \epsilon_0 = 0.5\,\mathrm{eV}$).
The Te atom is modeled by another atom at $j = 0$. For illustrative reasons, the on-site energy of the Te orbital has been adjusted slightly below the surface state energy but above the projected bulk band states $\epsilon_{\mathrm{Te}} - \epsilon_0 = 0.3\,\mathrm{eV}$. The hybridization strength V parameterizes the surface-state-mediated adsorption on the Ag surface, as described in Chapter 4.1.3.

A.1.3 Linear Dichroism of α

In Chapter 4.3.3, the LD of the OAM-carrying band $\beta_{\pm}$ has been analyzed and compared to the calculated chiral OAM texture. A similar analysis is done here for α, which corresponds to the $\langle L_t \rangle = 0$ band. In this regard, the momentum-distribution of the photoemission intensity for ARPES measurements taken with p polarized light is studied, as shown in Fig. A.2. The left and right panels correspond to an energy of $E - E_{\mathrm{F}} = -0.9\,\mathrm{eV}$ and $E - E_{\mathrm{F}} = -1.3\,\mathrm{eV}$, respectively. For small wave vectors an isotropic behavior is found, as can be seen in Fig. A.2 (a,c,e); the two-fold symmetry of the intensity distribution $I_p(\phi_k) \propto \sin^2(\phi_k)$, i.e., the suppression of the photoemission signal at $\phi_k = 0$ and $\phi_k = \pi$, reflects a tangential p orbital alignment in agreement to the measurements taken with s-polarized light. The LD is nearly completely zero as shown in Fig. A.2 (e). This is in excellent agreement with an expected vanishing OAM (Fig. 4.14). Thus, the LD does not only reflect the chiral OAM texture of the Rashba-type spin-split band $\beta_{\pm}$, but moreover $\langle L_t \rangle = 0$ for the band in which the Rashba effect is suppressed. For larger wave vectors, the anisotropic behavior of α – reflected for instance in the hexagonal-shaped CEC (Fig. A.2 (b)) – also comes into play. The intensity distribution and consequently the LD (Figs. A.2 (d and f), respectively) become more complex and are not two-fold symmetric anymore. Nevertheless, the normalized LD is still close to zero (see arrows) in the plane of light light incidence, which is again in line with a vanishing tangential OAM that is found in the DFT calculation.

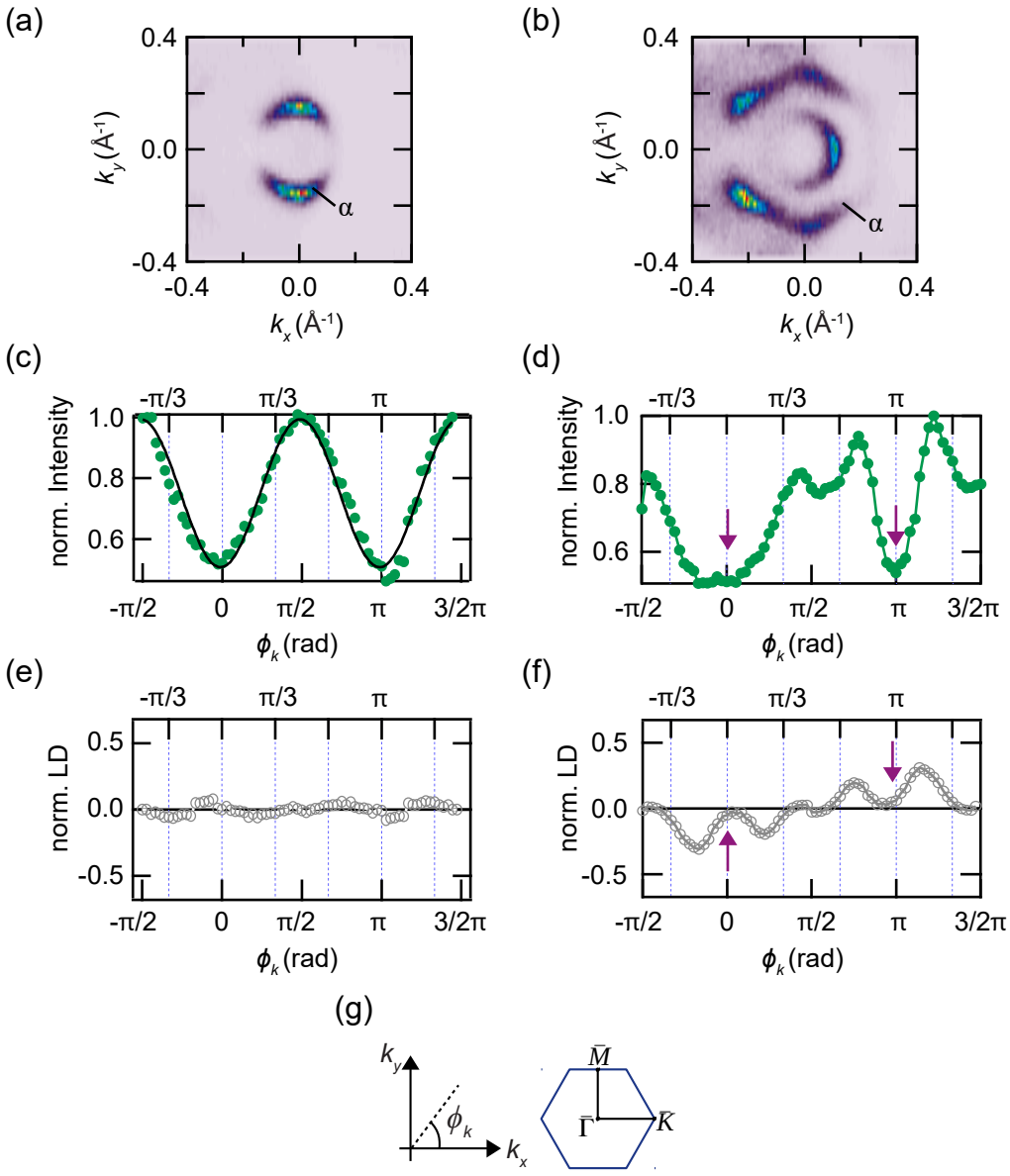

FIGURE A.2: Momentum-dependent linear dichroism (LD) of the band α in AgTe at $E - E_F = -0.9$ eV (left panel) and $E - E_F = -1.3$ eV (right panel). (a,b) Constant energy cuts. (c,d) Intensity distribution of state α as determined from (a,b). (e,f) Corresponding momentum distribution of the LD. (g) Definition of the azimuthal angle ϕ_k and sample orientation. *Figures (a,b,g) have already been published in [64].*

A.1.4 DFT Band Structure Calculation for Different AgTe Modifications

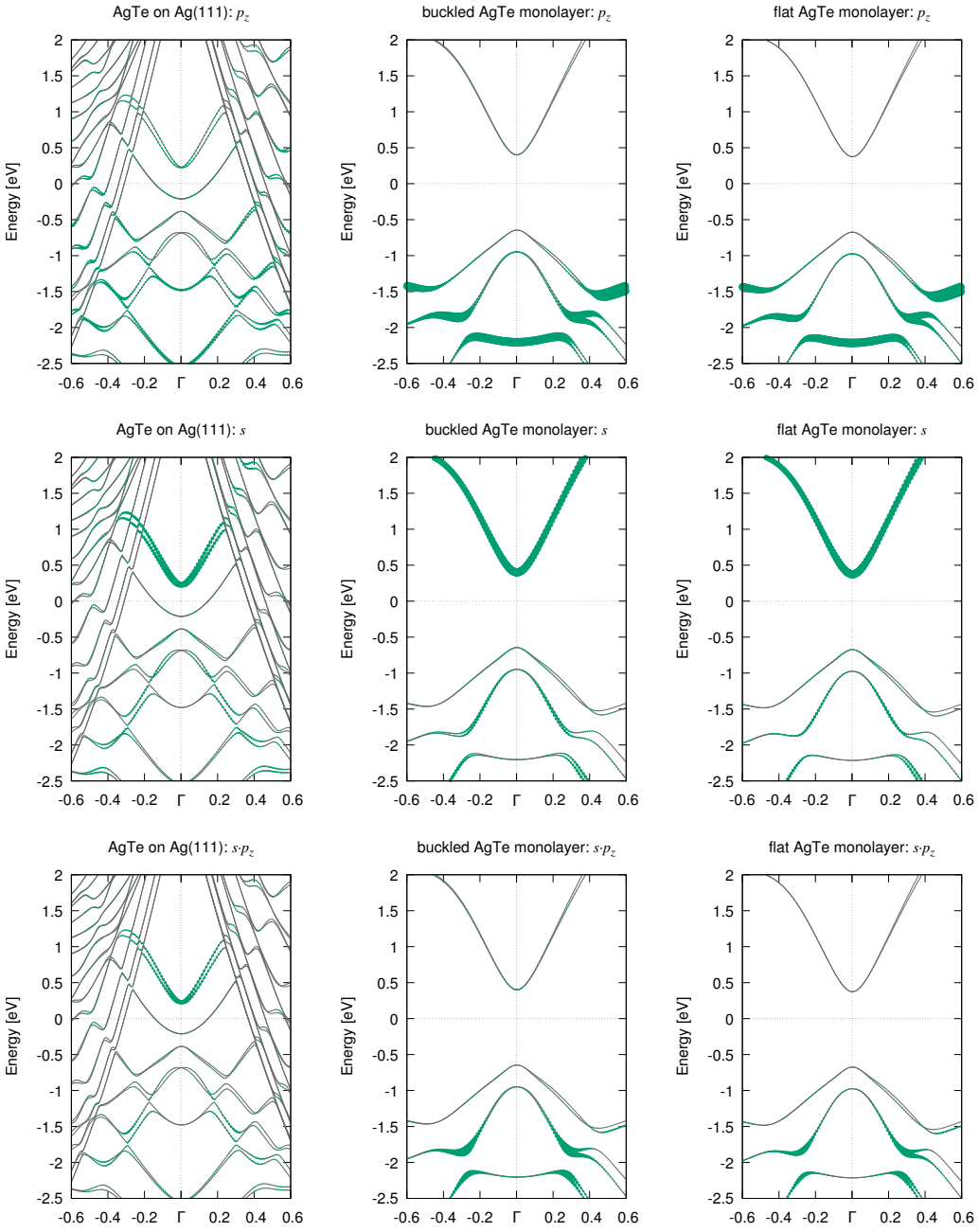

FIGURE A.3: DFT band structure calculation of AgTe in three different modifications: (left column) a buckled monolayer on a 7-layer Ag(111) slab, (middle column) a buckled free-standing monolayer, and (right column) a flat free-standing (inversion symmetric) AgTe. The dotsize represents wave function weight of the electronic states in the AgTe layer projected on (upper row) the Te-p_z orbitals and (middle row) the Ag-s orbitals. In the lower row, the product of s and p is depicted.

A.2 LD on Au(111) and Ag_2(Pb,Bi) – $h\nu$-dependence

In Chapter 4.4, the linear dichroism observed in various Rashba systems was discussed. In particular, LD data for the Au(111) surface state are presented (see Fig. 4.20) and compared with measurements on the surface alloys Ag_2(Pb,Bi)/Ag(111), which have been discussed in detail in previous works [132, 133]. In all these systems, a strong dependence of the LD on the photon energy is observed. In particular, complete LD sign changes occur in a $h\nu$ range of 22...26 eV, as shown in Fig. A.4 (b). This is likely due to a Bragg gap in the final state band structure [132] that occurs along ΓL in Ag [210] as well as Au [211] in this energy range. Importantly, the relative LD sign between the spin branches Ψ_+ and Ψ_- is – as discussed in Chapter 4.4 – always parallel in Au(111) and anti-parallel in Ag_2Bi/Ag(111), i.e., the two systems that belong to the strong ISB and strong SOC limit, respectively. Independent of the photon energy used, the relative LD reflects the expected relative OAM alignment in the two systems. The observations on Ag_2Pb are in contrast less clear. Here (see Fig. A.4), the relative LD sign is parallel for $h\nu < 24$ eV and anti-parallel for $h\nu > 24$ eV. A clear assignment to one of the two extreme regimes is therefore not possible. One possible explanation is that this system is rather in an intermediate regime where $E_{ISB} \approx E_{SOC}$, which would be consistent with earlier observations on Pb-based compounds [55]. In this case, it could be that strong final state effects lead to a modulation of the relative LD sign. However, this assumption needs to be confirmed by a more detailed theoretical analysis.

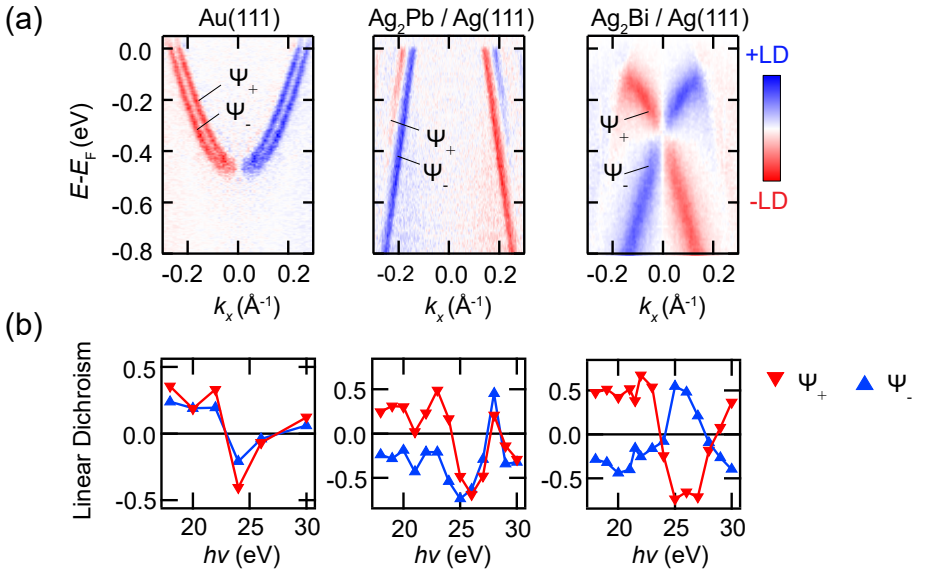

FIGURE A.4: Linear dichroism (LD) and spin-resolved (SR) ARPES measurements as a function of photon energy. (a) LD on Au(111) and Ag_2(Pb,Bi)/Ag(111) taken at $h\nu = 18$ eV. (b) Observed LD signal of $\Psi_\pm$ (red and blue as indicated) as a function of hν extracted at $k_x = 0.15\,\text{Å}^{-1}$, $k_x = 0.19\,\text{Å}^{-1}$ and $k_x = 0.05\,\text{Å}^{-1}$ for Au(111), Ag_2Pb and Ag_2Bi, respectively.

A.3 Winding of OAM, BC, and SAM around the Weyl Points

As written in Chapter 5.1.4, Berry curvature and OAM both are winding around the W_2 Weyl points in TaAs, while the field configuration of the spin angular momentum shows a trivial winding number, i.e., a Pontryagin index $\chi = 0$. For completeness, the corresponding calculated field configurations are depicted in Fig. A.5.

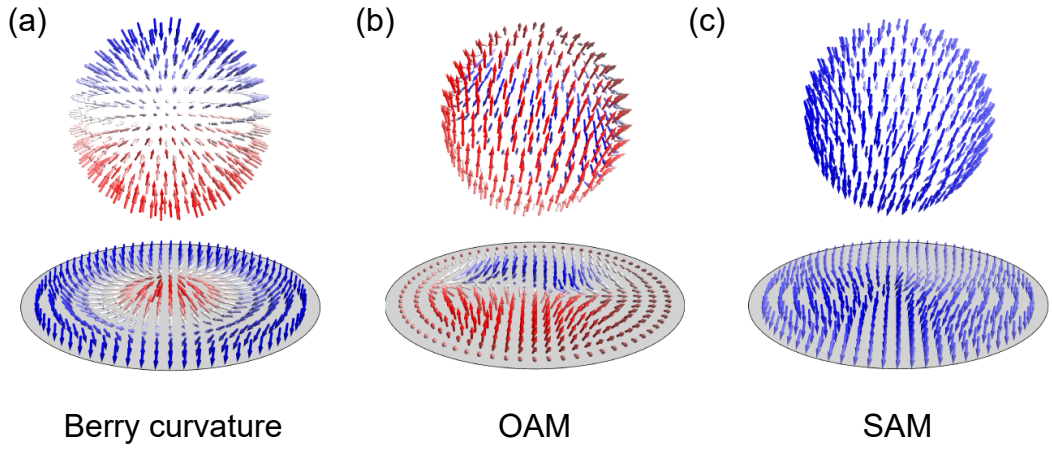

FIGURE A.5: Momentum space field configuration and azimuthal equidistant projections of BC (a), OAM (b) and SAM (c) on a small sphere around a Weyl point (see Fig. 5.8 and corresponding text in Chapter 5.1.4). Here, the color code represents the z component of the respective observable. *This figures have already been published in [87].*

Bibliography

1. Keimer, B. & Moore, J. E. The physics of quantum materials. *Nature Physics* **13,** 1045–1055 (2017).
2. Dirac, P. A. M. The quantum theory of the electron. *Proceedings of the Royal Society of London A* **117,** 610–624 (1928).
3. V. Klitzing, K., Dorda, G. & Pepper, M. New Method for High-Accuracy Determination of the Fine-Structure Constant Based on Quantized Hall Resistance. *Physical Review Letters* **45,** 494–497 (1980).
4. Thouless, D. J., Kohmoto, M., Nightingale, M. P. & den Nijs, M. Quantized Hall Conductance in a Two-Dimensional Periodic Potential. *Physical Review Letters* **49,** 405–408 (1982).
5. Haldane, F. D. M. Model for a Quantum Hall Effect without Landau Levels: Condensed-Matter Realization of the "Parity Anomaly". *Physical Review Letters* **61,** 2015–2018 (1988).
6. Murakami, S., Nagaosa, N. & Zhang, S.-C. Spin-Hall Insulator. *Physical Review Letters* **93,** 156804 (2004).
7. Kane, C. L. & Mele, E. J. Quantum Spin Hall Effect in Graphene. *Physical Review Letters* **95,** 226801 (2005).
8. Kane, C. L. & Mele, E. J. Z_2 Topological Order and the Quantum Spin Hall Effect. *Physical Review Letters* **95,** 146802 (2005).
9. Bernevig, B. A. & Zhang, S.-C. Quantum Spin Hall Effect. *Physical Review Letters* **96,** 106802 (2006).
10. Bernevig, B. A., Hughes, T. L. & Zhang, S.-C. Quantum Spin Hall Effect and Topological Phase Transition in HgTe Quantum Wells. *Science* **314,** 1757–1761 (2006).
11. König, M., Wiedmann, S., Brüne, C., Roth, A., Buhmann, H., Molenkamp, L. W., Qi, X. & Zhang, S. Quantum Spin Hall Insulator State in HgTe Quantum Wells. *Science* **318,** 766–770 (2007).
12. Fu, L., Kane, C. L. & Mele, E. J. Topological Insulators in Three Dimensions. *Physical Review Letters* **98,** 106803 (2007).
13. Fu, L. & Kane, C. L. Topological insulators with inversion symmetry. *Physical Review B* **76,** 045302 (2007).
14. Hsieh, D., Qian, D., Wray, L., Xia, Y., Hor, Y. S., Cava, R. J. & Hasan, M. Z. A topological Dirac insulator in a quantum spin Hall phase. *Nature* **452,** 970–974 (2008).

15. Zhang, H., Liu, C.-X., Qi, X.-L., Dai, X., Fang, Z. & Zhang, S.-C. Topological insulators in Bi_2Se_3, Bi_2Te_3 and Sb_2Te_3 with a single Dirac cone on the surface. *Nature Physics* **5,** 438–442 (2009).

16. Xia, Y., Qian, D., Hsieh, D., Wray, L., Pal, A., Lin, H., Bansil, A., Grauer, D., Hor, Y. S., Cava, R. J. & Hasan, M. Z. Observation of a large-gap topological-insulator class with a single Dirac cone on the surface. *Nature Physics* **5,** 398–402 (2009).

17. Chen, Y. L., Analytis, J. G., Chu, J.-H., Liu, Z. K., Mo, S.-K., Qi, X. L., Zhang, H. J., Lu, D. H., Dai, X., Fang, Z., Zhang, S. C., Fisher, I. R., Hussain, Z. & Shen, Z.-X. Experimental Realization of a Three-Dimensional Topological Insulator, Bi_2Te_3. *Science* **325,** 178–181 (2009).

18. Hsieh, D., Xia, Y., Qian, D., Wray, L., Dil, J. H., Meier, F., Osterwalder, J., Patthey, L., Checkelsky, J. G., Ong, N. P., Fedorov, A. V., Lin, H., Bansil, A., Grauer, D., Hor, Y. S., Cava, R. J. & Hasan, M. Z. A tunable topological insulator in the spin helical Dirac transport regime. *Nature* **460,** 1101–1105 (2009).

19. Hsieh, D., Xia, Y., Qian, D., Wray, L., Meier, F., Dil, J. H., Osterwalder, J., Patthey, L., Fedorov, A. V., Lin, H., Bansil, A., Grauer, D., Hor, Y. S., Cava, R. J. & Hasan, M. Z. Observation of Time-Reversal-Protected Single-Dirac-Cone Topological-Insulator States in Bi_2Te_3 and Sb_2Te_3. *Physical Review Letters* **103,** 146401 (2009).

20. Armitage, N. P., Mele, E. J. & Vishwanath, A. Weyl and Dirac semimetals in three-dimensional solids. *Reviews of Modern Physics* **90,** 015001 (2018).

21. Hasan, M. Z. & Kane, C. L. *Colloquium* : Topological insulators. *Reviews of Modern Physics* **82,** 3045–3067 (2010).

22. Qi, X.-L. & Zhang, S.-C. Topological insulators and superconductors. *Reviews of Modern Physics* **83,** 1057–1110 (2011).

23. Dzero, M., Sun, K., Galitski, V. & Coleman, P. Topological Kondo Insulators. *Physical Review Letters* **104,** 106408 (2010).

24. Bychkov, Y. A. & Rashba, E. I. Properties of a 2D electron-gas with lifted spectral degeneracy. *JETP Lett.* **39,** 78–81 (1984).

25. Manchon, A., Koo, H. C., Nitta, J., Frolov, S. M. & Duine, R. A. New perspectives for Rashba spin–orbit coupling. *Nature Materials* **14,** 871–882 (2015).

26. LaShell, S., McDougall, B. A. & Jensen, E. Spin Splitting of an Au(111) Surface State Band Observed with Angle Resolved Photoelectron Spectroscopy. *Physical Review Letters* **77,** 3419–3422 (1996).

27. Hoesch, M., Muntwiler, M., Petrov, V. N., Hengsberger, M., Patthey, L., Shi, M., Falub, M., Greber, T. & Osterwalder, J. Spin structure of the Shockley surface state on Au(111). *Physical Review B* **69,** 241401 (2004).

28. Ast, C. R., Henk, J., Ernst, A., Moreschini, L., Falub, M., Pacilé, D, Bruno, P, Kern, K & Grioni, M. Giant Spin Splitting through Surface Alloying. *Physical Review Letters* **98,** 186807 (2007).

29. Bentmann, H., Forster, F., Bihlmayer, G., Chulkov, E. V., Moreschini, L., Grioni, M. & Reinert, F. Origin and manipulation of the Rashba splitting in surface alloys. *Europhysics Letters* **87,** 37003 (2009).

30. Moreschini, L., Bendounan, A., Bentmann, H., Assig, M., Kern, K., Reinert, F., Henk, J., Ast, C. R. & Grioni, M. Influence of the substrate on the spin-orbit splitting in surface alloys on (111) noble-metal surfaces. *Physical Review B* **80,** 035438 (2009).

31. Gierz, I., Stadtmüller, B., Vuorinen, J., Lindroos, M., Meier, F., Dil, J. H., Kern, K. & Ast, C. R. Structural influence on the Rashba-type spin splitting in surface alloys. *Physical Review B* **81,** 245430 (2010).

32. Bentmann, H. & Reinert, F. Enhancing and reducing the Rashba-splitting at surfaces by adsorbates: Na and Xe on Bi/Cu(111). *New Journal of Physics* **15,** 115011 (2013).

33. El-Kareh, L., Sessi, P., Bathon, T. & Bode, M. Quantum Interference Mapping of Rashba-Split Bloch States in Bi/Ag(111). *Physical Review Letters* **110,** 176803 (2013).

34. El-Kareh, L., Bihlmayer, G., Buchter, A., Bentmann, H., Blügel, S., Reinert, F. & Bode, M. A combined experimental and theoretical study of Rashba-split surface states on the $(\sqrt{3} \times \sqrt{3})$ Pb/Ag(111)$R30^\circ$ surface. *New Journal of Physics* **16,** 045017 (2014).

35. King, P. D. C., Hatch, R. C., Bianchi, M., Ovsyannikov, R., Lupulescu, C., Landolt, G., Slomski, B., Dil, J. H., Guan, D., Mi, J. L., Rienks, E. D. L., Fink, J., Lindblad, A., Svensson, S., Bao, S., Balakrishnan, G., Iversen, B. B., Osterwalder, J., Eberhardt, W., Baumberger, F. & Hofmann, P. Large Tunable Rashba Spin Splitting of a Two-Dimensional Electron Gas in Bi_2Se_3. *Physical Review Letters* **107,** 096802 (2011).

36. Marchenko, D., Varykhalov, A., Scholz, M., Bihlmayer, G., Rashba, E., Rybkin, A., Shikin, A. & Rader, O. Giant Rashba splitting in graphene due to hybridization with gold. *Nature Communications* **3,** 1–6 (2012).

37. Sunko, V., Rosner, H., Kushwaha, P., Khim, S., Mazzola, F., Bawden, L., Clark, O. J., Riley, J. M., Kasinathan, D., Haverkort, M. W., Kim, T. K., Hoesch, M., Fujii, J., Vobornik, I., Mackenzie, A. P. & King, P. D. C. Maximal Rashba-like spin splitting via kinetic-energy-coupled inversion-symmetry breaking. *Nature* **549,** 492–496 (2017).

38. Sinova, J., Culcer, D., Niu, Q., Sinitsyn, N. A., Jungwirth, T. & MacDonald, A. H. Universal Intrinsic Spin Hall Effect. *Physical Review Letters* **92,** 126603 (2004).

39. Kurebayashi, H., Sinova, J., Fang, D., Irvine, A. C., Skinner, T. D., Wunderlich, J., Novák, V., Campion, R. P., Gallagher, B. L., Vehstedt, E. K., Zârbo, L. P., Výborný, K., Ferguson, A. J. & Jungwirth, T. An antidamping spin–orbit torque originating from the Berry curvature. *Nature Nanotechnology* **9,** 211–217 (2014).

40. Lesne, E., Fu, Y., Oyarzun, S., Rojas-Sanchez, J. C., Vaz, D. C., Naganuma, H., Sicoli, G., Attane, J.-P., Jamet, M., Jacquet, E., George, J.-M., Barthelemy, A., Jaffres, H., Fert, A., Bibes, M. & Vila, L. Highly efficient and tunable spin-to-charge conversion through Rashba coupling at oxide interfaces. *Nature Materials* **15,** 1261–1266 (2016).

41. Nicolay, G., Reinert, F., Hüfner, S. & Blaha, P. Spin-orbit splitting of theL-gap surface state on Au(111) and Ag(111). *Physical Review B* **65,** 033407 (2001).

42. Bihlmayer, G., Koroteev, Y., Echenique, P., Chulkov, E. & Blügel, S. The Rashba-effect at metallic surfaces. *Surface Science* **600,** 3888–3891 (2006).

43. Bihlmayer, G., Blügel, S. & Chulkov, E. V. Enhanced Rashba spin-orbit splitting in Bi/Ag(111) and Pb/Ag(111) surface alloys from first principles. *Physical Review B* **75,** 195414 (2007).

44. Bian, G., Wang, X., Miller, T. & Chiang, T.-C. Origin of giant Rashba spin splitting in Bi/Ag surface alloys. *Physical Review B* **88,** 085427 (2013).

45. Krasovskii, E. E. Microscopic origin of the relativistic splitting of surface states. *Physical Review B* **90,** 115434 (2014).

46. Ishida, H. Rashba spin splitting of Shockley surface states on semi-infinite crystals. *Physical Review B* **90,** 235422 (2014).

47. Park, S. R., Kim, C. H., Yu, J., Han, J. H. & Kim, C. Orbital-Angular-Momentum Based Origin of Rashba-Type Surface Band Splitting. *Physical Review Letters* **107,** 156803 (2011).

48. Park, J.-H., Kim, C. H., Rhim, J.-W. & Han, J. H. Orbital Rashba effect and its detection by circular dichroism angle-resolved photoemission spectroscopy. *Physical Review B* **85,** 195401 (2012).

49. Kim, B., Kim, P., Jung, W., Kim, Y., Koh, Y., Kyung, W., Park, J., Matsunami, M., ichi Kimura, S., Kim, J. S., Han, J. H. & Kim, C. Microscopic mechanism for asymmetric charge distribution in Rashba-type surface states and the origin of the energy splitting scale. *Physical Review B* **88,** 205408 (2013).

50. Park, S. R. & Kim, C. Microscopic mechanism for the Rashba spin-band splitting: Perspective from formation of local orbital angular momentum. *Journal of Electron Spectroscopy and Related Phenomena* **201,** 6–17 (2015).

51. Kim, B., Kim, C. H., Kim, P., Jung, W., Kim, Y., Koh, Y., Arita, M., Shimada, K., Namatame, H., Taniguchi, M., Yu, J. & Kim, C. Spin and orbital angular momentum structure of Cu(111) and Au(111) surface states. *Physical Review B* **85,** 195402 (2012).

52. Lee, H. & Choi, H. J. Role of d orbitals in the Rashba-type spin splitting for noble-metal surfaces. *Physical Review B* **86,** 045437 (2012).

53. Oh, S. & Choi, H. J. Orbital angular momentum analysis for giant spin splitting in solids and nanostructures. *Scientific Reports* **7,** 1–10 (2017).

54. Hong, J., Rhim, J.-W., Song, I., Kim, C., Park, S. R. & Shim, J. H. Giant Rashba-Type Spin Splitting in Bi/Ag(111) from Asymmetric Interatomic-Hopping. *Journal of the Physical Society of Japan* **88,** 124705 (2019).

55. Jakobs, S., Ruffing, A., Cinchetti, M., Mathias, S. & Aeschlimann, M. Orbital angular momentum structure of an unoccupied spin-split quantum-well state in Pb/Cu(111). *Physical Review B* **87,** 235438 (2013).

56. Marković, I., Hooley, C. A., Clark, O. J., Mazzola, F., Watson, M. D., Riley, J. M., Volckaert, K., Underwood, K., Dyer, M. S., Murgatroyd, P. A. E., Murphy, K. J., Fèvre, P. L., Bertran, F., Fujii, J., Vobornik, I., Wu, S., Okuda, T., Alaria, J. & King, P. D. C. Weyl-like points from band inversions of spin-polarised surface states in NbGeSb. *Nature Communications* **10,** 1–8 (2019).

57. Bernevig, B. A., Hughes, T. L. & Zhang, S.-C. Orbitronics: The Intrinsic Orbital Current in p-Doped Silicon. *Physical Review Letters* **95,** 066601 (2005).

58. Go, D., Jo, D., Kim, C. & Lee, H.-W. Intrinsic Spin and Orbital Hall Effects from Orbital Texture. *Physical Review Letters* **121,** 086602 (2018).

59. Jo, D., Go, D. & Lee, H.-W. Gigantic intrinsic orbital Hall effects in weakly spin-orbit coupled metals. *Physical Review B* **98,** 214405 (2018).

60. Go, D. & Lee, H.-W. Orbital torque: Torque generation by orbital current injection. *Physical Review Research* **2,** 013177 (2020).

61. Go, D., Jo, D., Lee, H.-W., Klaeui, M. & Mokrousov, Y. Orbitronics: Orbital currents in solids. *Europhysics Letters,* 37001 (2021).

62. Go, D., Hanke, J.-P., Buhl, P. M., Freimuth, F., Bihlmayer, G., Lee, H.-W., Mokrousov, Y. & Blügel, S. Toward surface orbitronics: giant orbital magnetism from the orbital Rashba effect at the surface of sp-metals. *Scientific Reports* **7,** 1–10 (2017).

63. Go, D., Jo, D., Gao, T., Ando, K., Blügel, S., Lee, H.-W. & Mokrousov, Y. Orbital Rashba effect in a surface-oxidized Cu film. *Physical Review B* **103,** L121113 (2021).

64. Ünzelmann, M., Bentmann, H., Eck, P., Kißlinger, T., Geldiyev, B., Rieger, J., Moser, S., Vidal, R. C., Kißner, K., Hammer, L., Schneider, M. A., Fauster, T., Sangiovanni, G., Sante, D. D. & Reinert, F. Orbital-Driven Rashba Effect in a Binary Honeycomb Monolayer AgTe. *Physical Review Letters* **124,** 176401 (2020).

65. Pacilé, D., Ast, C. R., Papagno, M., Silva, C. D., Moreschini, L., Falub, M., Seitsonen, A. P. & Grioni, M. Electronic structure of an ordered Pb/Ag(111) surface alloy: Theory and experiment. *Physical Review B* **73,** 245429 (2006).

66. Moreschini, L., Bendounan, A., Gierz, I., Ast, C. R., Mirhosseini, H., Höchst, H., Kern, K., Henk, J., Ernst, A., Ostanin, S., Reinert, F. & Grioni, M. Assessing the atomic contribution to the Rashba spin-orbit splitting in surface alloys: Sb/Ag(111). *Physical Review B* **79,** 075424 (2009).

67. Volkov, B. A. & Pankratov, O. A. Two-dimensional massless electrons in an inverted contact. *Soviet Journal of Experimental and Theoretical Physics Letters* **42,** 178 (1985).
68. Pankratov, O., Pakhomov, S. & Volkov, B. Supersymmetry in heterojunctions: Band-inverting contact on the basis of $Pb_{1-x}Sn_xTe$ and $Hg_{1-x}Cd_xTe$. *Solid State Communications* **61,** 93–96 (1987).
69. Murakami, S., Iso, S., Avishai, Y., Onoda, M. & Nagaosa, N. Tuning phase transition between quantum spin Hall and ordinary insulating phases. *Physical Review B* **76,** 205304 (2007).
70. Murakami, S. & ichi Kuga, S. Universal phase diagrams for the quantum spin Hall systems. *Physical Review B* **78,** 165313 (2008).
71. Murakami, S. Phase transition between the quantum spin Hall and insulator phases in 3D: emergence of a topological gapless phase. *New Journal of Physics* **10,** 029802 (2008).
72. Murakami, S., Hirayama, M., Okugawa, R. & Miyake, T. Emergence of topological semimetals in gap closing in semiconductors without inversion symmetry. *Science Advances* **3,** e1602680 (2017).
73. Berry, M. V. Quantal phase factors accompanying adiabatic changes. *Proceedings of the Royal Society of London. A. Mathematical and Physical Sciences* **392,** 45–57 (1984).
74. Cayssol, J & Fuchs, J. N. Topological and geometrical aspects of band theory. *Journal of Physics: Materials* **4,** 034007 (2021).
75. Wan, X., Turner, A. M., Vishwanath, A. & Savrasov, S. Y. Topological semimetal and Fermi-arc surface states in the electronic structure of pyrochlore iridates. *Physical Review B* **83,** 205101 (2011).
76. Weng, H., Fang, C., Fang, Z., Bernevig, B. A. & Dai, X. Weyl Semimetal Phase in Noncentrosymmetric Transition-Metal Monophosphides. *Physical Review X* **5,** 011029 (2015).
77. Xu, S.-Y., Belopolski, I., Alidoust, N., Neupane, M., Bian, G., Zhang, C., Sankar, R., Chang, G., Yuan, Z., Lee, C.-C., Huang, S.-M., Zheng, H., Ma, J., Sanchez, D. S., Wang, B., Bansil, A., Chou, F., Shibayev, P. P., Lin, H., Jia, S. & Hasan, M. Z. Discovery of a Weyl fermion semimetal and topological Fermi arcs. *Science* **349,** 613–617 (2015).
78. Yang, L. X., Liu, Z. K., Sun, Y., Peng, H., Yang, H. F., Zhang, T., Zhou, B., Zhang, Y., Guo, Y. F., Rahn, M., Prabhakaran, D., Hussain, Z., Mo, S.-K., Felser, C., Yan, B. & Chen, Y. L. Weyl semimetal phase in the noncentrosymmetric compound TaAs. *Nature Physics* **11,** 728–732 (2015).
79. Xu, S.-Y., Belopolski, I., Sanchez, D. S., Zhang, C., Chang, G., Guo, C., Bian, G., Yuan, Z., Lu, H., Chang, T.-R., Shibayev, P. P., Prokopovych, M. L., Alidoust, N., Zheng, H., Lee, C.-C., Huang, S.-M., Sankar, R., Chou, F., Hsu, C.-H., Jeng, H.-T., Bansil, A., Neupert, T., Strocov, V. N., Lin, H., Jia, S. & Hasan, M. Z. Experimental discovery of a topological Weyl semimetal state in TaP. *Science advances* **1,** e1501092 (2015).

80. Xu, S.-Y., Alidoust, N., Belopolski, I., Yuan, Z., Bian, G., Chang, T.-R., Zheng, H., Strocov, V. N., Sanchez, D. S., Chang, G., Zhang, C., Mou, D., Wu, Y., Huang, L., Lee, C.-C., Huang, S.-M., Wang, B., Bansil, A., Jeng, H.-T., Neupert, T., Kaminski, A., Lin, H., Jia, S. & Hasan, M. Z. Discovery of a Weyl fermion state with Fermi arcs in niobium arsenide. *Nature Physics* **11,** 748–754 (2015).

81. Xu, N., Weng, H. M., Lv, B. Q., Matt, C. E., Park, J., Bisti, F., Strocov, V. N., Gawryluk, D., Pomjakushina, E., Conder, K., Plumb, N. C., Radovic, M., Autès, G., Yazyev, O. V., Fang, Z., Dai, X., Qian, T., Mesot, J., Ding, H. & Shi, M. Observation of Weyl nodes and Fermi arcs in tantalum phosphide. *Nature Communications* **7,** 11006 (2016).

82. Liu, Z. K., Yang, L. X., Sun, Y., Zhang, T., Peng, H., Yang, H. F., Chen, C., Zhang, Y., Guo, Y. F., Prabhakaran, D., Schmidt, M., Hussain, Z., Mo, S.-K., Felser, C., Yan, B. & Chen, Y. L. Evolution of the Fermi surface of Weyl semimetals in the transition metal pnictide family. *Nature Materials* **15,** 4457 (2015).

83. Lv, B. Q., Weng, H. M., Fu, B. B., Wang, X. P., Miao, H., Ma, J., Richard, P., Huang, X. C., Zhao, L. X., Chen, G. F., Fang, Z., Dai, X., Qian, T. & Ding, H. Experimental Discovery of Weyl Semimetal TaAs. *Physical Review X* **5,** 031013 (2015).

84. Inoue, H., Gyenis, A., Wang, Z., Li, J., Oh, S. W., Jiang, S., Ni, N., Bernevig, B. A. & Yazdani, A. Quasiparticle interference of the Fermi arcs and surface-bulk connectivity of a Weyl semimetal. *Science* **351,** 1184–1187 (2016).

85. Zhang, C.-L., Xu, S.-Y., Belopolski, I., Yuan, Z., Lin, Z., Tong, B., Bian, G., Alidoust, N., Lee, C.-C., Huang, S.-M., Chang, T.-R., Chang, G., Hsu, C.-H., Jeng, H.-T., Neupane, M., Sanchez, D. S., Zheng, H., Wang, J., Lin, H., Zhang, C., Lu, H.-Z., Shen, S.-Q., Neupert, T., Hasan, M. Z. & Jia, S. Signatures of the Adler–Bell–Jackiw chiral anomaly in a Weyl fermion semimetal. *Nature Communications* **7,** 1–9 (2016).

86. Ma, Q., Xu, S.-Y., Chan, C.-K., Zhang, C.-L., Chang, G., Lin, Y., Xie, W., Palacios, T., Lin, H., Jia, S., Lee, P. A., Jarillo-Herrero, P. & Gedik, N. Direct optical detection of Weyl fermion chirality in a topological semimetal. *Nature Physics* **13,** 842–847 (2017).

87. Ünzelmann, M., Bentmann, H., Figgemeier, T., Eck, P., Neu, J. N., Geldiyev, B., Diekmann, F., Rohlf, S., Buck, J., Hoesch, M., Kalläne, M., Rossnagel, K., Thomale, R., Siegrist, T., Sangiovanni, G., Sante, D. D. & Reinert, F. Momentum-space signatures of Berry flux monopoles in the Weyl semimetal TaAs. *Nature Communications* **12,** 1–7 (2021).

88. Park, S. R., Han, J., Kim, C., Koh, Y. Y., Kim, C., Lee, H., Choi, H. J., Han, J. H., Lee, K. D., Hur, N. J., Arita, M., Shimada, K., Namatame, H. & Taniguchi, M. Chiral Orbital-Angular Momentum in the Surface States of Bi_2Se_3. *Physical Review Letters* **108,** 046805 (2012).

89. Cho, S., Park, J.-H., Hong, J., Jung, J., Kim, B. S., Han, G., Kyung, W., Kim, Y., Mo, S.-K., Denlinger, J. D., Shim, J. H., Han, J. H., Kim, C. & Park, S. R. Experimental Observation of Hidden Berry Curvature in Inversion-Symmetric Bulk $2H-WSe_2$. *Physical Review Letters* **121,** 186401 (2018).

90. Fedchenko, O., Medjanik, K., Chernov, S., Kutnyakhov, D., Ellguth, M., Oelsner, A., Schönhense, B., Peixoto, T. R. F., Lutz, P., Min, C.-H., Reinert, F., Däster, S., Acremann, Y., Viefhaus, J., Wurth, W., Braun, J., Minár, J., Ebert, H., Elmers, H. J. & Schönhense, G. 4D texture of circular dichroism in soft-x-ray photoemission from tungsten. *New Journal of Physics* **21,** 013017 (2019).

91. Petersen, L. & Hedegård, P. A simple tight-binding model of spin–orbit splitting of sp-derived surface states. *Surface Science* **459,** 49–56 (2000).

92. Sakurai, J. & Tuan, S. F. *Modern Quantum Mechanics* (Addison-Wesley Publishing Company, 1994).

93. Nitta, J., Akazaki, T., Takayanagi, H. & Enoki, T. Gate Control of Spin-Orbit Interaction in an Inverted $In_{0.53}Ga_{0.47}As/In_{0.52}Al_{0.48}As$ Heterostructure. *Physical Review Letters* **78,** 1335–1338 (1997).

94. Dresselhaus, G. Spin-Orbit Coupling Effects in Zinc Blende Structures. *Physical Review* **100,** 580–586 (1955).

95. Reinert, F., Nicolay, G., Schmidt, S., Ehm, D. & Hüfner, S. Direct measurements of the L-gap surface states on the (111) face of noble metals by photoelectron spectroscopy. *Physical Review B* **63,** 115415 (2001).

96. Henk, J., Ernst, A. & Bruno, P. Spin polarization of the *L* -gap surface states on Au(111). *Physical Review B* **68,** 165416 (2003).

97. Henk, J, Hoesch, M, Osterwalder, J, Ernst, A & Bruno, P. Spin-orbit coupling in the L-gap surface states of Au(111): spin-resolved photoemission experiments and first-principles calculations. *Journal of Physics: Condensed Matter* **16,** 7581 (2004).

98. Kosugi, T., Miyake, T. & Ishibashi, S. Slab Thickness Dependence of Rashba Splitting on Au(111) Surface: First-Principles and Model Analyses. *Journal of the Physical Society of Japan* **80,** 074713 (2011).

99. Forster, F. *Eigenschaften und Modifikation zweidimensionaler Elektronenzustände auf Edelmetallen* PhD thesis (Julius-Maximilians-Universität Würzburg, 2007).

100. Shanavas, K. V., Popović, Z. S. & Satpathy, S. Theoretical model for Rashba spin-orbit interaction in d electrons. *Physical Review B* **90** (2014).

101. Bauernfeind, M., Erhardt, J., Eck, P., Thakur, P. K., Gabel, J., Lee, T.-L., Schäfer, J., Moser, S., Sante, D. D., Claessen, R. & Sangiovanni, G. Design and realization of topological Dirac fermions on a triangular lattice. *Nature communications* **12,** 1–8 (2021).

102. Weyl, H. Elektron und Gravitation. I. *Zeitschrift für Physik* **56,** 330–352 (1929).

103. Xu, G., Weng, H., Wang, Z., Dai, X. & Fang, Z. Chern Semimetal and the Quantized Anomalous Hall Effect in $HgCr_2Se_4$. *Physical Review Letters* **107,** 186806 (2011).

104. Burkov, A. A. & Balents, L. Weyl Semimetal in a Topological Insulator Multilayer. *Physical Review Letters* **107,** 127205 (2011).

105. Bloch, F. Über die Quantenmechanik der Elektronen in Kristallgittern. *Zeitschrift für Physik* **52,** 555–600 (1929).

106. Simon, B. Holonomy, the Quantum Adiabatic Theorem, and Berry's Phase. *Physical Review Letters* **51,** 2167–2170 (1983).

107. Dirac, P. A. M. Quantised singularities in the electromagnetic field, *Proceedings of the Royal Society of London. Series A, Containing Papers of a Mathematical and Physical Character* **133,** 60–72 (1931).

108. Jackiw, R. & Rebbi, C. Solitons with fermion number ½. *Physical Review D* **13,** 3398–3409 (1976).

109. Su, W. P., Schrieffer, J. R. & Heeger, A. J. Solitons in Polyacetylene. *Physical Review Letters* **42,** 1698–1701 (1979).

110. Mahler, D. M., Mayer, J.-B., Leubner, P., Lunczer, L., Sante, D. D., Sangiovanni, G., Thomale, R., Hankiewicz, E. M., Buhmann, H., Gould, C. & Molenkamp, L. W. Interplay of Dirac Nodes and Volkov-Pankratov Surface States in Compressively Strained HgTe. *Physical Review X* **9,** 031034 (2019).

111. Huang, S.-M., Xu, S.-Y., Belopolski, I., Lee, C.-C., Chang, G., Wang, B., Alidoust, N., Bian, G., Neupane, M., Zhang, C., Jia, S., Bansil, A., Lin, H. & Hasan, M. Z. A Weyl Fermion semimetal with surface Fermi arcs in the transition metal monopnictide TaAs class. *Nature Communications* **6,** 7373 (2015).

112. Berry, M. V. in *Chaotic Behavior in Quantum Systems* 123–140 (Springer US, 1985).

113. Neto, A. H. C., Guinea, F., Peres, N. M. R., Novoselov, K. S. & Geim, A. K. The electronic properties of graphene. *Reviews of Modern Physics* **81,** 109–162 (2009).

114. Sun, Y., Wu, S.-C. & Yan, B. Topological surface states and Fermi arcs of the noncentrosymmetric Weyl semimetals TaAs, TaP, NbAs, and NbP. *Physical Review B* **92,** 115428 (2015).

115. Min, C.-H., Bentmann, H., Neu, J. N., Eck, P., Moser, S., Figgemeier, T., Ünzelmann, M., Kissner, K., Lutz, P., Koch, R. J., Jozwiak, C., Bostwick, A., Rotenberg, E., Thomale, R., Sangiovanni, G., Siegrist, T., Di Sante, D. & Reinert, F. Orbital Fingerprint of Topological Fermi Arcs in the Weyl Semimetal TaP. *Physical Review Letters* **122,** 116402 (2019).

116. Hertz, H. Ueber einen Einfluss des ultravioletten Lichtes auf die electrische Entladung. *Annalen der Physik* **267,** 983–1000 (1887).

117. Einstein, A. Über einem die Erzeugung und Verwandlung des Lichtes betreffenden heuristischen Gesichtspunkt. *Annalen der physik* **4** (1905).

118. Damascelli, A. Probing the Electronic Structure of Complex Systems by ARPES. *Physica Scripta* **T109,** 61 (2004).

119. Damascelli, A., Hussain, Z. & Shen, Z.-X. Angle-resolved photoemission studies of the cuprate superconductors. *Reviews of Modern Physics* **75,** 473–541 (2003).

120. Miller, T., McMahon, W. E. & Chiang, T.-C. Interference between Bulk and Surface Photoemission Transitions in Ag(111). *Physical Review Letters* **77,** 1167–1170 (1996).

121. Fauster, T., Hammer, L., Heinz, K. & Schneider, M. A. *Surface Physics* (de Gruyter Oldenbourg, 2020).

122. Wießner, M., Hauschild, D., Sauer, C., Feyer, V., Schöll, A. & Reinert, F. Complete determination of molecular orbitals by measurement of phase symmetry and electron density. *Nature Communications* **5,** 1–5 (2014).

123. Liu, Y., Bian, G., Miller, T. & Chiang, T.-C. Visualizing Electronic Chirality and Berry Phases in Graphene Systems Using Photoemission with Circularly Polarized Light. *Physical Review Letters* **107,** 166803 (2011).

124. Wang, Y. H., Hsieh, D., Pilon, D., Fu, L., Gardner, D. R., Lee, Y. S. & Gedik, N. Observation of a Warped Helical Spin Texture in Bi_2Se_3 from Circular Dichroism Angle-Resolved Photoemission Spectroscopy. *Physical Review Letters* **107,** 207602 (2011).

125. Ishida, Y., Kanto, H., Kikkawa, A., Taguchi, Y., Ito, Y., Ota, Y., Okazaki, K., Malaeb, W., Mulazzi, M., Okawa, M., Watanabe, S., Chen, C.-T., Kim, M., Bell, C., Kozuka, Y., Hwang, H. Y., Tokura, Y. & Shin, S. Common Origin of the Circular-Dichroism Pattern in Angle-Resolved Photoemission Spectroscopy of $SrTiO_3$ and $Cu_xBi_2Se_3$. *Physical Review Letters* **107,** 077601 (2011).

126. Bahramy, M., King, P., de la Torre, A., Chang, J., Shi, M., Patthey, L., Balakrishnan, G., Hofmann, P., Arita, R., Nagaosa, N. & Baumberger, F. Emergent quantum confinement at topological insulator surfaces. *Nature Communications* **3,** 1–7 (2012).

127. Scholz, M. R., Sánchez-Barriga, J., Braun, J., Marchenko, D., Varykhalov, A., Lindroos, M., Wang, Y. J., Lin, H., Bansil, A., Minár, J., Ebert, H., Volykhov, A., Yashina, L. V. & Rader, O. Reversal of the Circular Dichroism in Angle-Resolved Photoemission from Bi_2Te_3. *Physical Review Letters* **110,** 216801 (2013).

128. Bian, G., Zhang, L., Liu, Y., Miller, T. & Chiang, T.-C. Illuminating the Surface Spin Texture of the Giant-Rashba Quantum-Well System $Bi/Ag(111)$ by Circularly Polarized Photoemission. *Physical Review Letters* **108,** 186403 (2012).

129. Ryu, H., Song, I., Kim, B., Cho, S., Soltani, S., Kim, T., Hoesch, M., Kim, C. H. & Kim, C. Photon energy dependent circular dichroism in angle-resolved photoemission from Au(111) surface states. *Physical Review B* **95,** 115144 (2017).

130. Rosenzweig, P., Otto, S. & Fauster, T. Complex manifold of Rashba and image-potential states on Bi/Ag(111). *Physical Review B* **98,** 085430 (2018).

131. Tusche, C., Goslawski, P., Kutnyakhov, D., Ellguth, M., Medjanik, K., Elmers, H. J., Chernov, S., Wallauer, R., Engel, D., Jankowiak, A. & Schönhense, G. Multi-MHz time-of-flight electronic bandstructure imaging of graphene on Ir(111). *Applied Physics Letters* **108,** 261602 (2016).

132. Bentmann, H., Maaß, H., Krasovskii, E. E., Peixoto, T. R. F., Seibel, C., Leandersson, M., Balasubramanian, T. & Reinert, F. Strong Linear Dichroism in Spin-Polarized Photoemission from Spin-Orbit-Coupled Surface States. *Physical Review Letters* **119,** 106401 (2017).

133. Maaß, H. *Spin-dependence of angle-resolved photoemission from spin-orbit split surface states* PhD thesis (Julius-Maximilians-Universität Würzburg, 2016).

134. Clauberg, R., Gudat, W., Kisker, E., Kuhlmann, E. & Rothberg, G. M. Nature of the Resonant 6-eV Satellite in Ni: Photoelectron Spin-Polarization Analysis. *Physical Review Letters* **47,** 1314–1317 (1981).

135. Burnett, G. C., Monroe, T. J. & Dunning, F. B. High-efficiency retarding-potential Mott polarization analyzer. *Review of Scientific Instruments* **65,** 1893–1896 (1994).

136. Hillebrecht, F. U., Jungblut, R. M., Wiebusch, L., Roth, C., Rose, H. B., Knabben, D., Bethke, C., Weber, N. B., Manderla, S., Rosowski, U. & Kisker, E. High-efficiency spin polarimetry by very-low-energy electron scattering from Fe(100) for spin-resolved photoemission. *Review of Scientific Instruments* **73,** 1229–1234 (2002).

137. Vasilyev, D., Tusche, C., Giebels, F., Gollisch, H., Feder, R. & Kirschner, J. Low-energy electron reflection from Au-passivated Ir(0 0 1) for application in imaging spin-filters. *Journal of Electron Spectroscopy and Related Phenomena* **199,** 10–18 (2015).

138. Nuber, A. *Intrinsische und extrinsische Einflüsse auf zweidimensionale elektronische Zustände* PhD thesis (Julius-Maximilians-Universität Würzburg, 2011).

139. Schwalb, C. H., Sachs, S., Marks, M., Schöll, A., Reinert, F., Umbach, E. & Höfer, U. Electron Lifetime in a Shockley-Type Metal-Organic Interface State. *Physical Review Letters* **101,** 146801 (2008).

140. Niesner, D., Fauster, T., Dadap, J. I., Zaki, N., Knox, K. R., Yeh, P.-C., Bhandari, R., Osgood, R. M., Petrović, M. & Kralj, M. Trapping surface electrons on graphene layers and islands. *Physical Review B* **85,** 081402 (2012).

141. Miwa, J. A., Ulstrup, S., Sørensen, S. G., Dendzik, M., Čabo, A. G., Bianchi, M., Lauritsen, J. V. & Hofmann, P. Electronic Structure of Epitaxial Single-Layer MoS_2. *Physical Review Letters* **114,** 046802 (2015).

142. Reis, F., Li, G., Dudy, L., Bauernfeind, M., Glass, S., Hanke, W., Thomale, R., Schäfer, J. & Claessen, R. Bismuthene on a SiC substrate: A candidate for a high-temperature quantum spin Hall material. *Science* **357,** 287–290 (2017).

143. Tang, S., Zhang, C., Wong, D., Pedramrazi, Z., Tsai, H.-Z., Jia, C., Moritz, B., Claassen, M., Ryu, H., Kahn, S., Jiang, J., Yan, H., Hashimoto, M., Lu, D., Moore, R. G., Hwang, C.-C., Hwang, C., Hussain, Z., Chen, Y., Ugeda, M. M., Liu, Z., Xie, X., Devereaux, T. P., Crommie, M. F., Mo, S.-K. & Shen, Z.-X. Quantum spin Hall state in monolayer 1T'-WTe2. *Nature Physics* **13,** 683–687 (2017).

144. Xian, L., Paz, A. P., Bianco, E., Ajayan, P. M. & Rubio, A. Square selenene and tellurene: novel group VI elemental 2D materials with nontrivial topological properties. *2D Materials* **4,** 041003 (2017).

145. Hirayama, M., Okugawa, R., Ishibashi, S., Murakami, S. & Miyake, T. Weyl Node and Spin Texture in Trigonal Tellurium and Selenium. *Physical Review Letters* **114,** 206401 (2015).

146. Nakayama, K., Kuno, M., Yamauchi, K., Souma, S., Sugawara, K., Oguchi, T., Sato, T. & Takahashi, T. Band splitting and Weyl nodes in trigonal tellurium studied by angle-resolved photoemission spectroscopy and density functional theory. *Physical Review B* **95,** 125204 (2017).

147. Sakano, M., Hirayama, M., Takahashi, T., Akebi, S., Nakayama, M., Kuroda, K., Taguchi, K., Yoshikawa, T., Miyamoto, K., Okuda, T., Ono, K., Kumigashira, H., Ideue, T., Iwasa, Y., Mitsuishi, N., Ishizaka, K., Shin, S., Miyake, T., Murakami, S., Sasagawa, T. & Kondo, T. Radial Spin Texture in Elemental Tellurium with Chiral Crystal Structure. *Physical Review Letters* **124,** 136404 (2020).

148. Ast, C. R., Pacilé, D., Moreschini, L., Falub, M. C., Papagno, M., Kern, K., Grioni, M., Henk, J., Ernst, A., Ostanin, S. & Bruno, P. Spin-orbit split two-dimensional electron gas with tunable Rashba and Fermi energy. *Physical Review B* **77,** 081407 (2008).

149. Gierz, I., Meier, F., Dil, J. H., Kern, K. & Ast, C. R. Tuning the spin texture in binary and ternary surface alloys on Ag(111). *Physical Review B* **83,** 195122 (2011).

150. Ma, Y., Kou, L., Dai, Y. & Heine, T. Two-dimensional topological insulators in group-11 chalcogenide compounds: M_2Te (M=Cu,Ag). *Physical Review B* **93,** 235451 (2016).

151. Liu, B., Liu, J., Miao, G., Xue, S., Zhang, S., Liu, L., Huang, X., Zhu, X., Meng, S., Guo, J., Liu, M. & Wang, W. Flat AgTe Honeycomb Monolayer on Ag(111). *The journal of physical chemistry letters* **10,** 1866–1871 (2019).

152. Geldiyev, B. *One- and two-photon photoemission from Te/Ag(111)* MA thesis (Lehrstuhl fur Festkörperphysik, Friedrich-Alexander-Universität Erlangen-Nürnberg, 2019).

153. Biedermann, K., Regensburger, S., Fauster, T., Himpsel, F. J. & Erwin, S. C. Spin-split silicon states at step edges of Si(553)-Au. *Physical Review B* **85,** 245413 (2012).

154. Golias, E., Xenogiannopoulou, E., Tsoutsou, D., Tsipas, P., Giamini, S. A. & Dimoulas, A. Surface electronic bands of submonolayer Ge on Ag(111). *Physical Review B* **88,** 075403 (2013).

155. Wang, W., Sohail, H. M., Osiecki, J. R. & Uhrberg, R. I. G. Broken symmetry induced band splitting in the Ag_2Ge surface alloy on Ag(111). *Physical Review B* **89,** 125410 (2014).

156. Osiecki, J. R. & Uhrberg, R. I. G. Alloying of Sn in the surface layer of Ag(111). *Physical Review B* **87,** 075441 (2013).

157. Feng, B., Fu, B., Kasamatsu, S., Ito, S., Cheng, P., Liu, C.-C., Feng, Y., Wu, S., Mahatha, S. K., Sheverdyaeva, P., Moras, P., Arita, M., Sugino, O., Chiang, T.-C., Shimada, K., Miyamoto, K., Okuda, T., Wu, K., Chen, L., Yao, Y. & Matsuda, I. Experimental realization of two-dimensional Dirac nodal line fermions in monolayer Cu_2Si. *Nature Communications* **8,** 1–6 (2017).

158. Shockley, W. On the Surface States Associated with a Periodic Potential. *Physical Review Journals* **56,** 317–323 (1939).

159. Matzdorf, R. & Goldmann, A. Photo-hole lifetimes of adsorbate-bands at the Cu(110)(2×1)O surface. *Surface Science* **412-413,** 61–68 (1998).

160. Echenique, P., Berndt, R., Chulkov, E., Fauster, T., Goldmann, A. & Höfer, U. Decay of electronic excitations at metal surfaces. **52,** 219–317 (2004).

161. Cao, Y., Waugh, J. A., Zhang, X.-W., Luo, J.-W., Wang, Q., Reber, T. J., Mo, S. K., Xu, Z., Yang, A., Schneeloch, J., Gu, G. D., Brahlek, M., Bansal, N., Oh, S., Zunger, A. & Dessau, D. S. Mapping the orbital wavefunction of the surface states in three-dimensional topological insulators. *Nature Physics* **9,** 499–504 (2013).

162. Armbrust, N., Schiller, F., Güdde, J. & Höfer, U. Model potential for the description of metal/organic interface states. *Scientific Reports* **7** (2017).

163. Newns, D. M. Self-Consistent Model of Hydrogen Chemisorption. *Physical Review* **178,** 1123–1135 (1969).

164. Anderson, P. W. Localized Magnetic States in Metals. *Physical Review* **124,** 41–53 (1961).

165. Greiner, M. T., Jones, T. E., Beeg, S., Zwiener, L., Scherzer, M., Girgsdies, F., Piccinin, S., Armbrüster, M., Knop-Gericke, A. & Schlögl, R. Free-atom-like d states in single-atom alloy catalysts. *Nature Chemistry* **10,** 1008–1015 (2018).

166. Ast, C. R., Pacilé, D., Papagno, M., Gloor, T., Mila, F., Fedrigo, S., Wittich, G., Kern, K., Brune, H. & Grioni, M. Orbital selective overlayer-substrate hybridization in a Pb monolayer on Ag(111). *Physical Review B* **73,** 245428 (2006).

167. Fu, L. Hexagonal Warping Effects in the Surface States of the Topological Insulator Bi_2Te_3. *Physical Review Letters* **103,** 266801 (2009).

168. Souma, S., Kosaka, K., Sato, T., Komatsu, M., Takayama, A., Takahashi, T., Kriener, M., Segawa, K. & Ando, Y. Direct Measurement of the Out-of-Plane Spin Texture in the Dirac-Cone Surface State of a Topological Insulator. *Physical Review Letters* **106,** 216803 (2011).

169. Henk, J., Ernst, A., Eremeev, S. V., Chulkov, E. V., Maznichenko, I. V. & Mertig, I. Complex Spin Texture in the Pure and Mn-Doped Topological Insulator Bi_2Te_3. *Physical Review Letters* **108,** 206801 (2012).

170. Bentmann, H., Maaß, H., Braun, J., Seibel, C., Kokh, K. A., Tereshchenko, O. E., Schreyeck, S., Brunner, K., Molenkamp, L. W., Miyamoto, K., Arita, M., Shimada, K., Okuda, T., Kirschner, J., Tusche, C., Ebert, H., Minár, J. & Reinert, F. Profiling spin and orbital texture of a topological insulator in full momentum space. *Physical Review B* **103,** L161107 (2021).

171. Meier, F., Dil, H., Lobo-Checa, J., Patthey, L. & Osterwalder, J. Quantitative vectorial spin analysis in angle-resolved photoemission: Bi/Ag(111) and Pb/Ag(111). *Physical Review B* **77,** 165431 (2008).

172. Chen, G.-Y., Huang, A., Lin, Y.-H., Chen, C.-J., Lin, D.-S., Chang, P.-Y., Jeng, H.-T., Bihlmayer, G. & Hsu, P.-J. Orbital-enhanced warping effect in px,py-derived Rashba spin splitting of monatomic bismuth surface alloy. *npj Quantum Materials* **5** (2020).

173. Riley, J. M., Mazzola, F., Dendzik, M., Michiardi, M., Takayama, T., Bawden, L., Granerod, C., Leandersson, M., Balasubramanian, T., Hoesch, M., Kim, T. K., Takagi, H., Meevasana, W., Hofmann, P., Bahramy, M. S., Wells, J. W. & King, P. D. C. Direct observation of spin-polarized bulk bands in an inversion-symmetric semiconductor. *Nature Physics* **10,** 835–839 (2014).

174. Bawden, L., Riley, J. M., Kim, C. H., Sankar, R., Monkman, E. J., Shai, D. E., Wei, H. I., Lochocki, E. B., Wells, J. W., Meevasana, W., Kim, T. K., Hoesch, M., Ohtsubo, Y., Fèvre, P. L., Fennie, C. J., Shen, K. M., Chou, F. & King, P. D. C. Hierarchical spin-orbital polarization of a giant Rashba system. *Science advances* **1,** e1500495 (2015).

175. Cercellier, H., Fagot-Revurat, Y., Kierren, B., Reinert, F., Popović, D. & Malterre, D. Spin-orbit splitting of the Shockley state in the Ag/Au(111) interface. *Physical Review B* **70,** 193412 (2004).

176. Shen, Z.-X. & Sobota, J. Taking control of spin currents. *Nature* **549,** 464–465 (2017).

177. Schirone, S., Krasovskii, E. E., Bihlmayer, G., Piquerel, R., Gambardella, P. & Mugarza, A. Spin-Flip and Element-Sensitive Electron Scattering in the $BiAg_2$ Surface Alloy. *Physical Review Letters* **114,** 166801 (2015).

178. Ärrälä, M., Nieminen, J., Braun, J., Ebert, H. & Lindroos, M. Photon energy dependence of circular dichroism of the Au(111) surface state. *Physical Review B* **88,** 195413 (2013).

179. Neupane, M., Basak, S., Alidoust, N., Xu, S.-Y., Liu, C., Belopolski, I., Bian, G., Xiong, J., Ji, H., Jia, S., Mo, S.-K., Bissen, M., Severson, M., Lin, H., Ong, N. P., Durakiewicz, T., Cava, R. J., Bansil, A. & Hasan, M. Z. Oscillatory surface dichroism of the insulating topological insulator Bi_2Te_2Se. *Physical Review B* **88,** 165129 (2013).

180. Jung, W., Kim, Y., Kim, B., Koh, Y., Kim, C., Matsunami, M., Kimura, S., Arita, M., Shimada, K., Han, J. H., Kim, J., Cho, B. & Kim, C. Warping effects in the band and angular-momentum structures of the topological insulator Bi_2Te_3. *Physical Review B* **84,** 245435 (2011).

181. Panaccione, G., Vobornik, I., Fujii, J., Krizmancic, D., Annese, E., Giovanelli, L., Maccherozzi, F., Salvador, F., Luisa, A. D., Benedetti, D., Gruden, A., Bertoch, P., Polack, F., Cocco, D., Sostero, G., Diviacco, B., Hochstrasser, M., Maier, U., Pescia, D., Back, C. H., Greber, T., Osterwalder, J., Galaktionov, M., Sancrotti, M. & Rossi, G. Advanced photoelectric effect experiment beamline at Elettra: A surface science laboratory coupled with Synchrotron Radiation. *Review of Scientific Instruments* **80,** 043105 (2009).

182. Bigi, C., Das, P. K., Benedetti, D., Salvador, F., Krizmancic, D., Sergo, R., Martin, A., Panaccione, G., Rossi, G., Fujii, J. & Vobornik, I. Very efficient spin polarization analysis (VESPA): new exchange scattering-based setup for spin-resolved ARPES at APE-NFFA beamline at Elettra. *Journal of Synchrotron Radiation* **24,** 750–756 (2017).

183. Jozwiak, C., Park, C.-H., Gotlieb, K., Hwang, C., Lee, D.-H., Louie, S. G., Denlinger, J. D., Rotundu, C. R., Birgeneau, R. J., Hussain, Z. & Lanzara, A. Photoelectron spin-flipping and texture manipulation in a topological insulator. *Nature Physics* **9,** 293–298 (2013).

184. Tusche, C., Krasyuk, A. & Kirschner, J. Spin resolved bandstructure imaging with a high resolution momentum microscope. *Ultramicroscopy* **159,** 520–529 (2015).

185. Yaji, K., Harasawa, A., Kuroda, K., Li, R., Yan, B., Komori, F. & Shin, S. Rashba spin splitting of L -gap surface states on Ag(111) and Cu(111). *Physical Review B* **98,** 041404 (2018).

186. Lv, B. Q., Muff, S., Qian, T., Song, Z. D., Nie, S. M., Xu, N., Richard, P., Matt, C. E., Plumb, N. C., Zhao, L. X., Chen, G. F., Fang, Z., Dai, X., Dil, J. H., Mesot, J., Shi, M., Weng, H. M. & Ding, H. Observation of Fermi-Arc Spin Texture in TaAs. *Physical Review Letters* **115,** 217601 (2015).

187. Xu, S.-Y., Belopolski, I., Sanchez, D. S., Neupane, M., Chang, G., Yaji, K., Yuan, Z., Zhang, C., Kuroda, K., Bian, G., Guo, C., Lu, H., Chang, T.-R., Alidoust, N., Zheng, H., Lee, C.-C., Huang, S.-M., Hsu, C.-H., Jeng, H.-T., Bansil, A., Neupert, T., Komori, F., Kondo, T., Shin, S., Lin, H., Jia, S. & Hasan, M. Z. Spin Polarization and Texture of the Fermi Arcs in the Weyl Fermion Semimetal TaAs. *Physical Review Letters* **116,** 096801 (2016).

188. Noguchi, R., Kuroda, K., Yaji, K., Kobayashi, K., Sakano, M., Harasawa, A., Kondo, T., Komori, F. & Shin, S. Direct mapping of spin and orbital entangled wave functions under interband spin-orbit coupling of giant Rashba spin-split surface states. *Physical Review B* **95,** 041111 (2017).

189. Gotlieb, K., Li, Z., Lin, C.-Y., Jozwiak, C., Ryoo, J. H., Park, C.-H., Hussain, Z., Louie, S. G. & Lanzara, A. Symmetry rules shaping spin-orbital textures in surface states. *Physical Review B* **95,** 245142 (2017).

190. Yaji, K., Kuroda, K., Toyohisa, S., Harasawa, A., Ishida, Y., Watanabe, S., Chen, C., Kobayashi, K., Komori, F. & Shin, S. Spin-dependent quantum interference in photoemission process from spin-orbit coupled states. *Nature communications* **8,** 1–6 (2017).

191. Maaß, H., Bentmann, H., Seibel, C., Tusche, C., Eremeev, S. V., Peixoto, T. R. F., Tereshchenko, O. E., Kokh, K. A., Chulkov, E. V., Kirschner, J. & Reinert, F. Spin-texture inversion in the giant Rashba semiconductor BiTeI. *Nature Communications* **7,** 11621 (2016).

192. Crepaldi, A., Cilento, F., Zacchigna, M., Zonno, M., Johannsen, J. C., Tournier-Colletta, C., Moreschini, L., Vobornik, I., Bondino, F., Magnano, E., Berger, H., Magrez, A., Bugnon, P., Autès, G., Yazyev, O. V., Grioni, M. & Parmigiani, F. Momentum and photon energy dependence of the circular dichroic photoemission in the bulk Rashba semiconductors BiTeX (X=I, Br, Cl). *Physical Review B* **89,** 125408 (2014).

193. Xie, Z., He, S., Chen, C., Feng, Y., Yi, H., Liang, A., Zhao, L., Mou, D., He, J., Peng, Y., Liu, X., Liu, Y., Liu, G., Dong, X., Yu, L., Zhang, J., Zhang, S., Wang, Z., Zhang, F., Yang, F., Peng, Q., Wang, X., Chen, C., Xu, Z. & Zhou, X. J. Orbital-selective spin texture and its manipulation in a topological insulator. *Nature Communications* **5,** 4382 (2014).

194. Yazyev, O. V., Moore, J. E. & Louie, S. G. Spin Polarization and Transport of Surface States in the Topological Insulators Bi_2Se_3 and Bi_2Te_3 from First Principles. *Physical Review Letters* **105,** 266806 (2010).

195. Zhu, Z.-H., Veenstra, C., Zhdanovich, S., Schneider, M., Okuda, T., Miyamoto, K., Zhu, S.-Y., Namatame, H., Taniguchi, M., Haverkort, M., Elfimov, I. & Damascelli, A. Photoelectron Spin-Polarization Control in the Topological Insulator Bi_2Te_3. *Physical Review Letters* **112,** 076802 (2014).

196. Waugh, J. A., Nummy, T., Parham, S., Liu, Q., Zhang, X., Zunger, A. & Dessau, D. S. Minimal ingredients for orbital-texture switches at Dirac points in strong spin–orbit coupled materials. *npj Quantum Materials* **1** (2016).

197. Zhang, H., Liu, C.-X. & Zhang, S.-C. Spin-Orbital Texture in Topological Insulators. *Physical Review Letters* **111,** 066801 (2013).

198. Schüler, M., Giovannini, U. D., Hübener, H., Rubio, A., Sentef, M. A. & Werner, P. Local Berry curvature signatures in dichroic angle-resolved photoelectron spectroscopy from two-dimensional materials. *Science advances* **6,** eaay2730 (2020).

199. Figgemeier, T. *Wachstum, Präparation und elektronische Struktur der Weyl-Halbmetalle TaP und TaAs* MA thesis (Julius-Maximilians-Universität Würzburg, 2018).

200. Lv, B. Q., Xu, N., Weng, H. M., Ma, J. Z., Richard, P., Huang, X. C., Zhao, L. X., Chen, G. F., Matt, C. E., Bisti, F., Strocov, V. N., Mesot, J., Fang, Z., Dai, X., Qian, T., Shi, M. & Ding, H. Observation of Weyl nodes in TaAs. *Nature Physics* **11,** 724–727 (2015).

201. Hasan, M. Z., Xu, S.-Y., Belopolski, I. & Huang, S.-M. Discovery of Weyl Fermion Semimetals and Topological Fermi Arc States. *Annual Review of Condensed Matter Physics* **8,** 289–309 (2017).

202. Hofmann, P., Søndergaard, C., Agergaard, S., Hoffmann, S. V., Gayone, J. E., Zampieri, G., Lizzit, S. & Baraldi, A. Unexpected surface sensitivity at high energies in angle-resolved photoemission. *Physical Review B* **66,** 245422 (2002).

203. Strocov, V. N., Schmitt, T., Flechsig, U., Schmidt, T., Imhof, A., Chen, Q., Raabe, J., Betemps, R., Zimoch, D., Krempasky, J., Wang, X., Grioni, M., Piazzalunga, A. & Patthey, L. High-resolution soft X-ray beamline ADRESS at the Swiss Light Source for resonant inelastic X-ray scattering and angle-resolved photoelectron spectroscopies. *Journal of Synchrotron Radiation* **17,** 631–643 (2010).

204. Fadley, C. X-ray photoelectron spectroscopy: Progress and perspectives. *Journal of Electron Spectroscopy and Related Phenomena* **178-179,** 2–32 (2010).

205. Day, R. P., Zwartsenberg, B., Elfimov, I. S. & Damascelli, A. Computational framework chinook for angle-resolved photoemission spectroscopy. *npj Quantum Materials* **4** (2019).

206. Sun, Y., Zhang, Y., Felser, C. & Yan, B. Strong Intrinsic Spin Hall Effect in the TaAs Family of Weyl Semimetals. *Physical Review Letters* **117,** 146403 (2016).

207. Bhowal, S. & Satpathy, S. Intrinsic orbital moment and prediction of a large orbital Hall effect in two-dimensional transition metal dichalcogenides. *Physical Review B* **101,** 121112 (2020).

208. Bhowal, S. & Satpathy, S. Intrinsic orbital and spin Hall effects in monolayer transition metal dichalcogenides. *Physical Review B* **102,** 035409 (2020).

209. Sahu, P., Bhowal, S. & Satpathy, S. Effect of the inversion symmetry breaking on the orbital Hall effect: A model study. *Physical Review B* **103,** 085113 (2021).

210. Krasovskii, E. E. & Schattke, W. Calculation of the wave functions for semi-infinite crystals with linear methods of band theory. *Physical Review B* **59,** R15609–R15612 (1999).

211. Christensen, N. E. High-energy band structure of gold. *Physical Review B* **13,** 2698–2701 (1976).

List of Publications

- **M. Ünzelmann**, H. Bentmann, T. Figgemeier, P. Eck, J. N. Neu, B. Geldiyev, F. Diekmann, S. Rohlf, J. Buck, M. Hoesch, M. Kalläne, K. Rossnagel, R. Thomale, T. Siegrist, G. Sangiovanni , D. Di Sante and F. Reinert, Momentum-space signatures of Berry flux monopoles in the Weyl semimetal TaAs, *Nature Communications*, **12**, 1–7 (2021)

- **M. Ünzelmann**, H. Bentmann, P. Eck, T. Kißlinger, B. Geldiyev, J. Rieger, S. Moser, R. C. Vidal, K. Kißner, L Hammer, M. A. Schneider, T. Fauster, G. Sangiovanni, D. Di Sante and F. Reinert, Orbital-Driven Rashba Effect in a Binary Honeycomb Monolayer AgTe, *Physical Review Letters* **124**, 176401 (2020)

- M. M. Otrokov, I. I. Klimovskikh, H. Bentmann, D. Estyunin, A. Zeugner, Z. S. Aliev, S. Gaß, A. U. B. Wolter, A. V. Koroleva, A. M. Shikin, M. Blanco-Rey, M. Hoffmann, I. P. Rusinov, A. Yu. Vyazovskaya, S. V. Eremeev, Yu. M. Koroteev, V. M. Kuznetsov, F. Freyse, J. Sánchez-Barriga, I. R. Amiraslanov, M. B. Babanly, N. T. Mamedov, N. A. Abdullayev, V. N. Zverev, A. Alfonsov, V. Kataev, B. Büchner, E. F. Schwier, S. Kumar, A. Kimura, L. Petaccia, G. Di Santo, R. C. Vidal, S. Schatz, K. Kißner, **M. Ünzelmann**, C. H. Min, S. Moser, T. R. F. Peixoto, F. Reinert, A. Ernst, P. M. Echenique, A. Isaeva and E. V. Chulkov, Prediction and observation of an antiferromagnetic topological insulator, *Nature* **576**, 416–422 (2019)

- R. C. Vidal, H. Bentmann, T. R. F. Peixoto, A. Zeugner, S. Moser, C.-H. Min, S. Schatz, K. Kißner, **M. Ünzelmann**, C. I. Fornari, H. B. Vasili, M. Valvidares, K. Sakamoto, D. Mondal, J. Fujii, I. Vobornik, S. Jung, C. Cacho, T. K. Kim, R. J. Koch, C. Jozwiak, A. Bostwick, J. D. Denlinger, E. Rotenberg, J. Buck, M. Hoesch, F. Diekmann, S. Rohlf, M. Kalläne, K. Rossnagel, M. M. Otrokov, E. V. Chulkov, M. Ruck, A. Isaeva and F. Reinert, Surface states and Rashba-type spin polarization in antiferromagnetic $MnBi_2Te_4$(0001), *Physical Review B* **100**, 121104(R) (2019)

- C.-H. Min, H. Bentmann, J. N. Neu, P. Eck, S. Moser, T. Figgemeier, **M. Ünzelmann**, K. Kissner, P. Lutz, R. J. Koch, C. Jozwiak, A. Bostwick, E. Rotenberg, R. Thomale, G. Sangiovanni, T. Siegrist, D. Di Sante and F. Reinert, Orbital Fingerprint of Topological Fermi Arcs in the Weyl Semimetal TaP, *Physical Review Letters* **122**, 116402 (2019)

Danksagung

Angekommen an diesem Teil der Doktorarbeit gehen mir so viele Emotionen und Gedanken durch den Kopf, dass es gar nicht so leicht ist, diese wirklich zu sortieren. Das Wissen, dass mit der Abgabe der Arbeit eine unglaublich gute Zeit zu Ende geht, stimmt einen wehmütig. Doch gerade dabei kommt so viel Dankbarkeit auf, gegenüber all den Menschen, die zum Gelingen dieser Arbeit – auf wissenschaftlicher, aber genauso auch zwischenmenschlicher Ebene – beigetragen haben. Ich fühle mich nicht zu Dank verpflichtet, sondern bin einfach dankbar. Allen Personen, die sich an dieser Stelle angesprochen fühlen, danke ich von ganzem Herzen! Mein besonderer Dank gilt

- meinem Doktorvater Prof. Dr. Friedrich Reinert, dafür, mich am Lehrstuhl aufgenommen und mir die Möglichkeit gegeben zu haben, meine Arbeit dort anzufertigen. Vorallem danke ich für das tolle Arbeitsklima, den damit verbundenen freundlichen und offenen Umgang sowie die großen wissenschaftlichen Freiheiten und Möglichkeiten, die mir jeder Zeit gegeben waren. Besonders danke ich außerdem für die vielen Gelegenheiten zur Teilnahme an Konferenzen und Synchrotronstrahlzeiten in verschiedenen Ländern. Danke für die insgesamt so schöne Zeit. Ich freue mich auf alles was kommt!

- Dr. Hendrik Bentmann, für all die Hilfe, die Betreuung, sämtliche Tipps, Ratschläge und Anregungen und ein immer offenes Ohr. Danke für das riesige Interesse an meiner Forschung und meinen Ideen sowie für das gemeinsame Anfertigen verschiedener Manuskripte. Besonders bedanken möchte ich mich außerdem für die vielen physikalischen Diskussionen, Kaffepausen und die gemeinsam verbrachte Zeit auf Strahlzeiten.

- allen Lehrstuhlkolleg/innen der EP-7 für die schöne gemeinsame Zeit. Insbesondere danke ich meinen Bürokolleg/innen Katharina Kißner, Raphael Crespo Vidal und Tim Figgemeier für all die Gespräche, Diskussionen, die gegenseitige Hilfe, das Singen, Mundtrompeten und Flossdancen sowie für Kaffee und Tee. Dass die Bürozeit so abrupt durch eine Pandemie beendet wurde, ist so unendlich schade; umso dankbarer bin ich für unseren privaten Kontakt! Vielen Dank an Dr. Peter Lutz sowie Katharina Kißner für das Einlernen im Labor. Darüberhinaus danke ich Dr. Chul-Hee Min, Dr. Thiago Peixoto und Dr. Celso Fornari für die Hilfe und die gemeinsame Zeit auf Messzeiten sowie dem Durchbringen der zahlreichen Strahlzeitanträge. Großer Dank gilt außerdem den Studierenden Dean Nestorov, Tim Figgemeier, Johannes

Heßdörfer und Robert Zürl, deren Master- bzw. Bachelorarbeiten ich betreuen durfte, für die große Hilfe und Unterstützung insbesondere beim Wachstum, der Präparation und der Charakterisierung der unterschiedlichen Proben. Besonders hervorheben möchte ich Tim, dessen Arbeit an TaAs nicht mit seiner Masterarbeit endete; das gesamte Weyl-Projekt ist eine Gemeinschaftsarbeit, an der er einen entsprechend großen Anteil hat. Am wichtigesten jedoch ist, dass aus dieser Zusammenarbeit Freundschaft wurde, die auch außerhalb der Uni bzw. der Petra-Halle Bestand hat. *Eine Weihnachtsfeier organisieren wir noch (aber dann ist Schluss, ...bestimmt...).* Darüberhinaus danke ich Begmuhammet Geldiyev, für die Durchführung der 2PPE-Messungen an AgTe in Erlangen und dafür, die Untersuchungen von Tellurfilmen an der EP-7 weiterzuführen. Ich bedanke mich außerdem bei den Ehemaligen Sonja Schatz, Dr. Manuel Grimm, Dr. Martin Graus und Dr. Achim Schöll, die gerade in meiner Anfangszeit am Lehrstuhl dafür gesorgt haben, dass ich mich gut einfinde und vorallem wohlfühle. Besonderer Dank gilt dem Rest des harten Kerns, Philipp Kagerer und Tim Figgemeier, für die enthusiastische und konsequente Teilnahme an analog und (gezwungenermaßen) auch digital durchgeführten Afterwork-Veranstaltungen.

- Rosmarie Riegel und Hiltrud Eaton für jegliche nicht-physikalische und organisatorische Hilfe. Darüberhinaus danke ich den Mitarbeitern der wissenschaftlichen Werkstätten und der Heliumverflüssigung.

- Phillip Eck, Dr. Domenico Di Sante und Prof. Dr. Giorgio Sangiovanni ohne deren enormen Beitrag in Form von DFT Rechnungen – sowohl zu AgTe als auch TaAs – man diese Arbeit in der Form nicht hätte anfertigen können. Besonders bedanken möchte ich mich dabei für die nette und unkomplizierte Zusammenarbeit, die von Beginn meiner Doktorandenzeit an die komplette Zeit über stattgefunden hat. Danke vorallem auch für das Einbringen von zahlreichen Ideen und die unkomplizierte Bereitstellung von Rechnungen und Daten.

- den Kielern Dr. Matthias Kalläne, Dr. Sebastian Rohlf, Florian Diekmann, Dr. Jens Buck sowie allen anderen Mitarbeitern aus der Gruppe von Prof. Dr. Kai Roßnagel, die ich bei den zahlreichen ASPHERE Messzeiten kennenlernen durfte und die mir insbesondere bei der Handhabung der Apparatur eine große Hilfe waren. Ohne deren unendliche Geduld und Hilfsbereitschaft wären die TaAs Messungen nicht möglich gewesen. Am meisten bedanken möchte ich mich aber für die schöne gemeinsame Zeit, für Bildschirmlagerfeuer während den Nachtschichten und für Hoverboard-Fahrstunden. Weiterer Dank gilt außerdem Dr. Moritz Hoesch sowie allen anderen P04 Mitarbeitern.

- den FKP'lern Prof. Dr. Thomas Fauster, Tilman Kißlinger, Dr. Lutz Hammer, Prof. Dr. M. Alexander Schneider, Dr. Sebastian Otto, Philipp

Rosenzweig, Janek Rieger sowie allen weiteren "alten" Kollegen. Bedanken möchte ich mich zunächst dafür, während meiner Zeit der Zulassungsarbeit und als Masterand mein Interesse für Forschung und insbesondere für die Photoemission und Oberflächenphysik geweckt zu haben. Bedanken möchte ich mich außerdem dafür, dass ich sowohl zu der ein oder anderen Feier als auch noch zweimal zum Messen nach Erlangen kommen durfte. Insgesamt gilt mein Dank vorallem denen, die am AgTe-Projekt beteiligt waren und dieses damit entscheidend voranbrachten. Mich freut es, dass es ein fortbestehendes Interesse an Tellurfilmen auf Metalloberflächen gibt.

- Dr. Jennifer Neu und Prof. Dr. Theo Siegrist für das Wachstum, die Charakterisierung und das Bereitstellen der TaAs, TaP und NbP Kristalle. Ohne diese Kollaboration wäre das gesamte Weyl-Projekt nicht zustande gekommen.

- allen Kolleg/innen an den verschiedenen Synchrotronstrahlungsquellen für die große Hilfe bei der Durchführung der Experimente. Großer Dank gilt Jonathan Denlinger, Aaron Bostwick, Chris Jozwiak und Eli Rotenberg vom ALS in Berkeley. Besonders bedanken möchte ich mich an dieser Stelle bei Dr. Simon Moser für seine Hilfe bei den Messungen bei MAESTRO, seine insgesamt riesige Hilfsbereitschaft – unabhängig davon ob es um Physik oder Umzüge geht – sowie die Möglichkeit, mit zum PTB zu fahren. Danke außerdem für die interessanten Diskussionen über Meister Mosers Matrixelemente! Davon habe ich immer sehr profitiert. Darüberhinaus vielen Dank an das gesamte Team der APE Beamline bei ELETTRA in Trieste.

- meiner gesamten Familie und all meinen Freunden für ihre Unterstützung zu jeder Zeit und bei jeder Entscheidung, die ich getroffen habe; danke, dass ihr immer da seid! Besonderer Dank gilt meinen Eltern Regina und Klaus Ünzelmann, die mir nicht nur ermöglicht haben zu studieren, sondern mir vorallem in jeder Beziehung Rückhalt bieten, Vorbilder sind und wegen denen ich der bin, der ich bin.

- meiner Freundin Larissa für den Rückhalt, die Geduld, die Liebe; für alles!